



LUND UNIVERSITY

Modeling of new particle formation and growth in the atmospheric boundary layer

Öström, Emilie

2017

Document Version:

Publisher's PDF, also known as Version of record

[Link to publication](#)

Citation for published version (APA):

Öström, E. (2017). *Modeling of new particle formation and growth in the atmospheric boundary layer*. [Doctoral Thesis (compilation), Centre for Environmental and Climate Science (CEC)]. Lund University, Faculty of Science, Centre for Environmental and Climate research (CEC) & Department of Physics, Division of Nuclear Physics.

Total number of authors:

1

General rights

Unless other specific re-use rights are stated the following general rights apply:

Copyright and moral rights for the publications made accessible in the public portal are retained by the authors and/or other copyright owners and it is a condition of accessing publications that users recognise and abide by the legal requirements associated with these rights.

- Users may download and print one copy of any publication from the public portal for the purpose of private study or research.
- You may not further distribute the material or use it for any profit-making activity or commercial gain
- You may freely distribute the URL identifying the publication in the public portal

Read more about Creative commons licenses: <https://creativecommons.org/licenses/>

Take down policy

If you believe that this document breaches copyright please contact us providing details, and we will remove access to the work immediately and investigate your claim.

LUND UNIVERSITY

PO Box 117
221 00 Lund
+46 46-222 00 00



Modeling of new particle formation and growth in the atmospheric boundary layer

EMILIE ÖSTRÖM

ENVIRONMENTAL SCIENCE | DEPARTMENT OF PHYSICS & CEC | LUND UNIVERSITY



Modeling of new particle formation and growth in the atmospheric boundary layer

Emilie Öström (née Hermansson)



LUND
UNIVERSITY

DOCTORAL DISSERTATION


by due permission of the Faculty of Science, Lund University, Sweden.
To be defended in the Rydberg Hall, Physics Department, Professorsgatan 1,
Lund. October 27th 2017 09:00.

Faculty opponent

Dr. Harri Kokkola, Finnish Meteorological Institute, Atmospheric Research Centre
of Eastern Finland

Organization LUND UNIVERSITY		Document name: Doctoral thesis	
Centre for Environmental and Climate Research (CEC) & Dept. Physics, Div. Nuclear Physics		Date of issue: 2017-10-03	
Author: Emilie Öström			
Modeling of new particle formation and growth in the atmospheric boundary layer			
<p>Abstract</p> <p>Atmospheric aerosols affect climate, but to what degree still remains one of the largest uncertainties in global climate models. To improve the representation of aerosols in future climate models we need a greater understanding of aerosol processes. In this thesis the process-based model ADCHEM has been used and further developed to study aerosol processes. Specifically; new particle formation and growth have been studied in boreal environments, but also over polluted marine environments.</p> <p>In the boreal forest, particles largely grow by condensation of oxidized organic compounds to form secondary organic aerosols (SOA). There are thousands of organic oxidation products and far from all are known, causing large uncertainties in the modeled aerosol population. Models that simulate the growth of particles must therefore make assumptions of which organic compounds, or group of compounds, that are potential condensation products and what properties they have. The modeled mass concentration of the resulting aerosol particles are dependent on the estimated saturation vapor pressures of the condensation products, but also on the further gas-phase aging of the organic oxidation products.</p> <p>Many models underestimate the SOA mass; one explanation could be missing gas-phase oxidation products. A newly proposed reaction pathway of monoterpenes containing endocyclic double bonds that form highly oxidized multifunctional organic molecules (HOMs) in the gas phase was implemented in the gas-phase chemistry module. The model was tested against observed HOM gas-phase composition and observed SOA formation during α-pinene ozonolysis experiments and field measurements. The model was able to reproduce the observed new particle formation events and particle growth if the HOM mechanism was included.</p> <p>ADCHEM was also used to study new particle formation in the marine boundary layer, to address whether particles formed over sea, or emitted anthropogenic gases over sea, have any importance on the cloud formation potential over land. If the air mass over the marine boundary layer is already polluted due to continental emissions, the importance of new particle formation over sea seems to be minor. The new particle formation and the further growth of particles are sensitive to the concentration of sulfuric acid. If strong new particle formation and rapid growth occurs close to the coast, the formed particles will act as a condensation sink for newly formed particles over land, with the potential to decrease the amount of particles that can act as cloud condensation nuclei over land.</p> <p>To achieve a greater understanding of aerosol processes and reduce the uncertainties in models, it is important that models are evaluated against observations at various locations and conditions. Much work remains to ensure that models give the right results for the right reasons.</p>			
Key words: New particle formation, secondary organic aerosols, process-based modeling, climate			
Supplementary bibliographical information		Language: English	
ISSN and key title		ISBN 978-91-7753-427-3	
Recipient's notes		Number of pages <u>200</u>	Price
		Security classification	

I, the undersigned, being the copyright owner of the abstract of the above-mentioned dissertation, hereby grant to all reference sources permission to publish and disseminate the abstract of the above-mentioned dissertation.

Signature  Date 2017-09-20

Modeling of new particle formation and growth in the atmospheric boundary layer

Emilie Öström (née Hermansson)



LUND
UNIVERSITY

Coverphoto by Emilie Öström

Copyright Emilie Öström

Faculty of Science
Centre for Environmental and Climate Research
Department of Physics, Division of Nuclear Physics

ISBN 978-91-7753-427-3 (print)

ISSN 978-91-7753-428-0 (pdf)

Printed in Sweden by Media-Tryck, Lund University
Lund 2017



Tillägnas Mathias och Oliver

Contents

Papers included in this thesis	1
Author's contributions to the papers	3
Related publications	4
Abbreviations and symbols	5
Populärvetenskaplig sammanfattning	7
Aerosolers klimatpåverkan	7
Modellering för en bättre framtid	8
Prologue	11
Aim	12
Background	15
Atmospheric aerosols	15
Atmospheric aerosols in the Anthropocene	17
Atmospheric aerosols in models	18
ADCHEM	21
Aerosol dynamics	22
BSOA formation	24
Biogenic gas emissions	25
Gas-phase chemistry	25
Growth of SOA	27
Nanoparticle growth in the subarctic	29
Different approaches to model gas-phase chemistry	29
Modeled BSOA formation compared to observations	33
New particle formation in polluted marine environments	43
Particle number size distribution at the coastal stations	43
Conclusions and outlook	47
Acknowledgements	49
References	51

Papers included in this thesis

- I. **Hermansson, E.**, Roldin, P., Rusanen, A., Mogensen, D., Kivekäs, N., Väänänen, R., Boy, M., and Swietlicki, E. (2014). Biogenic SOA formation through gas-phase oxidation and gas-to-particle partitioning – a comparison between process models of varying complexity. *Atmospheric Chemistry and Physics*, 14, 11853-11869, doi:10.5194/acp-14-11853-2014
- II. **Öström, E.**, Putian, Z., Schurgers, G., Mishurov, M., Kivekäs, N., Lihavainen, H., Ehn, M., Rissanen, M.P., Kurtén, T., Boy, M., Swietlicki, E. and Roldin, P. (2016). Modeling the role of highly oxidized multifunctional organic molecules for the growth of new particles over the boreal forest region. *Atmospheric Chemistry and Physics*, 17, 8887-8901, doi: 10.5194/acp-17-8887-2017
- III. Roldin, P., **Öström, E.**, Kurtén, T., Olenius, T., Rissanen, M., Rantala, P., Hao, L., Kulmala, M., Virtanen, A., Riipinen, I., Ehn, M. and Boy, M. Constraining the concentrations and contribution of highly oxidized organic molecules to the growth of new particles over the Boreal forest. Manuscript in preparation.
- IV. **Öström, E.**, Roldin, P., Julin, J., Massling, A., Lange, R., Glasius, M., Berg-Malmberg, V., Manninen, H., Kalivitis N., Olenius, T., Riipinen, I. and Kristensson, A. Potential influence on CCN from new particle formation and emissions in the polluted marine boundary layer. Manuscript in preparation.

Author's contributions to the papers

- I. I set up the ADCHEM model simulations with the appropriate input data. I did all model runs and analyzed the model and measurement data. I wrote the majority of the paper.
- II. I had a substantial part in the work of translating ADCHEM from Matlab to Fortran. I was involved in the selection of new particle formation events to be evaluated with ADCHEM against observations and setting up the model on Lunarc. I did all model runs and analyzed the model and measurement data. I wrote the majority of the paper.
- III. I helped setting up and running the model on Lunarc. I assisted the lead author in writing the part of the manuscript concerning ADCHEM.
- IV. I was involved in the selection of particle size distribution data to evaluate with ADCHEM against observations. I analyzed the model data from ADCHEM and wrote most part of the manuscript concerning ADCHEM.

Related publications

Roldin, P., Eriksson, A., Nordin, E., **Hermansson, E.**, Mogensen, D., Rusanen, A., Boy, M., Swietlicki, E., Svenningsson, B., Zelenyuk, A. and Pagels, J. (2014) Modelling non-equilibrium secondary organic aerosol formation and evaporation with the aerosol dynamics, gas- and particle-phase chemistry kinetic multilayer model ADCHAM. *Atmospheric Chemistry and Physics*, 14, 11853-11869, doi: 10.5194/acp-14-7953-2014

Martinsson, J., Abdul Azeen, H., Sporre, M. K., Bergström, R., Ahlberg, E., **Öström E.**, Kristensson, A., Swielicki, E. and Eriksson Stenström K. (2017) Carbonaceous aerosol source apportionment using the Aethalometer model - evaluation by radiocarbon and levoglucosan analysis at a rural background site in southern Sweden. *Atmospheric Chemistry and Physics*, 17, 4265-4281, doi: 10.5194/acp-17-4265-2017

Eriksson, A.C., Wittbom, C., Roldin, P., Sporre, M., **Öström, E.**, Nilsson, P., Martinsson, J., Rissler, J., Nordin, E. Z., Svenningsson, B., Pagels, J. and Swietlicki, E. Diesel soot aging in urban plumes within hours under cold dark and humid conditions. Accepted for publication, Scientific Reports.

Abbreviations and symbols

1DVBS	one-dimensional Volatility Basis Set
2DVBS	two-dimensional Volatility Basis Set
ACDC	Atmospheric Cluster Dynamics Code
ADCHAM	Aerosol Dynamics gas- and particle phase chemistry model for laboratory CHAMber studies
ADCHEM	Aerosol Dynamics, gas and particle phase CHEMistry and radiative transfer model
BSOA	Biogenic Secondary Organic Aerosol
BVOC	Biogenic Volatile Organic Compound
CCN	Cloud Condensation Nuclei
ESM	Earth System Model
GDAS	Global Data Assimilation System
HOM	Highly Oxidized Multifunctional organic molecule
HYSPLIT	Hybrid Single Particle Lagrangian Integrated Trajectory model
IN	Ice Nuclei
IPCC	Intergovernmental Panel on Climate Change
JPAC	Jülich Plant Atmosphere Chamber
KPP	Kinetic PreProcessor
MCM	Master Chemical Mechanism
NPF	New Particle Formation
SOA	Secondary Organic Aerosol
VBS	Volatility Basis Set
WHO	World Health Organization

Populärvetenskaplig sammanfattning

Globalt sett lever 8 av 10 människor i miljöer där luftföroreningar i form av små luftburna partiklar ligger över riktlinjer satta av världshälsoorganisationen WHO. WHO uppskattar även att luftföroreningar ligger bakom 3.7 miljoner dödsfall varje år. Värst är det i delar av Asien, men även här i Sverige är luftkvaliteten ett problem; i Skåne t ex bedöms den genomsnittliga livslängden förkortas med 7-10 månader på grund av luftföroreningar.

Luftburna partiklar, eller aerosoler, påverkar också klimatet genom att dels interagera med det inkommande solljuset och dels vara en nödvändig kugge när moln bildas. Till skillnad från växthusgaser såsom koldioxid så har aerosoler överlag en kylande effekt på klimatet. Det betyder alltså att de till viss del kan dämpa en del av den pågående globala uppvärmningen.

Då utsläpp av både luftföroreningar och växthusgaser påverkar klimatet och vår hälsa och dessutom ofta har samma källor finns det mycket att vinna på att bekämpa utsläppen tillsammans.

Aerosolers klimatpåverkan

Genom årtal av forskning och observationer står det idag klart att vi människor påverkar klimatet främst genom vårt ökande utsläpp av växthusgaser. Hur och till vilken grad aerosolers roll spelar in i detta utgör den största osäkerheten i hur mänsklig aktivitet förändrar klimatet.

En förklaring till varför det är så ligger i att en aerosol inte är den andra lik - till skillnad från t ex två koldioxidmolekyler som alltid ser likadana ut. Aerosolpartiklar kan vara allt från nanometer stora till ungefär en 10-dels millimeter (vilket ungefär motsvarar tjockleken på ett hårstrå, vilket då betyder att en nanometer är 100 000 gånger mindre än tjockleken på hårstrået!). Beroende på var aerosolerna kommer ifrån och vad som händer med dem i atmosfären kan de dessutom bestå av hundratusentals olika kemiska ämnen och antingen vara flytande eller fasta partiklar eller ett mellanting av dessa. Hur aerosolerna påverkar klimatet beror på deras egenskaper och vissa aerosoler har därför en kylande effekt

på klimatet medan andra har en värmande effekt. Sett från ett globalt perspektiv så dominerar den kylande effekten.

Aerosolernas egenskaper påverkar också molnens egenskaper. För att en molndroppe ska kunna bildas krävs det nämligen en aerosolpartikel. Olika aerosolpartiklar har olika lätt att plocka upp vatten och bilda molndroppar. Hur många partiklar det finns påverkar även molnets egenskaper, vilket i sin tur påverkar hur mycket solljus som molnet reflekterar tillbaka ut i rymden. Ju mer solljus som reflekteras desto mindre solljus når ner till jordytan. Denna växelverkan mellan aerosoler och moln utgör den största osäkerheten i aerosolernas klimatpåverkan.

I storstäder är det vanligt att partiklarna uppkommer till följd av mänskliga aktiviteter, framförallt förbränningsprocesser, men de flesta aerosoler i atmosfären har naturliga källor såsom uppvirvlat stoft från t ex öknar, saltpartiklar från haven och partiklar och gaser från vulkanutbrott. Sedan industrialismens start har antalet partiklar ökat då utsläpp orsakade av oss människor har ökat.

Modellering för en bättre framtid

För att uppskatta vilken effekt den ökande koncentrationen av både växthusgaser och aerosoler har på framtidens klimat så används avancerade klimatmodeller. Dessa modeller används som beslutsunderlag för t ex utsläppsregleringar. För att aerosolprocesser ska kunna representeras i klimatmodeller krävs förenklade beskrivningar av dessa.

Det övergripande målet med denna avhandling har varit att, med hjälp av en detaljerat modell, studera specifika aerosolprocesser. Den ökande kunskapen om dessa aerosolprocesser kan förhoppningsvis ligga till grund för hur aerosoler bättre kan representeras i framtida klimatmodeller. Framförallt har vi studerat hur gaser i atmosfären kan skapa partiklar och sedan växa dem större, samt vad som sedan händer med dessa partiklar i atmosfären. En del av de gaser som gör att partiklarna växer till större storlekar är organiska, som dels har sitt ursprung från mänskliga aktiviteter, men framförallt har uppkommit av naturliga anledningar som till exempel utsöndring av gaser från träd. Då det är många hundratusentals organiska ämnen som är inblandade i tillväxten av aerosolpartiklarna går det inte att representera detta i en global klimatmodell utan att först förenkla processen. Vi behöver därför veta mer om hur organiska ämnen bidrar till tillväxt av aerosolpartiklar för att kunna göra representativa förenklningar och här kan mer detaljerade modeller, såsom den jag har använt mig av i denna avhandling, komma väl till pass.

Trots att aerosoler inte bara påverkar vår hälsa utan också klimatet så är det vanligt att luftföroreningar bekämpas som ett problem skilt från klimatförändringen. Det kan vara ett kostsamt misstag eftersom utsläpp av växthusgaser och partiklar ofta har samma källor vilket gör att mer kostnadseffektiva lösningar kan hittas om problemen bekämpas tillsammans. Okunskap om hur olika komponenter i klimatsystemet påverkar varandra kan dessutom leda till oönskade effekter. Till exempel så kan en minskad koncentration av partiklar i atmosfären, som har haft en kylande effekt på klimatet, leda till att den globala uppvärmningen förstärks om inte utsläpp av växthusgaser minskas ännu mer för att motverka detta. För trots sin dämpande effekt på uppvärmningen är luftföroreningar fortfarande ett stort hälsoproblem och långt ifrån önskvärda. Det viktiga bör vara att ta välgrundade beslut, och här kan klimatmodeller spela en viktig roll. Därför utvecklas dessa modeller ständigt för att kunna ta hänsyn till allt fler processer och på så sätt kunna ge oss bättre prognoser om vårt framtida klimat.

Prologue

LONDON... Implacable November weather... Smoke lowering down from chimney-pots, making a soft black drizzle, with flakes of soot in it as big as full-grown snow-flakes — gone into mourning, one might imagine, for the death of the sun... Fog everywhere. Fog up the river, where it flows among green aits and meadows; fog down the river, where it rolls defiled among the tiers of shipping and the waterside pollutions of a great (and dirty) city.

-Charles Dickens, Bleak house (Dickens, 1853).

Even though Charles Dickens wrote the above introduction to Bleak House in 1853, this description of a much polluted city would fit well into the great smog event that occurred in London in December 1952. During a few cold winter days airborne pollutants, mainly from coal burning activities, accumulated over the city, causing one of the worst air-pollution events in the United Kingdom where thousands of people died prematurely as a consequence. These airborne pollutants include tiny aerosol particles (from nanometer to micrometers in diameter), which apart from being health hazardous also affect our climate.

Due to the adverse health effects of aerosols, legislations on how to reduce the emission of aerosol particles and their precursor gases have been developed, and during the last 10 to 20 years, mainly Europe and North America have seen reductions in air pollutants where the mass concentration of the smallest particles (smaller than 2.5 μm) has decreased with $\sim 35\%$ (EEA, 2014; EPA, 2016). They do however still remain a global problem as 80 % of the world's population is estimated to be exposed to air pollution levels that exceed those recommended by the World Health Organization (WHO) (Rao et al., 2013).

As mentioned earlier, aerosol particles also affect our climate. Some of them scatter solar radiation back to space and therefore cool the climate and some of them absorb radiation, causing a warming effect. Overall, aerosols cool the climate as they are also an important part of the formation of clouds (IPCC, 2013). Greenhouse gases on the other hand warm our climate when gases such as carbon dioxide trap the outgoing radiation from the surface. Since the beginning of the industrial era we have been and still are emitting so much greenhouse gases that we are now risking pushing Earth out of the stable environmental conditions we have enjoyed the last 10 millennia (Rockström et al., 2009). In order to avoid this,

governments around the world met during the United Nations climate change negotiations in Paris 2015 and agreed to try to limit the warming to 1.5 °C above pre-industrial levels.

Traditionally, the air pollution problem and the threat that climate change poses have been treated separately when developing emission control strategies. This might be a costly mistake when possible co-benefits might be overlooked. Since many of the sources of air pollution and greenhouse gases are the same (mainly burning of fossil fuels), the mitigation strategies of climate change should also be able to reduce air pollution. In fact, model studies have shown that applying strategies to reduce greenhouse gases also leads to reduction in air pollutants (Radu et al., 2016; Rafaj et al., 2013) and that the costs of adopting climate change policies can partly be offset by the decrease in air pollution, causing economic benefits for society such as better health and less acidification and eutrophication in our ecosystems (Rafaj et al., 2013; Schucht et al., 2015).

By treating the air pollution and climate change problem separately, there is also a risk of solving one problem and making the other worse. For example; reducing aerosols might actually, in the short term, make climate change worse due to their overall cooling effect on climate. This is of course still true when the problems are treated together, but the knowledge will hopefully lead to more informed decision making, where a much needed reduction in air pollution is followed by even more powerful policies on climate change.

In order to make the best decisions it is important that these are based on the best available knowledge. The cooling effect that aerosols have on climate is still uncertain and more research is needed in the field. This thesis is a small part of that research.

Aim

Even though much research has gone into assessing the effects that aerosols have on the global energy budget of the Earth system, aerosols and aerosol-cloud interactions are still the most uncertain processes in the radiative budget (IPCC, 2013). The spatial and temporal scales used by models to understand and predict our climate are much bigger than the scales used when modeling aerosol and cloud properties and processes, meaning that they cannot be physically represented in climate models. So in order to include aerosol and cloud processes, these have to be represented in a simplified way, using parameters that are resolved by global climate models. This is often done by developing conceptual models to study the individual processes.

In this thesis, the process-based model ADCHEM (Roldin et al., 2011) has been further developed and used to study aerosol properties. The overall aim has been to achieve a greater understanding of the formation processes of aerosols in the atmosphere in order to improve the representation of aerosols in future climate models.

More specifically:

- Aerosol formation and subsequent growth have been modeled with ADCHEM in boreal environments where new particle formation events are frequent during summertime (Paper I-III).
- ADCHEM has also been used to study aerosols over polluted marine environments with the aim to investigate the importance of these aerosol particles on the cloud formation potential over land (Paper IV).

Background

Atmospheric aerosols

Atmospheric aerosols, which are solid or liquid particles suspended in the atmosphere, affect both human health and the Earth system. Directly through their radiative properties or their involvement in the cloud-forming process they have the ability to change climate patterns and act as a coupling mechanism between the atmosphere and the Earth surface. Particles can be emitted directly to the atmosphere or be formed in the atmosphere by gas-to-particle conversion processes. In the former case they are called primary particles and can originate from natural sources such as dust, volcanic eruption and sea spray, or they can be emitted through anthropogenic activities, e.g. fuel combustion. Particles formed in the atmosphere are called secondary particles and an important natural source of these is the vegetation which emits biogenic volatile organic compounds (BVOCs) (Carslaw et al., 2010). Figure 1 presents typical particle number and volume size distribution for different environments.

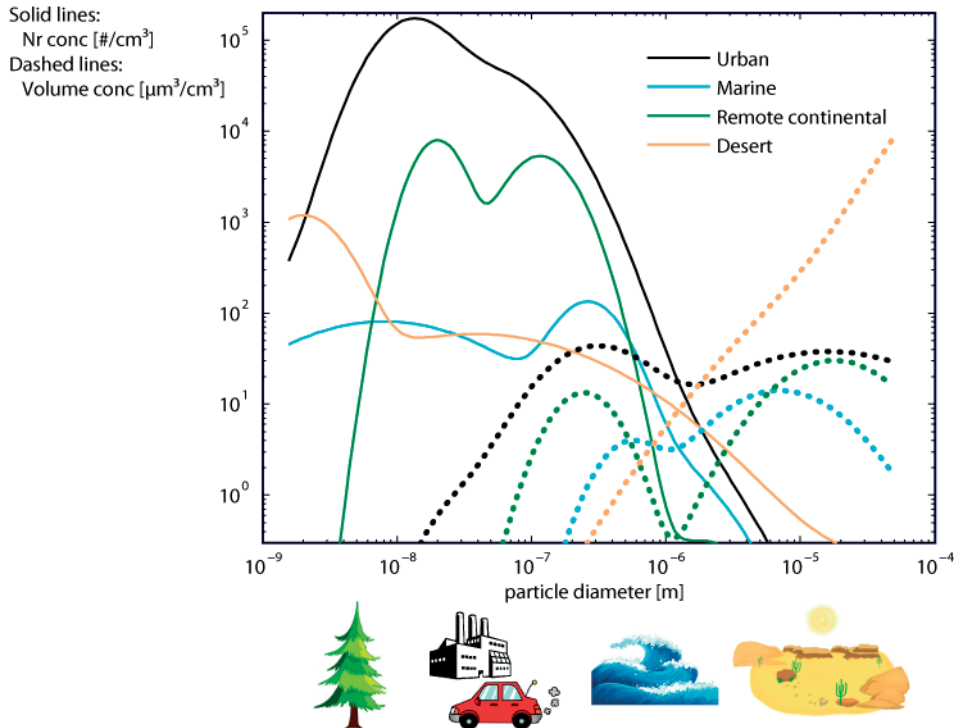


Figure 1. Typical aerosol size distributions in different environment (Jaenicke, 1993). The solid lines are the particle number size distributions and the dashed lines are the particle volume size distributions. The illustrations at the bottom show typical particle sources (primary or secondary), emitting particles (or gases in the case of secondary particles) of different sizes.

From Fig. 1 it is clear that atmospheric aerosols span over large size and concentration ranges. The size of the aerosol particles affects their impact on both climate and human health. It is also the size of the particles that determines how long they will stay suspended in the atmosphere, which may vary from less than a day to a few weeks. The smallest particles, less than $0.1 \mu\text{m}$ are rapidly lost by collision and coalescence with larger particles (coagulation). Particles larger than $2.5 \mu\text{m}$ also have a short residence time due to sedimentation and wet deposition. Between these size ranges are the accumulation mode particles (0.1 to $2.5 \mu\text{m}$) which have the longest residence times because the removal mechanisms are least effective in this size range (Seinfeld and Pandis, 2006). The residence time of aerosol particles is short compared to most atmospheric greenhouse gases.

Atmospheric aerosols affect the climate by interacting with the incoming shortwave radiation from the sun and the longwave radiation emitted from the earth system. Particles can both scatter and absorb radiation, to what amount

depends on the wavelength of the incident radiation, the size of the particles and the optical properties of the particles.

Particles in the accumulation mode are highly efficient at scattering solar radiation resulting in less incoming solar energy reaching the surface which consequently cools the Earth. As opposed to most atmospheric particles, soot particles are strong absorbers of shortwave radiation and will instead warm the Earth.

All cloud droplets are formed around particles. Aerosols that serve as nuclei for water droplet formation and ice crystals thus have a profound effect not only on climate but also the entire Earth system. These cloud condensation nuclei (CCN) or ice nuclei (IN) alter the global radiation balance indirectly by affecting the formation and properties of clouds.

Atmospheric aerosols in the Anthropocene

For about the last 11 millennia Earth has been in a geological epoch called the Holocene, an interglacial epoch characterized by climatic stability and good living conditions for us humans. This has enabled us to go from hunter and gatherers to living in the high technology society of today. More and more scientific evidence are however implying that human activities are on the way to push Earth out of the stable environmental conditions of Holocene, to a new epoch – the Anthropocene (Crutzen, 2002; Rockström et al., 2009).

Since the beginning of the industrialization, the amount of aerosols in the atmosphere has increased due to human activities. This has affected both Earth's radiation balance (the climate) and our health. The inhaled particles can cause respiratory and cardiovascular diseases, and the WHO estimated that in 2012, ambient air pollution was responsible for 3.7 million deaths (WHO Regional Office for Europe, 2015).

In the latest assessment report (AR5) from the Intergovernmental Panel on Climate Change (IPCC) they conclude that since the beginning of the industrial era (1750) until present (2011), anthropogenic aerosols have caused an estimated radiative forcing of -0.82 W/m^2 (IPCC, 2013), meaning that they have changed the energy balance of the earth system, causing a cooling. This can be put into relation with the estimated positive forcing caused by the well-mixed greenhouse gases of 3 W/m^2 . Figure 2 summarizes the estimation of radiative forcing for the main drivers of climate change. The uncertainty range of the radiative forcing of each component is represented by the horizontal black bars. The large uncertainty range for the total anthropogenic radiative forcing in 2011 relative to 1750 is largely due to the uncertainty of the aerosol forcing.

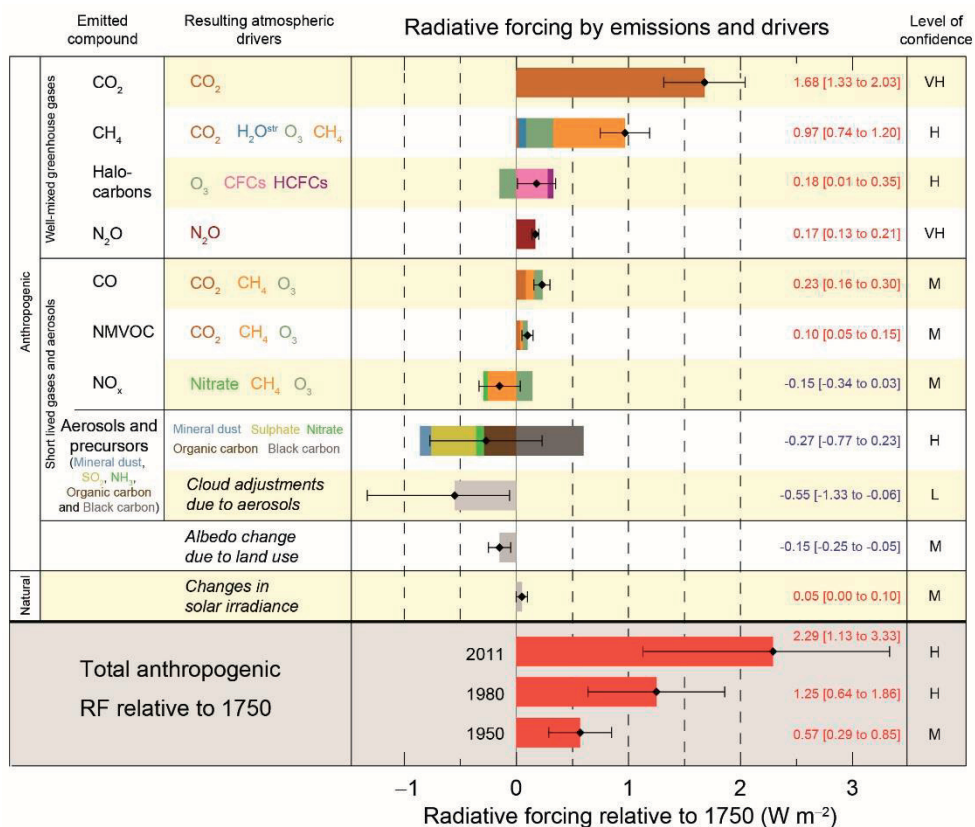


Figure 2. Radiative forcing estimates in 2011 relative to 1750 and aggregated uncertainties for the main drivers of climate change (from IPCC 2013, figure SPM.5). Values are global average radiative forcing, partitioned according to the emitted compounds or processes that result in a combination of drivers. The best estimates of the net radiative forcing are shown as black diamonds with corresponding uncertainty intervals; the numerical values are provided on the right of the figure, together with the confidence level in the net forcing (VH – very high, H – high, M – medium, L – low, VL – very low). Albedo forcing due to black carbon on snow and ice is included in the black carbon aerosol bar. Small forcings due to contrails (0.05 W m⁻², including contrail induced cirrus), and HFCs, PFCs and SF6 (total 0.03 W m⁻²) are not shown. Concentration-based RFs for gases can be obtained by summing the like-coloured bars. Volcanic forcing is not included as its episodic nature makes it difficult to compare to other forcing mechanisms. Total anthropogenic radiative forcing is provided for three different years relative to 1750.

Atmospheric aerosols in models

The effect aerosols have on the radiative energy budget is more difficult to predict than the effect that the greenhouse gases have. This is partly due to the shorter lifetime of aerosols compared to most greenhouse gases, causing the spatial distribution of aerosols to be greater. All aerosol particles are unique and span several magnitudes in sizes and once in the atmosphere they undergo chemical and physical aging.

Climate models, like the ones assessed in AR5 (discussed in previous section) are continuously being developed and improved. Many of the models are now being developed into Earth System Models (ESMs) that couple the atmosphere, terrestrial biosphere, cryosphere and ocean. These models have the ability to include biogeochemical cycles that respond to climate change; e.g. the increased emission of BVOCs in a warmer climate leading to an increased loading of biogenic secondary organic aerosols (BSOA) and a cooling effect (Carslaw et al., 2010; Kulmala et al., 2004; Tsigaridis and Kanakidou, 2007).

The BVOC-BSOA climate feedback does however include many complex processes which are not fully understood. Due to their complexity, the processes need to be simplified in order to be included in ESMs. But before developing methods to represent the BVOC-BSOA climate link in ESMs, a process-based understanding is needed in order to make the parameterizations more credible.

SOA formation includes processes both in the gas- and particle phase. The gas-phase chemistry includes a vast number of organic and some inorganic compounds that react and evolve in the atmosphere. How they react will influence their ability to condense on the aerosol particles. All reactions cannot be explicitly included in climate models and different methods exist that more or less include lumping different organic products into groups that can be assumed to have similar properties, e.g. similar volatility (e.g. Donahue et al., 2006; Odum et al., 1996). Compounds that continue to react in the particle phase influence properties and the further growth of SOA (Roldin et al., 2014).

It is not only the complexity involved in SOA formation, but also the time-scale on which it takes place (seconds to hours), that makes it impossible to treat SOA formation explicitly in climate models. With the use of small-scaled process models and observation, SOA formation can however be studied, and parameterizations suited for larger-scale climate models can be developed.

ADCHEM

ADCHEM can be used as a two, one or zero dimensional Lagrangian aerosol dynamics model. In this thesis ADCHEM has been used either as a zero-dimensional box model (paper I) or as a one-dimensional column model (paper II, III and IV), moving along air-mass trajectories.

The structure of ADCHEM used in this thesis is illustrated in Fig. 3. The aerosol dynamics include homogeneous nucleation, coagulation, condensation/evaporation and particle deposition.

Different gas-phase models can be coupled to the model domain and dry deposition of selected gases is included (in paper IV; wet deposition of selected gases are also modeled). In order to solve the gas-phase chemistry, which includes photochemical reactions, the radiant intensity from the sun is needed (also called radiance). Based on the top of the atmosphere solar radiance, a radiative transfer model (Roldin et al., 2011) is used to provide the gas-phase code with the spectral actinic flux, which is the wavelength dependent radiance incident from all directions.

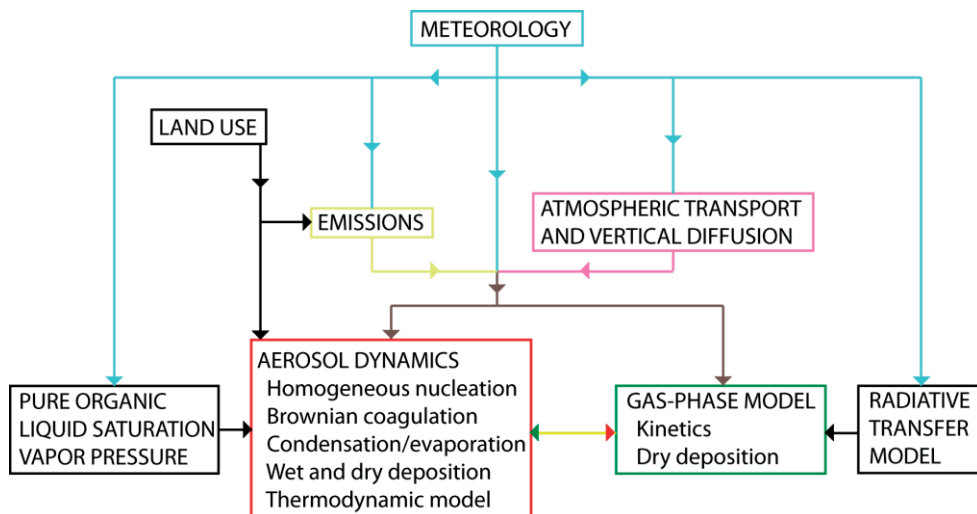


Figure 3. An illustration of the model structure of ADCHEM. The different boxes are described in this chapter.

When ADCHEM is used as a 1D-column model (paper II, III and IV) the diffusion equation in the vertical direction, z , needs to be solved:

$$\frac{dc}{dt} = \frac{\partial}{\partial z} \left(K_z \frac{\partial c}{\partial z} \right)$$

;where K_z is the eddy diffusion coefficient and c is the concentration of an arbitrary species. The eddy diffusion coefficient can be parameterized in different ways, in this thesis K_z depends on the height above ground, the friction velocity and the height of the atmospheric boundary layer (Jericevic et al., 2010).

Since ADCHEM is a Lagrangian model, it follows air-mass trajectories. The trajectories are calculated using the Hybrid Single Particle Lagrangian Integrated Trajectory model (HYSPLIT) (Draxler and Rolph, 2013) with meteorological data from the Global Data Assimilation System (GDAS) (downloaded from NOAA Air Resource Laboratory Real-time Environmental Application and Display sYstem (READY) (Rolph, 2016)). Along the trajectories, gas and particle emission are fed to the model as input data.

ADCHEM was originally written in MatLab, but has during the work of this thesis been translated into FORTRAN. This was mainly done so that the gas-phase chemistry more easily could be solved using the Kinetic PreProcessor (KPP) (Damian et al., 2002). This increased the efficiency of the code which was needed as the gas-phase chemistry was extended from about 100 reactions (Roldin et al., 2011) to thousands of reactions (paper I, II, III and IV). ADCHEM has also been adapted so it can be used on a high performance computing (HPC) cluster available at the center for scientific and technical computing at Lund University called Lunarc.

Aerosol dynamics

Aerosol dynamics change the number and/or mass concentration of particle populations over time. Coagulation will conserve the mass concentration but decrease the number concentration. There are different coagulation mechanisms, the work in this thesis include Brownian coagulation which depends on the size of the particles and particle diffusion.

Homogeneous nucleation is the formation of stable clusters about 1 nm, from gas molecules. The formation rate of 1.5 nm clusters, $J_{1.5}$, is often correlated to sulfuric acid concentration with a proportionality coefficient, k :

$$J_{1.5} = k[H_2SO_4]^x$$

;where x is found from empirical studies to be 1 or 2 (e.g. Kuang et al., 2008; Kulmala et al., 2006; Sipilä et al., 2010; Weber et al., 1997). The correlation

coefficient varies substantially depending on where and when the nucleation event occurs. Other empirical mechanisms can be used, Paasonen et al. (2010) tested several relationships between both sulfuric acid and organics and the formation rate. In paper II, the following mechanism was used:

$$J_{1.5} = k[H_2SO_4] \cdot [org]$$

;where $[org]$ is the concentration of low volatile organic vapors.

In paper III and IV the binary nucleation scheme, Atmospheric Cluster Dynamics Code (ACDC) (Olenius et al., 2013), was implemented in ADCHEM. This scheme calculates the formation, growth and evaporation of NH_3 - H_2SO_4 clusters, and the new particle formation is thus dependent of sulfuric acid and ammonia.

Atmospheric particles are lost to the surface either by dry or wet deposition. Dry deposition speed is often modeled with a resistor model and depends on the aerodynamic resistance, resistance to molecular diffusion very close to the surface and sedimentation. Most particles are however lost to the surface via wet deposition. Wet deposition is often divided into in-cloud scavenging and below-cloud scavenging. In this work only below-cloud scavenging is considered (except in paper IV where in-cloud scavenging is parameterized), and an empirical parameterization as a function of precipitation rate and particle size, based on measurement from Hyytiälä, is used (Laakso et al., 2003).

Condensation is the growth of particles as gas molecules diffuse to the surface of the particles and change phase. The growth rate, I_q , depends on the mass transfer coefficient k and the difference in concentration of the condensable compound q far from the particle surface, C_q , and its equilibrium concentration on the surface, $C_{q,s}$:

$$I_q = k_q(C_q - C_{q,s})$$

The equilibrium concentration of the compound is calculated from its pure liquid saturation vapor pressure, that is; the equilibrium vapor pressure of the compound over a flat surface composed of only compound q . When a compound is in equilibrium with the particle phase, no net transport occurs between the phases. Small particles cannot be considered to have flat surfaces, and furthermore, most particles are composed of many compounds. To calculate the equilibrium vapor pressure of the compound, these effects are therefore taken into consideration and $C_{q,s}$ therefore depends on the size, or curvature, of the particle the compound condenses upon (the Kelvin effect). Furthermore; the ability of a compound to partition to the particle phase also depends on the composition of the particle and the interaction between the molecules in the solution (Raoult's law). The mass transfer coefficient, k_q , includes the molecular diffusion coefficient that needs to be corrected for when the particle sizes are not comparable to the distance between molecular collisions (Fuchs and Sutugin, 1971).

BSOA formation

The boreal forest is suitable for studying BSOA formation. New particle formation (NPF) events are frequent here during the months with sunlight when adequate temperatures are reached and the oxidation products from gases emitted by the trees provide the material needed for the particles to grow. Figure 4 shows a typical NPF event at the research station in Pallas, northern Finland.

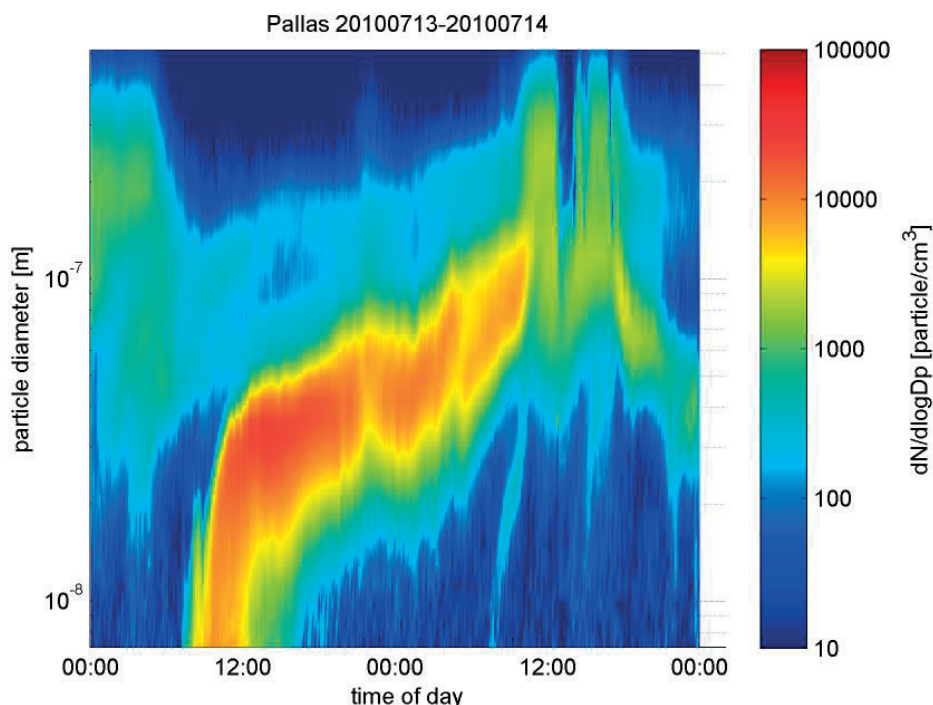


Figure 4. Measured number size distribution with a differential mobility particle sizer during a new particle formation event the 13th-14th of July 2010 in Pallas.

New particles are formed from molecular clusters that activate and start to grow by condensation of low volatile vapors. The further growth of these particles proceeds by condensation and/or coagulation. However, if the background air already consists of many particles, the vapors available for condensation might condense on these particles instead of the newly formed and thus inhibit the growth of the smallest particles. The larger background particles might also coagulate with the newly formed particles, disrupting the new particle formation event. Particle concentration often decreases the morning after the event due to vertical mixing as the boundary layer height increases. Other mechanisms which can decrease the

particle concentration are dry and wet deposition. To be able to accurately model an event like this all of the above processes need to be understood and parameterized.

While sulfuric acid is an important compound for molecule cluster formation, studies have shown that its concentration is too low in remote areas like the boreal forest to explain the subsequent growth of the newly formed clusters (Boy et al., 2005; Weber et al., 1997). Instead, BVOCs emitted by the trees and oxidized in the atmosphere play an important role for the growth of the particles (Kulmala et al., 2013). The focus of paper I, II and III was to get a better understanding of the gas to particle conversion process. A process that includes the emission and aging of the biogenic gas precursors and the condensation and evaporation of these gases to, respectively, from the particle phase. Many uncertainties are involved in these steps, largely due to the vast number of oxidation products, of which many are unknown. The aim of paper I was to compare different approaches to model the aging of the gas precursors, in paper II and III the modeled SOA formation is compared with measurements.

Biogenic gas emissions

The boreal forest emits many biogenic volatile organic compounds. The emission depends on the tree species and environmental conditions like temperature and sunlight.

In paper I, the BVOC emissions in the boreal forest were assumed to be represented by the monoterpene α -pinene. A relatively simple approach was used to estimate the emission using the same emission potential for the entire region since it was assumed to consist only of coniferous trees with the same biomass density (Tunved et al., 2006).

Instead of assuming a homogeneous vegetation cover, which are in most cases a too simplistic approach; vegetation models can be used to estimate this. Species specific emission potentials can then be assigned. In paper II, the dynamic vegetation model LPJ-GUESS (Smith et al., 2014) was used, while the MEGAN model (Guenther et al., 2012) was applied in paper III and IV.

Gas-phase chemistry

BVOCs are oxidized by ozone, the hydroxyl radical and the nitrate radical, often in many subsequent steps, creating a vast number of oxidation products. Due to the amount of oxidation products, and the fact that far from all are known, gas-phase

chemistry models need to be simplified. In paper I, three model approaches was explored: two volatility basis sets and one near-explicit scheme.

The oxidation products can be lumped into different bins depending on their volatility. Products that end up in the same bin represent one hypothetical oxidation product. Since the volatility range of the products often spans over several order of magnitudes, the volatility bins are logarithmically spaced. This method of lumping oxidation products was proposed by Donahue et al. (2006) and is known as the volatility basis set (VBS) approach.

In a one-dimensional VBS (1DVBS) only the volatility of the oxidation products are tracked as they are oxidized further in the gas-phase. The oxidation is assume to reduce the volatility as functional groups are added and a typical 1DVBS scheme moves the products down one volatility bin per oxidation step (Bergström et al., 2012; Lane et al., 2008). Oxidation can also lead to molecules being fragmented. This fragmentation generally leads to an increase in volatility as the carbon chain of the molecule breaks.

One way to include fragmentation during the chemical aging of the oxidation products is to include another dimension in the VBS, making it a two-dimensional VBS (2DVBS). In paper I, a 2DVBS, based on studies by Donahue et al. (2011) and Jimenez et al. (2009), where volatility and oxygen-to-carbon (O:C) atomic ratio were tracked, was tested to be able to include fragmentation.

A more computational heavy way to estimate the oxidation products is to use near-explicit chemical schemes where the degradation of the precursor is described with explicit chemistry reactions up to a certain point where the products are lumped into groups. Master Chemical Mechanism (MCM) (Jenkin et al., 1997; Saunders et al., 2003) is an example of a near-explicit scheme, which was one of the three model approaches tested in paper I. Table 1 summarizes the three different approaches described above.

Table 1. Details of three gas-phase schemes used in this thesis.

Gas-phase schemes	Distribution of first stable oxidation products	Gas-phase kinetics
1DVBS	Volatility distribution based on chamber studies	Products react with OH to reduce volatility
2DVBS	Volatility distribution based on chamber studies O : C-ratio as a function of volatility	Products react with OH to reduce or increase volatility based on their O : C-ratio
Near-explicit schemes (e.g. MCM)	Chemical mechanisms (e.g. MCM) where volatility is estimated by group contribution methods	Chemical mechanisms (e.g. MCM)

Models that use the 1DVBS to describe the aging of BVOCs, such as terpenes, often overestimate the SOA formation since fragmentation is not modeled explicitly (Lane et al., 2008; Murphy and Pandis, 2009). In a 2DVBS, the fragmentation can be parameterized with e.g. the O:C-ratio. The 2DVBS however demands more computational power since the number of products are increased. Both VBS schemes are empirical in their nature, and how the products are distributed and moved between the bins are mostly based on chamber measurements at relatively fixed conditions: conditions which might change during the SOA formation process and during future climate warming.

None of the model approaches above include highly oxidized multifunctional organic molecules (HOMs) formed from autoxidation. In recent studies these compounds have been detected (Ehn et al., 2014) and even though they are only a minor fraction of all oxidation products they probably play an important part in SOA formation. The importance of HOMs during new particle formation events is investigated in paper II (at the subarctic station in Pallas) and in Paper III (at the boreal station in Hyttiälä).

Growth of SOA

The growth of SOA depends on both the properties of the gases that are available for condensation and the particles on which those gases condense upon. In ADCHEM the mass transfer between the gas and particle phase is solved every time step by calculating the equilibrium between the phases. In paper I, the particles are assumed to be well-mixed liquid droplets and the equilibrium between the gas and particle phase is offset mainly by temperature changes and changes in the concentration of the condensable gases. Paper II and III also include a detailed particle-phase chemistry module, adopted from the ADCHAM model (Roldin et al., 2014), to include the effect of particle acidity and humidity on growth. Furthermore, a kinetic multilayer model (Roldin et al., 2014) is included to treat the mass transfer limited gas to particle partitioning.

Nanoparticle growth in the subarctic

In order to study the processes behind BSOA formation in chamber or ambient atmospheric environments, an aerosol dynamics, gas- and particle phase model has been used. In paper I we show that the gas-phase chemistry of the compounds involved in BSOA formation greatly influence particle growth. Due to the vast number of compounds and the need to simplify the chemistry, especially in large-scale global models, the uncertainties involved in the gas-phase chemistry are large. To reduce the uncertainties, observations are needed both in the gas- and particle phase. In paper III, a recently proposed formation mechanism of highly oxidized multifunctional organic molecules (HOMs) believed to be important for BSOA formation is developed and tested against chamber measurements. The result from this study is then implemented in atmospheric trajectory models in paper II and III. Results from these papers imply that the HOMs are an important part of BSOA formation but that it might not be enough to only consider gas-phase oxidation followed by partitioning to the particle phase but also reactions in the particle phase.

Different approaches to model gas-phase chemistry

In paper I, gas-phase mechanisms with different complexities describing the oxidation of α -pinene were modeled along an air mass trajectory in the northern Europe subarctic region (Fig. 5). We tested three different mechanisms (MCM, 1DVBS and 2DVBS, described in the section Gas-phase chemistry), with the aim to see how the complexity of these schemes affected the BSOA formation.

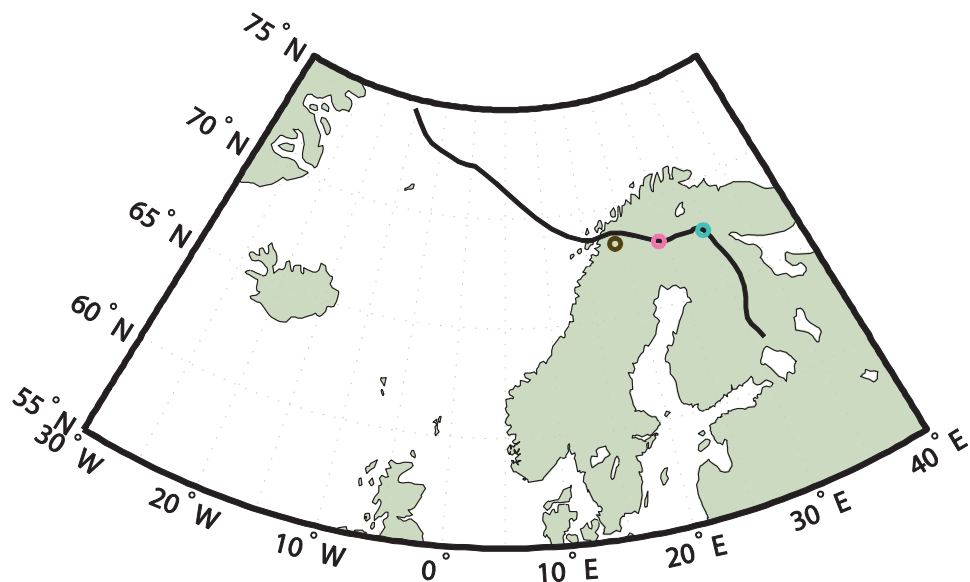


Figure 5. The studied air-mass trajectory, starting over northern Atlantic and passing the three measurement stations; Abisko (brown circle), Pallas (pink circle) and Värriö (blue circle).

α -pinene reacts with O_3 , OH and NO_3 in the atmosphere producing oxidation products. The first stable products are called first generation products and these products will in turn react and produce more compounds. This process is referred to as chemical aging. Out of the three mechanisms tested, MCM was the most complex scheme, producing 153 condensable oxidation products based on laboratory and theoretical data for studied chemical reactions, or based on the functional groups of the products for unstudied reactions. The 1DVBS and 2DVBS schemes produced 12 and 144 products respectively, where the products were not followed explicitly but lumped into groups depending on their volatility determined from chamber studies and, in the case of the 2DVBS, their O:C ratio.

From Fig. 6 it is evident that the distribution of the first generation products (grey areas) produced by the three mechanisms differs both in volatility (saturation concentration) and O:C ratio. The three mechanisms also handle the aging of these products differently and when the air mass has reached Pallas (18 hours downwind from the coast), a spread in the distribution of the products in particle phase between the mechanisms (pink areas) is evident. Since the volatility affects the equilibrium partitioning from gas to particle phase, this will influence the growth of the particles, and the 2DVBS gives considerable higher particle mass concentrations than the two other mechanisms.

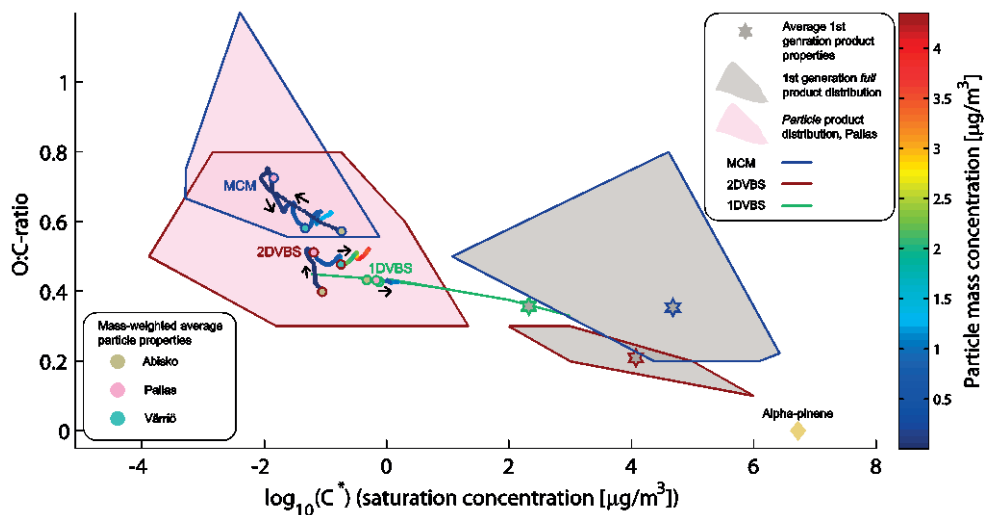


Figure 6. Distribution of oxidation products. The grey areas are the first-generation distributions of the oxidation products (in gas or particle phase) in the MCM (enclosed with blue lines), 2DVBS (brown lines) and 1DVBS (green lines), where the stars represent the corresponding mass-weighted average properties. The pink areas are the distributions of the products in particle phase at Pallas. Also shown are the time evolutions (in the direction of the respective arrows) of the mass-weighted average particle properties and SOA concentration along the air-mass trajectory starting from Abisko (beige circles) and passing Pallas (pink circles) and Värriö (blue circles).

The VBS schemes have many free variables that can be set by the user, e.g. the amount of groups to lump the products into and how to distribute them in the volatility space, the aging rate and temperature response of the products. Furthermore, fragmentation needs to be handled since far from all reactions lead to products of lower volatility as functional groups are added, but some instead lead to fragmentation as their carbon chains break, causing an increase in volatility of the resulting products.

In paper I, we tweaked some of the free variables in the 2DVBS scheme to test how sensitive the BSOA formation was to different parameters. In Fig. 7, the particle mass concentration along the studied air-mass trajectory is shown for different versions of the 2DVBS, including the base-case version (brown line) and the MCM base case (dashed blue line). In Fig. 7a parameters involving the properties of the first generation products have been tweaked, which caused the particle mass concentration to differ by up to a factor of ~ 3 between the different versions. The different versions of the 2DVBS concerning further aging of the products caused an even larger variation, up to a factor of ~ 7 (Fig. 7b).

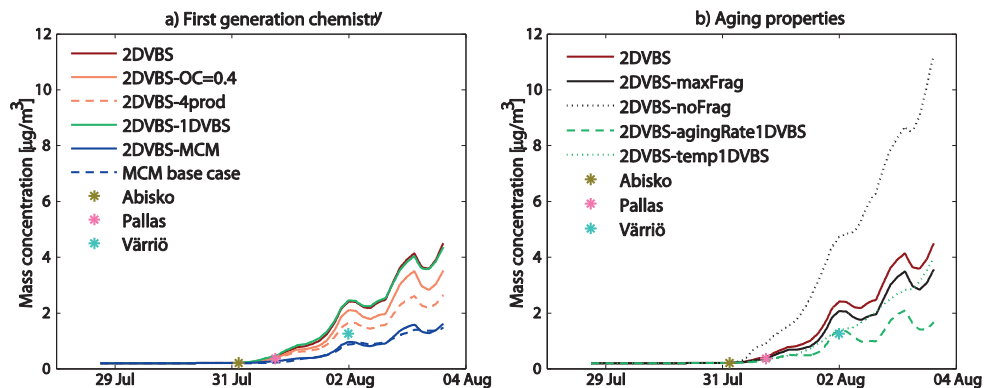


Figure 7. Particle growth along the air-mass trajectory modeled with different versions of the 2DVBS. In (a) different parameterizations of first-generation chemistry are tested and in (b) different parameterizations of gas-phase aging are tested.

The base-case 2DVBS sorts the first generation products into 7 volatility groups (with saturation concentrations from 0 to 6 $\mu\text{g}/\text{m}^3$) based on mass yields from chamber measurements and mass balance calculations (Donahue et al., 2009), with O:C-ratios of the products as a function of their volatility. In the 1DVBS the products are sorted into 4 volatility bins (from 0 to 3 $\mu\text{g}/\text{m}^3$) based on a different study (Lane et al., 2008).

When the four-product basis set from the 1DVBS scheme is used in the 2DVBS (green line in Fig. 7a) it yields nearly the same particle mass concentration even though the mass-weighted average volatility of the first generation products are lower in the 1DVBS than in the 2DVBS (Fig. 6). This might give the impression that the volatility of the first generation products has little influence on SOA formation. In the 2DVBS, the O:C-ratio is however a function of volatility, where first generation products with lower volatilities are assumed to have higher O:C-ratio. The higher O:C-ratio will in turn cause a higher fragmentation during aging and thus cause a larger fraction of higher generation oxidation products to have higher volatilities. When first generation products from the MCM scheme is used in the 2DVBS (blue line in Fig. 7a), the SOA formation is substantially reduced. These products have on average higher volatilities and O:C-ratios.

That the volatilities of the first generation products in the 1DVBS are lower compared to the volatilities in 2DVBS mostly have to do with the products in the 2DVBS that are not constrained by laboratory data (those with saturation concentrations from 4 to 6 $\mu\text{g}/\text{m}^3$) but are based on mass balance calculations. In the 1DVBS products with higher saturation concentrations than 3 $\mu\text{g}/\text{m}^3$ are not included since they are assumed to have too high volatilities to partition to the particle phase. If these products are allowed to chemically age, this assumption might not be true. When we removed the unconstrained first generation products

from the 2DVBS base-case, the SOA formation was reduced (dashed orange line in Fig. 7a), implying that even though these first generation products cannot partition to the particle phase, they can be further oxidized and gain low enough volatility to partition at a later stage.

The aging properties in a VBS also include many free parameters. Some of these parameters are very uncertain. The fragmentation rate is one of them. To test the influence of fragmentation we ran one simulation with the 2DVBS without fragmentation during aging (dotted black line in Fig. 7b) and one where each oxidation reaction includes fragmentation (solid black line in Fig 7b). Clearly, fragmentation affects SOA formation.

The first generation oxidation products in the 1DVBS and 2DVBS schemes are chemically aged by reacting with the OH-radical. The rate of these reactions is another free parameter. In the 1DVBS the aging rate is almost an order of magnitude lower than in the 2DVBS. When this lower aging rate is used in the 2DVBS scheme, the SOA formation is reduced (dashed green line in Fig. 7b). The 1DVBS does not include fragmentation which might motivate the lower aging rate.

The purpose of paper I was not to find the most reliable model parameterizations, but to highlight which parameters that influence the SOA formation and therefore needs to be further studied. That is why only one air-mass trajectory was studied and the model set-up was kept rather simple. For example, a box model was used where all the compounds were assumed to be instantaneously mixed within a vertical domain of 1000 meters. α -pinene was the only BSOA precursor considered, assumed to be emitted from homogeneous coniferous forest of constant biomass density when the air mass was over land (see section Biogenic gas emissions).

Modeled BSOA formation compared to observations

In paper II and III, the model output was compared to observations and the relatively simple model set-up from paper I was modified. The box model was extended to a one-dimensional column model in order to handle the vertical mixing. The vegetation cover over land was no longer assumed to be homogeneous and as a consequence the biogenic emissions had to be parameterized differently (see section Biogenic gas emissions).

Figure 8 shows the monoterpene emissions along the same air-mass trajectory as in previous section, estimated with the three different model approaches used in this thesis to model BVOC emissions.

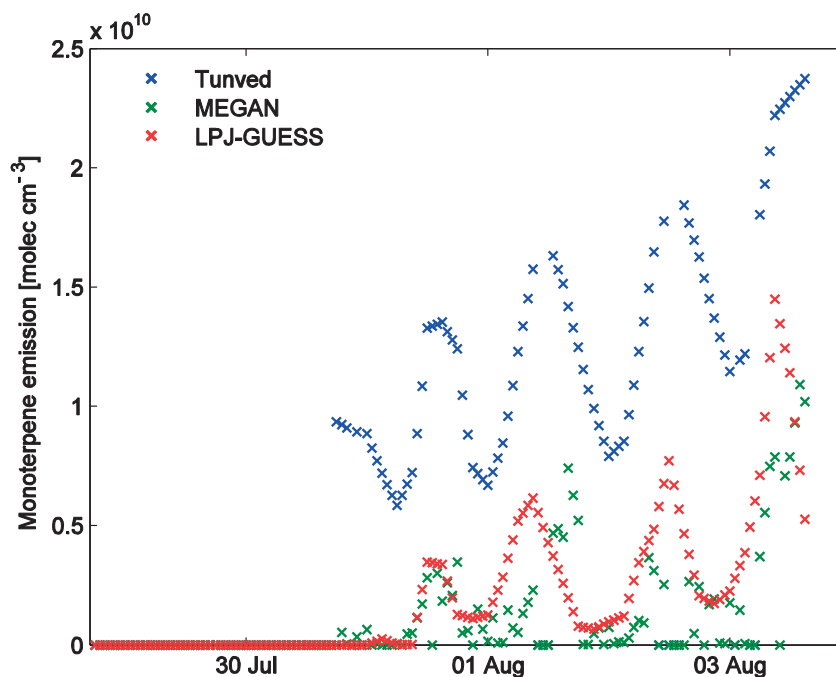


Figure 8. Monoterpene emissions along an air-mass trajectory in the northern Europe boreal region estimated with three different models. The monoterpenes in LPJ-GUESS includes α -pinene, β -pinene, limonene and an uncategorized group of monoterpenes, MEGAN includes α -pinene, β -pinene, limonene and carene. Tunved does not group the monoterpenes.

The Tunved-approach (blue crosses in Fig. 8) was used in paper I and predicts on average a factor of ~ 4 higher monoterpene emissions than LPJ-GUESS (red crosses) and MEGAN (green crosses), which are more similar.

The differences in modeled BVOC emissions as well as the parameterizations regarding vertical mixing affect the SOA formation. The MCM base case model scenario from paper I was implemented in the 1D-ADCHEM version with updated emission input in order to test for these differences. The results are presented in Fig. 9. When the one-dimensional model structure is used, vertical mixing can be accounted for, which leads to larger diurnal variations in SOA mass concentration due to the shrinking of the boundary layer at nighttime compared to the box-model version (compare the blue solid line to the dashed blue line in Fig. 9). When the monoterpene emissions are estimated with LPJ-GUESS the particles are not able to grow to the observed sizes and therefore give substantially less SOA mass (red solid lines in Fig. 9). This is likely due to missing reactions in the MCM v3.2 chemistry that would lead to gas-phase compounds with low or extremely low

volatility. The red dashed line in Fig. 9 is the resulting SOA mass when a small fraction of the first products produced from oxidation of α -pinene, β -pinene and limonene have undergone autoxidation and formed highly oxidized multifunctional organic compounds (HOMs), using the same mechanism as described in paper II and III. When the air mass has reached Värriö, the particles in this model scenario have reached approximately the same sizes as the observed particles at the station (right panel in Fig. 9).

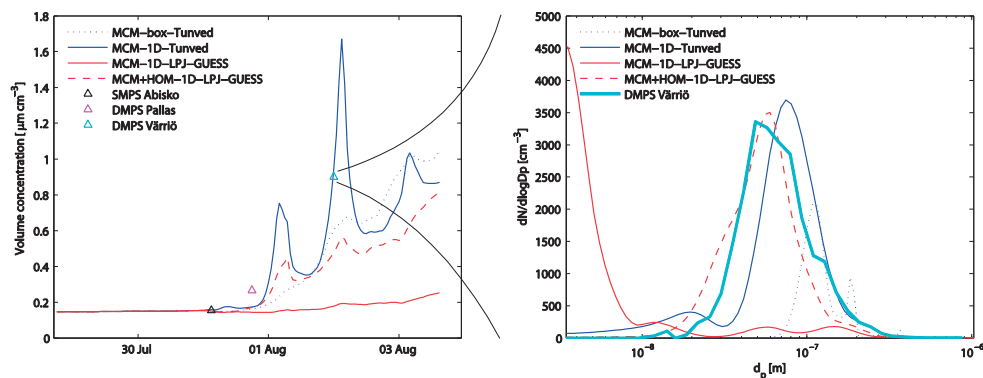


Figure 9. The left panel shows the particle mass concentration along the air-mass trajectory from paper I. The triangles are the observed particle volume concentrations (calculated from the particle number size distributions, assuming spherical particles) at the time the air mass passed the respective station. At Värriö, the particle number size distribution is shown in the right panel. The dashed blue lines are the MCM base-case scenario from paper I simulated with the box model while the other modeled results are simulated with the 1D-version of ADCHEM, either with BVOC emissions modeled with the Tunved approach (solid blue lines) or with the LPJ-GUESS model (red lines). The dashed red lines show the modeled results when the MCM chemistry is extended to include highly oxidized multifunctional organic compounds (HOMs).

The HOM mechanism is adopted from Ehn et al. (2014) and further developed and implemented for simulations in both chamber experiments and atmospheric measuring campaigns in paper II and III. The mechanism was calibrated against measurements in Jülich Plant Atmosphere Chamber (JPAC) where HOMs in the gas-phase were detected with a high-resolution chemical ionization mass spectrometer (CI-API-TOF). Figure 10 depicts the modeled and measured HOMs during α -pinene ozonolysis experiments in JPAC. The autoxidation (involving intramolecular H-shifts and O₂ additions) are terminated by either unimolecular reaction or reactions with NO, HO₂ and RO₂. Only the latter reaction can form dimers. Figure 10a shows the modeled and measured mass spectrum during the experiment, with clear monomer (to the left) and dimer (to the right) peaks. Because the constructed HOM mechanism includes only 74 species, the individual peaks of the observed and modeled mass spectra are not directly comparable. The mechanism was calibrated against the observed total HOM concentration in the gas phase (Fig. 10b), the peroxy radical (RO₂) concentration and the concentration

of the non-radical HOM monomers and dimers (Fig. 10c) for a wide range of α -pinene + O_3 reaction rates.

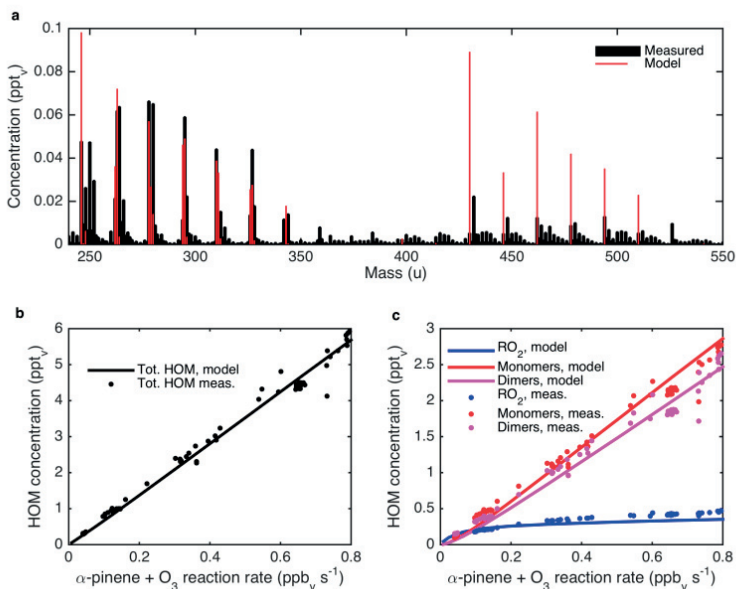


Figure 10. Modeled and measured (Ehn et al., 2014) gas-phase concentrations of HOM during a α -pinene ozonolysis experiment in JPAC. The ozone concentration was kept at approximately 85 ppb during the experiment while the concentration of α -pinene was varied. (a) shows the HOM(g) mass spectrum at an atmospheric relevant α -pinene concentration. In (b) the total modeled and measured gas-phase concentration of HOM are shown as a function of the amount of α -pinene reacting with ozone. (c) shows how the modeled and measured HOM peroxy radicals (RO₂), the HOM non-radical monomer and dimers change with the amount of reacting α -pinene.

The HOM mechanism and its influence on the SOA formation at ambient conditions was investigated by comparing the model to measurements made in a boreal environment at the Station for Measuring Ecosystem-Atmosphere Relations (SMEAR II) in Hyytiälä, Southern Finland. Figure 11 shows the measured and modeled average diurnal gas-phase concentration of HOMs during the campaign.

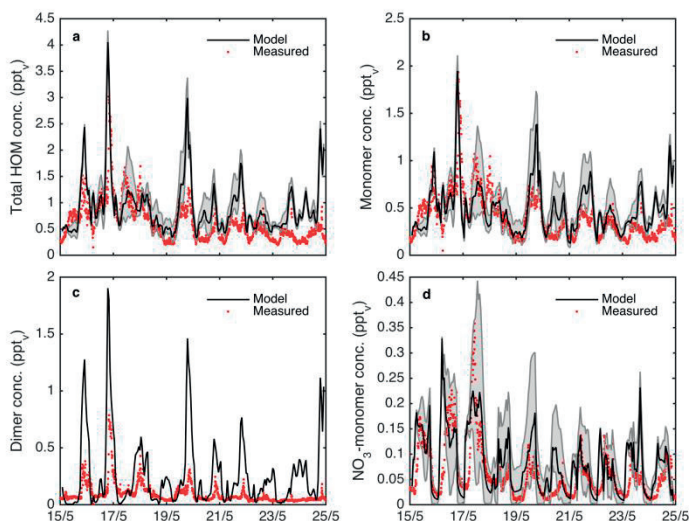


Figure 11. Modeled and measured average gas-phase concentration of (a) total HOM, (b) HOM monomers without nitrate functional groups, (c) HOM monomers with nitrate functional groups and (d) HOM dimer at the field station SMEAR II 15th to 25th of May, 2013. The shaded areas in (a), (b) and (d) represent the range of the model results achieved between the upper (SIMPOLx3) and lower (non-volatile) estimate of the HOM pure liquid saturation pressures.

The measured absolute concentration of the HOMs cannot be calibrated with known standards and therefore has an uncertainty of at least a factor of two. The modeled concentrations are within this estimated uncertainty range. The model also has many uncertainties, where, apart from the HOM mechanism itself, the volatility of the HOM compounds are a major uncertainty.

Figure 12 shows the modeled and measured particle number size distribution at SMEAR II during 22 days in spring 2014. The model is able to capture most of the observed formation events and particle growth when the HOM mechanism is included, without it, the model fails to capture the observed particle number size distribution.

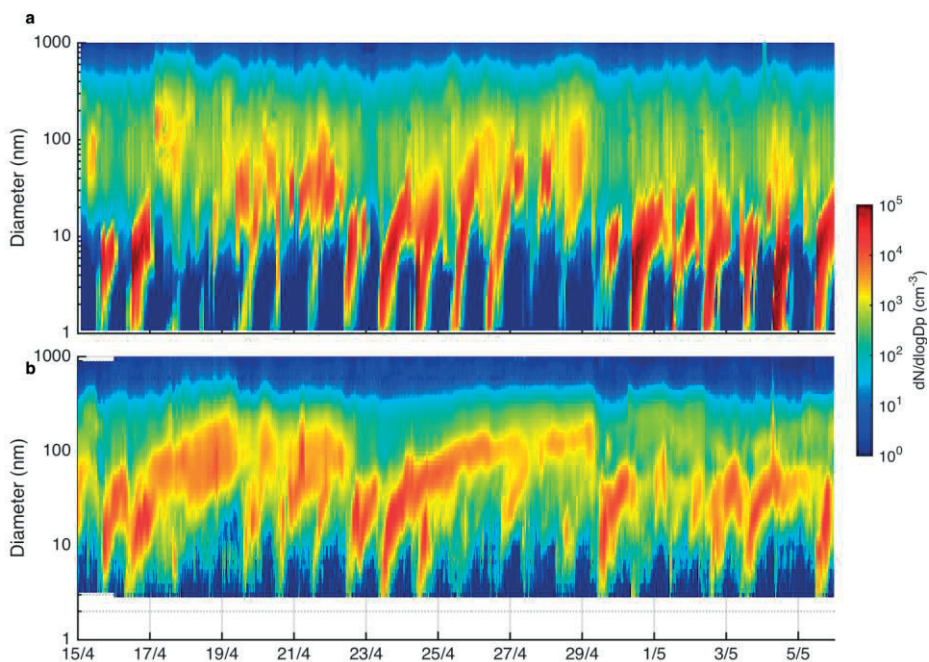


Figure 12. (a) Modeled and (b) measured particle number size distribution at SMEAR II in spring 2014.

In paper II, the importance of HOM in SOA formation was tested by comparing model output from the ADCHEM-1D version with or without the HOM mechanism against field measurements at the Pallas Atmosphere-Ecosystem Supersite in northern Finland. The SOA formation was modeled along 136 air-mass trajectories (17 days with 8 trajectories per day) that ended in Pallas (Fig. 13). On 10 of these days, new particle formation events were detected. The other 7 days are the subsequent days of the abovementioned NPF events when the growth of the newly formed particle mode could be observed also for these days.

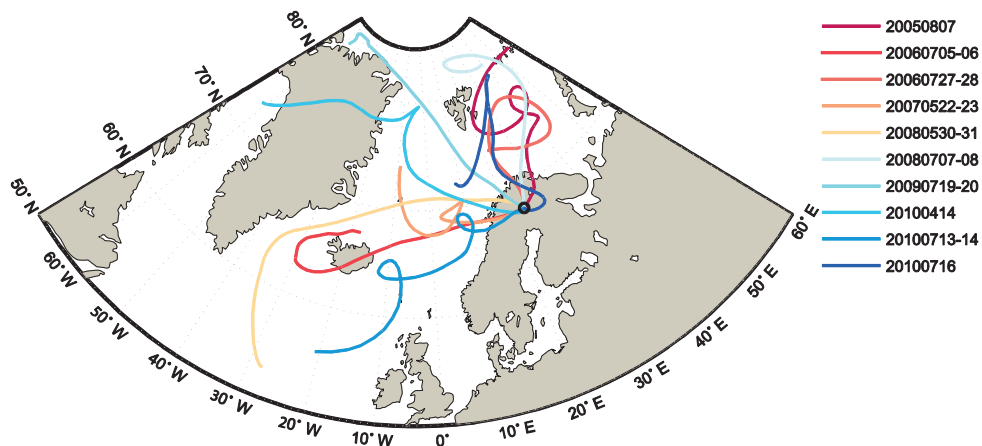


Figure 13. Mean HYSPLIT trajectories of each new particle formation event, all ending at Pallas.

In Fig. 14 the median particle number size distributions at different times during the NPF-event are shown. The model is able to reproduce the SOA formation process if the HOM mechanism is included. If the HOMs are excluded, the newly formed particles are not able to grow to the observed sizes

The vapor pressures of the HOMs are uncertain. Group contribution methods are a common way to estimate the vapor pressures of organic molecules. They are based on empirical data of the functional groups in the molecules. Two widely used group contribution methods are SIMPOL (Pankow and Asher, 2008) and the Nannoolal (Nannoolal et al., 2008) method, both of which have been applied in this thesis. These methods are not however adopted to include complex multifunctional hydroperoxides or peroxy acids which are present in HOMs. Compared to quantum chemical calculations done in a study by Kurtén et al. (2016), the group contribution methods gave substantially lower vapor pressures of the HOMs.

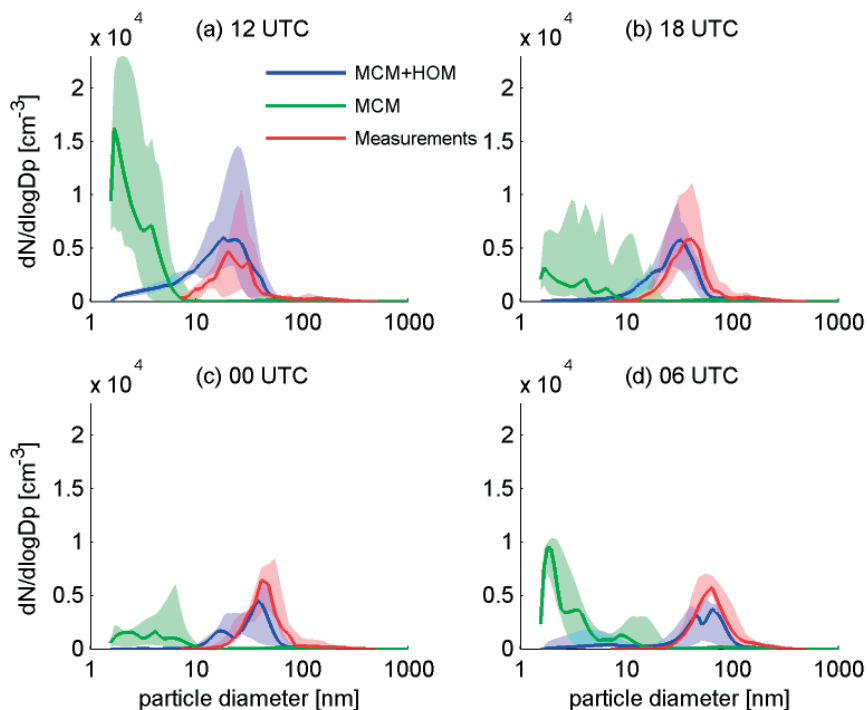


Figure 14. Measured and modeled (with or without the HOM mechanism) median particle number size distributions at (a) 12 and (b) 18 UTC the day of the new particle formation event and (c) 00 and (d) 06 UTC the following day. The shaded areas are the values that fall between the 25th and 75th percentiles.

In paper II we conducted sensitivity test to investigate how the method used to estimate the vapor pressures of HOM influenced the SOA formation (Fig. 15 and 16). With SIMPOL, the vapor pressures of the HOMs are low enough to be practically non-volatile and the median number of particles during the NPF-event modeled with vapor pressures calculated with SIMPOL or assumed non-volatile show little differences.

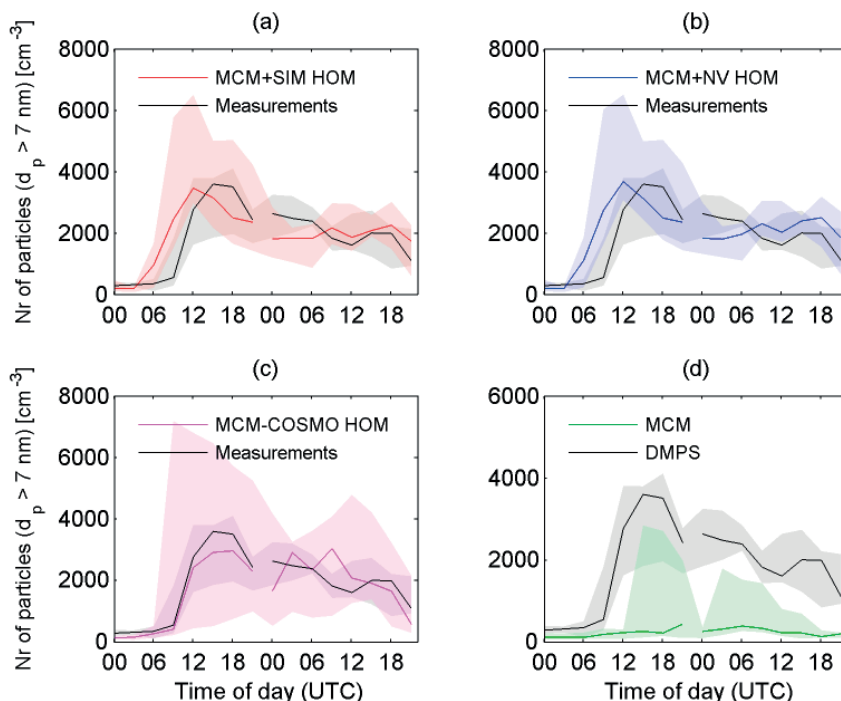


Figure 15. Median number of particles above 7 nm of all modeled NPF-events at Pallas (from midnight at the day of the event to the evening the day after the start of the event) together with the 25 and 75 percentiles (shaded areas). The black lines are the median observed number of particles at Pallas. The colored lines are the modeled median number of particles using (a) SIMPOL, (c) the quantum chemical model COSMO-RS to estimate the vapor pressures of HOM, or (c) assuming non-volatile HOMs or (d) not include the HOM mechanism.

Both the SIMPOL and non-volatile HOM model scenario overestimates the median number of particles above 7 nm in diameter at the beginning of the NPF-event (Fig. 15a and b), while the model scenario using the quantum chemical method to estimate the vapor pressure of HOM shows better agreement against the measurements (Fig. 15c). All model scenarios do however underestimate the number of particles larger than 50 nm in diameter (Fig. 16) and it was further shown in paper II that the O:C ratio were very high due to the high mass fraction of HOMs in the particle phase. This might imply that gas-phase reactions followed by gas-to-particle partitioning might not be the only important mechanism in SOA formation. Particle-phase reaction could also play an important role in the growth of the particles.

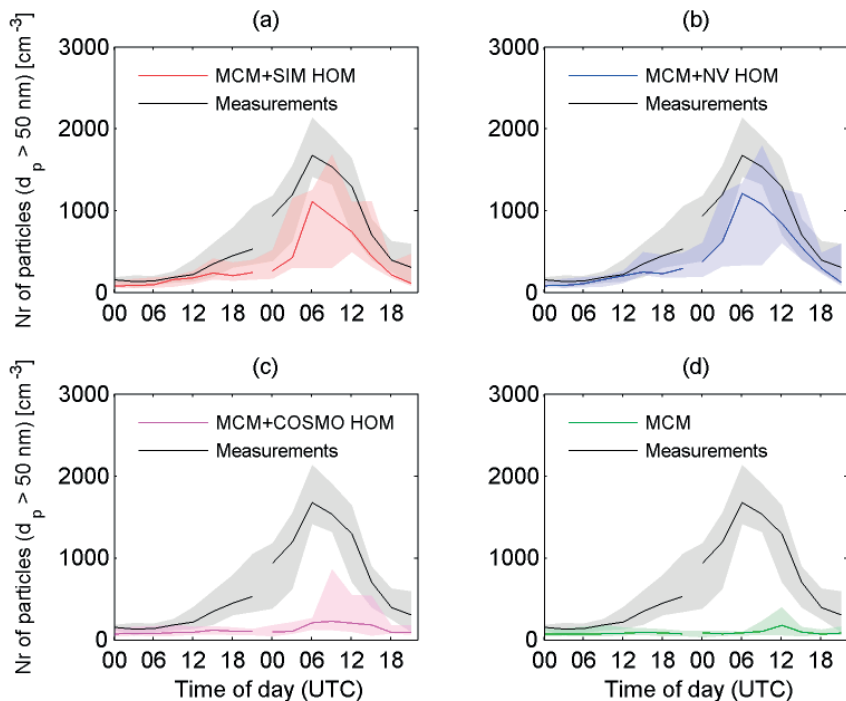


Figure 16. Median number of particles above 50 nm of all modeled NPF-events at Pallas (from midnight at the day of the event to the evening the day after the start of the event) together with the 25 and 75 percentiles (shaded areas). The black lines are the median observed number of particles at Pallas. The colored lines are the modeled median number of particles using (a) SIMPOL, (c) the quantum chemical model COSMO-RS to estimate the vapor pressures of HOM, or (c) assuming non-volatile HOMs or (d) not include the HOM mechanism.

New particle formation in polluted marine environments

The effect new particle formation and anthropogenic emission in marine environments have on the concentration of CCN over land is not well-studied. The aim in paper IV was to investigate this by analyzing field measurements at Høvsøre in Jutland (Denmark) and Finokalia, located at Crete (Greece) and model the aerosol particle and trace gas evolution along selected air-mass trajectories that pass either station. Our results imply that anthropogenic emissions over sea might have an impact on CCN concentration downwind Finokalia, whereas NPF over sea does not seem to have a significant effect. It was more difficult to draw any conclusions about CCN concentrations downwind Høvsøre due to an overestimation of atmospheric SO₂ concentration. This overestimation caused the model to predict too many particles in the CCN size range already at the station, compared to the observed particle number size distribution.

The results imply that the effect NPF and anthropogenic emissions over sea have on the amount of CCN over land depends on e.g. the condensation sink over land. This means that a process-based aerosol dynamics model might be needed to achieve a greater understanding of this issue.

Particle number size distribution at the coastal stations

The analysis for Høvsøre included four consecutive days in May 2012 where the air-mass trajectories originated from the North Atlantic Ocean. Half of the 32 modeled trajectories only passed over sea upwind Høvsøre. The analyzed air-mass trajectories passing Finokalia originated in Eastern Europe and had a strong continental contribution when arriving at Finokalia.

In Fig. 17 the median modeled particle number size distributions at Høvsøre and Finokalia are shown together with the observed size distribution. The model agrees quite well with the observations at Finokalia while it predicts too many particles larger than 40 nm in diameter at Høvsøre. The growth of particles along the air-mass trajectories upwind Høvsøre was too fast in the model, causing an

overestimation of particles larger than 40 nm in diameter at Høvsøre compared to observed particle number size distributions.

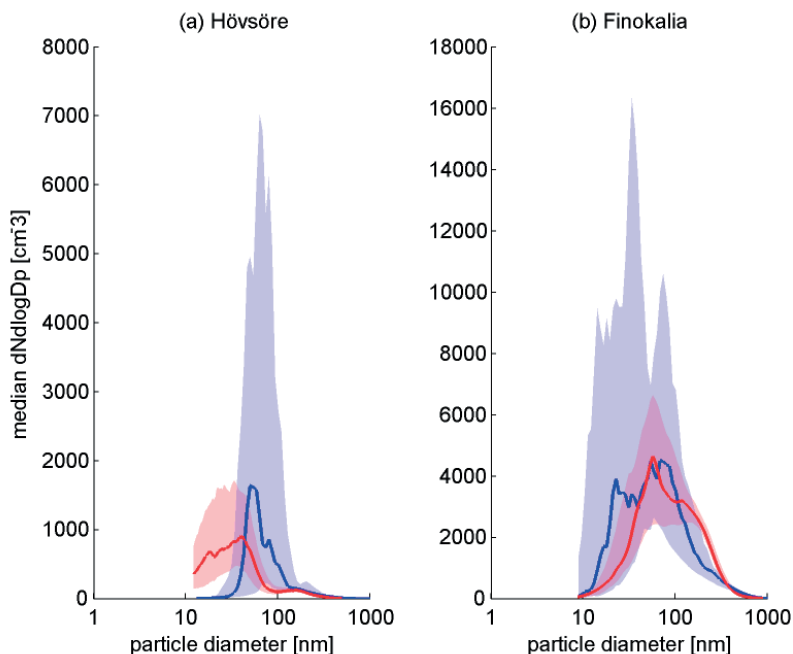


Figure 17. Median particle number size distributions during 4 days at (a) Høvsøre and (b) Finokalia. The red lines are the observed size distributions, the blue line the modelled (with the base-case set up). The shaded areas are the values that fall between the 25th and 75th percentiles.

To test the influence NPF and anthropogenic emissions over sea have on the amount of particles in the CCN size range over the continent, two additional model case scenarios were set up where NPF and anthropogenic emissions over sea were switched off.

The model simulations with no NPF over sea only had a minor effect on the amount of potential CCN two days downwind Finokalia (on average 0.82 % fewer particles above 80 nm in diameter). NPF and growth of the newly formed particles upwind Finokalia, over the Mediterranean Sea, were inhibited by the relatively polluted air mass from the European continent. When anthropogenic emissions were switched off in the model, the amount of particles larger than 80 nm in diameter two days downwind Finokalia decreased by on average 7.1 %. Anthropogenic gases emitted over sea thus had a small contribution to the growth of the particles. Some of the particles in the CCN size range downwind Finokalia were also advected primary particles from ship traffic.

The modeled particle number concentration at Høvsøre decreased by a large fraction when NPF and anthropogenic emissions over sea were switched off (Fig 18). This had a large impact on the amount of particles potentially able to act as CCN one day downwind Høvsøre. In the model scenario without anthropogenic emissions over sea, the number concentration of particles larger than 80 nm increased by on average 55 %. In this scenario, the condensation sink is reduced, allowing strong NPF and subsequent growth downwind Høvsøre. This effect is probably too large due to an overestimation of the condensation sink in the base-case model scenario. Switching off NPF over sea had a smaller effect on the potential CCN downwind the station (on average 1.5 % more particles above 80 nm in diameter). This scenario caused the size distribution at Høvsøre to shift somewhat towards larger diameters, since more vapors were available to grow the existing particles when no NPF occurred over sea. Due to a higher number concentration of larger particles at Høvsøre than in the scenario without anthropogenic emission over sea, the newly formed particles downwind the station did not grow as fast.

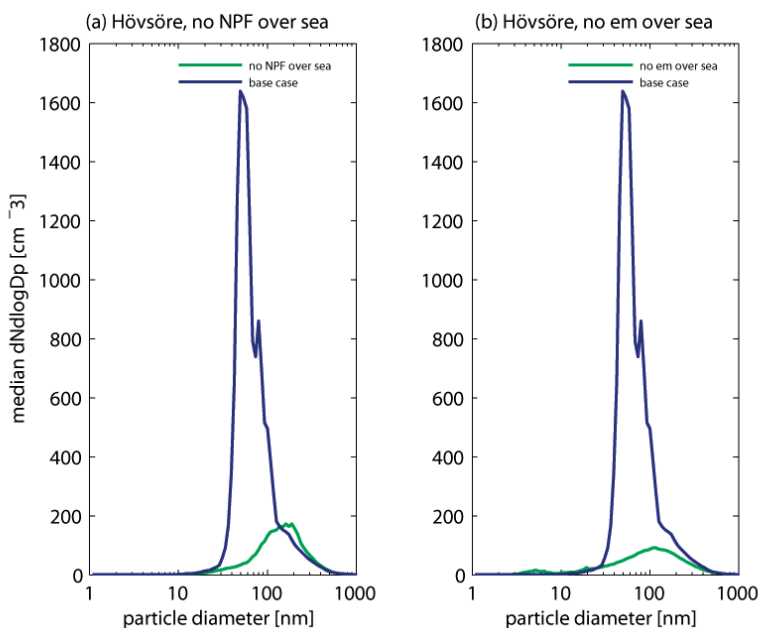


Figure 18. The median particle number size distribution at Høvsøre modelled with (a) the no-NPF over sea scenario and (b) the no anthropogenic emission over sea scenario, compared to the modelled base-case scenario (blue lines).

The growth of particles downwind Høvsøre might be overestimated due to the high modeled concentration of SO_2 . Future studies should look closer into finding closure between observed and modelled SO_2 concentrations.

Conclusions and outlook

A process-based aerosol dynamics model has been used in this thesis with the aim to gain more knowledge about SOA formation and its influence on CCN concentration in boreal environments and downwind polluted marine environments. These are the main conclusions of the research presented in this thesis:

The modeled particle mass concentration during BSOA formation in boreal environments is influenced by how the gas-phase chemistry is handled. Precursor gases emitted by the vegetation, like α -pinene, are rapidly oxidized and form many oxidation products. Due to the vast number of oxidation products and the fact that most of them are unknown, different methods to model the gas-phase chemistry has evolved – all including uncertainties. In paper I, we show that the BSOA formation is sensitive to the how the parameterizations of saturation vapor pressures of the first generation oxidation products are done and also to what oxidation state they are assumed to have. The first generation products will continue to be oxidized (or aged) in the atmosphere, either to form less volatile compounds as functional groups are added, or to form more volatile compounds when their carbon chains are fragmented. In paper I, we further show that the parameterizations of the aging rate and fragmentation during aging influence the BSOA formation.

In paper II and III, the modeled BSOA formation is compared with laboratory and ambient field data. A recently developed reaction pathway of monoterpenes containing endocyclic double bonds that form highly oxidized multifunctional molecules (HOMs) in the gas phase was implemented in the model. With this reaction pathway included, the model could reproduce the observed activation and growth of the newly formed particles between ~ 1.5 to 20 nm in diameter. The model does however seem to underestimate the growth of particles between ~ 20 and 80 nm in diameter. The saturation vapor pressures of the HOMs are uncertain and, furthermore; gas-phase reactions followed by gas-to-particle partitioning might not be the only important mechanism in SOA formation. Particle-phase reaction could also play an important role in the growth of the particles. More work is needed in this area.

In paper IV, modeled particle number size distributions with ADCHEM were compared to measured ones at the coastal stations of Høvsøre in Denmark and

Finokalia in Greece. The effect NPF and anthropogenic emissions over sea had downwind the stations were studied by running model simulations where these mechanisms were switched off. The results imply that the effect NPF and anthropogenic emissions over sea have on potential CCN over the continents are non-linear; i.e. switching off a mechanism might affect CCN over land differently depending on various conditions, such as the condensation sink. Downwind Finokalia, a small decrease in potential CCN were seen when the model excluded anthropogenic emissions over sea. The model simulations without NPF over sea did not significantly affect the potential CCN downwind Finokalia. For Høvsøre, the potential CCN instead increased downwind the station when anthropogenic emissions were switched off due to a lower condensation sink. The model did however overestimate the SO_2 concentration in Høvsøre, making the results less reliable.

Global climate and earth system models are important tools in climate and environmental policy-making. These models are continuously being developed but are at the same time constrained by computational resources. They include a vast number of processes, and therefore it is important to find out which processes that are important enough to be included in these models. Furthermore; the included processes often need to be greatly simplified but at the same time be described in a physical correct way. Process-based models, such as the ones applied in this thesis can be used to test and develop parameterizations for selected processes.

For example, parameterizations used in large-scale models can be tested in process-based models and evaluated against observations at various places around the globe to answer the question if the parameterization in question is described adequately or if it needs to be further developed.

Overall, much work is still needed in atmospheric science to evaluate models on all scales against observations in order to reduce the uncertainties in the models but also to ensure that the models do not give the right results for the wrong reasons.

Acknowledgements

Doing a PhD is a journey like no other; a journey I would never have been able to do alone. I would like to thank some people who made it possible.

My main supervisor, Erik Swietlicki who introduced me to the field of aerosol science almost 10 years ago when I did my bachelor. For helping me put my research into perspective and guiding me back to my research aims when needed. For being available to discuss the significance of my results and introducing me to people within the field. My co-supervisor, Pontus Roldin; your help with setting up the model and analyzing the results have been invaluable. Discussing results with you has always been rewarding. Also, thanks for good company in Helsinki. My co-supervisor Guy Schurgers, for your knowledge and help with BVOC emissions. My co-supervisor Birgitta Svenningsson; we did not end up working together so much, but you made me feel welcome in the aerosol group. Adam Kristensson, especially for your help with paper IV but also for good company and assistance with instruments during work at Vavihill.

Michael Boy, who helped and encouraged me during the start-up of my first project that became paper I. For inviting me to come and work with him and his atmospheric modeling group at the University of Helsinki. These visits were a great inspirational source and just what I needed to finalize both paper I and II.

My many office mates throughout the years as I've moved around in the IKDC building: Pontus, Axel, Erik, Moa and Cerina; it has been great getting to know you. Together we have discussed our research (or research in general), helped each other with teaching issues and talked about life in general.

Patrik and Christian; for making me laugh when I most needed it. I miss our fikas.

All the people at Nuclear Physics and IKDC for providing a nice working environment and nice company during travels and get-togethers. A special thanks to Anneli Nilsson-Ahlm and Yulia Lindholm who helped me with all the administrative questions, which couldn't have been an easy task when helping a PhD-student employed at two departments and physically located at a third.

The PhD students and the people at CEC working to make the PhD program in Environmental Science possible. For putting my research into a bigger context and

for providing the opportunity to learn about other interesting topics within environmental science.

Min familj och mina vänner för att ni sätter allt i perspektiv; det viktigaste har aldrig varit en doktorstitel. Mina vänner; ni vet vilka ni är: spelkvällar, utflykter, skidresor och en massa skratt är ett bra sätt att glömma bort både press och stress. Mamma och pappa för att ni alltid har trott på mig och att ni alltid finns där för mig. Mina syskon: Sanna, Dan och Fanny, hos er känner jag mig alltid hemma.

Min son Oliver, du är det bästa som hänt mig och min största inspirationskälla. Mathias, min älskade man och bästa vän, tillsammans klarar vi allt. Utan dig hade de här åren och den här boken blivit så mycket sämre.

References

- Bergström, R., Denier van der Gon, H. A. C., Prévôt, A. S. H., Yttri, K. E. and Simpson, D.: Modelling of organic aerosols over Europe (2002–2007) using a volatility basis set (VBS) framework: application of different assumptions regarding the formation of secondary organic aerosol, *Atmos. Chem. Phys.*, 12, 8499–8527, doi:10.5194/acp-12-8499-2012, 2012.
- Boy, M., Kulmala, M., Ruuskanen, T. M., Pihlatie, M., Reissell, A., Aalto, P. P., Keronen, P., Dal Maso, M., Hellen, H., Hakola, H., Jansson, R., Hanke, M. and Arnold, F.: Sulphuric acid closure and contribution to nucleation mode particle growth, *Atmos. Chem. Phys.*, 5, 863–878, 2005.
- Carslaw, K. S., Boucher, O., Spracklen, D. V., Mann, G. W., Rae, J. G. L., Woodward, S. and Kulmala, M.: A review of natural aerosol interactions and feedbacks within the Earth system, *Atmos. Chem. Phys.*, 10(4), 1701–1737, 2010.
- Crutzen, P. J.: Geology of mankind, *Nature*, 415(January), 23, 2002.
- Damian, V., Sandu, A., Damian, M., Potra, F. and Carmichael, G. R.: The kinetic preprocessor KPP-a software environment for solving chemical kinetics, *Comput. Chem. Eng.*, 26, 1567–1579, doi:10.1016/S0098-1354(02)00128-X, 2002.
- Dickens, C.: Bleak House, Bradbury & Evans, London., 1853.
- Donahue, N. M., Epstein, S. A., Pandis, S. N. and Robinson, A. L.: A two-dimensional volatility basis set: 1. organic-aerosol mixing thermodynamics, *Atmos. Chem. Phys.*, 11(7), 3303–3318, doi:10.5194/acp-11-3303-2011, 2011.
- Donahue, N. M., Robinson, A. L. and Pandis, S. N.: Atmospheric organic particulate matter: From smoke to secondary organic aerosol, *Atmos. Environ.*, 43(1), 94–106, doi:10.1016/j.atmosenv.2008.09.055, 2009.
- Donahue, N. M., Robinson, A. L., Stanier, C. O. and Pandis, S. N.: Coupled Partitioning, Dilution, and Chemical Aging of Semivolatile Organics, *Environ. Sci. Technol.*, 40(8), 2635–2643, doi:10.1021/es052297c, 2006.
- Draxler, R. . and Rolph, G. D.: HYSPLIT (HYbrid Single-Particle Lagrangian Integrated Trajectory) Model access via NOAA ARL READY Website, NOAA Air Resour. Lab. Silver Spring, MD [online] Available from: <http://ready.arl.noaa.gov/HYSPLIT.php>, 2013.
- EEA: Emissions of primary PM_{2.5} and PM₁₀ particulate matter. [online] Available from: <http://www.eea.europa.eu/data-and-maps/indicators/emissions-of-primary-particles-and-5/assessment-3>, 2014.
- Ehn, M., Thornton, J. A., Kleist, E., Sipilä, M., Junninen, H., Pullinen, I., Springer, M., Rubach, F., Tillmann, R., Lee, B., Lopez-Hilfiker, F., Andres, S., Acir, I.-H., Rissanen, M., Jokinen, T., Schobesberger, S., Kangasluoma, J., Kontkanen, J., Nieminen, T., Kurtén, T., Nielsen, L. B., Jørgensen, S., Kjaergaard, H. G., Canagaratna, M., Dal Maso, M., Berndt,

T., Petäjä, T., Wahner, A., Kerminen, V.-M., Kulmala, M., Worsnop, D. R., Wildt, J. and Mentel, T. F.: A large source of low-volatility secondary organic aerosol, *Nature*, 506, 476–479, doi:10.1038/nature13032, 2014.

EPA: Particulate Matter (PM_{2.5}) Trends, [online] Available from: <https://www.epa.gov/air-trends/particulate-matter-pm25-trends> (Accessed 1 January 2016), 2016.

Fuchs, N. A. and Sutugin, A. G.: High-dispersed aerosols, in *Topics in Current Aerosol Research*, edited by G. M. Hidy and J. R. Brock, pp. 1–60, Pergamon, New York., 1971.

Guenther, A. B., Jiang, X., Heald, C. L., Sakulyanontvittaya, T., Duhl, T., Emmons, L. K. and Wang, X.: Model Development The Model of Emissions of Gases and Aerosols from Nature version 2.1 (MEGAN2.1): an extended and updated framework for modeling biogenic emissions, *Geosci. Model Dev.*, 5, 1471–1492, doi:10.5194/gmd-5-1471-2012, 2012.

IPCC: Climate Change 2013: The Physical and Science Basis. Contribution of Working Group I to the Fifth Assessment Report of the Intergovernmental Panel of Climate Change, edited by T. F. Stocker, D. Qin, G.-K. Plattner, M. Tignor, S. K. Allen, J. Boschung, A. Nauels, Y. Xia, V. Bex, and P. M. Midgley, Cambridge University Press, Cambridge, United Kingdom and New York, NY, USA., 2013.

Jaenicke, R.: Tropospheric aerosols, in *Aerosol-Cloud-Climate Interactions*, edited by P. V. Hobbs, pp. 1–31, Academic Press, San Diego, CA., 1993.

Jenkin, M. E., Saunders, S. M. and Pilling, M. J.: The tropospheric degradation of volatile organic compounds: a protocol for mechanism development, *Atmos. Environ.*, 31, 81–104, doi:10.1016/S1352-2310(96)00105-7, 1997.

Jericevic, A., Kraljevic, L., Grisogono, B., Fagerli, H. and Vecenaj, Z.: Parameterization of vertical diffusion and the atmospheric boundary layer height determination in the EMEP model, *Atmos. Chem. Phys.*, 10, 341–364, doi:10.5194/acp-10-341-2010, 2010.

Jimenez, J. L., Canagaratna, M. R., Donahue, N. M., Prevot, A. S. H., Zhang, Q., Kroll, J. H., DeCarlo, P. F., Allan, J. D., Coe, H., Ng, N. L., Aiken, A. C., Docherty, K. S., Ulbrich, I. M., Grieshop, A. P., Robinson, A. L., Duplissy, J., Smith, J. D., Wilson, K. R., Lanz, V. A., Hueglin, C., Sun, Y. L., Tian, J., Laaksonen, A., Raatikainen, T., Rautiainen, J., Vaattovaara, P., Ehn, M., Kulmala, M., Tomlinson, J. M., Collins, D. R., Cubison, M. J., Dunlea, E. J., Huffman, J. A., Onasch, T. B., Alfarra, M. R., Williams, P. I., Bower, K., Kondo, Y., Schneider, J., Drewnick, F., Borrmann, S., Weimer, S., Demerjian, K., Salcedo, D., Cottrell, L., Griffin, R., Takami, A., Miyoshi, T., Hatakeyama, S., Shimojo, A., Sun, J. Y., Zhang, Y. M., Dzepina, K., Kimmel, J. R., Sueper, D., Jayne, J. T., Herndon, S. C., Trimborn, A. M., Williams, L. R., Wood, E. C., Middlebrook, A. M., Kolb, C. E., Baltensperger, U. and Worsnop, D. R.: Evolution of organic aerosols in the atmosphere., *Science*, 326(5959), 1525–1529, doi:10.1126/science.1180353, 2009.

Kuang, C., McMurry, P. H., McCormick, A. V. and Eisele, F. L.: Dependence of nucleation rates on sulfuric acid vapor concentration in diverse atmospheric locations, *J. Geophys. Res.*, 113, D10209, doi:10.1029/2007JD009253, 2008.

Kulmala, M., Kontkanen, J., Junninen, H., Lehtipalo, K., Manninen, H. E., Nieminen, T., Petäjä, T., Sipilä, M., Schobesberger, S., Rantala, P., Franchin, A., Jokinen, T., Jävinen, E., Äijälä, M., Kangasluoma, J., Hakala, J., Aalto, P. P., Paasonen, P., Mikkilä, J., Vanhanen, J., Aalto, J., Hakola, H., Makkonen, U., Ruuskanen, T., Mauldin III, R. L., Duplissy, J.,

Vehkamäki, H., Bäck, J., Kortelainen, A., Riipinen, I., Kurtén, T., Johnston, M. V., Smith, J. N., Ehn, M., Mentel, T. F., Lehtinen, K. E. J., Laaksonen, A., Kerminen, V.-M. and Worsnop, D. R.: Direct Observations of Atmospheric Aerosol Nucleation, *Science* (80-.), 339(February), 943–947, 2013.

Kulmala, M., Lehtinen, K. E. J. and Laaksonen, A.: Cluster activation theory as an explanation of the linear dependence between formation rate of 3 nm particles and sulphuric acid concentration, *Atmos. Chem. Phys.*, 6, 787–793, 2006.

Kulmala, M., Suni, T., Lehtinen, K. E. J., Dal Maso, M., Boy, M., Reissell, A., Rannik, Ü., Aalto, P., Keronen, P., Hakola, H., Bäck, J., Hoffmann, T., Vesala, T. and Hari, P.: A new feedback mechanism linking forests, aerosols, and climate, *Atmos. Chem. Phys.*, 4(2), 557–562, 2004.

Kurtén, T., Tiusanen, K., Roldin, P., Rissanen, M., Luy, J.-N., Boy, M., Ehn, M. and Donahue, N.: α -Pinene Autoxidation Products May Not Have Extremely Low Saturation Vapor Pressures Despite High O:C Ratios, *J. Phys. Chem. A*, 120, 2569–2582, doi:10.1021/acs.jpca.6b02196, 2016.

Laakso, L., Grönholm, T., Rannik, Ü., Kosmale, M., Fiedler, V., Vehkamäki, H. and Kulmala, M.: Ultrafine particle scavenging coefficients calculated from 6 years field measurements, *Atmos. Environ.*, 37, 3605–3613, doi:10.1016/S1352-2310(03)00326-1, 2003.

Lane, T. E., Donahue, N. M. and Pandis, S. N.: Simulating secondary organic aerosol formation using the volatility basis-set approach in a chemical transport model, *Atmos. Environ.*, 42, 7439–7451, doi:10.1016/j.atmosenv.2008.06.026, 2008.

Murphy, B. N. and Pandis, S. N.: Simulating the Formation of Semivolatile Primary and Secondary Organic Aerosol in a Regional Chemical Transport Model, *Environ. Sci. Technol.*, 43(13), 4722–4728, doi:10.1021/es803168a, 2009.

Nannoolal, Y., Rarey, J. and Ramjugernath, D.: Estimation of pure component properties, *Fluid Phase Equilib.*, 269(1–2), 117–133, doi:10.1016/j.fluid.2008.04.020, 2008.

Odum, J. R., Hoffmann, T., Bowman, F., Collins, D., Flagan, R. C. and Seinfeld, J. H.: Gas/Particle Partitioning and Secondary Organic Aerosol Yields, *Environ. Sci. Technol.*, 30, 2580–2585, doi:10.1021/es950943+, 1996.

Olenius, T., Kupiainen-Määttä, O., Ortega, I. K., Kurtén, T. and Vehkamäki, H.: Free energy barrier in the growth of sulfuric acid–ammonia and sulfuric acid–dimethylamine clusters, *J. Chem. Phys.*, 139(8), 84312, doi:10.1063/1.4819024, 2013.

Paasonen, P., Nieminen, T., Asmi, E., Manninen, H. E., Petäjä, T., Plass-Dülmer, C., Flentje, H., Birmili, W., Wiedensohler, A., Hõrrak, U., Metzger, A., Hamed, A., Laaksonen, A., Facchini, M. C., Kerminen, V.-M. and Kulmala, M.: On the roles of sulphuric acid and low-volatility organic vapours in the initial steps of atmospheric new particle formation, *Atmos. Chem. Phys.*, 10, 11223–11242, doi:10.5194/acp-10-11223-2010, 2010.

Pankow, J. F. and Asher, W. E.: SIMPOL.1: a simple group contribution method for predicting vapor pressures and enthalpies of vaporization of multifunctional organic compounds, *Atmos. Chem. Phys.*, 8(10), 2773–2796, doi:10.5194/acp-8-2773-2008, 2008.

Radu, O. B., van den Berg, M., Klimont, Z., Deetman, S., Janssens-Maenhout, G., Muntean, M., Heyes, C., Dentener, F. and van Vuuren, D. P.: Exploring synergies between

climate and air quality policies using long-term global and regional emission scenarios, *Atmos. Environ.*, 140, 577–591, doi:10.1016/j.atmosenv.2016.05.021, 2016.

Rafaj, P., Schöpp, W., Russ, P., Heyes, C. and Amann, M.: Co-benefits of post-2012 global climate mitigation policies, *Mitig. Adapt. Strateg. Glob. Chang.*, 18, 801–824, doi:10.1007/s11027-012-9390-6, 2013.

Rao, S., Pachauri, S., Dentener, F., Kinney, P., Klimont, Z., Riahi, K. and Schoepp, W.: Better air for better health : Forging synergies in policies for energy access , climate change and air pollution, *Glob. Environ. Chang.*, 23, 1122–1130, doi:10.1016/j.gloenvcha.2013.05.003, 2013.

Rockström, J., Steffen, W., Noone, K., Persson, Å., Stuart III Chapin, F., Lambin, E., Lenton, T. M., Scheffer, M., Folke, C., Schellnhuber, H. J., Nykvist, B., de Wit, C. A., Hughes, T., van der Leeuw, S., Rodhe, H., Sörlin, S., Snyder, P. K., Costanza, R., Svedin, U., Falkenmark, M., Karlberg, L., Corell, R. W., Fabry, V. J., Hansen, J., Walker, B., Liverman, D., Richardson, K., Crutzen, P. and Foley, J.: Planetary Boundaries : Exploring the Safe Operating Space for Humanity, *Ecol. Soc.*, 14(2), 32, 2009.

Roldin, P., Eriksson, A. C., Nordin, E. Z., Hermansson, E., Mogensen, D., Rusanen, A., Boy, M., Swietlicki, E., Svenningsson, B., Zelenyuk, A. and Pagels, J.: Modelling non-equilibrium secondary organic aerosol formation and evaporation with the aerosol dynamics, gas- and particle-phase chemistry kinetic multilayer model ADCHAM, *Atmos. Chem. Phys.*, 14, 7953–7993, doi:10.5194/acp-14-7953-2014, 2014.

Roldin, P., Swietlicki, E., Schurgers, G., Arneth, A., Lehtinen, K. E. J., Boy, M. and Kulmala, M.: Development and evaluation of the aerosol dynamics and gas phase chemistry model ADCHEM, *Atmos. Chem. Phys.*, 11, 5867–5896, doi:10.5194/acp-11-5867-2011, 2011.

Rolph, G. D.: Real-time Environmental Applications and Display sYstem (READY) Website (<http://ready.arl.noaa.gov>), Silver Spring, MD., 2016.

Saunders, S. M., Jenkin, M. E., Derwent, R. G. and Pilling, M. J.: Protocol for the development of the Master Chemical Mechanism, MCM v3 (Part A): tropospheric degradation of non-aromatic volatile organic compounds, *Atmos. Chem. Phys.*, 3, 161–180, doi:10.5194/acp-3-161-2003, 2003.

Schucht, S., Colette, A., Rao, S., Holland, M., Schöpp, W., Kolp, P., Klimont, Z., Bessagnet, B., Szopa, S., Vautard, R., Brignon, J.-M. and Roui, L.: Moving towards ambitious climate policies : Monetised health benefits from improved air quality could offset mitigation costs in Europe, *Environ. Sci. Policy*, 50, 252–269, doi:10.1016/j.envsci.2015.03.001, 2015.

Seinfeld, J. H. and Pandis, S. N.: Atmospheric Chemistry and Physics: from air pollution to climate change, 2nd editio., John Wiley & Sonc, Inc, Hoboken, New Jersey, USA., 2006.

Sipilä, M., Berndt, T., Petäjä, T., Brus, D., Vanhanen, J., Stratmann, F., Patokoski, J., Mauldin III, R. L., Hyvärinen, A.-P., Lihavainen, H. and Kulmala, M.: The Role of Sulfuric Acid in Atmospheric Nucleationn, *Science* (80-.), 327, 1243–1246, 2010.

Smith, B., Wärlind, D., Arneth, A., Hickler, T., Leadley, P., Siltberg, J. and Zaehle, S.: Implications of incorporating N cycling and N limitations on primary production in an individual-based dynamic vegetation model, *Biogeosciences*, 11, 2027–2054,

doi:10.5194/bg-11-2027-2014, 2014.

Tsigaridis, K. and Kanakidou, M.: Secondary organic aerosol importance in the future atmosphere, *Atmos. Environ.*, 41, 4682–4692, doi:10.1016/j.atmosenv.2007.03.045, 2007.

Tunved, P., Hansson, H.-C., Kerminen, V.-M., Ström, J., Maso, M. D., Lihavainen, H., Viisanen, Y., Aalto, P. P., Komppula, M. and Kulmala, M.: High natural aerosol loading over boreal forests., *Science*, 312(5771), 261–263, doi:10.1126/science.1123052, 2006.

Weber, R. J., Marti, J. J., McMurry, P. H., Eisele, F. L., Tanner, D. J. and Jefferson, A.: Measurements of new particle formation and ultrafine particle growth rates at a clean continental site, *J. Geophys. Res.*, 102, 4375–4385, doi:10.1029/96JD03656, 1997.

WHO Regional Office for Europe, O.: Economic cost of the health impact of air pollution in Europe: Clean air, health and wealth, Copenhagen., 2015.

Paper I





Biogenic SOA formation through gas-phase oxidation and gas-to-particle partitioning – a comparison between process models of varying complexity

E. Hermansson^{1,2}, P. Roldin^{1,3}, A. Rusanen³, D. Mogensen³, N. Kivekäs^{1,*}, R. Väänänen³, M. Boy³, and E. Swietlicki^{1,2}

¹Division of Nuclear Physics, Lund University, P.O. Box 118, 221 00, Lund, Sweden

²Centre for Environmental and Climate Research, Lund University, P.O. Box 118, 221 00, Lund, Sweden

³Department of Physics, P.O. Box 64, 00014 University of Helsinki, Helsinki, Finland

*now at: Atmospheric Composition, Finnish Meteorological Institute, P.O. Box 503, 00101, Helsinki, Finland

Correspondence to: E. Hermansson (emilie.hermansson@nuclear.lu.se)

Received: 21 February 2014 – Published in Atmos. Chem. Phys. Discuss.: 5 May 2014

Revised: 1 October 2014 – Accepted: 2 October 2014 – Published: 12 November 2014

Abstract. Biogenic volatile organic compounds (BVOCs) emitted by vegetation play an important role for aerosol mass loadings since the oxidation products of these compounds can take part in the formation and growth of secondary organic aerosols (SOA). The concentrations and properties of BVOCs and their oxidation products in the atmosphere are poorly characterized, which leads to high uncertainties in modeled SOA mass and properties. In this study, the formation of SOA has been modeled along an air-mass trajectory over northern European boreal forest using two aerosol dynamics box models where the prediction of the condensable organics from the gas-phase oxidation of BVOC is handled with schemes of varying complexity. The use of box model simulations along an air-mass trajectory allows us to compare, under atmospheric relevant conditions, different model parameterizations and their effect on SOA formation. The result of the study shows that the modeled mass concentration of SOA is highly dependent on the organic oxidation scheme used to predict oxidation products. A near-explicit treatment of organic gas-phase oxidation (Master Chemical Mechanism version 3.2) was compared to oxidation schemes that use the volatility basis set (VBS) approach. The resulting SOA mass modeled with different VBS schemes varies by a factor of about 7 depending on how the first-generation oxidation products are parameterized and how they subsequently age (e.g., how fast the gas-phase oxidation products react with the OH radical, how they respond to temperature changes, and if they are allowed to fragment dur-

ing the aging process). Since the VBS approach is frequently used in regional and global climate models due to its relatively simple treatment of the oxidation products compared to near-explicit oxidation schemes, a better understanding of the above-mentioned processes is needed. Based on the results of this study, fragmentation should be included in order to obtain a realistic SOA formation. Furthermore, compared to the most commonly used VBS schemes, the near-explicit method produces less – but more oxidized – SOA.

1 Introduction

Secondary organic aerosols (SOA), formed through gas-to-particle partitioning in the atmosphere, constitute a large part of the global organic aerosol load (Crippa et al., 2014; Hallquist et al., 2009; Jimenez et al., 2009) and affect the climate by absorbing or scattering radiation and acting as cloud condensation nuclei (CCN) (Scott et al., 2014). Over boreal forests, with little anthropogenic influences, most particles are comprised of organic constituents (O'Dowd et al., 2002; Tunved et al., 2006; Yttri et al., 2011), formed when biogenic volatile organic compounds (BVOCs), such as terpenes, are oxidized to form less volatile compounds. Despite the importance of SOA as a climate forcer, large uncertainties remain about the formation mechanisms and properties.

A lot of effort has been put into gaining better knowledge of how SOA is formed (Hallquist et al., 2009) and

how it can grow nucleation-mode particles into CCN (Kerminen et al., 2012). There are still large uncertainties remaining in the SOA formation process, mostly due to the vast number of known – but especially unknown – oxidation products of BVOCs. It has therefore been common practice in global model studies to simplify the gas-phase oxidation using only two hypothetical oxidation products with laboratory-constrained equilibrium partitioning coefficients to estimate the formation of SOA (Kroll and Seinfeld, 2008), based on the two-product model developed by Odum et al. (1996). This method does not account for continuous oxidation in the gas- or particle-phase, and atmospheric models that use this method generally underestimate organic aerosol mass (e.g., Heald et al., 2005; Spracklen et al., 2011; Volkamer et al., 2006). To reduce these limitations, Donahue et al. (2006) proposed a volatility basis set (VBS) approach, where the oxidation products are sorted into logarithmically spaced volatility bins, making it possible to represent a wider range of organic compounds in the atmosphere. The gas-phase aging (i.e., the continuous gas-phase oxidation of the products) can be taken into consideration by moving the oxidation products in the volatility space. To account for the reduction in volatility when functional groups are added during oxidation, these schemes typically move the products down one volatility bin per oxidation step (Bergström et al., 2012; Lane et al., 2008). Oxidation might however also lead to fragmentation, and models that only consider functionalization of biogenic compounds tend to overestimate the SOA mass concentration (Lane et al., 2008; Murphy and Pandis, 2009). A two-dimensional volatility basis set can be used to keep track of the oxygen-to-carbon (O:C) ratio during the aging process (Donahue et al., 2011; Jimenez et al., 2009), making it possible to also include fragmentation. Studies that have included fragmentation indicate that it is an important process to consider (Chen et al., 2013; Murphy et al., 2012; Shrivastava et al., 2013). The above-mentioned approaches are however empirical or semi-empirical and thus rely on experimental studies conducted under environmental conditions that resemble those in the atmosphere; conditions which might change during the SOA formation process and during future climate warming.

Another way to represent SOA formation is to use a gas-phase mechanism that explicitly predicts the condensable oxidation products. While this process makes it possible to predict growth under conditions and timescales beyond those conducted in laboratory studies, it is computationally heavy and needs to be simplified in order to be applicable (Hallquist et al., 2009). Additionally, the lack of knowledge of the properties of many oxidation products leads to uncertainties in these explicit schemes. A number of studies have modeled SOA formation in chamber experiments using explicit – or near explicit – gas-phase chemistry (e.g., Camredon et al., 2010; Capouet et al., 2008; Jenkin, 2004; Roldin et al., 2014; Valorso et al., 2011). The discrepancies between the modeled and measured SOA formation in many of these studies indi-

cate that there exist knowledge gaps that need to be filled in order to better understand the processes behind SOA formation.

In this study, uncertain parameters regarding the evolution of the biogenic oxidation products are identified using two aerosol dynamics box models coupled to different gas-phase oxidation schemes. The following processes are specifically studied:

1. the volatility distribution and oxygenation distribution of stable products formed in the first oxidation step of α -pinene oxidation
2. the gas-phase aging rate of the above-mentioned products with the OH radical
3. the temperature response of the oxidation products
4. fragmentation reactions during the aging process

The aim is to investigate the implementation of different gas-phase oxidation schemes and condensation schemes of various complexities, and what effect they have on the modeled evolution of SOA at atmospheric conditions. SOA formation is modeled along an air-mass trajectory over the northern European boreal forest using two aerosol dynamics box models: an updated version of the Aerosol Dynamics, gas-phase CHEMistry and radiative transfer model (ADCHEM) (Roldin et al., 2011a) and MALTE-BOX (Boy et al., 2013), which is the zero-dimensional model version of MALTE (Model to predict new Aerosol formation in the Lower Troposphere) (Boy et al., 2006). Both models are coupled to the near-explicit Master Chemical Mechanism version 3.2 (MCMv3.2) (Jenkin et al., 1997; Saunders et al., 2003) which is used when predicting the oxidation products of the BVOCs (here represented by α -pinene). Different VBS approaches, which have all been applied in previous modeling studies, are compared with near-explicit modeling of SOA formation to get an indication of the uncertainties involved and the importance of different processes in the VBS regarding SOA formation.

2 Method

For all simulations in this study, the models were implemented along an air-mass trajectory retrieved from the Hybrid Single Particle Lagrangian Integrated Trajectory Model (HYSPLIT) model (Draxler and Rolph, 2013) with meteorological data from the Global Data Assimilation System (GDAS), downloaded from NOAA Air Resource Laboratory Real-time Environmental Application and Display sYstem (READY) (Rolph, 2013), linearly interpolated from 3 h to 1 min (the main time step used in the simulations).

2.1 Model descriptions

2.1.1 ADCHEM

The two-dimensional trajectory model ADCHEM was primarily developed to be used for urban plume studies in the atmosphere (Roldin et al., 2011b). In order to capture the vertical and horizontal dispersion of urban plumes, ADCHEM solves the atmospheric diffusion equation perpendicular to the air-mass trajectory. However, in this study we will only use ADCHEM as a box model (zero-dimensional). The aerosol dynamics scheme in ADCHEM includes homogeneous nucleation, dry deposition, Brownian coagulation and detailed condensation/evaporation. ADCHEM also contains a radiative transfer model which calculates the spectral actinic flux (for more detailed information about ADCHEM, see Roldin et al., 2011a). Different gas-phase oxidation schemes can be coupled to ADCHEM; for more information about these, and also how the pure-liquid saturation vapor pressures of the condensing species are estimated, see Sect. 2.3. The condensation/evaporation module in ADCHEM can be combined either with the non-equilibrium 2DVBS approach, as described in Roldin et al. (2011a), or with a detailed particle-phase chemistry and kinetic multi-layer model (Roldin et al., 2014). The saturation vapor pressures for each particle size bin are corrected with Raoult's law, taking into account the non-ideal interactions between compounds in the organic particle phase (activity coefficients) and the Kelvin effect. In this study, we will treat the SOA as a well-mixed liquid and neglect any heterogeneous chemistry.

2.1.2 MALTE-BOX

MALTE-BOX is a zero-dimensional model based on the one-dimensional column model MALTE (Boy et al., 2006). The box version is described in Boy et al. (2013) and Wang et al. (2013). The model consists of modules for gas-phase chemical reactions and photochemistry together with aerosol dynamics. In this study, emissions of inorganic trace gases and α -pinene are treated as explained in Sect. 2.2.1, while the chemistry and the saturation vapor pressures used are explained in Sect. 2.3.3. The aerosol dynamics in MALTE-BOX is solved by UHMA, which is described in detail in Korhonen et al. (2004). The model includes Brownian coagulation, condensation/evaporation, dry deposition and several nucleation schemes; however, only condensation/evaporation was considered in this study. The model uses sectional methods and a Runge–Kutta solver to solve the general dynamic equation for aerosols.

The main difference between UHMA and ADCHEM lies in the various vapor property parameterizations and additional mechanisms for the activity coefficients in the condensation algorithm. The densities of the condensing pure organic compounds in UHMA are estimated based on their

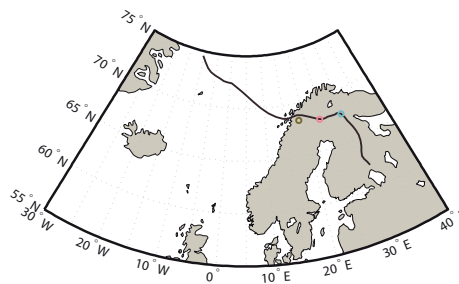


Figure 1. The studied air-mass trajectory retrieved from the HYSPLIT model. The brown, pink and blue circles display the location of the measurement stations Abisko, Pallas and Värriö, respectively.

molecular weights and atomic volumes, taking into consideration the changes in volume due to intramolecular bonding (Girolami, 1994). In ADCHEM, on the other hand, the densities are assumed to be 1400 kg m^{-3} for all condensing organic species (Hallquist et al., 2009). The models also calculate the molecular diffusion coefficients of the vapors differently; ADCHEM uses a method described in Jacobson (2005), whereas MALTE-BOX derives them from Fuller et al. (1966).

2.2 Model setup

All model simulations start over the Atlantic Ocean ($74^{\circ}34' \text{ N}$, $10^{\circ}19' \text{ W}$) on 28 July 2005, 18:00 UTC. The air mass then passes close to three remote research stations: first Abisko ($68^{\circ}52' \text{ N}$, $18^{\circ}30' \text{ E}$, 360 m a.s.l.) on 31 July 2005 at 03:00 UTC, then Pallas ($67^{\circ}56' \text{ N}$, $24^{\circ}22' \text{ E}$, 565 m a.s.l.) on 31 July 2005 at 18:00 UTC and finally Värriö ($67^{\circ}45' \text{ N}$, $29^{\circ}38' \text{ E}$, 395 m a.s.l.) on 2 August 2005 at 00:00 UTC, see Fig. 1. The three stations are located on a west-to-east line roughly 200 km apart from each other. Description of the stations and the instrumentation can be found in Väänänen et al. (2013). Even though the Pallas station is located on a hilltop, all three stations are considered as ground level sites in this study. Since the boundary layer is assumed to be well-mixed, the air arriving at the stations represents the boundary layer on a larger scale. The specific trajectory was chosen by analyzing hourly HYSPLIT trajectories (Draxler and Rolph, 2013) between the years 2005 and 2007 arriving at Värriö at the altitude of the station. The analysis was limited to trajectories arriving from the Atlantic Ocean and passing over Scandinavia between latitude parallels $67^{\circ}6' \text{ N}$ and 69° N within 1000 m above ground level in order to ensure similar source areas and a clear transport route between the stations. Furthermore, the trajectories had to pass over Abisko and Pallas, within 25 km of the respective station, during its path. This is in line with the general 10–30 % un-

Table 1. Initial concentrations applied to all model simulations.

Inorganic species	NO	NO ₂	SO ₂	CO	O ₃	H ₂ O ₂	HNO ₃
Concentration [ppb]	0.1	0.2	0.2	100	20	0.1	0.1

Table 2. Details of the three base case gas-phase schemes investigated in this study.

Scenarios	Organic oxidation products	First generation chemistry	Higher-order-generation chemistry (aging)
1DVBS; Simpson et al. (2012)	nine products distributed in a 1DVBS, with temperature dependence explained by $\Delta H_{\text{Eff}}^{\text{Vap}} = 30 \text{ kJ mol}^{-1}$; Bergström et al. (2012)	four-product basis set: $\alpha_{\text{mass}} = [0.072 \quad 0.061 \quad 0.239 \quad 0.405]$ for $\log_{10} C_{298}^*$ 0 to 3 Lane et al. (2008)	aging rate: $k_{\text{OH}} = 4 \times 10^{-12} \text{ cm}^3 \text{ molec}^{-1} \text{ s}^{-1}$ Bergström et al. (2012)
2DVBS, Jimenez et al. (2009)	144 products distributed in a 2DVBS, with temperature dependence explained by $\Delta H^{\text{Vap}} = -5.8 \log_{10} C_0^* + 100 \text{ kJ mol}^{-1}$; Donahue et al. (2006)	seven-product basis set: $\alpha_{\text{mass}} = [0.05 \quad 0.085 \quad 0.125 \quad 0.19 \quad 0.4 \quad 0.35 \quad 0.2]$ for $\log_{10} C_{298}^*$ 0 to 6; Donahue et al. (2009)	aging rate: $k_{\text{OH}} = 3 \times 10^{-11} \text{ cm}^3 \text{ molec}^{-1} \text{ s}^{-1}$ Jimenez et al. (2009)
MCM; Jenkin et al. (1997); Saunders et al. (2003)	153 products with vapor pressures estimated from Nannoolal et al. (2008)	MCMv3.2	MCMv3.2

certainty of trajectories (Stohl, 1998). The aerosol particle number size distributions at the three stations were analyzed at the times when the trajectories passed them. An air mass that had a low particle number concentration in Abisko which increased between the stations was chosen. Additionally, the trajectory of this air mass had to remain in the boundary layer between the stations with no precipitation along its path. The data from Abisko were used as the initial particle size distribution in the model by using the automatic lognormal-fitting algorithm DO-FIT, version 4.20 (Hussein et al., 2005). Due to the low particle concentration and the origin of the air mass, it was assumed to have a chemical composition of marine aerosol. O'Dowd et al. (2004) measured the physical and chemical properties of aerosols at the research station Mace Head originating from the North Atlantic Ocean during periods of both high and low biological activity in 2002. The chemical information from their study during periods of high biological activity (here assumed to represent summer conditions) was used to estimate the particle-size-dependent organic fraction. The initial concentrations of the inorganic compounds, not set to zero, are estimated based on average background concentrations and listed in Table 1.

2.2.1 Emissions

The inorganic gas emissions (SO₂, NO_x and CO) along the air-mass trajectory were retrieved from the emission database for the year 2005 from EMEP (European Monitoring and Evaluation Programme). The BVOC emissions, assumed to

include only α -pinene, were estimated using a method described in Tunved et al. (2006), where the flux of α -pinene is dependent on the emission potential of coniferous trees, the biomass density of these species along the trajectory (estimated to 950 g m^{-2} ; Lindfors et al., 1999) and the ambient temperature. Since the simulations are done with zero-dimensional models, the α -pinene emissions were assumed, as in the study by Tunved et al. (2006), to be confined in a well-mixed boundary layer of a constant height of 1000 m.

2.3 Description of base case simulations

In all simulations MCMv3.2 is used to model the gas phase, i.e., the inorganic chemistry and the first oxidation step of α -pinene. However, the resulting oxidation products from this step, and their subsequent gas-phase evolution, are modeled with varying complexity. The three schemes used to model the evolution of these condensable organic oxidation products are listed in Table 2 (1DVBS, 2DVBS and MCM) and used throughout this study as base case simulations. The MCM models the organic oxidation products near explicitly with MCMv3.2, while the two VBS approaches, after the first oxidation step of α -pinene, distribute the products into groups with different volatility based on chamber measurements. After the products in the VBS simulations have been distributed in their respective VBS space due the gas-phase reactions, their temperature-dependent saturation vapor pressures are calculated. These pressures, no longer bound to the VBS grid, are used in the condensa-

tion/evaporation module. The 2DVBS simulation is based on the two-dimensional VBS described in Jimenez et al. (2009), and 1DVBS is based on the one-dimensional VBS scheme used in the EMEP model (Bergström et al., 2012). The simulations are described in the sections below and, if not otherwise noted, coupled to ADCHEM.

2.3.1 1DVBS

The 1DVBS scheme distributes all organic oxidation products between nine volatility classes separated by powers of 10 in saturation vapor concentration, C^* , ranging from 10^{-5} to $10^3 \mu\text{g m}^{-3}$. The scheme is based on how SOA are treated in the EMEP chemical transport model (Bergström et al., 2012). The first-generation products from the oxidation of α -pinene and ozone are distributed according to a four-product basis set parameterization based on chamber studies (Lane et al., 2008), see Table 2. The products continue to react with the OH radical with a reaction rate of $4 \times 10^{-12} \text{ cm}^3 \text{ molec}^{-1} \text{ s}^{-1}$. At a reference temperature of 298 K, each reaction leads to a reduction in C^* by 1 order of magnitude and a 7.5 % increase in mass due to the added oxygen. The Clausius–Clapeyron equation (see Eq. (A2) in Appendix A) is used to calculate the temperature dependence with a constant ΔH^{vap} of 30 kJ mol^{-1} . Fragmentation is not considered.

2.3.2 2DVBS

The 2DVBS base case simulation in this study distributes all organic oxidation products across 12 volatility classes separated by powers of 10 in C^* , ranging from 10^{-5} to $10^6 \mu\text{g m}^{-3}$, and 12 discrete O : C ratios from 0.1 to 1.2, in steps of 0.1. The first-generation products from the oxidation of α -pinene by ozone are distributed in the volatility space according to a seven-product basis set parameterization based on chamber studies (Donahue et al., 2009), see Table 2. In order to distribute the products in the second dimension (O : C ratio), Eq. (A1) is used together with the assumption that most first-generation products have the same number of carbon atoms (n_C) as the parent hydrocarbon, here α -pinene with $n_C = 10$ (Jimenez et al., 2009). This means that the oxidation of α -pinene by ozone is assumed to include no fragmentation. Further oxidation in the gas-phase is based on Jimenez et al. (2009), where the products are assumed to react with the OH radical with a reaction rate constant of $3 \times 10^{-11} \text{ cm}^3 \text{ molec}^{-1} \text{ s}^{-1}$. For more information of functionalization and fragmentation of the oxidation products, see Appendix A.

2.3.3 MCM

The MCM base case simulation considers the degradation of α -pinene by using the near-explicit gas-phase kinetic mechanism MCMv3.2, which includes – in the case of α -pinene degradation – 942 reactions involving 293 organic and 19

inorganic gas-phase compounds. The pure liquid saturation vapor pressures of the 153 most important oxidation products (the non-radicals that contribute to particle growth in the condensation scheme) are estimated using a group contribution method described by Nannoolal et al. (2008). In the first oxidation step, α -pinene can react with ozone and the two radicals OH and NO_3 . The volatility and O : C ratio distribution of the first stable, non-radical generation products formed are compared with the first-generation products derived from chamber experiments (which are used in the VBS simulations). In order to do this, a simulation was done where the first-generation products generated in MCMv3.2 did not continue to react. A low NO_x environment was assumed with a constant OH radical concentration of $2 \times 10^5 \text{ cm}^{-3}$ (about the average concentration over land in the base case simulations) and a starting concentration of O_3 of $5 \times 10^{11} \text{ cm}^{-3}$. The starting concentration of α -pinene was $8 \times 10^9 \text{ cm}^{-3}$, and the simulation was run for 72 h to ensure that all α -pinene had been consumed. The result of this simulation is discussed in Sect. 3.2.

2.4 Processes not investigated in this study

This study explores different ways to model SOA formation through homogeneous gas-phase reactions and subsequent gas-to-particle partitioning. It is foremost a model comparison study aimed at investigating the impact that different parameterizations regarding homogeneous gas-phase reactions have on modeled particle growth. Other processes that may influence the growth (e.g., emissions, boundary layer meteorology) are treated with relatively simple assumptions. Moreover, SOA formation of course depends on many other complex processes (e.g., nucleation, coagulation, dry deposition, particle-phase chemistry), some of them included in this study but not investigated further. The simulations conducted should therefore not be compared to the measurements presented, but with each other. The measurements are instead shown as an indicator for realistic particle mass concentrations in boreal environments.

3 Results and discussion

The influence of the different gas-phase oxidation schemes, described in Sect. 2.3, on the distribution and properties of the α -pinene oxidation products is presented in this section. The subsequent effect on the SOA formation along the chosen air-mass trajectory shown in Fig. 1 is compared and discussed. Aside from the three base case scenarios listed in Table 2 and described in Sect. 2.3 above, different sensitivity tests were performed on the 2DVBS to investigate the impact of different assumptions made in the VBS model setup. Details of these simulations are listed in Table 3. In all simulations, if not otherwise mentioned, the gas-phase oxidation schemes were coupled to the aerosol dynamics box model,

Table 3. Sensitivity test performed on the 2DVBS base case (top row). Changed parameters are described in bold text, all other parameters are kept unchanged.

Scenario	Organic oxidation products	First-generation chemistry	Higher-order-generation chemistry (aging)
2DVBS	144 products in a 2DVBS, with temperature dependence: $\Delta H^{\text{vap}} = -5.8 \log_{10} C_{298}^* + 100 \text{ kJ mol}^{-1}$ Donahue et al. (2006)	seven-product basis set: $\alpha_{\text{mass}} = [0.05 \ 0.085 \ 0.125 \ 0.19 \ 0.4 \ 0.35 \ 0.2]$ for $\log_{10} C_{298}^*$ 0 to 6; Donahue et al. (2009) $O : C = f(\log_{10} C_{298}^*)^*$ O : C = 0.4; Chhabra et al. (2010) Four-product basis set: $\alpha_{\text{mass}} = [0.05 \ 0.085 \ 0.125 \ 0.19]$ Donahue et al. (2009) but not including products in bins with $C^* > 10^3$ Four-product basis set: $\alpha_{\text{mass}} = [0.072 \ 0.061 \ 0.239 \ 0.405]$ for $\log_{10} C_{298}^*$ 0 to 3 Lane et al. (2008) First-generation product distribution from MCMv3.2: $\alpha_{\text{mole}} = [0.0036 \ 0.062 \ 0.0343 \ 0.0266 \ 0.0975 \ 0.294 \ 0.204 \ 0.368]$ for $\log_{10} C_{298}^*$ -1 to 6	aging rate: $k_{\text{OH}} = 3 \times 10^{-11} \text{ cm}^3 \text{ molec}^{-1} \text{ s}^{-1}$ Jimenez et al. (2009) fragmentation ratio = $O : C^{(1/6)}$
2DVBS-OC = 0.4 2DVBS-4prod	see 2DVBS see 2DVBS	O : C = 0.4; Chhabra et al. (2010) Four-product basis set: $\alpha_{\text{mass}} = [0.05 \ 0.085 \ 0.125 \ 0.19]$ Donahue et al. (2009) but not including products in bins with $C^* > 10^3$ Four-product basis set: $\alpha_{\text{mass}} = [0.072 \ 0.061 \ 0.239 \ 0.405]$ for $\log_{10} C_{298}^*$ 0 to 3 Lane et al. (2008) First-generation product distribution from MCMv3.2: $\alpha_{\text{mole}} = [0.0036 \ 0.062 \ 0.0343 \ 0.0266 \ 0.0975 \ 0.294 \ 0.204 \ 0.368]$ for $\log_{10} C_{298}^*$ -1 to 6	see 2DVBS see 2DVBS
2DVBS-1DVBS	see 2DVBS	see 2DVBS	see 2DVBS
2DVBS-MCM	see 2DVBS	see 2DVBS	see 2DVBS
2DVBS-maxFrag 2DVBS-noFrag 2DVBS-agingRate1DVBS	see 2DVBS see 2DVBS see 2DVBS	see 2DVBS see 2DVBS see 2DVBS	fragmentation ratio = 1 fragmentation ratio = 0 aging rate: $k_{\text{OH}} = 4 \times 10^{-12} \text{ cm}^3 \text{ molec}^{-1} \text{ s}^{-1}$, Bergström et al. (2012)
2DVBS-temp1DVBS	144 products in a 2DVBS, with temperature dependence: $\Delta H_{\text{eff}}^{\text{vap}} = 30 \text{ kJ mol}^{-1}$, Bergström et al. (2012)	see 2DVBS	see 2DVBS

* Derived from Eq. (A1), using the volatility distribution from the seven-product basis set together with the assumption that most first oxidation steps do not include fragmentation, i.e., each first-generation product ends up in the O : C bin closest to having 10 carbon atoms at its specific saturation concentration.

ADCHEM. First however, the condensation modules in the two box models ADCHEM and MALTE-BOX will be compared.

3.1 Condensation in ADCHEM and MALTE-BOX

In order to test the sensitivity of the condensation module in ADCHEM, a simulation was done where the aerosol dynamics box model MALTE-BOX, was coupled to MCMv3.2 instead of ADCHEM. Condensation was the only aerosol dynamics process included in both box models for the comparison and the result is shown in Fig. 2. The upper panel shows the volume concentration of SOA along the trajectory, where the dotted blue line is the result from the MCM-ADCHEM coupling and the dashed pink line the result from the MCMv3.2 being coupled to the MALTE-BOX model. The discrepancy between the modeled mass concentrations is mainly due to the overall lower densities of condensable organics in MALTE-BOX compared to those in ADCHEM. These densities are used when the change of particle mass during condensation (or evaporation) is translated to the corresponding change in particle volume. The solid blue line in the upper panel in Fig. 2 is the result of using the same

method as in MALTE-BOX to parameterize the densities of the condensing organic oxidation products in ADCHEM (see Sect. 2.1.2 for more details about the parameterizations). The lower panel in Fig. 2 shows the number size distribution at different times along the trajectory (represented by different colors). The smaller particles seem to grow faster in MALTE-BOX compared to those in ADCHEM, especially during nighttime when the temperature is low. Considering the complexities of both models, they agree fairly well, with a maximum difference in volume concentration of 14 % at $t = 129 \text{ h}$ along the trajectory (3 August 03:00 UTC), corresponding to a maximum difference in the modeled geometric mean diameter of about 10 %.

The pure-liquid saturation vapor pressures of each organic oxidation product, needed to model the condensational growth in near-explicit models, can be estimated using different group contribution methods; both ADCHEM and MALTE-BOX normally use the method described by Nannoolal et al. (2008) (see Sect. 2.3.3). In Fig. 3, SOA formation modeled with ADCHEM using this method is compared to a simulation where ADCHEM instead uses the group contribution method SIMPOL (Pankow and Asher, 2008).

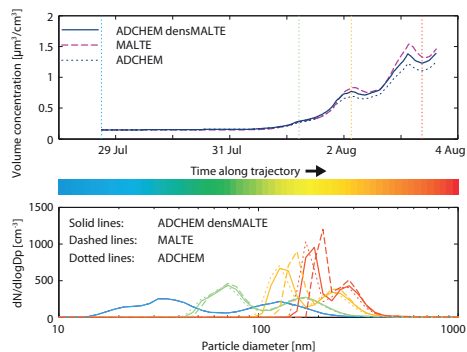


Figure 2. Evolution of particle volume concentration (upper panel) and particle number size distribution (lower panel) modeled with the aerosol dynamics box model MALTE-BOX or ADCHEM (modeled with a constant SOA density of 1400 kg m^{-3} or SOA densities from MALTE-BOX). The color of each size distribution plot represents the size distribution at a specific time along the trajectory, indicated by the corresponding color of the vertical line in the upper panel.

This method causes slower SOA formation since it predicts somewhat higher saturation vapor pressures, illustrating that the estimation of saturation vapor pressures is uncertain and needs to be investigated further.

Moreover, a recent study by Ehn et al. (2014) indicates that the ozonolysis of α -pinene might lead to products of extremely low volatility that condense irreversibly to form SOA and thus have the potential to increase the SOA yield significantly. These products are currently not included in the model simulations in this study but we are planning to implement them in future studies.

3.2 Base case simulations

The growth of SOA along the chosen trajectory, modeled by the three base case scenarios described in Table 2, is shown in Fig. 4. The figure also includes the calculated mass concentrations from size distribution measurements in Abisko, Pallas and Värriö at the time the air mass passed by. The measurements from Pallas and Värriö are further compared with estimations of particle mass concentrations from two studies, Tunved et al. (2006) and Väänänen et al. (2013), scaled with the size distribution measurement from Abisko. In both of these studies, the mass concentrations are expressed as a function of time the air mass has spent over land. The former study based its estimation on measurements conducted during the growing season (April to September) between 1999 and 2004, and the latter on measurements during the growing season between 2005 and 2007. Aside from the different measurement periods in the studies, Tunved et al. (2006) used

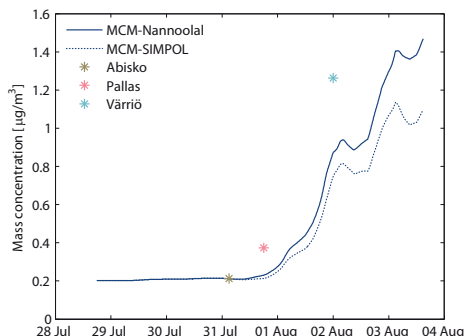


Figure 3. Particle mass concentration along the air-mass trajectory modeled with ADCHEM using different methods of estimating the saturation vapor pressures of the organic oxidation products.

the same expression to estimate the mass concentration both in Pallas and Värriö, while Väänänen et al. (2013) generated two separate estimations: one for Pallas and another for Värriö. This resulted in lower estimated mass concentrations in the study by Tunved et al. (2006) compared to Väänänen et al. (2013), especially in the case of Värriö.

Neither the measurements conducted when the air mass passed the site nor the estimations of the mass concentration from Tunved et al. (2006) and Väänänen et al. (2013) indicate that the particle mass concentration should reach the value it does in the 2DVBS simulation. This simulation also diverges most from the other simulations. In order to understand why the growth of SOA is higher in the 2DVBS, the mass evolution of not only the particle phase, but also that of the gas phase, needs to be studied.

Since a lot of the oxidation products from α -pinene exist in significant fractions both in the particle and gas phase at atmospheric conditions, it is informative to look at how they are distributed between the two phases depending on the amount of time they have spent over land. Figure 5b–d show the volatility distribution of the condensable products at the three measurement sites, modeled by the three base case scenarios. Figure 5a shows the distribution of the first-generation products, i.e., the first stable, non-radical products from the reaction between α -pinene and ozone (in MCM, the first oxidation step also includes reaction with the OH radical and NO_3). The darker colors in each bar in Fig. 5b–d illustrate the portion of products in the particle phase; for example, in Abisko almost all products are in the gas phase in all three scenarios. As the air mass moves, α -pinene is emitted and its oxidation products are accumulated and oxidized, leading to an increased portion of products partitioning to the particle phase. In Värriö, where the SOA mass concentration is on the order of magnitude of $1 \mu\text{g m}^{-3}$, compounds with saturation concentration lower than $\sim 10 \mu\text{g m}^{-3}$ par-

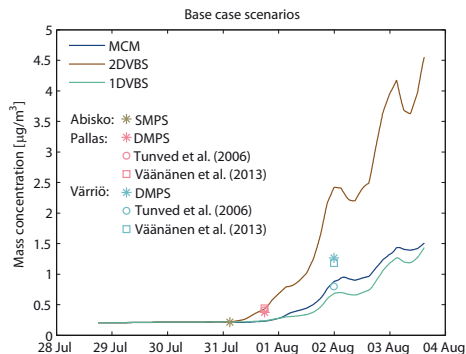


Figure 4. Modeled evolution of particle mass along the studied air-mass trajectory. The SMPS (scanning mobility particle sizer) and DMPS (differential mobility particle sizer) data points are the measured size distribution at Abisko, Pallas and Värriö at the time the air mass passed. Also shown are estimated average mass concentrations as functions of the time the air mass spent over land. The rings are based on measurement during the growing season between 1999 and 2004 (Tunved et al., 2006) and the squares are based on measurements between 2005 and 2007 (Väänänen et al., 2013).

tion substantially to the particle phase. The 2DVBS simulation has about 40% more total mass (gas and particle) in this range in Värriö than the other two base case simulations. The higher mass is partly due to the different first-generation chemistry between the model scenarios: compared to the other two base case simulations, the first oxidation step in 2DVBS generates more mass, especially compared to 1DVBS; this will be discussed further in Sect. 3.3. Most of this “extra” mass is located in high-volatility bins and therefore resides in the gas phase; however, if allowed to age, it will increase the particle mass.

Here, it is also evident that while the evolution of particle mass in the MCM and 1DVBS simulations in Fig. 4 show similar patterns, the volatility distribution of their oxidation products does not. The 1DVBS distributes its first-generation products more evenly in the volatility space and – due to the relatively simple parameterization of the aging process – the distribution remains even throughout the simulation. Moreover, the 1DVBS only distributes first-generation products in four bins, products with higher volatilities are (in this scheme) assumed to have no effect on the particle growth and are thus ignored.

Gas-phase oxidation does not necessarily lead to products with lower volatility; the more oxygenated the products are, the higher is the probability that they fragment and form products with lower carbon number (Kroll et al., 2009). Oxidation does however tend to increase the O : C ratio of the products (Kroll et al., 2011; Murphy et al., 2011); thus, the

O : C ratio can provide valuable information on the amount of aging the compounds have experienced. The O : C ratio in regional organic aerosol is about 0.7 (Hallquist et al., 2009).

Figure 6 illustrates both the evolution of O : C ratio and volatility of the oxidation products in the SOA formation process, where the grey areas represent the state of the first-generation oxidation products (in the gas or particle phase), while the pink ones represent only the particle properties in Pallas (when the air mass has spent 18 h over land). The mass-weighted average O : C ratio of the first-generation products, represented by the stars, are higher in the MCM simulation than in the 2DVBS. Since the MCM volatility is also higher, this implies that fragmentation could play a larger role in the MCM in the first oxidation step, which in turn would mean that more oxidation steps are needed before the products can partition to the particle phase, causing a higher mass-weighted average of the O : C ratio of the resulting products in particle phase. The first-generation products in the 1DVBS simulation have about the same O : C ratio as the MCM; however, the 1DVBS does not include fragmentation – instead every oxidation step leads to products with lower volatilities, but the aging rate is so slow that almost no aging takes place.

The time evolution of the mass-weighted average SOA properties along the air-mass trajectory starting from Abisko, modeled by the three base case scenarios, are also shown in Fig. 6. In the direction of the arrows, the colors indicate how the particle mass concentration changes during transportation. Except during the first hours, the saturation concentrations in all simulations slightly increase over time since α -pinene is continuously emitted along the trajectory. The lower mole fractions of especially the more volatile organic compounds in the particle phase during the first hours probably cause the initial decrease in saturation concentrations (Raoult’s law). The MCM and 2DVBS simulations show a stronger diurnal trend in the O : C ratio due to temperature variations compared to the 1DVBS. This is probably the result of the simpler aging mechanism in the 1DVBS simulation, e.g., the use of a constant and low enthalpy of vaporization in the 1DVBS.

3.3 2DVBS sensitivity simulations

The results of the sensitivity tests performed on the 2DVBS simulation are presented in this section. The names and details of these simulations are described in Table 3. The studied parameters are the first-generation chemistry, the aging rate, the enthalpy of vaporization and the role of fragmentation in the 2DVBS. The results of these tests are presented in Fig. 7a and b.

Figure 7a includes results from simulations where different methods have been used to predict the distribution of first-generation products from the oxidation of α -pinene. The effect of using the first-generation volatility distribution from the 1DVBS base case in the 2DVBS (2DVBS-1DVBS, green

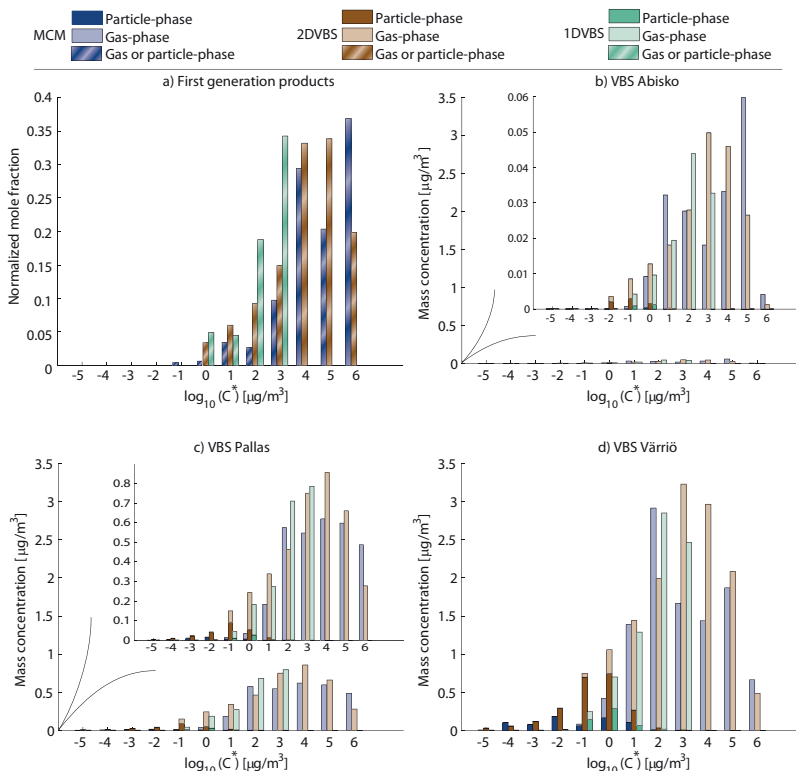


Figure 5. Volatility distribution of the oxidation products in both gas and particle phase from the MCM, 2DVBS and 1DVBS base case simulations. In (a), only products from the first oxidation step are shown, while (b–d) include products from higher-generation oxidation as well. The distributions in (b–d) are at Abisko, Pallas and Värriö, respectively, the dark colors represent the portion of products in the particle phase and the light colors, the portion in the gas phase.

line) is small even though the distributions from the two simulations differ from each other (see Fig. 5a). This does not mean that the volatility distribution of first-generation products have no influence on how the products evolve in the atmosphere. The distribution from the 1DVBS causes the first-generation oxidation products in the 2DVBS-1DVBS to distribute toward lower saturation concentrations, which should lead to a higher SOA growth in the 2DVBS-1DVBS than in the base case 2DVBS scenario. However, due to the relationship between carbon number and volatility in the 2DVBS simulation (Eq. A1) and the assumption that the oxidation of α -pinene by ozone does not include fragmentation (i.e., most first-generation products will have carbon number of 9 or 10), the O : C ratio of the first-generation products will be higher in 2DVBS-1DVBS than in the base case

2DVBS. This is illustrated in Fig. 8 and explained as follows: since the carbon number of the products are known, the O : C distribution of the products can be calculated based on the known volatility distribution of the first-generation products. Figure 8 illustrates how the O : C ratio is a function of the volatility when the carbon number is 10 (black line). The first-generation products in the 2DVBS-1DVBS (lower panel, Fig. 8) are distributed towards lower volatilities than the 2DVBS (upper panel, Fig. 8) which explains their higher O : C ratios. This will cause a larger fraction of products to fragment in higher-generation oxidation reactions compared to the base case scenario (fragmentation ratio = $\text{O} : \text{C}^{(1/6)}$), leading to a smaller SOA growth in the 2DVBS-1DVBS. The overall difference between the scenarios is very small.

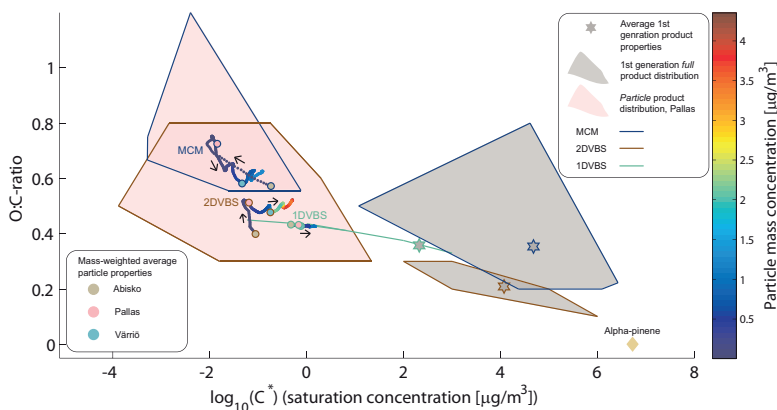


Figure 6. The full (gas or particle) first-generation distributions of the oxidation products in the MCM, 2DVBS and 1DVBS base case simulations are shown as grey areas enclosed with lines, representing each model simulation (MCM – blue, 2DVBS – brown and 1DVBS – green). The grey stars are the corresponding mass-weighted average properties of the first-generation products. The distributions of the products in particle phase in Pallas are shown as pink areas. Also shown, for all three model simulations, are the time evolutions (in the direction of the respective arrows) of the mass-weighted average particle properties and SOA concentration along the air-mass trajectory starting from Abisko (beige circles) and passing Pallas (pink circles) and Värriö (blue circles).

The solid orange line in Fig. 7a shows the resulting growth of SOA when the O : C ratio of all first-generation products in the 2DVBS simulation are set to 0.4 (2DVBS-OC = 0.4). This further confirms that higher O : C ratio of first-generation products lead to lower SOA mass due to the increased fragmentation. This initial O : C ratio is closer to the O : C ratio of oxidation products from α -pinene ozonolysis measured in chamber studies (Chhabra et al., 2010) and also closer to the corresponding value in the MCM simulation, implying that fragmentation is already important in the first oxidation steps.

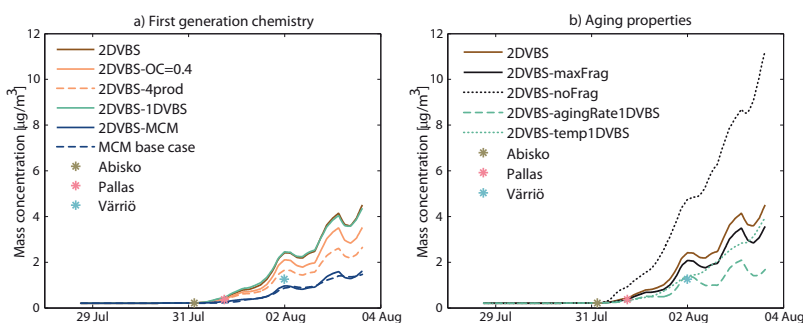
The distribution of the first-generation products in the 2DVBS base case scenario, based on Donahue et al. (2009), are constrained by chamber measurements for the products in the volatility bins with saturation concentrations (C^*) between 1 and 1000 $\mu\text{g m}^{-3}$. Based on mass balance calculations, Donahue et al. (2009) concluded that the majority of the mass is unaccounted for and placed the remainder of the mass in bins with higher C^* within the VBS. Products in these bins are too volatile to partition to the particle phase; through aging they will however eventually acquire low-enough volatility to condense. The dashed orange line in Fig. 7a (2DVBS-4prod) implies that the aging of these products is an important process since the particle growth is reduced when they are excluded. The distribution of the high-volatility products are however very uncertain. Explicit or near-explicit modeling may provide a more realistic method for predicting these products, keeping in mind that these approaches also include uncertainties (such as the estima-

tion of saturation vapor pressures discussed in Sect. 3.1). In the 2DVBS-MCM simulation, the distribution of first-generation products in the two-dimensional VBS is predicted using MCMv3.2, while further oxidation is modeled with the 2DVBS. The result of this simulation is represented by the blue line in Fig. 7a (2DVBS-MCM). The reduction in particle growth is caused by the, on average, higher C^* and higher O : C ratio of the first-generation products modeled by MCMv3.2 compared to the chamber-based mass distribution used in 2DVBS base case scenario. Overall, the different simulations in Fig. 7a vary by about a factor of 3, highlighting the need for more knowledge of the oxidation products, and their distribution, already after the first oxidation step.

In Fig. 7b, the result of using different aging parameterizations in the VBS is illustrated. The first-generation products are modeled as in the base case 2DVBS. To test how sensitive the 2DVBS base case scenario is to fragmentation during aging, a simulation without fragmentation (2DVBS-noFrag; dashed black line) and a simulation when all oxidation steps include fragmentation (2DVBS-maxFrag; black line) were conducted. Without fragmentation, the mass of SOA increases to unrealistically high values implying that fragmentation is needed in order to predict realistic values of SOA growth in environments where aging is important for the mass concentration. The effect of the other extreme (fragmentation occurring in each oxidation step) is not as big since compounds in the base case scenario with an O : C ratio of 0.5 (about the average O : C ratio of SOA in the 2DVBS

Table 4. Importance of processes that affect particle mass concentration when modeling long-term aging of biogenic SOA in the atmosphere. The uncertainties of the processes are mostly based on results from this study, where processes placed to the left are the most uncertain.

Uncertainty of parameterization		
Processes affecting SOA formation	Very uncertain	=> Less uncertain
First-generation volatility distribution and oxygenation distribution of α -pinene oxidation products	Important	
OH aging rate constant with the gas-phase oxidation products		Important
Temperature response of the oxidation products		Potentially important
Fragmentation during aging process (if included)	Important	

**Figure 7.** Particle growth along the air-mass trajectory modeled with different versions of 2DVBS (see Table 3 for more details). In (a) different parameterizations of first-generation chemistry are tested and in (b) different parameterizations of gas-phase aging are tested.

base case) already have an 89 % fragmentation probability when oxidized further.

Compared to the 2DVBS base case, products in the 1DVBS simulation react with the OH radical with a rate constant 1 order of magnitude smaller (based on the aging rate of biogenic SOA in the EMEP model (Bergström et al., 2012)). Using this aging rate that is 1 order of magnitude smaller (2DVBS-agingRate1DVBS; dashed, green line) causes substantial reduction of SOA mass. However, since the products do not age much in this scenario, the average O : C ratio of the resulting particles show even lower values (~ 0.4) compared to the base case (~ 0.5). Models that only distribute SOA mass based on their volatilities (one-dimensional VBS) do not usually include fragmentation, often forcing them to use unrealistically low aging rates, or exclude aging of biogenic SOA altogether, to keep SOA concentrations at realistic values (Bergström et al., 2012; Murphy and Pandis, 2009).

In the 2DVBS-temp1DVBS simulation (dotted green line in Fig. 7b), the enthalpy of vaporization has been set to a constant value of 30 kJ mole^{-1} (while keeping everything else as in the 2DVBS base case). The result is a reduced

temperature response of the particle growth, as well as a somewhat smaller growth; this is due to a distribution of the oxidation products towards higher volatilities compared to the 2DVBS base scenario which uses a ΔH^{Vap} that varies with saturation concentration ($65\text{--}129 \text{ kJ mole}^{-1}$). Donahue et al. (2006), however, argued that models which include many semi-volatile species should use more realistic values of ΔH^{Vap} , i.e., values that depend on the volatility of the products.

The assumptions regarding gas-phase aging made in this study have a high impact on SOA formation. Further research is needed in order to make more reliable parameterization, especially when explicit chemistry cannot be used.

4 Conclusions

The main conclusions of this study are summarized in Table 4, in which four processes that have the potential to affect SOA formation are stated: (1) first-generation volatility distribution and oxygenation distribution of α -pinene oxidation

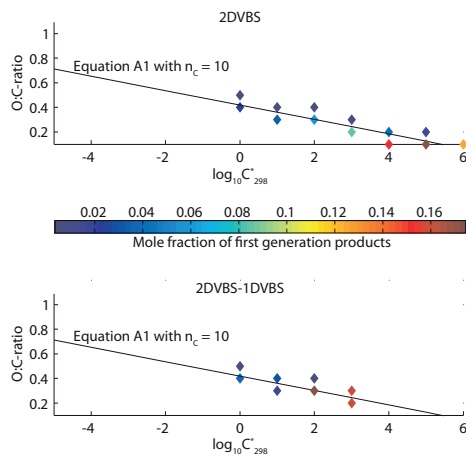


Figure 8. First-generation product distribution in the two-dimensional VBS space modeled with the 2DVBS simulation (upper panel) and the 2DVBS-1DVBS simulation (lower panel). The black line shows the linear dependence between the O : C ratio and volatility when a carbon number of 10 is assumed.

products, (2) OH reaction rate constant with the gas-phase oxidation products, (3) temperature response of the oxidation products and (4) the fraction of second- and multi-generation reactions that give fragmentation, assuming that fragmentation is included. The uncertainty and impact these processes have on SOA formation, inferred from the simulations done, are discussed below and summarized in the table:

1. In this study, first-generation oxidation products have been modeled explicitly with MCMv3.2 and compared to two other studies (Bergström et al., 2012; Donahue et al., 2009), where the volatility distributions are parameterized using chamber data. Depending on which was method used, the results differed by about a factor of 3, implying that the volatility distribution of the first-generation products can have a high impact on SOA formation. The amount of products created through oxidation of BVOCs makes their volatility distribution uncertain, especially for the experimentally derived distribution of the products with high volatility ($C^* > 1000 \mu\text{g m}^{-3}$) that do not partition to the particle phase at atmospheric conditions, but can nevertheless be important for SOA formation if allowed to oxidize further. The O : C ratios of the initial oxidation products are also uncertain parameters. The 2DVBS simulation, based on Jimenez et al. (2009), assumed no fragmentation during the first oxidation step, while some first oxidation steps in the MCM included fragmenta-

tion. As a result, the mass-weighted average O : C ratio of the products were a little bit higher in simulations using MCMv3.2. The higher O : C ratio resulted in a slower particle growth when fragmentation in higher-generation gas-phase reactions were included.

2. The first-generation products are further oxidized by reactions in the gas phase (particle-phase reactions are not considered in this study). In the VBS simulations, it was assumed that the products aged by reacting with the OH radical with a reaction rate that was independent of where they were located in the VBS space. Based on previous studies, two reaction rate constants were used: $3 \times 10^{-11} \text{ cm}^3 \text{ molec}^{-1} \text{ s}^{-1}$ and $4 \times 10^{-12} \text{ cm}^3 \text{ molec}^{-1} \text{ s}^{-1}$. The lower rate constant resulted in products with unrealistically low O : C ratios and substantially reduced the mass concentration of SOA. When the higher reaction rate constant was applied, the aging effect was comparable to the aging in the MCM simulation where the products are predicted near explicitly.
3. Temperature will affect the gas-to-particle partitioning. When a VBS approach is used, individual product information is lost as they are lumped into bins depending on their volatility. In the VBS simulations conducted here, the temperature response was modeled by either letting all bins respond equally to temperature changes or respond accordingly to their saturation concentration. This was controlled by choosing a constant or volatility-dependent enthalpy of vaporization, respectively. In the near-explicit modeling of oxidation products, the temperature response can be modeled in more detail, where each specific product can have their own response. When a volatility-dependent temperature response was used in the VBS, as opposed to letting all products respond equally, the result was in closer agreement with the result from the near-explicit simulation. The importance of the temperature response regarding SOA formation depends on the environment. In a boreal environment, there are many organic semi-volatile compounds which makes the compound-dependent temperature response more important.
4. The results of this study show that fragmentation is important to include during the aging process. It has been shown that fragmentation becomes more important the more oxygenated the compounds are, and a sharp increase in fragmentation from products with O : C ratio of 0 up to 0.4 has been observed (Kroll et al., 2009). However, it is very uncertain how to describe the features of fragmentation, especially in the VBS approach. Based on the results from this study, fragmentation should be included to get a realistic SOA formation.

Other uncertainties beyond the scope of this study include particle-phase chemistry and aerosol-phase state. Studies

have shown that these processes have the potential to affect SOA formation (Chan et al., 2007; Kroll and Seinfeld, 2008; Perraud et al., 2012; Roldin et al., 2014). The diurnal trend, caused by the temperature variation, of the particle mass concentration in the base case scenarios in this study might in part be a result of excluding particle chemistry and assuming equilibrium partitioning. If the condensing gas-phase species are allowed to undergo chemical reactions in the particle phase to form low volatile products, evaporation and re-condensation of these species will be inhibited.

Discrepancies exist between measured and modeled SOA, especially in global model studies, indicating a lack of knowledge about certain processes involving SOA formation. All processes cannot be included in large, global models, but important processes need to be parameterized and included. Box models with process-based representation of aerosol dynamics and gas- and particle-phase chemistry are important tools to understand these processes and explore how to best parameterize them.

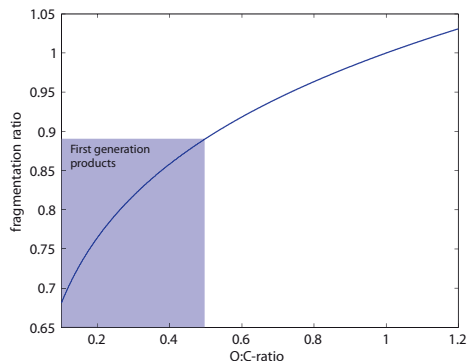


Figure A1. Fraction of products that undergo fragmentation in the 2DVBS scheme as a function of their O : C ratio. The shaded area shows the range of O : C ratio of the first-generation products in the 2DVBS.

Appendix A: Functionalization and fragmentation in the 2DVBS scheme

Each oxidation step after the oxidation of α -pinene in the 2DVBS includes functionalization where between one and three oxygen atoms are added, causing a reduction in saturation vapor concentration (C^*) and an increase in the O : C ratio. The increase in O : C ratio depends on the number of carbon atoms (n_C) in the bin of the reacting compound, which is estimated using a simple empirical three-parameter group contribution relationship between the pure compound saturation concentration at a reference temperature of 298 K ($\log_{10} C_{298}^*$) and the number of carbon and oxygen atoms (n_O) (Eq. A1) (Donahue et al., 2011):

$$\log_{10} C_{298}^* = (n_C^0 - n_C) b_C - n_O b_O, \quad (\text{A1})$$

where $n_C^0 = 25$ represents the reference point, defined as the number of carbon atoms in an alkane with $C_{298}^* = 1 \mu\text{g m}^{-3}$. $b_C = 0.475$ is the slope in the linear relationship between $\log_{10} C_{298}^*$ and n_C , i.e., the effect of increasing the number of carbon atoms by one is a 0.475 decade decrease in saturation concentration. $b_O = 1.7$; resulting in a 1.7 decade decrease in saturation concentration of each added oxygen. To account for the temperature dependence of the saturation concentration, the Clausius–Clapeyron equation (Eq. A2) is used:

$$C^* = C_{298}^* \frac{T_{298}}{T} \exp \left(\frac{\Delta H^{\text{vap}}}{R} \left(\frac{1}{T_{298}} - \frac{1}{T} \right) \right), \quad (\text{A2})$$

where T_{298} is the reference temperature and R is the ideal gas constant. ΔH^{vap} is the enthalpy of vaporization assumed to depend on C_{298}^* (Donahue et al., 2006) (see Table 2).

After the functionalization step, a fraction (f) of the products formed can fragment into at least two products with lower carbon numbers. This fraction is an uncertain parameter, but, as suggested by Jimenez et al. (2009), is treated as a function of the O : C ratio of the products: $f = \text{O} : \text{C}^{(1/6)}$. Figure A1 illustrates the fragmentation probability as a function of the O : C ratio, where the range of O : C ratios of first-generation products in the 2DVBS is represented by the shaded area. As described in Jimenez et al. (2009), the C–C cleavage is assumed to have an equal probability to take place anywhere along the carbon backbone, and the resulting products will have higher volatility than the reactant. Unlike in Jimenez et al. (2009), however, we assume that the fragmentation does not change the O : C ratio of the products.

Acknowledgements. This work was carried out with the support by Nordic Center of Excellence program (CRAICC – Cryosphere-Atmosphere Interactions in a Changing Arctic Climate), the EU FP7 projects ACTRIS (Aerosols, Clouds, and Trace gases Research Infra Structure Network) and the European Commission Seventh Framework Programme (FP7) in the project PEGASOS (Pan-European Gas-AeroSOI-climate interaction Study), the Swedish Strategic Research Program MERGE, Modeling the Regional and Global Earth System, and the Lund Centre for studies of Carbon Cycle and Climate Interaction – LUCCI. We also gratefully acknowledge the support of the Swedish Research Council and the Helsinki University Centre for Environment (HENV), Academy of Finland Centre of Excellence program (project no. 1118615).

The authors would like to thank Almut Arneht at Karlsruhe Institute of Technology for the size distribution measurements at Abisko, Heikki Lihavainen at the Finnish Meteorological Institute for the measurement at Pallas and Markku Kulmala and Pasi Aalto at University of Helsinki for the measurement at Värriö.

Edited by: S. M. Noe

References

- Bergström, R., Denier van der Gon, H. A. C., Prévôt, A. S. H., Yttri, K. E., and Simpson, D.: Modelling of organic aerosols over Europe (2002–2007) using a volatility basis set (VBS) framework: application of different assumptions regarding the formation of secondary organic aerosol, *Atmos. Chem. Phys.*, 12, 8499–8527, doi:10.5194/acp-12-8499-2012, 2012.
- Boy, M., Hellmuth, O., Korhonen, H., Nilsson, E. D., ReVelle, D., Turnipseed, A., Arnold, F., and Kulmala, M.: MALTE – model to predict new aerosol formation in the lower troposphere, *Atmos. Chem. Phys.*, 6, 4499–4517, doi:10.5194/acp-6-4499-2006, 2006.
- Boy, M., Mogensen, D., Smolander, S., Zhou, L., Nieminen, T., Paasonen, P., Plass-Dülmer, C., Sipilä, M., Petäjä, T., Mauldin, L., Berresheim, H., and Kulmala, M.: Oxidation of SO₂ by stabilized Criegee intermediate (sCI) radicals as a crucial source for atmospheric sulfuric acid concentrations, *Atmos. Chem. Phys.*, 13, 3865–3879, doi:10.5194/acp-13-3865-2013, 2013.
- Camredon, M., Hamilton, J. F., Alam, M. S., Wyche, K. P., Carr, T., White, I. R., Monks, P. S., Rickard, A. R., and Bloss, W. J.: Distribution of gaseous and particulate organic composition during dark α -pinene ozonolysis, *Atmos. Chem. Phys.*, 10, 2893–2917, doi:10.5194/acp-10-2893-2010, 2010.
- Capouet, M., Müller, J.-F., Ceulemans, K., Compernelle, S., Vereecken, L., and Peeters, J.: Modeling aerosol formation in alpha-pinene photo-oxidation experiments, *J. Geophys. Res.*, 113, D02308, doi:10.1029/2007JD008995, 2008.
- Chan, A. W. H., Kroll, J. H., Ng, N. L., and Seinfeld, J. H.: Kinetic modeling of secondary organic aerosol formation: effects of particle- and gas-phase reactions of semivolatile products, *Atmos. Chem. Phys.*, 7, 4135–4147, doi:10.5194/acp-7-4135-2007, 2007.
- Chen, S., Brune, W. H., Lambe, A. T., Davidovits, P., and Onasch, T. B.: Modeling organic aerosol from the oxidation of α -pinene in a Potential Aerosol Mass (PAM) chamber, *Atmos. Chem. Phys.*, 13, 5017–5031, doi:10.5194/acp-13-5017-2013, 2013.
- Chhabra, P. S., Flagan, R. C., and Seinfeld, J. H.: Elemental analysis of chamber organic aerosol using an aerodyne high-resolution aerosol mass spectrometer, *Atmos. Chem. Phys.*, 10, 4111–4131, doi:10.5194/acp-10-4111-2010, 2010.
- Crippa, M., Canonaco, F., Lanz, V. A., Äijälä, M., Allan, J. D., Carbone, S., Capes, G., Ceburnis, D., Dall'Osto, M., Day, D. A., Decarlo, P. F., Ehn, M., Eriksson, A., Freney, E., Hildebrandt Ruiz, L., Hillamo, R., Jimenez, J. L., Junninen, H., Kiendler-Scharr, A., Kortelainen, A.-M., Kulmala, M., Laaksonen, A., Mensah, A. A., Mohr, C., Nemitz, E., O'Dowd, C., Ovadnevaite, J., Pandis, S. N., Petäjä, T., Poulain, L., Saarikoski, S., Sellegri, K., Swietlicki, E., Tiitta, P., Worsnop, D. R., Baltensperger, U., and Prévôt, A. S. H.: Organic aerosol components derived from 25 AMS data sets across Europe using a consistent ME-2 based source apportionment approach, *Atmos. Chem. Phys.*, 14(12), 6159–6176, doi:10.5194/acp-14-6159-2014, 2014.
- Donahue, N. M., Robinson, A. L., Stanier, C. O., and Pandis, S. N.: Coupled Partitioning, Dilution, and Chemical Aging of Semivolatile Organics, *Environ. Sci. Technol.*, 40, 2635–2643, doi:10.1021/es052297c, 2006.
- Donahue, N. M., Robinson, A. L., and Pandis, S. N.: Atmospheric organic particulate matter: From smoke to secondary organic aerosol, *Atmos. Environ.*, 43, 94–106, doi:10.1016/j.atmosenv.2008.09.055, 2009.
- Donahue, N. M., Epstein, S. A., Pandis, S. N., and Robinson, A. L.: A two-dimensional volatility basis set: 1. organic-aerosol mixing thermodynamics, *Atmos. Chem. Phys.*, 11, 3303–3318, doi:10.5194/acp-11-3303-2011, 2011.
- Draxler, R. and Rolph, G. D.: HYSPLIT (HYbrid Single-Particle Lagrangian Integrated Trajectory) Model access via NOAA ARL READY Website, NOAA Air Resour. Lab. Silver Spring, MD, available from: <http://ready.arl.noaa.gov/HYSPLIT.php>, 2013.
- Ehn, M., Thornton, J. A., Kleist, E., Sipilä, M., Junninen, H., Pullinen, I., Springer, M., Rubach, F., Tillmann, R., Lee, B., Lopez-Hilfiker, F., Andres, S., Acir, I.-H., Rissanen, M., Jokinen, T., Schobesberger, S., Kangasluoma, J., Kontkanen, J., Nieminen, T., Kurtén, T., Nielsen, L. B., Jørgensen, S., Kjaergaard, H. G., Canagaratna, M., Maso, M. D., Berndt, T., Petäjä, T., Wahner, A., Kerminen, V.-M., Kulmala, M., Worsnop, D. R., Wildt, J., and Mentel, T. F.: A large source of low-volatility secondary organic aerosol, *Nature*, 506, 476–479, doi:10.1038/nature13032, 2014.
- Fuller, E. N., Schettler, P. D., and Giddings, J. C.: New method for prediction of binary gas-phase diffusion coefficients, *Ind. Eng. Chem.*, 58, 18–27, doi:10.1021/ie50677a007, 1966.
- Girolami, G. S.: A Simple “Back of the Envelope” Method for Estimating the Densities and Molecular Volumes of Liquids and Solids, *J. Chem. Educ.*, 71, 962–964, doi:10.1021/ed071p962, 1994.
- Hallquist, M., Wenger, J. C., Baltensperger, U., Rudich, Y., Simpson, D., Claeys, M., Dommen, J., Donahue, N. M., George, C., Goldstein, A. H., Hamilton, J. F., Herrmann, H., Hoffmann, T., Iinuma, Y., Jang, M., Jenkin, M. E., Jimenez, J. L., Kiendler-Scharr, A., Maenhaut, W., McFiggans, G., Mentel, T. F., Monod, A., Prévôt, A. S. H., Seinfeld, J. H., Surratt, J. D., Szmigielski, R., and Wildt, J.: The formation, properties and impact of secondary organic aerosol: current and emerging issues, *Atmos. Chem. Phys.*, 9, 5155–5236, doi:10.5194/acp-9-5155-2009, 2009.

- Heald, C. L., Jacob, D. J., Park, R. J., Russell, L. M., Huebert, B. J., Seinfeld, J. H., Liao, H., and Weber, R. J.: A large organic aerosol source in the free troposphere missing from current models, *Geophys. Res. Lett.*, 32, L18809, doi:10.1029/2005GL023831, 2005.
- Hussein, T., Maso, M. D., Petäjä, T., Koponen, I. K., Paatero, P., Aalto, P. P., Hämeri, K., and Kulmala, M.: Evaluation of an automatic algorithm for fitting the particle number size distributions, *Boreal Environ.*, 10, 337–355, 2005.
- Jacobson, M. Z.: *Fundamentals of atmospheric modeling*, second edition, Cambridge University Press, New York, 528–529, 2005.
- Jenkin, M. E.: Modelling the formation and composition of secondary organic aerosol from α - and β -pinene ozonolysis using MCM v3, *Atmos. Chem. Phys.*, 4, 1741–1757, doi:10.5194/acp-4-1741-2004, 2004.
- Jenkin, M. E., Saunders, S. M., and Pilling, M. J.: The tropospheric degradation of volatile organic compounds: a protocol for mechanism development, *Atmos. Environ.*, 31, 81–104, doi:10.1016/S1352-2310(96)00105-7, 1997.
- Jimenez, J. L., Canagaratna, M. R., Donahue, N. M., Prevot, A. S. H., Zhang, Q., Kroll, J. H., DeCarlo, P. F., Allan, J. D., Coe, H., Ng, N. L., Aiken, A. C., Docherty, K. S., Ulbrich, I. M., Grieshop, A. P., Robinson, A. L., Duplissy, J., Smith, J. D., Wilson, K. R., Lanz, V. A., Hueglin, C., Sun, Y. L., Tian, J., Laaksonen, A., Raatikainen, T., Rautiainen, J., Vaattovaara, P., Ehn, M., Kulmala, M., Tomlinson, J. M., Collins, D. R., Cubison, M. J., Dunlea, E. J., Huffman, J. A., Onasch, T. B., Alfarra, M. R., Williams, P. I., Bower, K., Kondo, Y., Schneider, J., Drewnick, F., Borrmann, S., Weimer, S., Demerjian, K., Salcedo, D., Cottrell, L., Griffin, R., Takami, A., Miyoshi, T., Hatakeyama, S., Shimojo, A., Sun, J. Y., Zhang, Y. M., Dzepina, K., Kimmel, J. R., Sueper, D., Jayne, J. T., Herndon, S. C., Trimborn, A. M., Williams, L. R., Wood, E. C., Middlebrook, A. M., Kolb, C. E., Baltensperger, U., and Worsnop, D. R.: Evolution of organic aerosols in the atmosphere, *Science*, 326, 1525–1529, doi:10.1126/science.1180353, 2009.
- Kerminen, V.-M., Paramonov, M., Anttila, T., Riipinen, I., Fountoukis, C., Korhonen, H., Asmi, E., Laakso, L., Lihavainen, H., Swietlicki, E., Svenningsson, B., Asmi, A., Pandis, S. N., Kulmala, M., and Petäjä, T.: Cloud condensation nuclei production associated with atmospheric nucleation: a synthesis based on existing literature and new results, *Atmos. Chem. Phys.*, 12, 12037–12059, doi:10.5194/acp-12-12037-2012, 2012.
- Korhonen, H., Lehtinen, K. E. J., and Kulmala, M.: Multicomponent aerosol dynamics model UHMA: model development and validation, *Atmos. Chem. Phys.*, 4, 757–771, doi:10.5194/acp-4-757-2004, 2004.
- Kroll, J. H. and Seinfeld, J. H.: Chemistry of secondary organic aerosol: Formation and evolution of low-volatility organics in the atmosphere, *Atmos. Environ.*, 42, 3593–3624, doi:10.1016/j.atmosenv.2008.01.003, 2008.
- Kroll, J. H., Smith, J. D., Che, D. L., Kessler, S. H., Worsnop, D. R., and Wilson, K. R.: Measurement of fragmentation and functionalization pathways in the heterogeneous oxidation of oxidized organic aerosol, *Phys. Chem. Chem. Phys.*, 11, 8005–8014, doi:10.1039/b905289e, 2009.
- Kroll, J. H., Donahue, N. M., Jimenez, J. L., Kessler, S. H., Canagaratna, M. R., Wilson, K. R., Altieri, K. E., Mazzoleni, L. R., Wozniak, A. S., Bluhm, H., Mysak, E. R., Smith, J. D., Kolb, C. E., and Worsnop, D. R.: Carbon oxidation state as a metric for describing the chemistry of atmospheric organic aerosol, *Nat. Chem.*, 3, 133–139, doi:10.1038/nchem.948, 2011.
- Lane, T. E., Donahue, N. M., and Pandis, S. N.: Simulating secondary organic aerosol formation using the volatility basis-set approach in a chemical transport model, *Atmos. Environ.*, 42, 7439–7451, doi:10.1016/j.atmosenv.2008.06.026, 2008.
- Lindfors, V., Rinne, J., and Laurila, T.: Upscaling the BIPHOREP Results – Regional Biogenic VOC Emissions in the European Boreal Zone, *Eur. Comm., Brussels*, 127–150, 1999.
- Murphy, B. N. and Pandis, S. N.: Simulating the Formation of Semivolatile Primary and Secondary Organic Aerosol in a Regional Chemical Transport Model, *Environ. Sci. Technol.*, 43, 4722–4728, doi:10.1021/es803168a, 2009.
- Murphy, B. N., Donahue, N. M., Fountoukis, C., and Pandis, S. N.: Simulating the oxygen content of ambient organic aerosol with the 2D volatility basis set, *Atmos. Chem. Phys.*, 11, 7859–7873, doi:10.5194/acp-11-7859-2011, 2011.
- Murphy, B. N., Donahue, N. M., Fountoukis, C., Dall'Osto, M., O'Dowd, C., Kiendler-Scharr, A., and Pandis, S. N.: Functionalization and fragmentation during ambient organic aerosol aging: application of the 2-D volatility basis set to field studies, *Atmos. Chem. Phys.*, 12, 10797–10816, doi:10.5194/acp-12-10797-2012, 2012.
- Nannoolal, Y., Rarey, J., and Ramjugernath, D.: Estimation of pure component properties, *Fluid Phase Equilib.*, 269, 117–133, doi:10.1016/j.fluid.2008.04.020, 2008.
- O'Dowd, C. D., Aalto, P., Hmeri, K., Kulmala, M., and Hoffmann, T.: Aerosol formation: atmospheric particles from organic vapours, *Nature*, 416, 497–498, doi:10.1038/416497a, 2002.
- O'Dowd, C. D., Facchini, M. C., Cavalli, F., Ceburnis, D., Mircea, M., Decesari, S., Fuzzi, S., Yoon, Y. J., and Putaud, J.-P.: Biogenically driven organic contribution to marine aerosol, *Nature*, 431, 676–680, doi:10.1038/nature02959, 2004.
- Odum, J. R., Hoffmann, T., Bowman, F., Collins, D., Flagan, R. C., and Seinfeld, J. H.: Gas/Particle Partitioning and Secondary Organic Aerosol Yields, *Environ. Sci. Technol.*, 30, 2580–2585, doi:10.1021/es950943+, 1996.
- Pankow, J. F. and Asher, W. E.: SIMPOL.1: a simple group contribution method for predicting vapor pressures and enthalpies of vaporization of multifunctional organic compounds, *Atmos. Chem. Phys.*, 8, 2773–2796, doi:10.5194/acp-8-2773-2008, 2008.
- Perraud, V., Bruns, E. a., Ezell, M. J., Johnson, S. N., Yu, Y., Alexander, M. L., Zelenyuk, A., Imre, D., Chang, W. L., Dabdub, D., Pankow, J. F., and Finlayson-Pitts, B. J.: Nonequilibrium atmospheric secondary organic aerosol formation and growth, *Proc. Natl. Acad. Sci. USA*, 109, 2836–2841, 2012.
- Roldin, P., Swietlicki, E., Schurgers, G., Arneth, A., Lehtinen, K. E. J., Boy, M., and Kulmala, M.: Development and evaluation of the aerosol dynamics and gas phase chemistry model ADCHEM, *Atmos. Chem. Phys.*, 11, 5867–5896, doi:10.5194/acp-11-5867-2011, 2011a.
- Roldin, P., Swietlicki, E., Massling, A., Kristensson, A., Löndahl, J., Eriksson, A., Pagels, J., and Gustafsson, S.: Aerosol ageing in an urban plume – implication for climate, *Atmos. Chem. Phys.*, 11, 5897–5915, doi:10.5194/acp-11-5897-2011, 2011b.
- Roldin, P., Eriksson, A. C., Nordin, E. Z., Hermansson, E., Mogensén, D., Rusanen, A., Boy, M., Swietlicki, E., Svenningsson, B., Zelenyuk, A., and Pagels, J.: Modelling non-equilibrium

- secondary organic aerosol formation and evaporation with the aerosol dynamics, gas- and particle-phase chemistry kinetic multilayer model ADCHAM, *Atmos. Chem. Phys.*, 14, 7953–7993, doi:10.5194/acp-14-7953-2014, 2014.
- Rolph, G. D.: NOAA Air Resource Laboratory Real-time Environmental Application and Display sYstem (READY) Website, available at: <http://www.ready.noaa.gov>, NOAA Air Resources Laboratory, College Park, MD, 2013.
- Saunders, S. M., Jenkin, M. E., Derwent, R. G., and Pilling, M. J.: Protocol for the development of the Master Chemical Mechanism, MCM v3 (Part A): tropospheric degradation of non-aromatic volatile organic compounds, *Atmos. Chem. Phys.*, 3, 161–180, doi:10.5194/acp-3-161-2003, 2003.
- Scott, C. E., Rap, A., Spracklen, D. V., Forster, P. M., Carslaw, K. S., Mann, G. W., Pringle, K. J., Kivekäs, N., Kulmala, M., Lihavainen, H., and Tunved, P.: The direct and indirect radiative effects of biogenic secondary organic aerosol, *Atmos. Chem. Phys.*, 14, 447–470, doi:10.5194/acp-14-447-2014, 2014.
- Shrivastava, M., Zelenyuk, A., Imre, D., Easter, R., Beranek, J., Zaveri, R. A., and Fast, J.: Implications of low volatility SOA and gas-phase fragmentation reactions on SOA loadings and their spatial and temporal evolution in the atmosphere, *J. Geophys. Res. Atmos.*, 118, 3328–3342, doi:10.1002/jgrd.50160, 2013.
- Simpson, D., Benedictow, A., Berge, H., Bergström, R., Emberson, L. D., Fagerli, H., Flechard, C. R., Hayman, G. D., Gauss, M., Jonson, J. E., Jenkin, M. E., Nyiri, A., Richter, C., Semeena, V. S., Tsyro, S., Tuovinen, J.-P., Valdebenito, Á., and Wind, P.: The EMEP MSC-W chemical transport model – technical description, *Atmos. Chem. Phys.*, 12, 7825–7865, doi:10.5194/acp-12-7825-2012, 2012.
- Spracklen, D. V., Jimenez, J. L., Carslaw, K. S., Worsnop, D. R., Evans, M. J., Mann, G. W., Zhang, Q., Canagaratna, M. R., Allan, J., Coe, H., McFiggans, G., Rap, A., and Forster, P.: Aerosol mass spectrometer constraint on the global secondary organic aerosol budget, *Atmos. Chem. Phys.*, 11, 12109–12136, doi:10.5194/acp-11-12109-2011, 2011.
- Stohl, A.: Computation, accuracy and applications of trajectories—A review and bibliography, *Atmos. Environ.*, 32, 947–966, 1998.
- Tunved, P., Hansson, H.-C., Kerminen, V.-M., Ström, J., Maso, M. D., Lihavainen, H., Viisanen, Y., Aalto, P. P., Komppula, M. and Kulmala, M.: High natural aerosol loading over boreal forests, *Science*, 312, 261–263, doi:10.1126/science.1123052, 2006.
- Väänänen, R., Kyrö, E.-M., Nieminen, T., Kivekäs, N., Junninen, H., Virkkula, A., Dal Maso, M., Lihavainen, H., Viisanen, Y., Svenningsson, B., Holst, T., Arneth, A., Aalto, P. P., Kulmala, M., and Kerminen, V.-M.: Analysis of particle size distribution changes between three measurement sites in northern Scandinavia, *Atmos. Chem. Phys.*, 13, 11887–11903, doi:10.5194/acp-13-11887-2013, 2013.
- Valorso, R., Aumont, B., Camredon, M., Raventos-Duran, T., Mouchel-Vallon, C., Ng, N. L., Seinfeld, J. H., Lee-Taylor, J., and Madronich, S.: Explicit modelling of SOA formation from α -pinene photooxidation: sensitivity to vapour pressure estimation, *Atmos. Chem. Phys.*, 11, 6895–6910, doi:10.5194/acp-11-6895-2011, 2011.
- Volkamer, R., Jimenez, J. L., San Martini, F., Dzepina, K., Zhang, Q., Salcedo, D., Molina, L. T., Worsnop, D. R., and Molina, M. J.: Secondary organic aerosol formation from anthropogenic air pollution: Rapid and higher than expected, *Geophys. Res. Lett.*, 33, L17811, doi:10.1029/2006GL026899, 2006.
- Wang, Z. B., Hu, M., Mogensén, D., Yue, D. L., Zheng, J., Zhang, R. Y., Liu, Y., Yuan, B., Li, X., Shao, M., Zhou, L., Wu, Z. J., Wiedensohler, A., and Boy, M.: The simulations of sulfuric acid concentration and new particle formation in an urban atmosphere in China, *Atmos. Chem. Phys.*, 13, 11157–11167, doi:10.5194/acp-13-11157-2013, 2013.
- Yttri, K. E., Simpson, D., Nøjgaard, J. K., Kristensen, K., Genberg, J., Stenström, K., Swietlicki, E., Hillamo, R., Aurela, M., Bauer, H., Offenberg, J. H., Jaoui, M., Dye, C., Eckhardt, S., Burkhardt, J. F., Stohl, A., and Glasius, M.: Source apportionment of the summer time carbonaceous aerosol at Nordic rural background sites, *Atmos. Chem. Phys.*, 11, 13339–13357, doi:10.5194/acp-11-13339-2011, 2011.

Paper II





Modeling the role of highly oxidized multifunctional organic molecules for the growth of new particles over the boreal forest region

Emilie Öström^{1,2}, Zhou Putian³, Guy Schurgers⁴, Mikhail Mishurov⁵, Niku Kivekäs⁶, Heikki Lihavainen⁶, Mikael Ehn³, Matti P. Rissanen³, Theo Kurtén⁷, Michael Boy³, Erik Swietlicki¹, and Pontus Roldin^{1,3}

¹Division of Nuclear Physics, Lund University, Lund, P.O. Box 118, 221 00, Sweden

²Centre for Environmental and Climate Research, Lund University, Lund, P.O. Box 118, 221 00, Sweden

³Department of Physics, University of Helsinki, Helsinki, P.O. Box 64, 00014, Finland

⁴Department of Geosciences and Natural Resource Management, University of Copenhagen, Copenhagen, 1350, Denmark

⁵Department of Physical Geography and Ecosystem Science, Lund University, Lund, 223 62, Sweden

⁶Finnish Meteorological Institute, Helsinki, P.O. Box 503, 00101, Finland

⁷Department of Chemistry, University of Helsinki, Helsinki, P.O. Box 55, 00014, Finland

Correspondence to: Emilie Öström (emilie.ostrom@nuclear.lu.se)

Received: 10 October 2016 – Discussion started: 9 December 2016

Revised: 13 April 2017 – Accepted: 2 May 2017 – Published: 24 July 2017

Abstract. In this study, the processes behind observed new particle formation (NPF) events and subsequent organic-dominated particle growth at the Pallas Atmosphere–Ecosystem Supersite in Northern Finland are explored with the one-dimensional column trajectory model ADCHEM. The modeled sub-micron particle mass is up to $\sim 75\%$ composed of SOA formed from highly oxidized multifunctional organic molecules (HOMs) with low or extremely low volatility. In the model the newly formed particles with an initial diameter of 1.5 nm reach a diameter of 7 nm about 2 h earlier than what is typically observed at the station. This is an indication that the model tends to overestimate the initial particle growth. In contrast, the modeled particle growth to CCN size ranges (> 50 nm in diameter) seems to be underestimated because the increase in the concentration of particles above 50 nm in diameter typically occurs several hours later compared to the observations. Due to the high fraction of HOMs in the modeled particles, the oxygen-to-carbon (O:C) atomic ratio of the SOA is nearly 1. This unusually high O:C and the discrepancy between the modeled and observed particle growth might be explained by the fact that the model does not consider any particle-phase reactions involving semi-volatile organic compounds with relatively low O:C. In the model simulations where condensation of low-

volatility and extremely low-volatility HOMs explain most of the SOA formation, the phase state of the SOA (assumed either liquid or amorphous solid) has an insignificant impact on the evolution of the particle number size distributions. However, the modeled particle growth rates are sensitive to the method used to estimate the vapor pressures of the HOMs. Future studies should evaluate how heterogeneous reactions involving semi-volatility HOMs and other less-oxidized organic compounds can influence the SOA composition- and size-dependent particle growth.

1 Introduction

Atmospheric particles affect climate by scattering and absorbing solar radiation and by influencing cloud formation and cloud optical properties. Their climate effect depends on both the size and composition of the particles and remains one of the largest uncertainties in global climate predictions (IPCC, 2013). Small-scale, process-based models are important tools for studying different mechanisms behind aerosol formation and growth. It is crucial to understand these processes in order to improve the predictability of next-generation climate and weather forecast models.

In this study, the growth of biogenic secondary organic aerosols (BSOA) over the boreal forest in northern Europe is modeled and the results are compared to particle number size distribution measurements. New particle formation (NPF) events in boreal forests are frequent (Asmi et al., 2011; Kulmala et al., 2001; Tunved et al., 2003) and the newly formed particles can grow by condensation to the climate-relevant cloud condensation nuclei (CCN) size range, which starts at a diameter of ~ 50 nm (Kerminen et al., 2012). Komppula et al. (2005) found that particles in the boreal region in Northern Finland are typically able to activate into cloud droplets when they reach diameters larger than 80 nm (the minimum activation diameter varied from 50 to 128 nm). In boreal forests, the growth of the particles is dominated by condensation of organic compounds formed from oxidation of biogenic volatile organic compounds (BVOCs) emitted by the vegetation (Kulmala et al., 2013). Studies have shown that NPF can provide a significant amount of CCN and thereby have a substantial climate impact (e.g., Jokinen et al., 2015; Kerminen et al., 2012; Merikanto et al., 2009; Scott et al., 2014; Spracklen et al., 2008).

The different ways to model the formation of BSOA found in the literature reflect the uncertainties of the formation mechanisms and also the often unknown properties of the condensable vapors. In many studies (e.g., Bergström et al., 2012; Farina et al., 2010; Fountoukis et al., 2014; Hodzic et al., 2009; Lane et al., 2008; Murphy et al., 2012) the vapors are assumed to be semi-volatile and in equilibrium with the (liquid, well-mixed) particles, making it possible to model formation of BSOA by simple gas-particle equilibrium partitioning (Pankow, 1994). In other studies (e.g., Scott et al., 2015; Spracklen et al., 2008; Tunved et al., 2010; Westervelt et al., 2013) the vapors are assumed to be nonvolatile and the irreversible particle growth is only limited by the collision rate between the vapor molecules and the particles. Recently, large-scale model studies (Jokinen et al., 2015; Langmann et al., 2014; Li et al., 2015; Riipinen et al., 2011; Yu, 2011) have included both mechanisms to be able to treat semi-volatile and nonvolatile vapors, which have yielded a better agreement between model results and observations. This hybrid SOA formation mechanism is an important step forward. However, in order to explicitly simulate the size-resolved condensational growth, models need to take into account how the chemical composition and curvature (Kelvin) effect vary with the size of the particles. Smog-chamber studies have often focused on the SOA formation from semi-volatile organic compounds (SVOCs). Recently the presence of highly oxidized multifunctional organic molecules (HOMs) in the gas phase has been shown in both lab and field studies (e.g., Ehn et al., 2014; Jokinen et al., 2015). Many HOMs can be low-volatility organic compounds (LVOCs; $10^{-4.5} \mu\text{g m}^{-3} < \text{saturation concentration } (C^*) < 10^{-0.5} \mu\text{g m}^{-3}$) or even extremely low-volatility organic compounds (ELVOCs; $C^* < 10^{-4.5} \mu\text{g m}^{-3}$), while others are SVOCs ($10^{-0.5} \mu\text{g m}^{-3} < C^* < 10^{2.5} \mu\text{g m}^{-3}$)

(Kurtén et al., 2016). The volatility distribution and aging of SOA in models will significantly affect the model results of SOA formation (Hermansson et al., 2014). Furthermore, the phase state of the particles can affect the dynamics of the growth (Zaveri et al., 2014). Traditionally, SOA particles are assumed to be well-mixed liquids; however, recent experimental studies indicate that they can be solid-like at ambient conditions (Renbaum-Wolff et al., 2013; Saukko et al., 2012; Vaden et al., 2011; Virtanen et al., 2010), which may influence their growth and lifetime (with respect to evaporation) in the atmosphere (Roldin et al., 2014).

In this study, we assume the organic vapors to condense dynamically on the Fuchs-corrected surface area of the particles. The two extremes of particle-phase state are tested; either the particles are assumed to be well-mixed liquid droplets or they are assumed to be solid-like without diffusion in the particle phase and with the gas-particle partitioning being controlled by the composition at the surface. Based on Ehn et al. (2014), a formation pathway of HOMs by the oxidation of α -pinene, β -pinene and limonene is added. The aerosol dynamics are modeled along air-mass trajectories with an updated version of the Aerosol Dynamics, gas and particle phase CHEMistry and radiative transfer model (ADCHEM) (Roldin et al., 2011a). The modeled results are compared to particle number size distribution measurement at the subarctic station in Pallas, Northern Finland.

The aim is to evaluate the potential contribution of HOMs to the activation and growth of new particles over the boreal forest region. The model approach is described in Sect. 2, followed by results and discussion in Sect. 3 and conclusions in Sect. 4.

2 Method

ADCHEM was used to model the concentrations of gases and particles along air-mass trajectories ending at the Pallas Atmosphere–Ecosystem Supersite (67.97°N , 24.12°E ; 565 m a.s.l.) (Lohila et al., 2015) in Northern Finland. The emissions of different primary particulate and gaseous chemical species along the trajectories were derived from emission databases listed in Sect. 2.2. The modeled particle number size distributions for the Pallas site were compared to measured ones and the particle chemical composition to non-coincident aerosol mass spectrometer (AMS) measurements (Kivekäs et al., 2009; Jaatinen et al., 2014). The particle number size distributions measurements were conducted with a differential mobility particle sizer (DMPS) covering dry particle mobility range 7–500 nm (Komppula et al., 2003). The instrument was connected to a non-standard inlet with a cut-off diameter of approximately 5 μm (Lohila et al., 2015).

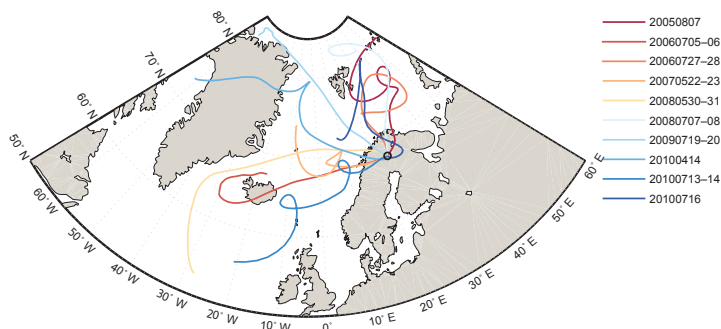


Figure 1. Mean HYSPLIT trajectories of each new particle formation event, all ending at Pallas. The trajectories start 7 days backward in time before they reach the measurement station.

2.1 Air-mass trajectories

Based on the particle number size distribution data measured at Pallas between 2005 and 2010, days with NPF events suitable for modeling SOA formation were selected for detailed analysis. This included days with strong new particle formation and subsequent growth of the new particle mode for at least 12 h. This selection is roughly in line with type 1a events as defined by Dal Maso et al. (2005). The corresponding air-mass trajectories for these days were determined using the Hybrid Single Particle Lagrangian Integrated Trajectory Model (HYSPLIT) (Draxler and Rolph, 2013) with meteorological data from the Global Data Assimilation System (GDAS), downloaded from NOAA Air Resource Laboratory Real-time Environmental Application and Display sYstem (READY) (Rolph, 2016). The meteorological data resolution was linearly interpolated from 3 h to 1 min (the main model time step used in the simulations). The air-mass trajectories were calculated 7 days backward in time and ending at Pallas at 00:00, 03:00, 06:00, 09:00, 12:00, 15:00, 18:00 and 21:00 UTC. The analyzed cases were further decreased by including only those where all air-mass trajectories originated from clean marine environments. For each chosen new particle formation event the particle- and gas-phase evolution along the air-mass trajectories were modeled. In 7 out of the in total 10 selected cases, the growth of the newly formed particle mode could also be observed on the day after the start of the event. For these cases we ran ADCHEM for the day after the NPF event as well. In total the model was run along 136 air-mass trajectories. Figure 1 shows the mean trajectories for each new particle formation and growth event.

Information on land use along the trajectories was retrieved from the Global Land Cover Map for the Year 2000, GLC2000 database, European Commission Joint Research Centre (<http://forobs.jrc.ec.europa.eu/products/glc2000/>

products.php). Land-use categories were used to calculate the dry deposition of gases and particles.

2.2 Emissions along the trajectory

All emissions were added at each model time step to the model layer closest to surface, where they were assumed to be instantaneously well mixed within this layer.

2.2.1 Gas emissions

Anthropogenic emissions of CO, NH₃, non-methane volatile organic compounds (NMVOCs) (represented by 25 species; see Table S1 in Supplement), NO_x and SO₂ were retrieved from the EMEP (European Monitoring and Evaluation Programme) database (EMEP/CEIP 2014, present state of emissions as used in EMEP models; http://www.ceip.at/webdab_emepdatabase/emissions_emepmodels/). Dimethyl sulfide (DMS) emissions from marine plankton were also retrieved from EMEP. The modeled SO₂ concentration in the surface layer 24 h upwind from Pallas was nudged towards the measured SO₂ concentration at the station by increasing the emission of the gas when the modeled concentration was below the measured one. This applied to ~50 % of the studied trajectories, and for these cases the SO₂ concentration was increased by a median factor of 1.8. Nudging was done in order to get a more realistic nucleation rate since the modeled nucleation rate depends on the concentration of H₂SO₄ (Eqs. 2 and 3 in Sect. 2.3), which is formed by the reaction between SO₂ and OH. The median modeled (with nudging) and measured SO₂ gas-phase concentrations during the NPF events are shown in Fig. S1b in Supplement.

Biogenic emissions (α -pinene, β -pinene, limonene, carene and isoprene) were estimated with the dynamic vegetation model LPJ-GUESS (Smith et al., 2014), which simulates the carbon and nitrogen cycling in terrestrial vegetation and

which contains algorithms for isoprene (Arnth et al., 2007) and monoterpene (Schurgers et al., 2009a) production and emission by plants. Vegetation is represented with plant functional types (PFTs), and we applied 11 tree species common for northern Europe, one generic shrub type and one herbaceous type (Table S2), applying the bioclimatic limits as in Hickler et al. (2012) and Schurgers et al. (2009b). The parameterization of the PFTs and their isoprene and monoterpene characteristics follows Schurgers et al. (2009b), but the monoterpene emissions were split into three separate sets (α -pinene, β -pinene and limonene), as well as a generic set for all other monoterpenes (Table S2). The emissions of the last set were treated as if they were emissions of carene only. Carene was chosen to represent the generic set of monoterpenes because measurements on individual trees indicate that after α -pinene, carene is dominating the emissions from boreal forest composed predominantly of Scots pine (e.g., Bäck et al., 2012; Smolander et al., 2014) or Norway spruce (Bourtsoukidis et al., 2014). The median fraction of the emitted monoterpenes along the air-mass trajectories that were not α -pinene, β -pinene and limonene was 32 %.

LPJ-GUESS was run with the same meteorological data as used for determining the air-mass trajectories (GDAS; Rolph, 2016) using 3-hourly data for 2005–2010, preceded by a spinup of 500 years to establish the vegetation and soil pools. Photosynthesis production and emissions of isoprene and monoterpenes were computed at the 3-hourly resolution of the GDAS data using air temperature and radiation, resulting in diurnal variations of the plants' transpirational demand and water stress. The maximum photosynthetic capacity along with water and leaf nitrogen content varied daily, following the daily averages of GDAS data. Land use was prescribed at the level of 2005 following Ahlström et al. (2012).

2.2.2 Primary particle emission

Primary particle emissions of wind-generated marine aerosol as well as from ship and road traffic were included.

The primary marine aerosol production was estimated when the air-mass trajectories passed over ocean (determined by the land-use map from GLC2000) based on a parameterization from Mårtensson et al. (2003), with the use of wind-speed data from GDAS. The particles were assumed to be composed of NaCl and organic material based on the measurements and analysis of marine aerosol particles from Mace Head in Ireland during high biological activity (O'Dowd et al., 2004).

The emission of particles from ship and road traffic were estimated based on the SO₂ emission from ship and NO_x emission from road traffic, respectively, both retrieved from EMEP. For the ship emissions, a conversion factor of 8.33×10^{14} particles g(SO₂)⁻¹ (Beecken et al., 2015) was used while a conversion factor of 2×10^{14} particles g(NO₂)⁻¹ (Kristensson et al., 2004) was used for the road traffic emis-

sions. Kristensson et al. (2004) also provided parameters for the size distribution of the traffic emissions. The size distribution of the particles from the ship emissions was based on a study done by Jonsson et al. (2011). The smallest particles (diameter less than or equal to 40 nm) were assumed to consist of 50 % H₂SO₄ and 50 % organic material. Particles larger than 40 nm were assumed to have a core of soot (black carbon) coated with a 5 nm thick layer of equal molar fractions of H₂SO₄ and organic material.

2.3 ADCHEM

ADCHEM can be used as a two-, one- or zero-dimensional model to simulate the aging of an air mass along a trajectory (Hermansson et al., 2014; Roldin et al., 2011a, b). This section will focus on the modifications done to the model; for a detailed description of the model the reader is referred to Roldin et al. (2011a). In this study ADCHEM was used as a one-dimensional column model that solves the atmospheric diffusion equation in the vertical direction. The model included 20 vertical grid cells with a linear grid resolution of 100 m, extending up to 2000 m a.g.l. The vertical diffusion coefficient (K_z) was calculated based on a slightly modified Grisogono scheme (Jericevic et al., 2010) so that K_z in Eq. (1) depends on the height above ground (z), the friction velocity (u_*) and the height of the atmospheric boundary layer (H):

$$K_z = C u_* z \exp \left[-0.5(z / (0.21 H))^2 \right], \quad C = 0.34, \quad (1)$$

where C is an empirical constant estimated from large eddy simulation (LES) data. The cloud base was always assumed to lie above the model domain, i.e., no in-cloud aerosol processing was considered. Low-level clouds might have been present 34 % of the modeled times in the modeled domain on average, indicated by relative humidity (RH) values above 98 %.

The gas-phase chemistry was solved using the Kinetic Pre-Processor (KPP) (Damian et al., 2002) with selected organic and inorganic reactions from the Master Chemical Mechanism (MCM) version 3.3 (Jenkin et al., 1997; Saunders et al., 2003) and with spectral irradiance modeled with the radiative transfer model described in Roldin et al. (2011a). Table S1 lists the gas-phase precursors included in the chemistry module. The two monoterpenes α -pinene and limonene that contain endocyclic double bonds were assumed to form HOMs initiated by their reaction with ozone. The HOM autoxidation mechanism was adopted from Ehn et al. (2014) and coupled to the MCMv3.3 mechanism. The HOM mechanism explicitly describes how the composition of the peroxy radicals (RO₂) formed from O₃ oxidation of monoterpenes evolves as a result of sequential steps of intramolecular H-shifts and O₂ additions (autoxidation) (Crounse et al., 2013). In this work in total 9 % of the first-generation α -pinene + O₃ oxidized products were assumed to undergo autoxidation, while for limonene this fraction was 22 %. These

numbers give upper limits for the molar yield of HOM formation from ozonolysis of α -pinene and limonene in our model. However, because of potential termination of the autoxidation mechanism with NO, HO₂ or RO₂ already after one or two H-shifts plus O₂ additions, not all autoxidation products become HOMs (O:C \geq 0.7). For conditions with low NO concentrations (as was generally the case for the simulations in this work) the modeled HOM molar yield of formation was close to the measured molar yields of \sim 7 % (for α -pinene) and \sim 17 % (limonene) in the Jülich Plant Atmosphere Chamber (JPAC) (Ehn et al., 2014). These HOM yields are substantially higher than what was reported from flow tube experiments by Jokinen et al. (2015). One possible explanation to the different yields between these two studies is that the residence time in JPAC was substantially longer than in the flow tube. With longer residence time the autoxidation is allowed to run closer to completion, and for limonene specifically there is potential to react twice with ozone. Thus, the yields reported by Ehn et al. (2014) most likely better resemble the HOM yields at low NO conditions in the atmosphere.

For β -pinene ozonolysis the autoxidation channel is minor (Ehn et al., 2014) and was not considered in the model. According to Ehn et al. (2014) and Jokinen et al. (2015) products from OH oxidation of α -pinene, limonene and β -pinene can also undergo autoxidation that leads to formation of HOMs. Jokinen et al. (2015) estimated that the molar yields of formation of HOMs from OH oxidation of α -pinene, limonene and β -pinene are 13, 27 and 17 % of the molar yield of HOM formation from α -pinene + O₃ reactions, respectively. Based on these results together with the molar yield of HOM formation from α -pinene ozonolysis from Ehn et al. (2014) we estimated and used an upper limit molar yield of HOM formation from OH oxidation of α -pinene, limonene and β -pinene of 1, 2.5 and 1.5 %, respectively. Figure S2 shows the modeled median gas-phase concentration of the HOMs during all modeled NPF events using different methods to estimate their vapor pressures (described below).

The aerosol dynamics module in ADCHEM considers new particle formation, Brownian coagulation, dry and wet deposition and condensation/evaporation. The changes in the particle number size distribution due to condensation, evaporation or coagulation were modeled using a full-stationary size grid (Jacobson, 2005) consisting of 100 size bins between 1.5 nm and 2.5 μ m in dry diameter.

The nucleation rate ($J_{1.5}$) was assumed to be a function of the concentration of sulfuric acid and a first-generation oxidation product of the included monoterpenes denoted ELVOC_{nuc1}, formed with a molar yield of 10^{−5} for each monoterpene that reacted with OH (see Eq. 2). The low molar yield was chosen in order to prevent ELVOC_{nuc1} to have a substantial contribution to the modeled particle growth. This parameterization was recommended by Roldin et al. (2015), based on model simulations of NPF experiments with real

plant emissions in JPAC. First-generation oxidation products from reactions with O₃ were not included in ELVOC_{nuc1} since these tend to give too many new particles during the night (Roldin et al., 2015).

$$J_{1.5} = K_1 [\text{H}_2\text{SO}_4] [\text{ELVOC}_{\text{nuc1}}], \quad (2)$$

where $K_1 = 2 \times 10^{-11} \text{ cm}^3 \text{ s}^{-1}$.

This value of K_1 was chosen in order for the model to give the approximately correct total particle number concentration if averaged over all model simulations. K_1 was kept constant for all modeled nucleation events.

As an alternative to Eq. (2) the model was also run with kinetic H₂SO₄ nucleation:

$$J_{1.5} = K_2 [\text{H}_2\text{SO}_4] [\text{H}_2\text{SO}_4], \quad (3)$$

where $K_2 = 2 \times 10^{-14} \text{ cm}^3 \text{ s}^{-1}$. In all model scenarios, the nucleation rate was determined by Eq. (2) if not otherwise noted.

Organic compounds with a pure liquid saturation vapor pressure (p_0) less than 0.01 Pa were included in the condensation mechanism, where p_0 was estimated with the group contribution method by Nannoolal et al. (2008) using the UManSysProp online system (Topping et al., 2016). The p_0 of the HOMs were estimated with the group contribution method SIMPOL (Pankow and Asher, 2008). The Nannoolal et al. (2008) method was not used for the HOMs because it was shown to produce unrealistic estimates of vapor pressures for multifunctional HOMs containing hydroperoxide or peroxy acid groups (Kurtén et al., 2016). According to Kurtén et al. (2016) the SIMPOL method seems to be more robust and shows better agreement with the pure liquid vapor pressures of HOMs calculated with the detailed quantum-chemistry-based continuum solvent model COSMO-RS (Conductor-like Screening Model for Real Solvents) (Eckert and Klamt, 2002) than the Nannoolal method. The SIMPOL method does, however, give substantially lower vapor pressures than COSMO-RS. Thus, a sensitivity test was done where the vapor pressures of the HOMs calculated with SIMPOL were corrected based on the difference between the SIMPOL and COSMO-RS HOM vapor pressures reported by Kurtén et al. (2016) (Fig. S3). This yielded a correction factor of $10^{2.8 \times \text{O:C} - 0.1}$, where O:C is the oxygen-to-carbon ratio of the HOM monomers. For the HOM dimers we used a fixed correction factor of 10⁴.

The HOMs are probably very reactive in the particle phase and could therefore possibly be considered to be effectively nonvolatile despite their surprisingly high pure liquid saturation vapor pressures (Kurtén et al., 2016; Zhang et al., 2015). We evaluated the potential impact of irreversible reactive uptake of HOMs by performing simulations where the p_0 for the HOMs were set to zero, i.e., assuming that because of rapid irreversible reactions at the particle surface the HOM uptake is only limited by the collision rate between the HOMs and the particles.

ADCHEM includes a detailed particle-phase chemistry module, adopted from the Aerosol Dynamics gas- and particle-phase chemistry model for laboratory CHAMber studies (ADCHAM) (Roldin et al., 2014). This module is used to calculate the particle equilibrium water content, the particle acidity, nitric acid and hydrochloric acid equilibrium vapor pressures for each particle size bin and the non-ideal interactions between organic compounds, water and inorganic ions using the activity coefficient model AIOMFAC (Zuend et al., 2008, 2011). In this work, we did not simulate the specific interactions between the organic and inorganic compounds but assumed a complete phase separation of the inorganic and organic particle phase. Topping et al. (2013a) concluded that the uncertainties in modeled SOA formation are far greater because of uncertainties in the organic compound pure liquid saturation vapor pressures than the omission of phase separation between organic and inorganic compounds. In line with this, we have previously shown that while the modeled SOA formation during α -pinene ozonolysis experiments is relatively sensitive to the choice of pure liquid saturation vapor estimation method, it is relative insensitive to the omission of non-ideal interactions between the condensable organic compounds and between the organic compounds and ammonium (Roldin et al., 2014). In Kurtén et al. (2016) we computed the activity coefficients of 16 different HOM in a water-insoluble organic matter phase using the COSMOTerm software (Eckert and Klamt, 2014) and found that the activity coefficients varied between 0.59 and 2.01. Thus, in this work we did not simulate the specific interactions between the organic and inorganic compounds but assumed a complete phase separation of the inorganic and organic particle phase. We used AIOMFAC to calculate the equilibrium water content in the inorganic particle phase and the individual compound activity coefficients. The organic compound activity coefficients in the organic particle phase were assumed to be unity (ideal solution). The equilibrium vapor pressures of the organic compounds over the particle surface were derived from p_0 using Raoult's law and correcting for the Kelvin effect, using a surface tension of 0.05 N m^{-1} (Riipinen et al., 2010). The condensation, dissolution and evaporation of NH_3 and HNO_3 were calculated using the non-equilibrium growth scheme from Jacobson (2005). H_2SO_4 was treated as a nonvolatile compound, with irreversible condensation.

ADCHEM can be combined with a kinetic multilayer model for particles (Roldin et al., 2014) where each particle consists of a surface bulk layer and several bulk layers. In this study, the particles were either treated as liquid-like with no mass-transport limitations between the layers or as solid-like with no diffusion in the particle-phase. In the base-case simulations all particulate material except the core of the particles formed from soot particles were treated as liquid-like. The solid-like particles were represented with three layers (a monolayer thick surface layer of 0.7 nm and two bulk layers).

When the particles grow by condensation, material is moved from the surface layer into the first bulk layer.

2.4 Initial conditions

The initial particle size distribution was assumed to be a typical distribution found in clean maritime air (Seinfeld and Pandis, 2006) where 90 % of the dry particle molar volume had the same chemical composition as the primary marine aerosols in Sect. 2.2.2 and the remaining dry volume consisted of ammonium sulfate.

The initial gas concentrations of NO_x , SO_2 , O_3 and CO were retrieved from MACC (Monitoring Atmospheric Composition and Climate) reanalysis dataset (Inness et al., 2013) archived in the ECMWF data server.

2.5 Sensitivity tests

Sensitivity tests were done to investigate the impact of the selected NPF mechanism (Eqs. 2 or 3) and how the growth of the particles was affected by the volatility of the HOMs and the SOA phase state of the particles. Table 1 lists the properties of the base-case simulation together with those of the sensitivity tests.

3 Results and discussion

This section presents the median characteristics of the modeled particle number concentration compared to the measured concentrations at Pallas. The results from the sensitivity tests of the model mentioned in Sect. 2.5 will also be presented. First, however, model results from a typical day of observed new particle formation event are discussed.

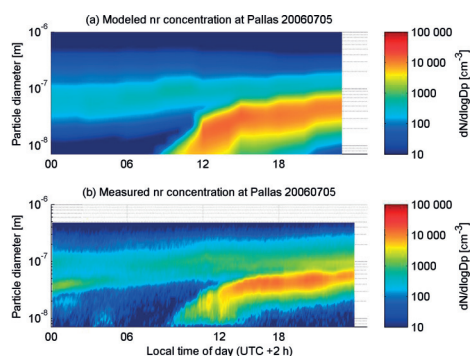
Figure 2 shows the modeled (base-case simulation) and measured particle number size distribution at Pallas on 5 July 2006. At the beginning of the new particle formation event, around 09:00 UTC (11:00 local standard time), almost 90 % of the modeled particle volume in the nucleation mode consists of HOMs, the remaining volume largely consists of organic oxidation products from the MCMv3.3 chemistry scheme and sulfate (Fig. S4a). Nine hours later that day (Fig. S4b) the particles originating from the NPF event form a new Aitken mode with a geometric mean diameter of $\sim 50 \text{ nm}$, according to both the model and the observations (Fig. 2). The volume fraction of VOC products from MCMv3.3 in the particle phase is now slightly larger than at 09:00 UTC (Fig. S4). This is partly because the Kelvin effect becomes insignificant when the particles have reached $\sim 50 \text{ nm}$ in diameter, which allows more SVOCs to dissolve in the organic aerosol particles.

Median particle number size distribution

In Fig. 3a–d the observed and modeled (base-case scenario) median particle number size distributions for all chosen tra-

Table 1. Different assumptions for the different model scenarios tested in this study.

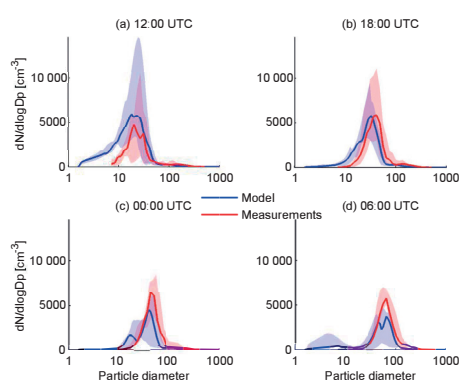
Model scenario	Phase state	HOM vapor pressure method	Nucleation rate ($\text{cm}^3 \text{s}^{-1}$)
liq-SIM HOM (base case)	liquid	SIMPOL	$J_{1.5} = 2 \times 10^{-11} [\text{H}_2\text{SO}_4] [\text{ELVOC}_{\text{nuct}}]$
liq-NV HOM	liquid	nonvolatile	$J_{1.5} = 2 \times 10^{-11} [\text{H}_2\text{SO}_4] [\text{ELVOC}_{\text{nuct}}]$
liq-COSMO HOM	liquid	SIMPOL, corrected with COSMO-RS	$J_{1.5} = 2 \times 10^{-11} [\text{H}_2\text{SO}_4] [\text{ELVOC}_{\text{nuct}}]$
solid-NV HOM	solid	nonvolatile	$J_{1.5} = 2 \times 10^{-11} [\text{H}_2\text{SO}_4] [\text{ELVOC}_{\text{nuct}}]$
solid-SIM HOM	solid	SIMPOL	$J_{1.5} = 2 \times 10^{-11} [\text{H}_2\text{SO}_4] [\text{ELVOC}_{\text{nuct}}]$
liq-no HOM	liquid	no HOMs included	$J_{1.5} = 2 \times 10^{-11} [\text{H}_2\text{SO}_4] [\text{ELVOC}_{\text{nuct}}]$
liq-kin nucl	liquid	nonvolatile	$J_{1.5} = 2 \times 10^{-14} [\text{H}_2\text{SO}_4] [\text{H}_2\text{SO}_4]$

**Figure 2.** (a) Modeled and (b) measured number size distribution at Pallas, 5 July 2006.

jectories are presented together with their respective 25 and 75 percentiles. The newly formed particles reach the DMPS detection limit size of 7 nm in diameter around noon local time (10:00 UTC) and have by early morning the day after produced particles around 80 nm, large enough to be able to act as CCN. From Fig. 3c–d it is clear that the model underestimates the concentration and geometric mean diameter (GMD) of the Aitken-mode particles originated from the NPF event the day before. For example, at midnight (Fig. 3c) the modeled median GMD of the complete size distribution is 30.8 nm and the total particle concentration 1820 cm^{-3} , while in the observations it is 47.5 nm and 2630 cm^{-3} .

While the median GMD and the concentration of the growing particles the day after the NPF events are underestimated, the model overpredicts the total number of particles larger than 7 nm in diameter (N_7) at the beginning of the NPF (Fig. 4a).

This might be caused by a too-fast initial growth of the newly formed particles (1.5–7 nm in diameter) or that the on-

**Figure 3.** The modeled particles are assumed to be liquid and the vapor pressures of the HOMs are estimated with SIMPOL. Measured (red lines) and modeled (blue lines) median number size distributions at (a) 12:00 and (b) 18:00 UTC the day of the new particle formation event and at (c) 00:00 and (d) 06:00 UTC the following day. The shaded areas are the values that fall between the 25th and 75th percentiles.

set of the NPF event happens about 2 h too early in the model. Two sensitivity tests were done to investigate the influence of the vapor pressures of the HOMs on the size- and time-dependent particle growth. When the HOMs were assumed to be nonvolatile the trends in the modeled N_7 was very similar to the base-case scenario (Fig. 4b). Thus, when SIMPOL was used to predict the vapor pressures, most HOMs were effectively nonvolatile and could activate and grow the particles already at 1.5 nm in diameter. However, the median results from the simulation where the vapor pressures of the HOMs were corrected based on COSMO-RS, which resulted in higher vapor pressures of the HOMs, better predicted the timing of the new particles growth past the lower diameter detection limit of the DMPS system (Fig. 4c). When the

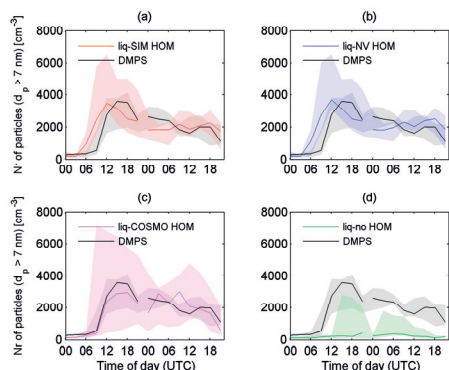


Figure 4. Median number of particles above 7 nm of all chosen NPF events at Pallas (from midnight on the day of the event to the evening the day after the start of the event) together with the 25 and 75 percentiles (shaded areas). The black lines are the median DMPS data from Pallas. The colored lines in (a–c) are the modeled median number of particles above 7 nm, using different methods to estimate the vapor pressures of the HOMs (see Table 1). In (d), HOMs are excluded.

HOM formation was excluded, the modeled NPF had only a minor influence on N_7 (Fig. 4d) because most of the newly formed particles were not able to grow to observable sizes (Fig. S5). Thus, in more polluted environments where the autoxidation is terminated by $\text{RO}_2 + \text{RO}_2$ or $\text{RO}_2 + \text{NO}$ reactions before the oxidation products become HOM, the particle growth may be suppressed.

The concentration of particles larger than 50 nm in diameter (N_{50}) during the evening and the day after the NPF event in all four model simulations mentioned above (liq-SIM HOM, liq-NV HOM, liq-COSMO HOM and liq-no HOM) are smaller than the observed N_{50} (Fig. 5a–d). Especially during the evening and the day after the NPF events the model underestimated N_{50} . This is the case even if we consider that the HOMs are nonvolatile (Fig. 5b). Most likely this is because the model underestimates the growth of the particles larger than 20 nm in diameter. Similar results for the number concentration of particles larger than 30 and 80 nm in diameter can be found in Figs. S6–S7.

Figure 6 shows the modeled median vertical concentration profiles of N_7 and N_{50} at the Pallas field station at 12:00 UTC the days of the NPF events and at 12:00 UTC the days after the NPF events. N_7 and N_{50} are elevated in the whole boundary layer to an altitude of ~ 800 m because of the previous day NPF events. Above the typical maximum boundary layer height of ~ 800 m N_7 decreases steeply from > 1000 to $< 10 \text{ cm}^{-3}$ above 1600 m. Thus, according to these model results NPF events in the sub-Arctic forest region can be

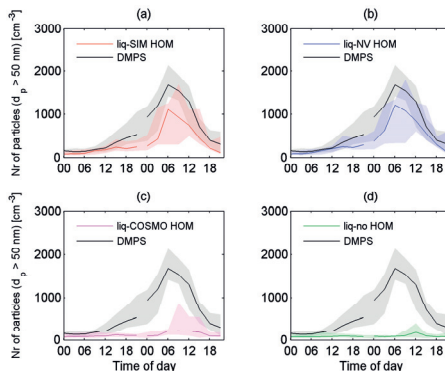


Figure 5. Median number of particles above 50 nm of all chosen NPF events at Pallas (from midnight on the day of the event to the evening the day after the start of the event) together with the 25 and 75 percentiles (shaded areas). The black lines are the median DMPS data from Pallas. The colored lines in (a–c) are the modeled median number of particles above 50 nm, using different methods to estimate the vapor pressures of the HOMs (see Table 1). In (d), HOMs are excluded.

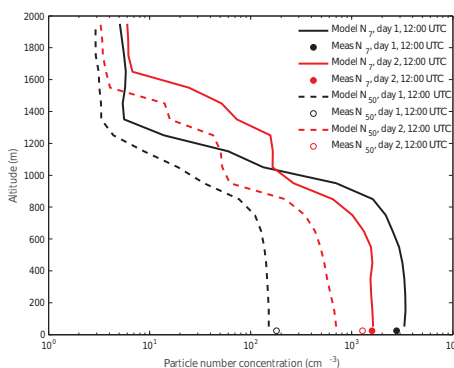


Figure 6. Modeled median vertical profiles of the particle number concentrations of particles larger than > 7 nm in diameter (N_7) and > 50 nm in diameter (N_{50}), respectively. Model results are shown both from the first day during the NPF events at 12:00 UTC and the second day after the NPF events at 12:00 UTC. Shown are also the observed median particle number concentrations at the surface.

an important source of CCN in the whole planetary boundary layer. Further, the observed N_7 and N_{50} at the ground can give reasonable accurate estimates of N_7 and N_{50} in the whole boundary layer but do not reflect the concentrations

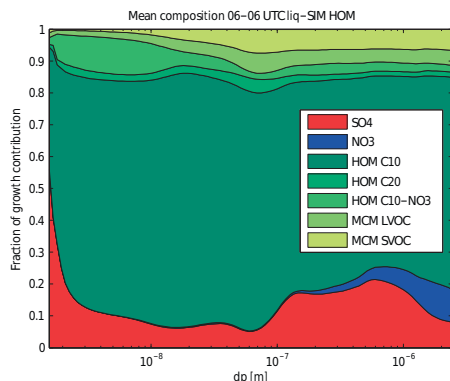


Figure 7. Mean mass fractions of each compound type that contributes to the growth of the particles during all chosen new particle formation events from the base-case simulations (from 06:00 UTC the morning of the event to 06:00 UTC the following day).

above the boundary layer either during the NPF events or the day after the events.

Figure 7 shows the mean mass fraction of each compound type that contributes to the growth during all chosen NPF events, from roughly the start time of the events (06:00 UTC) until the morning the next day (06:00 UTC). The growth of the particles is dominated by HOMs; the base-case simulation (Fig. 7) and the simulation with nonvolatile HOMs (Fig. S8b) both give HOM mass fractions of $\sim 75\%$ on average. The simulation where the vapor pressures of the HOMs are based on results from COSMO-RS gives HOM mass fractions of $\sim 50\%$ (Fig. S8c) due to the higher vapor pressures of the HOMs. The fractions of total VOC products from MCM in the particle phase (LVOC + SVOC) are $\sim 10\%$ for the base case and $\sim 20\%$ for the run using COSMO-RS. The small contribution of SVOCs to the particle growth is one likely reason why the model seems to underestimate the growth of particles larger than ~ 20 nm in diameter and thus causes too low concentration of particles with diameter > 50 nm (Fig. 5). The modeled particle composition can be compared with the few AMS observations that exist from the Pallas field station. According to Kivekäs et al. (2009) the average detectable inorganic aerosol mass fraction (nitrate, ammonia and sulfate) was 23 %, and the remaining 77 % was organics for aerosol particles originating from marine air masses during the second Pallas Cloud Experiment conducted between 16 September and 6 October 2005. During the third Pallas Cloud Experiment (21 September to 3 October 2009), when the air masses were originating from Northern Atlantic Ocean and the Arctic, the AMS measurements together with black carbon measurements with a Multi-Angle Absorption Photometer (MAAP)

gave an average composition of 47 % organics, 26 % sulfate, 13 % ammonia, 8 % nitrate and 6 % black carbon (Jaatinen et al., 2014). However, during the only strong new particle formation and growth event occurring during this campaign more than 70 % of the particles mass was composed of organics (Fig. 2c in Jaatinen et al., 2014). Because of the generally very low mass concentrations ($< 1 \mu\text{g m}^{-3}$) during the second and third Pallas Cloud Experiment no reliable size-resolved chemical composition could be derived from the AMS measurements. However, Jaatinen et al. (2014) compared the aerosol hygroscopicity parameter, κ , derived using the non-size-resolved AMS chemical compositions with the size-resolved κ derived with an HT-DMA and a CCN counter. According to this closure the AMS κ was generally above 0.2 and substantially higher than the κ values derived with HT-DMA and a CCN counter. For particles with diameters between 15 and 75 nm the κ values were in the range between 0.05 and 0.08 based on the HT-DMA and CCN counter measurements. Jaatinen et al. (2014) concluded that this was likely because the newly formed particles were mainly composed of organic compounds. In our base-case simulation the secondary aerosol particle mass is also strongly dominated by organic compounds with an average mass fraction of 85 % for the base-case simulation and with the remaining inorganic secondary aerosol mass fraction mainly being composed of sulfate (Fig. 7). Thus, the ratio between the modeled total organic mass and the inorganic secondary aerosol mass (nitrate, ammonia and sulfate) is somewhat larger than reported by Kivekäs et al. (2009) and substantially larger than the average values from Jaatinen et al. (2014). However, both AMS measurement campaigns were performed during the autumn when the BVOC emissions from the boreal forest generally are relatively low, while our modeled cases mainly are from the late spring and summer months when the BVOC emissions generally are higher because of higher temperatures and photosynthetic active radiation (e.g., Schurgers et al., 2009a). Additionally, we have only focused on days with strong new particle formation and consecutive particle growth. Jaatinen et al. (2014) conclude that particular during these days the sub-micron particles are likely mainly composed of secondary organic material. It is likely that the model underestimates the sulfate mass in the accumulation-mode particles because we did not consider aerosol in-cloud processing and heterogeneous sulfate formation by oxidation of SO_2 in the cloud droplets. Also water-soluble organic compounds may be involved in heterogeneous reactions leading to additional SOA formation in the accumulation mode (e.g., Topping et al., 2013b). However, it is unlikely that this can explain why the model underestimates N_{50} the day after the NPF events.

Due to the dominance of HOMs, the O : C of the modeled SOA are substantially higher (liq-SIM HOM: 0.99; liq-NV HOM: 0.98; liq-COSMO HOM: 0.93) compared to reported values from aerosol mass spectrometry of 0.73 for aged low-volatile SOA (Ng et al., 2010)). In a study by

Zhang et al. (2015) they imply that particle-phase reaction can lower the O : C of SOA formed from HOMs (O : C > 0.7) to ratios they observe in the aerosol mass spectrometer. In our study, particle-phase reactions of HOMs were not modeled explicitly. The reason for the high O : C of the HOMs is that the autoxidation and formation of HOMs are relatively rapid processes which are not strongly hindered by the gas-to-particle uptake of intermediate autoxidation products with lower O : C. Furthermore, in the model the relatively low BVOC concentrations in the atmosphere compared to most laboratory smog-chamber experiments prevent substantial HOM dimer formation via $\text{RO}_2 + \text{RO}_2$ reactions. These reactions lead to earlier termination of the autoxidation and formation of HOMs with lower O : C. One possible explanation to the high O : C ratio of the modeled SOA compared to atmospheric observations could be the lack of particle-phase reactions involving SVOCs with low O : C in the model, which would allow more SVOCs to partition to the particle phase. This, possibly together with the underestimated SVOC formation rates, can also explain why the model underestimates N_{50} the day after the NPF events (Fig. 5), even though it seems to overestimate the initial growth (Fig. 4).

Tröstl et al. (2016) showed that in order to explain the observed growth rates of particles in the full size range between ~ 1 and 30 nm in diameter, during an α -pinene ozonolysis experiment in the CERN CLOUD chamber, they needed to substantially increase the concentrations of SVOCs and LVOCs in their volatility basis set (VBS) model compared to what was observed with a nitrate chemical ionization atmospheric pressure interface time of flight mass spectrometer (nitrate-CI-API-TOF). The motivation behind this VBS modification is that the nitrate-CI-API-TOF likely underestimates the concentrations of HOMs in the SVOC and LVOC volatility range. The modeled average volatility distribution of the SOA and the condensable organic compounds in the gas phase at 00:00 UTC is shown in Fig. 8 (see Fig. S9 for additional VBS distributions at 12:00 UTC on day 1, 18:00 UTC on day 1 and 06:00 UTC on day 2). Of the SOA material, 79.1 % originates from HOM monomers (HOM C10), 1.44 % from HOM monomers containing nitrate functional groups (HOM NO_3) and 3.90 % of the SOA is composed of HOM dimers (HOM C20), which increases during nighttime when the NO is depleted. Although the experiments in Tröstl et al. (2016) do not fully represent the conditions in our atmospheric study, the SOA formation is in both cases dominated by ozonolysis and OH oxidation of monoterpenes. Thus, we think it is relevant to compare our modeled SOA volatility distribution with theirs. The VBS distribution in Fig. 8 is in good agreement with the fitted VBS distribution reported by Tröstl et al. (2016) (extended data, Fig. 5). They report a ELVOC : LVOC : SVOC ratio of 7 : 77 : 16. This can be compared to the average ELVOC : LVOC : SVOC ratio of 7.18 : 87.2 : 5.58 in Fig. 8. Figure S10 shows volatility distributions derived from the model results from the liq-COSMO HOM scenario.

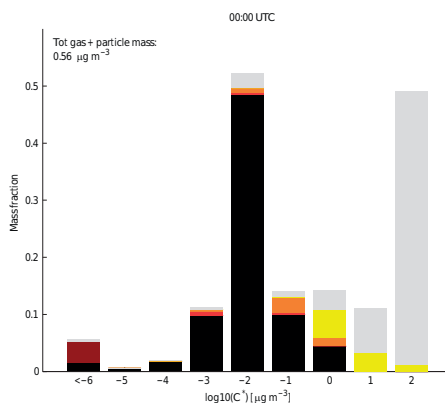


Figure 8. Modeled mean volatility distribution of SOA components at Pallas at 00:00 UTC. The gray bars are the sum of all oxidized organic compounds in the gas phase with $C^* \leq 10^2 \mu\text{g m}^{-3}$. The mass in each volatility bin is normalized to the total mass (gas and particle phase) of compounds with $C^* \leq 1 \mu\text{g m}^{-3}$. The black, dark red, red, orange and yellow bars are HOM C10, HOM C20, HOM C10- NO_3 , MCM LVOC and MCM SVOC, respectively. The particles are assumed to be liquid and the vapor pressures of the HOMs are estimated with SIMPOL with a temperature of 298 K.

We also evaluated the impact of the SOA phase by running the model as the base-case model run but with solid-like SOA particles instead of liquid. The differences between the base-case model runs and these simulations are minor (Fig. S11). One of the reasons for this is that the main fraction of the SOA is formed by condensation of LVOCs (Fig. 8). If a dominating fraction of the SOA instead were SVOCs, the SOA phase state would most likely have a larger impact on the model results (see, e.g., Zaveri et al., 2014). The most notable difference in our model results is that the fraction of nitrate is higher for particle sizes around 500 nm in diameter when the particles are assumed to be solid. The reason for this is that the solid surface layer, composed of low-volatility HOM SOA, traps the ammonium nitrate in the particle interior. The evaporation of ammonia and nitric acid will therefore be inhibited when the particles are solid as opposed to when they are liquid. The SVOCs from the MCM chemistry are not as much affected by the phase state of the particles as the ammonium nitrate. One likely reason for this is that, as opposed to the ammonium nitrate, the SVOCs are continuously replenished in the gas phase due to the continuous BVOC emissions over the forest. The result from this study implies that in environments with higher ammonia and NO_x emission or during conditions when the SOA formation mainly is driven by condensation of SVOCs, the phase state of the particles could be an important factor to take into consideration. However,

in the boreal environment of this study, at least the ammonium nitrate formation generally only contributes to a minor fraction of the secondary particle mass formation (e.g., Jaatinen et al., 2014, and Fig. 7) and does not contribute to the growth of the newly formed particles during the NPF events (Fig. S12).

Finally, to test the influence of the nucleation rate on particle growth, a sensitivity test was done where kinetic H_2SO_4 nucleation (Eq. 3) was used. On average, the kinetic sulfuric acid nucleation mechanism, as implemented in this work, caused more particles to form but the concentration of larger particles was fairly insensitive to the change in nucleation mechanism (Figs. S13 and S14).

4 Conclusions

During recent years the HOM formation from endocyclic monoterpenes has been studied in laboratory and field environments (e.g., Ehn et al., 2014; Jokinen et al., 2015). In this study we evaluated the importance of HOM formation from monoterpene autoxidation in a boreal environment. The modeled HOM formation rate is high enough to give sufficient condensable vapors to explain or even slightly overestimate the growth of the newly formed particles between 1.5 and ~ 20 nm in diameter, if most of the formed HOMs are LVOCs or ELVOCs. Between ~ 20 and 80 nm in diameter the model seems to underestimate the particle growth, even if the HOMs were assumed to be nonvolatile. At the same time the model gives a very high O:C ratio of nearly 1 for the SOA. Possible explanations to this could be that we did not consider particle-phase oligomerization involving SVOCs in the model or that the model underestimates the SVOC formation rate from BVOCs. With more SVOCs and particle-phase oligomerization, mainly the growth of the larger particles (> 20 nm in diameter) would increase and the O:C decrease. We suggest that future studies should follow up on how heterogeneous reactions involving HOMs and other SVOCs influence the particle number size distribution evolution and the aerosol chemical composition during new particle formation events.

The modeled SOA mass formation was dominated by condensation of HOMs. However, the estimation of the vapor pressures of HOMs is very uncertain. A recent study by Kurtén et al. (2016) suggests that the vapor pressures might be higher than previously thought and that the contribution of HOMs in the particle phase might be due to rapid reactions in the particle phase. We performed a sensitivity test where the vapor pressures of the HOMs were in line with values in Kurtén et al. (2016) and found that the model then seemed to explain the initial growth of the particles better than in the simulation with lower vapor pressures.

The growth of the particles was found to be independent on the phase state of the particles; the phase state might, however, be of importance when the fraction of semi-volatile par-

ticulate matter is higher. In these cases, enrichment of low-volatility organic compounds at the particle surface might act as a protective shield against evaporation of SVOCs, ammonia and nitric acid.

Data availability. Supplementary data are available at <https://doi.org/10.1594/PANGAEA.877695> (Öström et al., 2017).

The Supplement related to this article is available online at <https://doi.org/10.5194/acp-17-8887-2017-supplement>.

Competing interests. The authors declare that they have no conflict of interest.

Acknowledgements. This work was carried out with the support by Nordic Center of Excellence programs CRAICC (Cryosphere–Atmosphere Interactions in a Changing Arctic Climate) and eS-TICC (eScience tools for investigating Climate Change in Northern High Latitudes), the European Union’s Horizon 2020 research and innovation programme under grant agreement no. 654109, the European Research Council (grant 638703-COALA), the Swedish Strategic Research Program MERGE, Modeling the Regional and Global Earth System, the Lund Centre for studies of Carbon Cycle and Climate Interaction (LUCCI), the Swedish Research Council for Environment, Agricultural Sciences and Spatial Planning FORMAS (project no. 2014-1445) and the Academy of Finland Center of Excellence program (project no. 272041).

The authors would like to thank Fredrik Söderberg at the Centre for Environmental and Climate Research at Lund University for providing help to set up the model at the high-performance computing cluster available at the Centre for Scientific and Technical Computing at Lund University (Lunarc) and Finnish Meteorological Institute for providing the measurement data at Pallas.

Edited by: H. Grothe

Reviewed by: two anonymous referees

References

- Ahlström, A., Schurgers, G., Arneth, A., and Smith, B.: Robustness and uncertainty in terrestrial ecosystem carbon response to CMIP5 climate change projections, *Environ. Res. Lett.*, 7, 44008, <https://doi.org/10.1088/1748-9326/7/4/044008>, 2012.
- Arneth, A., Niinemets, Ü., Pressley, S., Bäck, J., Hari, P., Karl, T., Noe, S., Prentice, I. C., Serça, D., Hickler, T., Wolf, A., and Smith, B.: Process-based estimates of terrestrial ecosystem isoprene emissions: incorporating the effects of a direct CO_2 -isoprene interaction, *Atmos. Chem. Phys.*, 7, 31–53, <https://doi.org/10.5194/acp-7-31-2007>, 2007.

- Asmi, E., Kivekäs, N., Kerminen, V.-M., Komppula, M., Hyvärinen, A.-P., Hatakka, J., Viisanen, Y., and Lihavainen, H.: Secondary new particle formation in Northern Finland Pallas site between the years 2000 and 2010, *Atmos. Chem. Phys.*, 11, 12959–12972, <https://doi.org/10.5194/acp-11-12959-2011>, 2011.
- Bäck, J., Aalto, J., Henriksson, M., Hakola, H., He, Q., and Boy, M.: Chemodiversity of a Scots pine stand and implications for terpene air concentrations, *Biogeosciences*, 9, 689–702, <https://doi.org/10.5194/bg-9-689-2012>, 2012.
- Beecken, J., Mellqvist, J., Salo, K., Ekholm, J., Jalkanen, J.-P., Johansson, L., Litvinenko, V., Volodin, K., and Frank-Kamenetsky, D. A.: Emission factors of SO₂, NO_x and particles from ships in Neva Bay from ground-based and helicopter-borne measurements and AIS-based modeling, *Atmos. Chem. Phys.*, 15, 5229–5241, <https://doi.org/10.5194/acp-15-5229-2015>, 2015.
- Bergström, R., Denier van der Gon, H. A. C., Prévôt, A. S. H., Yttri, K. E., and Simpson, D.: Modelling of organic aerosols over Europe (2002–2007) using a volatility basis set (VBS) framework: application of different assumptions regarding the formation of secondary organic aerosol, *Atmos. Chem. Phys.*, 12, 8499–8527, <https://doi.org/10.5194/acp-12-8499-2012>, 2012.
- Bourtsoukdis, E., Bonn, B., and Noe, S. M.: On-line field measurements of BVOC emissions from Norway spruce (*Picea abies*) at the hemiboreal SMEAR-Estonia site under autumn conditions, *Boreal Environ. Res.*, 19, 153–167, 2014.
- Crounse, J. D., Nielsen, L. B., Jørgensen, S., Kjaergaard, H. G., and Wennberg, P. O.: Autoxidation of Organic Compounds in the Atmosphere, *J. Phys. Chem. Lett.*, 4, 3513–3520, 2013.
- Dal Maso, M., Kulmala, M., Riipinen, I., Wagner, R., Hussein, T., Aalto, P. P., and Lehtinen, K. E. J.: Formation and growth of fresh atmospheric aerosols: eight years of aerosol size distribution data from SMEAR II, Hyytiälä, Finland, *Boreal Environ. Res.*, 10, 323–336, 2005.
- Damian, V., Sandu, A., Damian, M., Potra, F., and Carmichael, G. R.: The kinetic preprocessor KPP—a software environment for solving chemical kinetics, *Comput. Chem. Eng.*, 26, 1567–1579, [https://doi.org/10.1016/S0098-1354\(02\)00128-X](https://doi.org/10.1016/S0098-1354(02)00128-X), 2002.
- Draxler, R. and Rolph, G. D.: HYSPLIT (HYbrid Single-Particle Lagrangian Integrated Trajectory) Model, NOAA Air Resources Laboratory's (ARL), Silver Spring, MD, available at: <http://ready.arl.noaa.gov/HYSPLIT.php> (last access: 1 October 2016), 2013.
- Eckert, F. and Klamt, A.: Fast Solvent Screening via Quantum Chemistry: COSMO-RS Approach, *AIChE J.*, 48, 369–385, 2002.
- Eckert, F. and Klamt, A.: COSMOTerm, Version C3.0, Release 15.01; COSMOlogic GmbH & Co. KG, Leverkusen, Germany, 2014.
- Ehn, M., Thornton, J. A., Kleist, E., Sipilä, M., Junninen, H., Pullinen, I., Springer, T., Rubach, F., Tillmann, R., Lee, B., Lopez-Hilfiker, F., Andres, S., Acir, I.-H., Rissanen, M., Jokinen, T., Schobesberger, S., Kangasluoma, J., Kontkanen, J., Nieminen, T., Kurtén, T., Nielsen, L. B., Jørgensen, S., Kjaergaard, H. G., Canagaratna, M., Dal Maso, M., Berndt, T., Petäjä, T., Wahner, A., Kerminen, V.-M., Kulmala, M., Worsnop, D. R., Wildt, J., and Mentel, T. F.: A large source of low-volatility secondary organic aerosol, *Nature*, 506, 476–479, <https://doi.org/10.1038/nature13032>, 2014.
- Farina, S. C., Adams, P. J., and Pandis, S. N.: Modeling global secondary organic aerosol formation and processing with the volatility basis set: Implications for anthropogenic secondary organic aerosol, *J. Geophys. Res.*, 115, D09202, <https://doi.org/10.1029/2009JD013046>, 2010.
- Fountoukis, C., Megaritis, A. G., Skyllakou, K., Charalampidis, P. E., Pilinis, C., Denier van der Gon, H. A. C., Crippa, M., Canonaco, F., Mohr, C., Prévôt, A. S. H., Allan, J. D., Poulain, L., Petäjä, T., Tiitta, P., Carbone, S., Kiendler-Scharr, A., Nemitz, E., O'Dowd, C., Swietlicki, E., and Pandis, S. N.: Organic aerosol concentration and composition over Europe: insights from comparison of regional model predictions with aerosol mass spectrometer factor analysis, *Atmos. Chem. Phys.*, 14, 9061–9076, <https://doi.org/10.5194/acp-14-9061-2014>, 2014.
- Hermansson, E., Roldin, P., Rusanen, A., Mogensen, D., Kivekäs, N., Väinänen, R., Boy, M., and Swietlicki, E.: Biogenic SOA formation through gas-phase oxidation and gas-to-particle partitioning – a comparison between process models of varying complexity, *Atmos. Chem. Phys.*, 14, 11853–11869, <https://doi.org/10.5194/acp-14-11853-2014>, 2014.
- Hickler, T., Vohland, K., Feehan, J., Miller, P. A., Smith, B., Costa, L., Giesecke, T., Fronzek, S., Carter, T. R., Cramer, W., Kühn, I., and Sykes, M. T.: Projecting the future distribution of European potential natural vegetation zones with a generalized, tree species-based dynamic vegetation model, *Global Ecol. Biogeogr.*, 21, 50–63, <https://doi.org/10.1111/j.1466-8238.2010.00613.x>, 2012.
- Hodzic, A., Jimenez, J. L., Madronich, S., Aiken, A. C., Bessagnet, B., Curci, G., Fast, J., Lamarque, J.-F., Onasch, T. B., Roux, G., Schauer, J. J., Stone, E. A., and Ulbrich, I. M.: Modeling organic aerosols during MILAGRO: importance of biogenic secondary organic aerosols, *Atmos. Chem. Phys.*, 9, 6949–6981, <https://doi.org/10.5194/acp-9-6949-2009>, 2009.
- Inness, A., Baier, F., Benedetti, A., Bouarar, I., Chabrillat, S., Clark, H., Clerbaux, C., Coheur, P., Engelen, R. J., Errera, Q., Flemming, J., George, M., Granier, C., Hadji-Lazarou, J., Huijnen, V., Hurtmans, D., Jones, L., Kaiser, J. W., Kapsomenakis, J., Lefever, K., Leitão, J., Razinger, M., Richter, A., Schultz, M. G., Simmons, A. J., Suttie, M., Stein, O., Thépaut, J.-N., Thouret, V., Vrekoussis, M., Zerefos, C., and the MACC team: The MACC reanalysis: an 8 yr data set of atmospheric composition, *Atmos. Chem. Phys.*, 13, 4073–4109, <https://doi.org/10.5194/acp-13-4073-2013>, 2013.
- IPCC: Climate Change 2013: The Physical Science Basis. Contribution of Working Group I to the Fifth Assessment Report of the Intergovernmental Panel on Climate Change, edited by: Stocker, T. F., Qin, D., Plattner, G.-K., Tignor, M., Allen, S. K., Boschung, J., Nauels, A., Xia, Y., Bex, V., and Midgley, P. M., Cambridge University Press, Cambridge, United Kingdom and New York, NY, USA, 1535 pp., 2013.
- Jacobson, M. Z.: Fundamentals of Atmospheric Modeling, 2nd Edn., Cambridge University Press, Cambridge, United Kingdom and New York, NY, USA, 2005.
- Jenkin, M. E., Saunders, S. M., and Pilling, M. J.: The tropospheric degradation of volatile organic compounds: a protocol for mechanism development, *Atmos. Environ.*, 31, 81–104, [https://doi.org/10.1016/S1352-2310\(96\)00105-7](https://doi.org/10.1016/S1352-2310(96)00105-7), 1997.
- Jericevic, A., Kraljevic, L., Grisogono, B., Fagerli, H., and Vecenaj, Ž.: Parameterization of vertical diffusion and the atmospheric

- boundary layer height determination in the EMEP model, *Atmos. Chem. Phys.*, 10, 341–364, <https://doi.org/10.5194/acp-10-341-2010>, 2010.
- Jokinen, T., Berndt, T., Makkonen, R., Kerminen, V.-M., Junninen, H., Paasonen, P., Stratmann, F., Herrmann, H., Guenther, A. B., Worsnop, D. R., Kulmala, M., Ehn, M., and Sipilä, M.: Production of extremely low volatile organic compounds from biogenic emissions: Measured yields and atmospheric implications, *P. Natl. Acad. Sci. USA*, 112, 7123–7128, <https://doi.org/10.1073/pnas.1423977112>, 2015.
- Jonsson, Å. M., Westerlund, J., and Hallquist, M.: Size-resolved particle emission factors for individual ships, *Geophys. Res. Lett.*, 38, L12809, <https://doi.org/10.1029/2011GL047672>, 2011.
- Kerminen, V.-M., Paramonov, M., Anttila, T., Riipinen, I., Fountoukis, C., Korhonen, H., Asmi, E., Laakso, J., Lihavainen, H., Swietlicki, E., Svenningsson, B., Asmi, A., Pandis, S. N., Kulmala, M., and Petäjä, T.: Cloud condensation nuclei production associated with atmospheric nucleation: a synthesis based on existing literature and new results, *Atmos. Chem. Phys.*, 12, 12037–12059, <https://doi.org/10.5194/acp-12-12037-2012>, 2012.
- Komppula, M., Lihavainen, H., Hatakka, J., and Paatero, J.: Observations of new particle formation and size distributions at two different heights and surroundings in subarctic area in northern Finland, *J. Geophys. Res.*, 108, 4295, <https://doi.org/10.1029/2002JD002939>, 2003.
- Komppula, M., Lihavainen, H., Kerminen, V.-M., Kulmala, M., and Viisanen, Y.: Measurements of cloud droplet activation of aerosol particles at a clean subarctic background site, *J. Geophys. Res.*, 110, D06204, <https://doi.org/10.1029/2004JD005200>, 2005.
- Kristensson, A., Johansson, C., Westerholm, R., Swietlicki, E., Gidhagen, L., Wideqvist, U., and Vesely, V.: Real-world traffic emission factors of gases and particles measured in a road tunnel in Stockholm, Sweden, *Atmos. Environ.*, 38, 657–673, <https://doi.org/10.1016/j.atmosenv.2003.10.030>, 2004.
- Kulmala, M., Hämeri, K., Aalto, P. P., Mäkelä, J. M., Pirjola, L., Douglas Nilsson, E., Buzorius, G., Rannik, Ü., Dal Maso, M., Seidl, W., Hoffmann, T., Janson, R., Hansson, H.-C., Viisanen, Y., Laaksonen, A., and O'Dowd, C. D.: Overview of the international project on biogenic aerosol formation in the boreal forest (BIOFOR), *Tellus B*, 53, 324–343, <https://doi.org/10.3402/tellusb.v53i4.16601>, 2001.
- Kulmala, M., Kontkanen, J., Junninen, H., Lehtipalo, K., Manninen, H. E., Nieminen, T., Petäjä, T., Sipilä, M., Schobesberger, S., Rantala, P., Franchin, A., Jokinen, T., Jävinen, E., Äijälä, M., Kangasluoma, J., Hakala, J., Aalto, P. P., Paasonen, P., Mikkilä, J., Vanhanen, J., Aalto, J., Hakola, H., Makkonen, U., Ruuskanen, T., Mauldin III, R. L., Duplissy, J., Vehkamäki, H., Bäck, J., Kortelainen, A., Riipinen, I., Kurtén, T., Johnston, M. V., Smith, J. N., Ehn, M., Mentel, T. F., Lehtinen, K. E. J., Laaksonen, A., Kerminen, V.-M., and Worsnop, D. R.: Direct Observations of Atmospheric Aerosol Nucleation, *Science*, 339, 943–947, 2013.
- Kurtén, T., Tiusanen, K., Roldin, P., Rissanen, M., Luy, J.-N., Boy, M., Ehn, M., and Donahue, N.: α -Pinene Autoxidation Products May Not Have Extremely Low Saturation Vapor Pressures Despite High O:C Ratios, *J. Phys. Chem. A*, 120, 2569–2582, <https://doi.org/10.1021/acs.jpca.6b02196>, 2016.
- Lane, T. E., Donahue, N. M., and Pandis, S. N.: Simulating secondary organic aerosol formation using the volatility basis-set approach in a chemical transport model, *Atmos. Environ.*, 42, 7439–7451, <https://doi.org/10.1016/j.atmosenv.2008.06.026>, 2008.
- Langmann, B., Sellegri, K., and Freney, E.: Secondary organic aerosol formation during June 2010 in Central Europe: measurements and modelling studies with a mixed thermodynamic-kinetic approach, *Atmos. Chem. Phys.*, 14, 3831–3842, <https://doi.org/10.5194/acp-14-3831-2014>, 2014.
- Li, J., Cleveland, M., Ziemba, L. D., Griffin, R. J., Barsanti, K. C., Pankow, J. F., and Ying, Q.: Modeling regional secondary organic aerosol using the Master Chemical Mechanism, *Atmos. Environ.*, 102, 52–61, <https://doi.org/10.1016/j.atmosenv.2014.11.054>, 2015.
- Lohila, A., Penttilä, T., Jortikka, S., Aalto, T., Anttila, P., Asmi, E., Aurela, M., Hatakka, J., Hellén, H., Henttonen, H., Hänninen, P., Kilkki, J., Kyllönen, K., Laurila, T., Lepistö, A., Lihavainen, H., Makkonen, U., Paatero, J., Rask, M., and Sutinen, R.: Preface to the special issue on integrated research of atmosphere, ecosystem and environment at Pallas, *Boreal Environ. Res.*, 20, 431–454, 2015.
- Mårtensson, E. M., Nilsson, E. D., de Leeuw, G., Cohen, L. H., and Hansson, H.-C.: Laboratory simulations and parameterization of the primary marine aerosol production, *J. Geophys. Res.*, 108, 4297, <https://doi.org/10.1029/2002JD002263>, 2003.
- Merikanto, J., Spracklen, D. V., Mann, G. W., Pickering, S. J., and Carslaw, K. S.: Impact of nucleation on global CCN, *Atmos. Chem. Phys.*, 9, 8601–8616, <https://doi.org/10.5194/acp-9-8601-2009>, 2009.
- Murphy, B. N., Donahue, N. M., Fountoukis, C., Dall'Osto, M., O'Dowd, C., Kiendler-Scharr, A., and Pandis, S. N.: Functionalization and fragmentation during ambient organic aerosol aging: application of the 2-D volatility basis set to field studies, *Atmos. Chem. Phys.*, 12, 10797–10816, <https://doi.org/10.5194/acp-12-10797-2012>, 2012.
- Nannoolal, Y., Rarey, J., and Ramjugernath, D.: Estimation of pure component properties, *Fluid Phase Equilib.*, 269, 117–133, <https://doi.org/10.1016/j.fluid.2008.04.020>, 2008.
- Ng, N. L., Canagaratna, M. R., Zhang, Q., Jimenez, J. L., Tian, J., Ulbrich, I. M., Kroll, J. H., Docherty, K. S., Chhabra, P. S., Bahreini, R., Murphy, S. M., Seinfeld, J. H., Hildebrandt, L., Donahue, N. M., DeCarlo, P. F., Lanz, V. A., Prévôt, A. S. H., Dinar, E., Rudich, Y., and Worsnop, D. R.: Organic aerosol components observed in Northern Hemispheric datasets from Aerosol Mass Spectrometry, *Atmos. Chem. Phys.*, 10, 4625–4641, <https://doi.org/10.5194/acp-10-4625-2010>, 2010.
- O'Dowd, C. D., Facchini, M. C., Cavalli, F., Ceburnis, D., Mircea, M., Decesari, S., Fuzzi, S., Yoon, Y. J., and Putaud, J.-P.: Biogenically driven organic contribution to marine aerosol, *Nature*, 431, 676–680, <https://doi.org/10.1038/nature02959>, 2004.
- Pankow, J. F.: An absorption model of gas/particle partitioning of organic compounds in the atmosphere, *Atmos. Environ.*, 28, 185–188, [https://doi.org/10.1016/1352-2310\(94\)90093-0](https://doi.org/10.1016/1352-2310(94)90093-0), 1994.
- Pankow, J. F. and Asher, W. E.: SIMPOL.1: a simple group contribution method for predicting vapor pressures and enthalpies of vaporization of multifunctional organic compounds, *Atmos. Chem. Phys.*, 8, 2773–2796, <https://doi.org/10.5194/acp-8-2773-2008>, 2008.
- Öström, E., Roldin, P., Schurgers, G., Mishurov, M., Putian, Z., Kivekäs, N., Lihavainen, H., Ehn, M., Rissanen, M. P., Kurtén, T., Boy, M., and Swietlicki, E.: Model data for sim-

- ulation of secondary organic aerosol formation over the boreal forest, link to NetCDF files in zip archive, PANGAEA, <https://doi.org/10.1594/PANGAEA.877695>, 2017.
- Renbaum-Wolff, L., Grayson, J. W., Bateman, A. P., Kuwata, M., Sellier, M., Murray, B. J., Shilling, J. E., Martin, S. T., and Bertram, A. K.: Viscosity of α -pinene secondary organic material and implications for particle growth and reactivity, *P. Natl. Acad. Sci. USA*, 110, 8014–8019, <https://doi.org/10.1073/pnas.1219548110>, 2013.
- Riipinen, I., Pierce, J. R., Donahue, N. M., and Pandis, S. N.: Equilibration time scales of organic aerosol inside thermodenuders?: Evaporation kinetics versus thermodynamics, *Atmos. Environ.*, 44, 597–607, <https://doi.org/10.1016/j.atmosenv.2009.11.022>, 2010.
- Riipinen, I., Pierce, J. R., Yli-Juuti, T., Nieminen, T., Häkkinen, S., Ehn, M., Junninen, H., Lehtipalo, K., Petäjä, T., Slowik, J., Chang, R., Shantz, N. C., Abbatt, J., Leaitch, W. R., Kerminen, V.-M., Worsnop, D. R., Pandis, S. N., Donahue, N. M., and Kulmala, M.: Organic condensation: a vital link connecting aerosol formation to cloud condensation nuclei (CCN) concentrations, *Atmos. Chem. Phys.*, 11, 3865–3878, <https://doi.org/10.5194/acp-11-3865-2011>, 2011.
- Roldin, P., Swietlicki, E., Schurgers, G., Arneth, A., Lehtinen, K. E. J., Boy, M., and Kulmala, M.: Development and evaluation of the aerosol dynamics and gas phase chemistry model ADCHEM, *Atmos. Chem. Phys.*, 11, 5867–5896, <https://doi.org/10.5194/acp-11-5867-2011>, 2011a.
- Roldin, P., Swietlicki, E., Massling, A., Kristensson, A., Löndahl, J., Eriksson, A., Pagels, J., and Gustafsson, S.: Aerosol ageing in an urban plume – implication for climate, *Atmos. Chem. Phys.*, 11, 5897–5915, <https://doi.org/10.5194/acp-11-5897-2011>, 2011b.
- Roldin, P., Eriksson, A. C., Nordin, E. Z., Hermansson, E., Mogensen, D., Rusanen, A., Boy, M., Swietlicki, E., Svenningson, B., Zelenyuk, A. and Pagels, J.: Modelling non-equilibrium secondary organic aerosol formation and evaporation with the aerosol dynamics, gas- and particle-phase chemistry kinetic multilayer model ADCHAM, *Atmos. Chem. Phys.*, 14, 7953–7993, <https://doi.org/10.5194/acp-14-7953-2014>, 2014.
- Roldin, P., Liao, L., Mogensen, D., Dal Maso, M., Rusanen, A., Kerminen, V.-M., Mentel, T. F., Wildt, J., Kleist, E., Kiendler-Scharr, A., Tillmann, R., Ehn, M., Kulmala, M., and Boy, M.: Modelling the contribution of biogenic volatile organic compounds to new particle formation in the Jülich plant atmosphere chamber, *Atmos. Chem. Phys.*, 15, 10777–10798, <https://doi.org/10.5194/acp-15-10777-2015>, 2015.
- Rolph, G. D.: Real-time Environmental Applications and Display sYstem (READY), NOAA Air Resources Laboratory's (ARL), Silver Spring, MD, available at: <http://ready.arl.noaa.gov>, last access: 1 October 2016.
- Saukko, E., Lambe, A. T., Massoli, P., Koop, T., Wright, J. P., Croasdale, D. R., Pedernera, D. A., Onasch, T. B., Laaksonen, A., Davidovits, P., Worsnop, D. R., and Virtanen, A.: Humidity-dependent phase state of SOA particles from biogenic and anthropogenic precursors, *Atmos. Chem. Phys.*, 12, 7517–7529, <https://doi.org/10.5194/acp-12-7517-2012>, 2012.
- Saunders, S. M., Jenkin, M. E., Derwent, R. G., and Pilling, M. J.: Protocol for the development of the Master Chemical Mechanism, MCM v3 (Part A): tropospheric degradation of non-aromatic volatile organic compounds, *Atmos. Chem. Phys.*, 3, 161–180, <https://doi.org/10.5194/acp-3-161-2003>, 2003.
- Schurgers, G., Arneth, A., Holzinger, R., and Goldstein, A. H.: Process-based modelling of biogenic monoterpene emissions combining production and release from storage, *Atmos. Chem. Phys.*, 9, 3409–3423, <https://doi.org/10.5194/acp-9-3409-2009>, 2009a.
- Schurgers, G., Hickler, T., Miller, P. A., and Arneth, A.: European emissions of isoprene and monoterpenes from the Last Glacial Maximum to present, *Biogeosciences*, 6, 2779–2797, <https://doi.org/10.5194/bg-6-2779-2009>, 2009b.
- Scott, C. E., Rap, A., Spracklen, D. V., Forster, P. M., Carslaw, K. S., Mann, G. W., Pringle, K. J., Kivekäs, N., Kulmala, M., Lihavainen, H., and Tunved, P.: The direct and indirect radiative effects of biogenic secondary organic aerosol, *Atmos. Chem. Phys.*, 14, 447–470, <https://doi.org/10.5194/acp-14-447-2014>, 2014.
- Scott, C. E., Spracklen, D. V., Pierce, J. R., Riipinen, I., D'Andrea, S. D., Rap, A., Carslaw, K. S., Forster, P. M., Artaxo, P., Kulmala, M., Rizzo, L. V., Swietlicki, E., Mann, G. W., and Pringle, K. J.: Impact of gas-to-particle partitioning approaches on the simulated radiative effects of biogenic secondary organic aerosol, *Atmos. Chem. Phys.*, 15, 12989–13001, <https://doi.org/10.5194/acp-15-12989-2015>, 2015.
- Seinfeld, J. H. and Pandis, S. N.: *Atmospheric Chemistry and Physics: from air pollution to climate change*, 2nd Edn., John Wiley & Sons, Inc, Hoboken, New Jersey, USA, 2006.
- Smith, B., Wärnlind, D., Arneth, A., Hickler, T., Leadley, P., Silberg, J., and Zaehle, S.: Implications of incorporating N cycling and N limitations on primary production in an individual-based dynamic vegetation model, *Biogeosciences*, 11, 2027–2054, <https://doi.org/10.5194/bg-11-2027-2014>, 2014.
- Smolander, S., He, Q., Mogensen, D., Zhou, L., Bäck, J., Ruuskanen, T., Noe, S., Guenther, A., Aaltonen, H., Kulmala, M., and Boy, M.: Comparing three vegetation monoterpene emission models to measured gas concentrations with a model of meteorology, air chemistry and chemical transport, *Biogeosciences*, 11, 5425–5443, <https://doi.org/10.5194/bg-11-5425-2014>, 2014.
- Spracklen, D. V., Bonn, B., and Carslaw, K. S.: Boreal forests, aerosols and the impacts on clouds and climate, *Philos. T. Roy. Soc. A*, 366, 4613–4626, <https://doi.org/10.1098/rsta.2008.0201>, 2008.
- Topping, D., Barley, M., and McFiggans, G.: Including phase separation in a unified model to calculate partitioning of vapours to mixed inorganic–organic aerosol particles, *Faraday Discuss.*, 165, 273–288, 2013a.
- Topping, D., Connolly, P., and McFiggans, G.: Cloud droplet number enhanced by co-condensation of organic vapours, *Nat. Geosci.*, 6, 443–446, <https://doi.org/10.1038/ngeo1809>, 2013b.
- Topping, D., Barley, M., Bane, M. K., Higham, N., Aumont, B., Dingle, N., and McFiggans, G.: UManSysProp v1.0: an online and open-source facility for molecular property prediction and atmospheric aerosol calculations, *Geosci. Model Dev.*, 9, 899–914, <https://doi.org/10.5194/gmd-9-899-2016>, 2016.
- Tröstl, J., Chuang, W. K., Gordon, H., Heinritzi, M., Yan, C., Molteni, U., Ahlm, L., Frege, C., Bianchi, F., Wagner, R., Simon, M., Lehtipalo, K., Williamson, C., Craven, J. S., Duplissy, J., Adamov, A., Almeida, J., Bernhammer, A.-K., Breitenlechner, M., Brilke, S., Dias, A., Ehrhart, S., Flagan, R. C.,

- Franchin, A., Fuchs, C., Guida, R., Gysel, M., Hansel, A., Hoyle, C. R., Jokinen, T., Junninen, H., Kangasluoma, J., Keskinen, H., Kim, J., Krapf, M., Kürten, A., Laaksonen, A., Lawler, M., Leiminger, M., Mathot, S., Möhler, O., Nieminen, T., Onnela, A., Petäjä, T., Piel, F. M., Miettinen, P., Rissanen, M. P., Rondo, L., Sarnela, N., Schobesberger, S., Sengupta, K., Sipilä, M., Smith, J. N., Steiner, G., Tomé, A., Virtanen, A., Wagner, A. C., Weingartner, E., Wimmer, D., Winkler, P. M., Ye, P., Carslaw, K. S., Curtius, J., Dommen, J., Kirkby, J., Kulmala, M., Riipinen, I., Worsnop, D. R., Donahue, N. M., and Baltensperger, U.: The role of low-volatility organic compounds in initial particle growth in the atmosphere, *Nature*, 533, 527–531, <https://doi.org/10.1038/nature18271>, 2016.
- Tunved, P., Hansson, H.-C., Kulmala, M., Aalto, P., Viisanen, Y., Karlsson, H., Kristensson, A., Swietlicki, E., Dal Maso, M., Ström, J., and Komppula, M.: One year boundary layer aerosol size distribution data from five nordic background stations, *Atmos. Chem. Phys.*, 3, 2183–2205, <https://doi.org/10.5194/acp-3-2183-2003>, 2003.
- Tunved, P., Partridge, D. G., and Korhonen, H.: New trajectory-driven aerosol and chemical process model Chemical and Aerosol Lagrangian Model (CALM), *Atmos. Chem. Phys.*, 10, 10161–10185, <https://doi.org/10.5194/acp-10-10161-2010>, 2010.
- Vaden, T. D., Imre, D., Beránek, J., Shrivastava, M., and Zelenyuk, A.: Evaporation kinetics and phase of laboratory and ambient secondary organic aerosol, *P. Natl. Acad. Sci. USA*, 108, 2190–2195, <https://doi.org/10.1073/pnas.1013391108>, 2011.
- Virtanen, A., Joutsensaari, J., Koop, T., Kannosto, J., Yli-Pirilä, P., Leskinen, J., Mäkelä, J. M., Holopainen, J. K., Pöschl, U., Kulmala, M., Worsnop, D. R., and Laaksonen, A.: An amorphous solid state of biogenic secondary organic aerosol particles, *Nature*, 467, 824–827, <https://doi.org/10.1038/nature09455>, 2010.
- Westervelt, D. M., Pierce, J. R., Riipinen, I., Trivitanurak, W., Hamed, A., Kulmala, M., Laaksonen, A., Decesari, S., and Adams, P. J.: Formation and growth of nucleated particles into cloud condensation nuclei: model-measurement comparison, *Atmos. Chem. Phys.*, 13, 7645–7663, <https://doi.org/10.5194/acp-13-7645-2013>, 2013.
- Yu, F.: A secondary organic aerosol formation model considering successive oxidation aging and kinetic condensation of organic compounds: global scale implications, *Atmos. Chem. Phys.*, 11, 1083–1099, <https://doi.org/10.5194/acp-11-1083-2011>, 2011.
- Zaveri, R. A., Easter, R. C., Shilling, J. E., and Seinfeld, J. H.: Modeling kinetic partitioning of secondary organic aerosol and size distribution dynamics: representing effects of volatility, phase state, and particle-phase reaction, *Atmos. Chem. Phys.*, 14, 5153–5181, <https://doi.org/10.5194/acp-14-5153-2014>, 2014.
- Zhang, X., Mcvay, R. C., Huang, D. D., Dalleska, N. F., Aumont, B., Flagan, R. C., and Seinfeld, J. H.: Formation and evolution of molecular products in α -pinene secondary organic aerosol, *P. Natl. Acad. Sci. USA*, 112, 14168–14173, <https://doi.org/10.1073/pnas.1517742112>, 2015.
- Zuend, A., Marcolli, C., Luo, B. P., and Peter, T.: A thermodynamic model of mixed organic-inorganic aerosols to predict activity coefficients, *Atmos. Chem. Phys.*, 8, 4559–4593, <https://doi.org/10.5194/acp-8-4559-2008>, 2008.
- Zuend, A., Marcolli, C., Booth, A. M., Lienhard, D. M., Soonsin, V., Krieger, U. K., Topping, D. O., McFiggans, G., Peter, T., and Seinfeld, J. H.: New and extended parameterization of the thermodynamic model AIOMFAC: calculation of activity coefficients for organic-inorganic mixtures containing carboxyl, hydroxyl, carbonyl, ether, ester, alkenyl, alkyl, and aromatic functional groups, *Atmos. Chem. Phys.*, 11, 9155–9206, <https://doi.org/10.5194/acp-11-9155-2011>, 2011.

Supplement of Atmos. Chem. Phys., 17, 8887–8901, 2017
<https://doi.org/10.5194/acp-17-8887-2017-supplement>
© Author(s) 2017. This work is distributed under
the Creative Commons Attribution 3.0 License.



Atmospheric
Chemistry
and Physics
Open Access
EGU

Supplement of

Modeling the role of highly oxidized multifunctional organic molecules for the growth of new particles over the boreal forest region

Emilie Öström et al.

Correspondence to: Emilie Öström (emilie.ostrom@nuclear.lu.se)

The copyright of individual parts of the supplement might differ from the CC BY 3.0 License.

Table S1. Gas-phase precursors

Gas-phase precursor	Emission database/Emission model
α -pinene	LPJ-GUESS
β -pinene	LPJ-GUESS
Limonene	LPJ-GUESS
Other monoterpenes (treated as carene)	LPJ-GUESS
Isoprene	LPJ-GUESS
Ethane	EMEP
Butane	EMEP
Etene	EMEP
Propene	EMEP
Oxylene	EMEP
Formaldehyde	EMEP
Acetaldehyde	EMEP
MEK (Methyl Ethyl Ketone)	EMEP
Glyoxal	EMEP
Methylglyoxal	EMEP
1-petene	EMEP
2-methylpropene	EMEP
Dodecane	EMEP
Benzene	EMEP
Decane	EMEP
Ethylbenzene	EMEP
Nonane	EMEP
p-xylene	EMEP
Toluene	EMEP
Undecane	EMEP
m-xylene	EMEP
1-butene	EMEP
1,2,4-trimethylbenzene	EMEP
1,3,5-trimethylbenzene	EMEP
1,2,3-trimethylbenzene	EMEP

Table S2. Plant functional types applied in LPJ-GUESS for the simulation of BVOC emissions, and their BVOC characteristics. Emission capacities for isoprene and total monoterpenes are described in Schurgers et al. (2009b), references for the separation into α -pinene, β -pinene and limonene are provided below.

PFT	emission capacity ($\mu\text{g g}^{-1} \text{dw h}^{-1}$)					fraction of monoterpenes stored	references for speciation
	isoprene	α -pinene	β -pinene	limonene	other monoterpenes		
<i>Betula pendula</i>	0.2	0.9	0.6	0.6	3.9	0	(Hakola et al., 1998, 2001; König et al., 1995)
<i>Betula pubescens</i>	0	0.05	0.05	0	0.9	0	(Hakola et al., 2001)
<i>Carpinus betulus</i>	0	0.004	0.008	0.016	0.052	0	(König et al., 1995)
<i>Corylus avellana</i>	0	0	0	0	0	0	
<i>Fagus sylvatica</i>	0	0.5	2.0	1.0	6.5	0	(König et al., 1995)
<i>Fraxinus excelsior</i>	0	0	0	0	0	0	
<i>Picea abies</i>	0.5	2.1	1.2	0.9	1.8	0.5	(Janson et al., 1999)
<i>Pinus sylvestris</i>	0	1.8	0.2	0.2	1.8	0.5	(Janson and de Serves, 2001)
<i>Populus tremula</i>	20.0	0.6	0.2	0.8	2.4	0	(Hakola et al., 1998)
<i>Quercus robur</i>	40.0	0	0	0	0	0	
<i>Tilia cordata</i>	0	0	0	0	0	0	
Boreal evergreen shrubs	2.0	0.8	0.6	0.8	1.8	0.5	(Hansen et al., 1997)
C ₃ herbaceous	0.	0.25	0.20	0.15	0.40	0.5	(König et al., 1995)

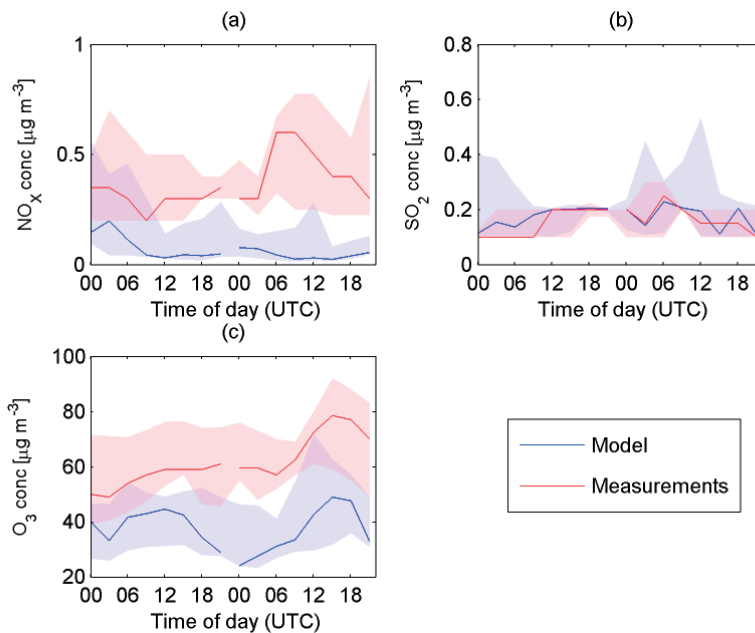


Figure S1. Median gas-phase concentration of (a) NO_x , (b) SO_2 and (c) O_3 during all chosen NPF-events at Pallas (from midnight at the day of the event to the evening the day after the start of the event) together with the 25 and 75 percentiles (shaded areas). The blue lines are the modeled results from the base-case simulation and the pink lines are the measured gas-phase concentrations.

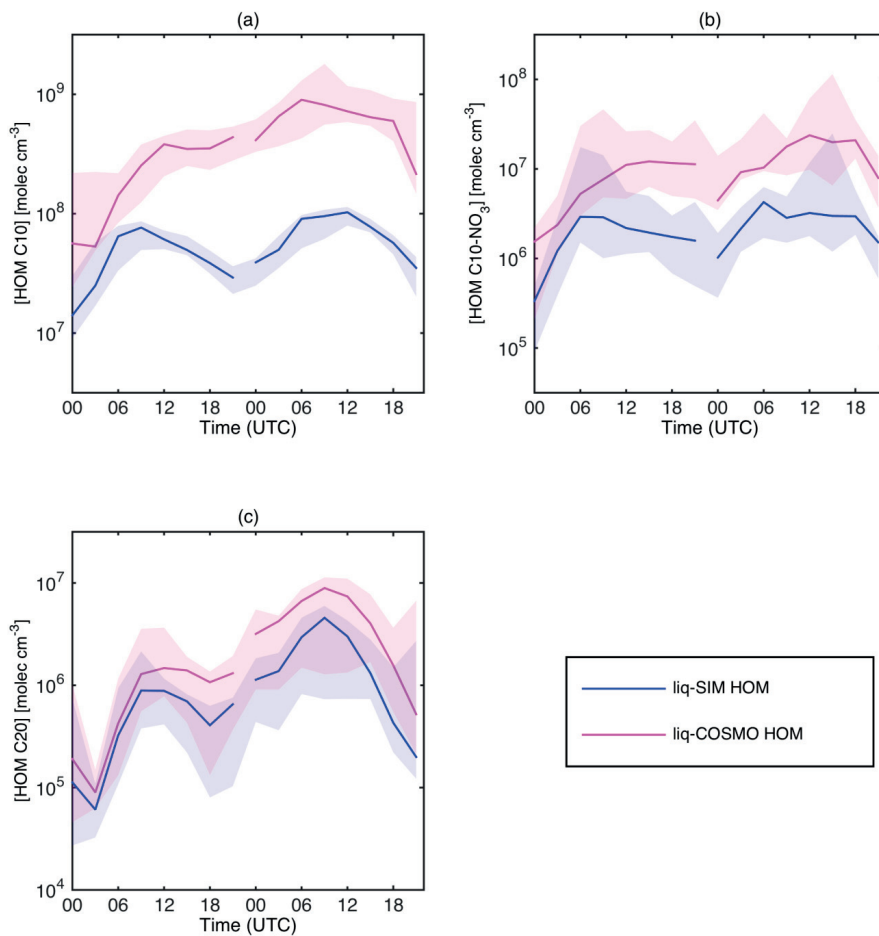


Figure S2. Median gas-phase concentration of HOMs of all chosen NPF-events at Pallas (from midnight at the day of the event to the evening the day after the start of the event) together with the 25 and 75 percentiles (shaded areas). The blue lines are the modeled results from the base-case simulation where the vapor pressures of the HOMs are estimated with SIMPOL. In the liq-COSMO HOM simulation (pink lines) the SIMPOL vapor pressures are corrected for using COSMO-RS (see table 1).

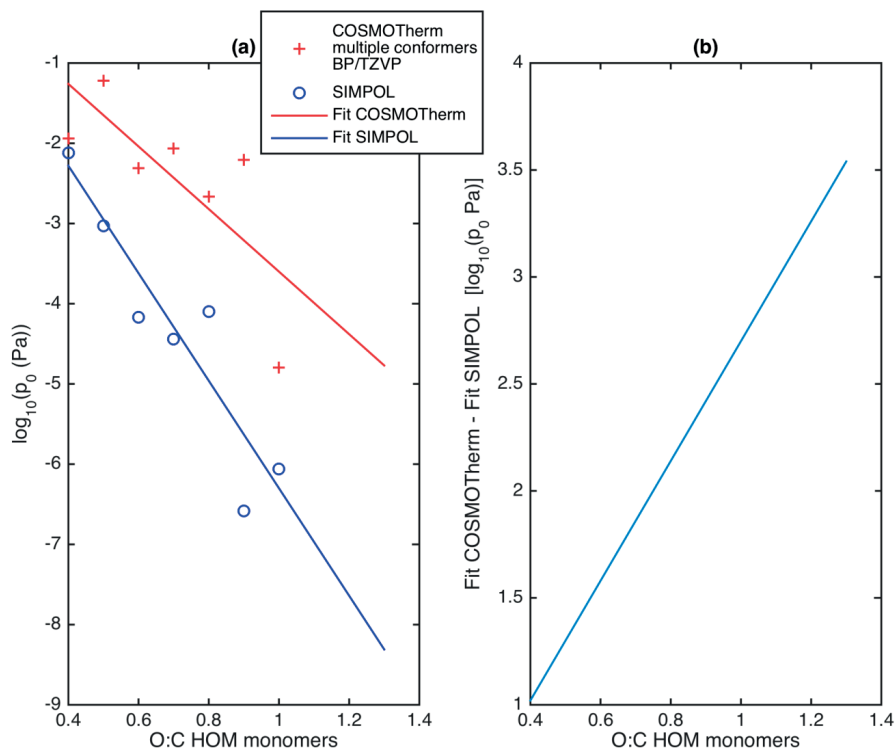


Figure S3. (a) Linear least-square fit to the pure liquid vapor pressure data points of different HOM monomers, divided into different O:C groups (O:C 0.4 – 1.0). The pure liquid vapor pressures are from Kurtén et al. (2016). The difference between the linear fits in (Fig. a) provides a correction factor (Fig. b) which was applied to the HOM pure liquid vapor pressures calculated with SIMPOL: $\log_{10}(p_0) = \log_{10}(p_{0,\text{SIMPOL}} \cdot (2.8 \cdot \text{O:C} - 0.1))$.

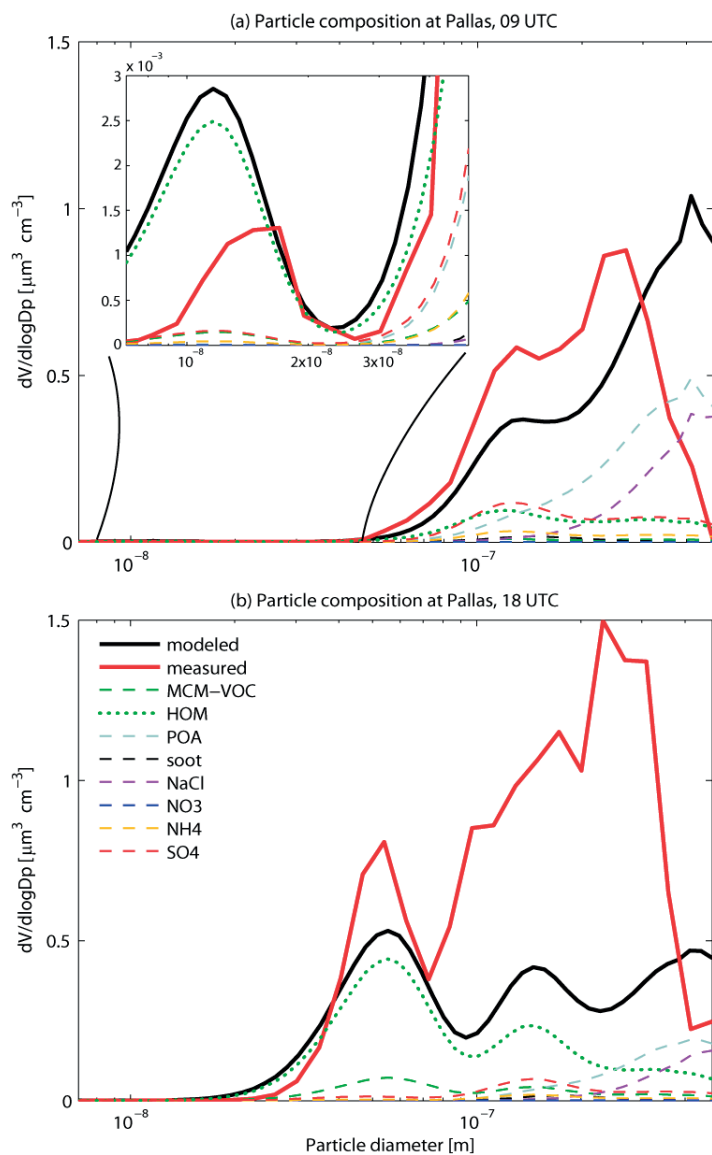


Figure S4. Particle composition at (a) 09 and (b) 18 UTC at Pallas the 5th of July 2016. Solid lines are total particle volume concentration. The dashed lines are the modeled contributions of different compounds in the particle-phase.

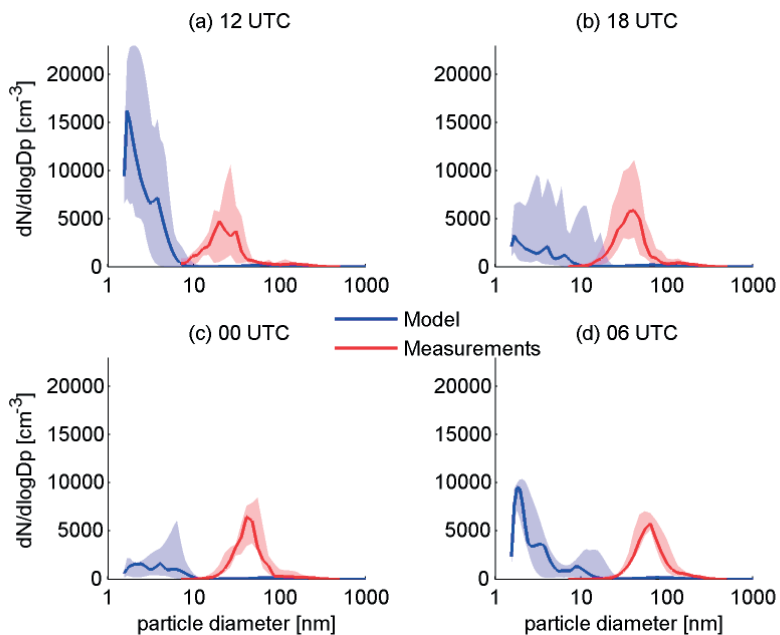


Figure S5. The modeled particles are assumed to be liquid and the formation of HOMs is excluded. Measured (red lines) and modeled (blue lines) median number size distributions at (a) 12 and (b) 18 UTC the day of the new particle formation event and (c) 00 and (d) 06 UTC the following day. The shaded areas are the values that fall between the 25th and 75th percentiles.

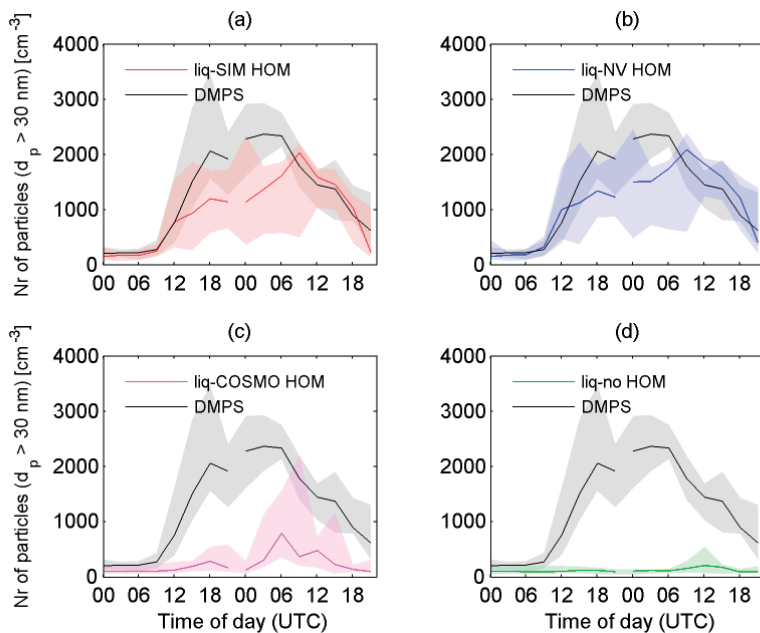


Figure S6. Median number of particles above 30 nm of all chosen NPF-events at Pallas (from midnight at the day of the event to the evening the day after the start of the event) together with the 25 and 75 percentiles (shaded areas). The black lines are the median DMPS-data from Pallas. The colored lines in (a)-(c) are the modeled median number of particles above 30 nm, using different methods to estimate the vapor pressures of the HOMs (see table 1). In (d), HOMs are excluded.

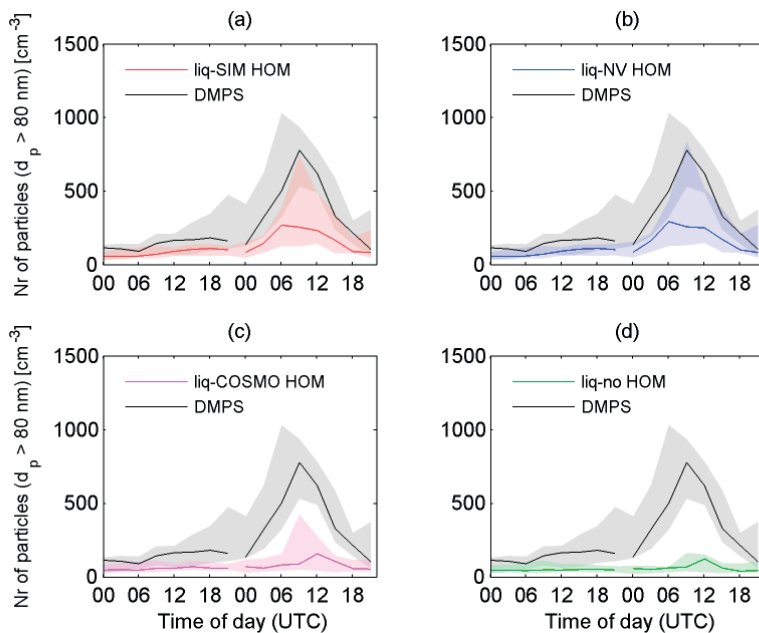


Figure S7. Median number of particles above 80 nm of all chosen NPF-events at Pallas (from midnight at the day of the event to the evening the day after the start of the event) together with the 25 and 75 percentiles (shaded areas). The black lines are the median DMP5-data from Pallas. The colored lines in (a)-(c) are the modeled median number of particles above 80 nm, using different methods to estimate the vapor pressures of the HOMs (see table 1). In (d), HOMs are excluded.

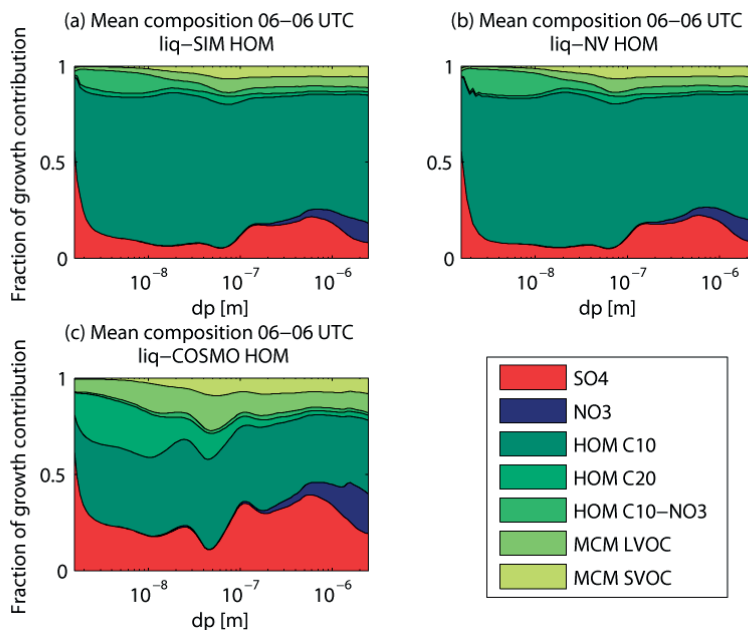


Figure S8. Mean mass fractions of each compound type that contributes to the growth of the particles during all chosen new particle formation events (from 06 UTC the morning of the event to 06 UTC the following day). In (a) the particles are assumed to be liquid with vapor pressures of HOMs estimated with SIMPOL. In (b) the particles are assumed to be liquid and the vapor pressures of HOM non-volatile. In (c) the particles are assumed to be liquid with vapor pressures of HOMs estimated with SIMPOL but corrected for with COSMO-RS. HOM C10 denote HOM monomers with 10 carbon atoms, HOM C20 is HOM dimers containing 20 carbon atoms and HOM C10–NO₃ is HOM monomers containing nitrate functional groups.

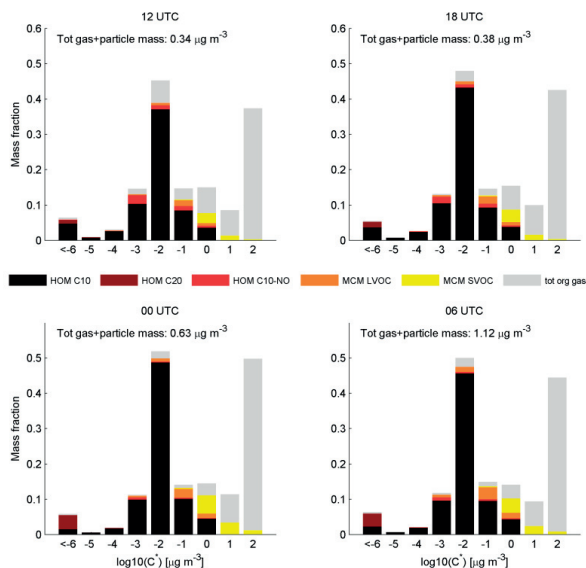


Figure S9. Modeled mean volatility distribution of SOA-components at Pallas for different times ((a) 12 UTC, (b) 18 UTC, (c) 00 UTC and (d) 06 UTC) during new particle formation events. The gray bars are the sum of all oxidized organic compounds in the gas phase with $C^* \leq 10^2 \mu\text{g m}^{-3}$. The mass in each volatility bin is normalized to the total mass (gas and particle phase) of compounds with $C^* \leq 1 \mu\text{g m}^{-3}$. The particles are assumed to be liquid and the vapor pressures of the HOMs are estimated with SIMPOL.

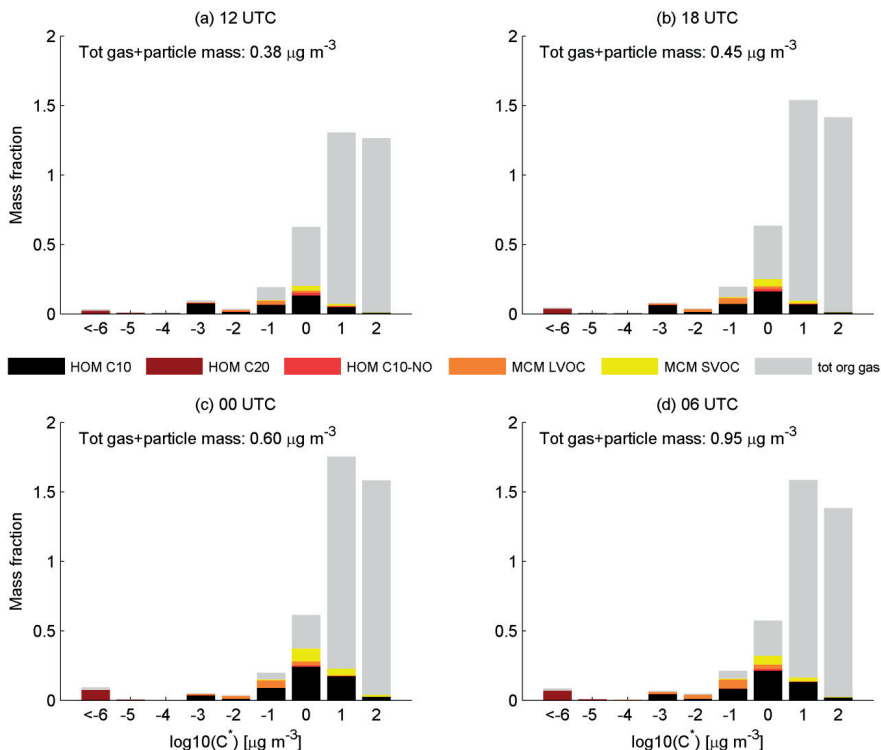


Figure S10. Modeled mean volatility distribution of SOA-components at Pallas for different times ((a) 12 UTC, (b) 18 UTC, (c) 00 UTC and (d) 06 UTC) during new particle formation events. The gray bars are the sum of all oxidized organic compounds in the gas phase with $C^* \leq 10^2 \mu\text{g m}^{-3}$. The mass in each volatility bin is normalized to the total mass (gas and particle phase) of compounds with $C^* \leq 1 \mu\text{g m}^{-3}$. The particles are assumed to be liquid and the vapor pressures of the HOMs are estimated with COSMO-RS.

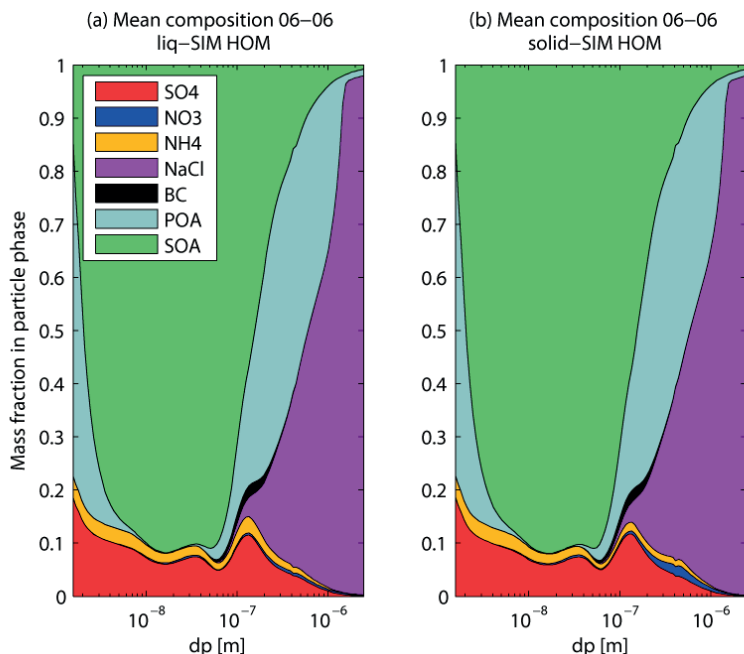


Figure S11. Mean mass fraction of each compound of the particles during all chosen new particle formation events (from 06 UTC the morning of the event to 06 UTC the following day). In (a) the particles are assumed to be liquid with vapor pressures of HOMs estimated with SIMPOL. In (b) the particles are assumed to be solid with the same vapor pressure estimation. The rather high fraction of POA (primary organic aerosols) at the smallest sizes is only subscribed as POA in the model and is actually the mole fraction of organics in the newly formed particles (assumed to be 50 %). The larger particles are background particles from the marine environment upwind Pallas.

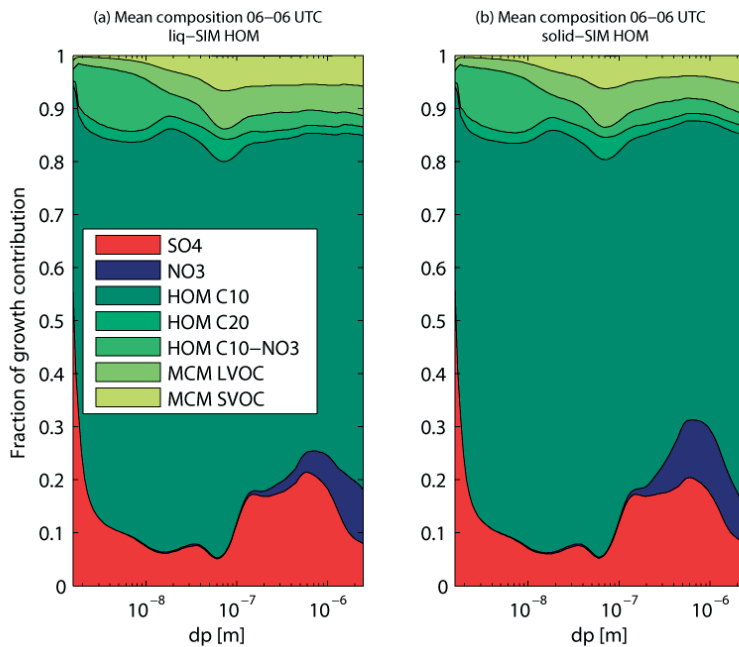


Figure S12. Mean mass fractions of the compound types that contribute to the growth of the particles during all chosen new particle formation events (from 06 UTC the morning of the event to 06 UTC the following day). In (a) the particles are assumed to be liquid with vapor pressures of HOMs estimated with SIMPOL. In (b) the particles are assumed to be solid with the same vapor pressure estimation.

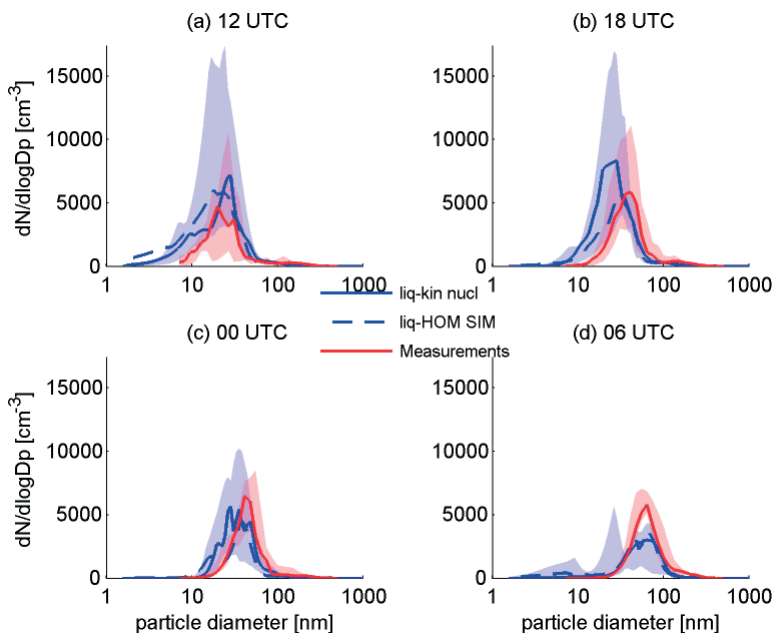


Figure S13. Measured (red lines), modeled with kinetic H_2SO_4 nucleation (solid blue lines) and modeled base-case scenario (dashed blue lines) median number size distributions at (a) 12 and (b) 18 UTC the day of the new particle formation event and (c) 00 and (d) 06 UTC the following day. The shaded areas are the values from the measurements and modeled liq-kin nucl that fall between the 25th and 75th percentiles.

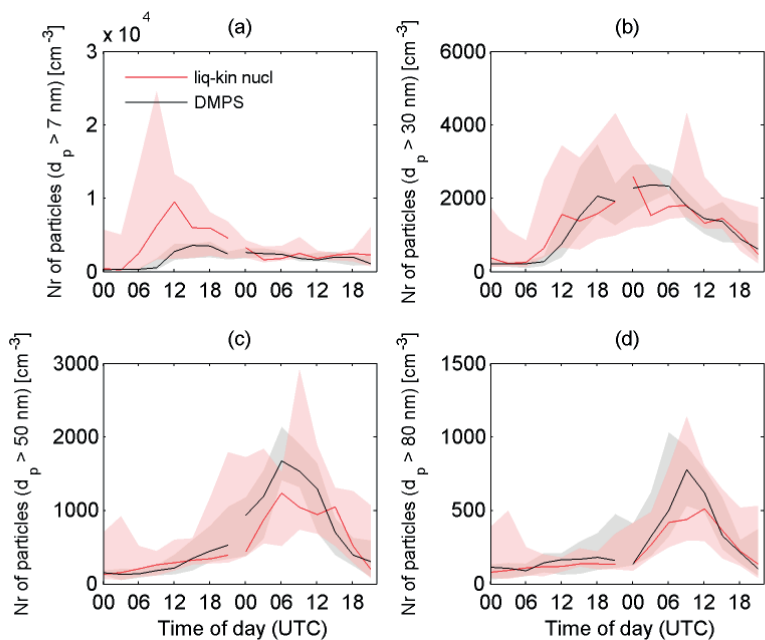


Figure S14. Median number of particles above (a) 7 nm, (b) 30 nm, (c) 50 nm and (d) 80nm of all chosen NPF-events at Pallas (from midnight at the day of the event to the evening the day after the start of the event) together with the 25 and 75 percentiles (shaded areas). The black lines are the median DMPS-data from Pallas and the red lines are the results from simulation liq-kin nucl where the nucleation rate was modeled with kinetic H_2SO_4 nucleation (Eq. 3).

Paper III



Constraining the concentrations and contribution of highly oxidized molecules to the growth of new particles over the Boreal forest

Pontus Roldin^{1,2}, Emilie Öström¹, Theo Kurtén³, Tinja Olenius⁴, Matti Rissanen², Pekka Rantala², Liqing Hao⁵, Markku Kulmala², Annele Virtanen⁵, Ilona Riipinen⁴, Mikael Ehn² and Michael Boy²

¹ Division of Nuclear Physics, Department of Physics, Lund University, P. O. Box 118, SE-221 00, Lund, Sweden, ²Department of Physics, University of Helsinki, P.O. Box 48, 00014 Helsinki, Finland, ³Department of Chemistry, University of Helsinki, P.O. Box 55, 00014 Helsinki, Finland, ⁴ Department of Environmental Science and Analytical Chemistry (ACES), Stockholm University, SE-106 91, Stockholm, Sweden, ⁵Department of Applied Physics, University of Eastern Finland, P.O. Box 1627, 70211 Kuopio, Finland

Biogenic volatile organic compounds (VOC) have a major contribution to the global secondary organic aerosol (SOA) mass. Over the boreal forest regions, monoterpenes are believed to be the biogenic VOC with largest impact on the SOA formation and the growth of new particles into the climatically important cloud condensation nuclei (CCN) size range. During recent years new novel measurement techniques have been developed which enables detection of VOC and their oxidation products in the atmosphere. Only very recently, it was discovered that highly oxidized molecules (HOM) can form rapidly and at high yields after one initial reaction between ozone and monoterpenes (1). Based on these findings we develop a unique HOM autooxidation mechanism for monoterpenes. We show that the mechanism can reproduce the observed HOM gas-phase composition and the observed SOA formation and elemental composition, both during α -pinene ozonolysis experiments and at the SMEAR II field station in Finland. Further, we show that the frequently observed new particle formation and growth events over the boreal forest region may be explained by the initial formation of sulphuric acid - ammonia molecule clusters, which subsequently grow by condensation of HOM and other organic vapours.

Atmospheric aerosols affect the radiation balance and climate on earth by scattering solar radiation and by acting as cloud condensation nuclei (CCN) and thereby altering the optical properties of the clouds. Volatile organic compounds (VOCs) emitted from forests are known to be a large source of secondary organic aerosol (SOA) with substantial contribution to the atmospheric aerosol composition in continental regions around the world (2). Over the vast boreal forest regions the VOCs that dominate the SOA production are monoterpenes, of which α -pinene is the most abundant. The impact of biogenic VOCs on the climate is still very uncertain because of incomplete process understanding of the VOC emission rates, how they are oxidized and how the formed oxidation products contribute to the SOA formation, in particularly the growth of newly formed particles (about one nanometre in diameter) to the size of CCN (about one hundred nanometres in diameter) (3-6). In order for a vapour to contribute to the initial growth of a new particle in the atmosphere it need to be an extremely low-volatility organic compound (ELVOC) or be very reactive in the condensed phase (7, 8).

Based on experimental (1, 9-16) and theoretical calculations (1, 11, 17-18) it has been shown that a process called autooxidation can lead to very rapid (seconds to minute time scale) formation of HOM after a first initial reaction between a VOC and an oxidant. HOM are preferentially formed from ozonolysis of monoterpenes with endocyclic double bonds (e.g. α -pinene and limonene) and to a lower extent by monoterpenes oxidized by the hydroxyl radical (OH) (1, 9). There is also experimental evidence that NO suppresses the formation of HOM from ozonolysis of α -pinene, especially the dimers (1).

In this work we will define HOM as organic molecules with at least 7 oxygen atoms formed from autooxidation of VOC. With this definition, a molecule formed from autooxidation with the molecular formula $C_{20}H_{30}O_{10}$ will be counted as a HOM species although its O:C is only 0.5. Up to recently HOM formed from monoterpene have been assumed to be ELVOC, inferring vapour pressures below $\sim 10^{-9}$ Pa ($\sim 2.5 \times 10^5$ molecules cm^{-3}) (19). If HOM are ELVOC they may be involved in initial molecule cluster formation that lead to new particles in the atmosphere. However, quantum chemical calculations show that their cluster-forming ability is much lower than expected (20), indicating a surprisingly high volatility. In our recent work (8), we compared the HOM pure liquid vapour pressures (p_0) derived from two different functional group contribution methods, SIMPOL (21) and EVAPORATION (22), with the quantum chemical calculations using the conductor-like screening model for real solvents (COSMO-RS) (23, 24). Both functional group contribution methods indicate that most HOM with more than 7 oxygen molecules indeed are Low Volatility Organic Compounds (LVOC) at room temperature, but the vapour pressures are too high to quantify them as ELVOC. COSMO-RS gave even higher vapour pressures, which can be attributed to intra-molecular hydrogen bonds. All calculations support that HOM dimers with 10 or more oxygen atoms most likely are true ELVOC, and thus could potentially be involved in the initial new particle formation (NPF). However, measurements from the SMEAR II station in Finland

(61.85° N, 24.28° E) show substantially lower HOM dimer concentrations during the day (when NPF is observed) than during the night (25).

Although many HOM are not true ELVOC most of them are still LVOC and will be based on traditional Raoult's law equilibrium partitioning theory at least partly dissolve in the organic particle phase. In common for most HOM formed via autooxidation is that they contain several hydroperoxide functional groups, which most likely make them very reactive once in the particle phase (8). Peroxyhemiacetal dimer formation between organic compounds containing aldehydes and hydroperoxide functional groups may proceed very fast and contribute to a large and rapid increase of the formed SOA mass during photooxidation experiments (26, 27). Thus, because of their very reactive nature, HOM, although not truly ELVOC, may still be effectively non-volatile and partition nearly irreversibly to the particle phase. This may also explain why SOA particles at low RH are highly viscous (28) and can have very long evaporation time scales (hour to days) (29).

In this work we develop a unique peroxy radical autooxidation mechanism (PRAM) for production of HOM from ozonolysis of monoterpenes with endocyclic double bonds (*SI Appendix*). We couple the mechanism to the Master Chemical Mechanism version 3.3.1 (MCMv3.3.1) (30-35) using the Kinetic PreProcessor (KPP) (36). The full gas-phase kinetic mechanism MCMv3.3.1 + PRAM is implemented into the Aerosol Dynamics gas- and particle phase chemistry model for laboratory CHAMber studies (ADCHAM) (*SI Appendix*) (37). ADCHAM is then used to simulate the α -pinene ozonolysis smog chamber experiments by Ehn et al. (1). After this we implement the identical gas-phase chemistry and aerosol dynamics schemes from ADCHAM into the chemistry transport model ADCHEM (38,39) (*SI Appendix*). Finally we used ADCHEM to simulate the HOM gas-phase concentrations and the contribution of HOM to the growth of new particles over the Boreal forest region. For these simulations the Atmospheric Cluster Dynamics Code (ACDC) (40) which explicitly simulates the growth, evaporation and coagulation losses of ammonia-sulphuric acid clusters were implemented into ADCHEM.

Results and discussion

Figure 1 shows model and measurement results from no NO_x addition α -pinene ozonolysis experiments in the Jülich Plant Atmosphere Chamber (JPAC) (1). In Fig. 1a we compare the modelled and measured autooxidation products mass spectrum at an atmospheric relevant α -pinene + O_3 reaction rate of $0.13 \text{ ppt}_v \text{ s}^{-1}$, e.g. corresponding to an O_3 concentration of 60 ppb_v at an α -pinene concentration of 1 ppb_v . Because PRAM represents the complete monomer and dimer HOM mass spectrum with only 74 species, the individual mass peaks in the modelled and observed mass spectra are not directly comparable, and this is the reason why single mass peaks in the modelled spectrum, especially for the HOM dimers, is substantially higher than the observations. The HOM mechanism was calibrated in order to give similar total HOM (Fig 1b), non-radical HOM monomers, RO_2 and dimer concentrations (Fig 1c), as the observations, for a wide range of α -pinene + O_3 reaction rates. We also calibrated PRAM in order to be able to represent how the observed HOM concentration changes with the NO concentration in JPAC. Both PRAM and the observations give a $\sim 40\%$ reduction in the HOM(g) concentration when the NO concentrations increase from 0 to 5 ppb_v , partly attributed to the loss of HOM dimers (Figure S1 a, b, c). NO reacts with the RO_2 autooxidation products, lowers their concentrations and can terminate the autooxidation chain before or after the RO_2 have become highly oxidized. According to the observations and PRAM, approximately one third of the HOM monomers formed from the RO_2 + NO reactions are organonitrates (Fig S1c). Up to 50 % of the α -pinene was oxidized by OH at NO concentrations $> 0.5 \text{ ppb}_v$, compared with $\sim 30\%$ at no NO conditions (Fig S2), which is an additional factor that causes the HOM(g) concentration to decrease when NO is present in JPAC.

Also at no NO_x conditions the relative fraction of the HOM that are dimers decreases in PRAM, and also according to the observations, if the α -pinene + O_3 reaction rate drops below $\sim 0.2 \text{ ppt}_v \text{ s}^{-1}$, which is the upper limit of the atmospheric relevant α -pinene + O_3 reaction rates (Fig S3). According to PRAM the reason for this is that the lifetime of the $\text{RO}_2(\text{g})$, and thus also the relative HOM fraction that is RO_2 , increases when the absolute RO_2 concentration decreases in the chamber. A possible additional factor could be that a fraction of the RO_2 reacts with HO_2 instead of other RO_2 . However, according to PRAM this fraction is insignificant during the experiments in JPAC even at very low α -pinene + O_3 reaction rates (Fig S3).

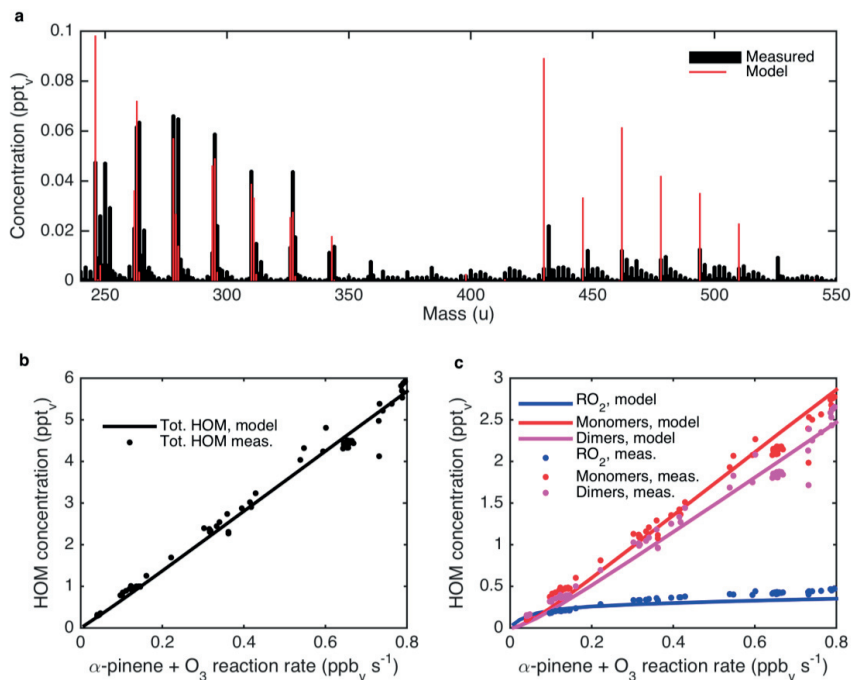


Figure 1. Modelled and measured HOM concentrations during an α -pinene ozonolysis experiment in the Jülich Plant Atmosphere Chamber, for no NO_x experiments. The O₃ concentration was kept approximately constant at around 85 ppb_v and the α -pinene concentration was varied (1). Figure **a** compares the modelled and measured HOM(g) mass spectrum at an atmospheric relevant α -pinene + O₃ reaction rate of 0.13 ppt_v s⁻¹, figure **b** shows how the modelled and measured total HOM(g) concentration increases when the α -pinene + O₃ reaction rate increases and figure **c** shows how the modelled and measured HOM peroxy radicals (RO₂), HOM non-radical monomers and dimers changes with increasing α -pinene + O₃ reaction rate.

Figure 2 shows results from an α -pinene ozonolysis, Ammonium Sulfate (AS) seed particle experiments in JPAC (1). According to the ADCHAM model simulations (*SI Appendix*), almost 60 % of the formed SOA mass is formed from HOM species (Fig 2a). The modelled elemental composition of the SOA (Fig 2c) is in perfect agreement with the AMS observations from Ehn et al. (1) and has an O:C of 0.62 and H:C 1.54. The SOA formed from the HOM species have a slightly higher O:C than the total SOA of 0.65. The reason for the relatively low O:C of the modelled HOM SOA is that a large fraction of the HOM SOA mass is formed from HOM dimers, which has a O:C \leq 0.6 (i.e. C₂₀H₃₀O₁₀, C₂₀H₃₀O₁₁ and C₂₀H₃₀O₁₂). In figure 2b we compare the modelled and measured HOM(g) dimer mole fraction evolution during the seed particle addition. The observed substantial decrease in the HOM(g) dimer mole fraction when the seed particle are introduced are attributed to the fact that while the HOM dimers are true ELVOC and condense irreversibly to the seed particles, all HOM monomers are not (8). The best agreement between the observed and modelled HOM(g) dimer and monomer concentration change upon seed particle addition is found if the HOM pure liquid saturation vapour pressures (p_0) are three times higher than the values predicted by the functional group contribution method SIMPOL (21), but substantially lower than the values predicted by the COSMO-RS quantum chemical calculations (Fig 2b, d), consistent with the conclusions from Kurtén et al. (8).

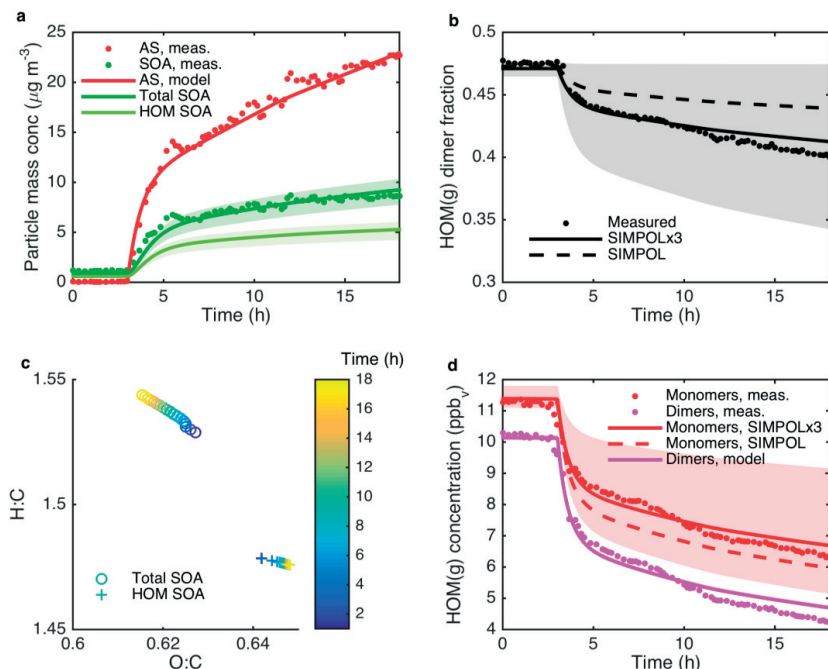


Figure 2. Modelled and measured **a** SOA formation during an Ammonium Sulphate (AS) seed particle experiments in the JPAC chamber (1), **b** fraction of HOM(g) molecular number concentration which is dimers, **c** elemental composition of the modelled SOA, and **d** HOM monomers and dimers concentrations. The shaded areas in figure **a**, **b** and **d** represent the range of model results achieved when ADCHEM uses the upper and lower estimate of the HOM p_0 , namely that all HOM either are completely non-volatile or that their pure liquid saturation vapour pressures are estimated based on COSMO-RS quantum chemical calculations. The solid lines represents the best-fit model results which was achieved by multiplying the HOM p_0 estimated by SIMPOL with a factor of 3 (SIMPOLx3), while the dashed lines represents the model results achieved when the HOM p_0 were estimated with SIMPOL.

Figure 3 shows the modelled and measured concentrations of (a) the total HOM(g), (b) HOM(g) monomers without nitrate functional groups, (c) HOM(g) monomers with nitrate functional groups and (d) HOM(g) dimers, at the SMEAR II field station 15th of May to 25th of May, 2013. Analogous to the ADCHEM smog chamber simulations, ADCHEM were operated using HOM p_0 estimated based on SIMPOL, SIMPOL $p_0 \times 3$ or assuming non-volatile HOM. The grey shaded areas in Fig 3 shows the difference between the concentrations from the simulation with non-volatile HOM (lowest values) and the simulation with SIMPOL $p_0 \times 3$ (highest values).

Table 1, summarizes the mean and coefficient of determination (R^2) between the model results from the different model runs and the measured HOM time series. The model generally gives higher HOM concentrations than the measurements, especially for the dimers concentration which is ~ 3 times higher than observed. When all HOM are assumed to be non-volatile in the model the average HOM monomer concentrations, both for the monomers with and without NO_3 groups have almost identical values as the observations. However, the R^2 values become substantially lower than if the HOM monomer p_0 are estimated with SIMPOL or SIMPOL $p_0 \times 3$, which indicates that the average concentrations improves but for the wrong reason.

It should be noted that although the observed temporal trends can be trusted, the measured absolute HOM(g) concentrations cannot be calibrated which known standards, and therefore the measured absolute HOM concentrations has an uncertainty of at least a factor of two (1). Thus, the modelled total HOM(g) concentration and HOM monomer concentrations are within the estimated uncertainty range of the observations for all simulations presented in Table 1. Additionally, the modelled HOM(g) concentrations are uncertain not only because of uncertainties in the PRAM mechanism and the HOM p_0 , but also due to uncertainties in the modelled vertical mixing and the observational data that ADCHEM used as input, especially the monoterpene and NO_x concentrations.

Table 1. Modelled and measured average and coefficient of determination (R^2) between the modelled and measured HOM concentrations 15th - 25th of May, 2013 at SMEAR II. The model results are given for the simulations with HOM p_0 from SIMPOL, SIMPOL $p_0 \times 3$ and assuming non-volatile HOM (NV-HOM).

Species	Mean, SIMPOL	R^2 , SIMPOL	Mean, SIMPOLx3	R^2 , SIMPOLx3	Mean, NV-HOM	R^2 , NV-HOM	Mean, meas.
Tot. HOM	0.90	0.40	1.12	0.41	0.77	0.36	0.64
Monomers	0.49	0.37	0.65	0.36	0.39	0.32	0.41
Dimers	0.26	0.56	0.26	0.56	0.26	0.56	0.09
NO ₃ -monomers	0.08	0.47	0.14	0.52	0.06	0.22	0.06

Both the model results and the observations consistently show a strong diurnal cycle of the HOM dimers and HOM-NO₃ monomers, with peaks in the HOM dimer concentration around 9 pm and in the HOM-NO₃ concentration in the morning around 10 am, which explains their relatively high R^2 in Table 1 (Fig S4 c, d). However, the average nighttime dimer concentration is almost four times higher in the model compared to the observations. The concentrations of the non-NO₃ HOM monomers show a weaker diurnal trend, with a maximum in the evening around 9 pm (Fig S4b). According to the model simulations in average 18 % of the formed HOM dimers contains NO₃ groups that originate from NO₃ radical oxidation of monoterpenes, consistent with recent observations at SMEAR II (25).

The modelled vertical HOM(g) concentration profiles resembles the monoterpene concentration profile which has a strong gradient already inside the forest canopy at SMEAR II (Fig S5). Both the monoterpene concentrations and HOM dimer concentration decreases with on average 50 % within the canopy, while the HOM monomer concentration decreases with 30 %. The HOM-NO₃ monomers have a much weaker concentration gradient with on average a 10 % reduction within the canopy. The reason for this is that they according to SIMPOL generally are more volatile than the other HOM monomers, which in turn are more volatile than the HOM dimers. At 500 m the HOM dimers, monomers and HOM-NO₃ monomers average concentrations are 5, 20 and 60 % of the modelled concentrations at 1.5 m altitude, respectively.

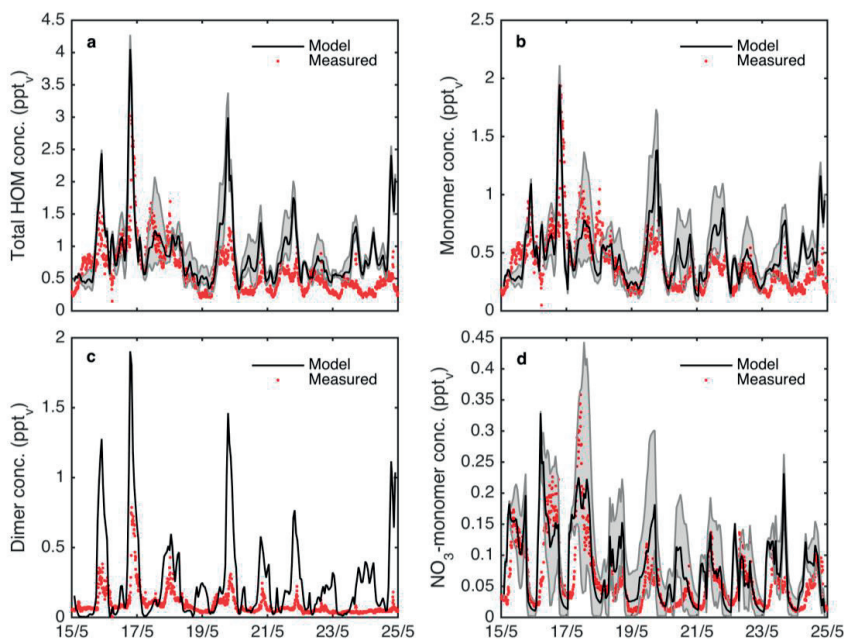


Figure 3. Modelled and measured average diurnal trends of the concentration of: (a) total HOM(g), (b) HOM(g) monomers, (c) HOM(g) dimers and (d) HOM organonitrate monomers, at the SMEAR II field station 15th to 25th of May, 2013.

Figure 4 compares the modelled SOA elemental composition and SOA species composition from JPAC α -pinene ozonolysis experiments at no NO conditions and from SMEAR II. According to the model simulations the formed SOA is more oxidized in the atmosphere and contains a larger fraction of SOA material originating from HOM species. The main reasons for this are: (i) the generally lower SOA mass loading in the atmosphere

prevents the semi-volatile less oxidized organic molecules from partitioning into the condensed phase, (ii) lower RO_2 concentrations in the atmosphere allows the peroxy autoxidation chain to proceed further before it is terminated by $\text{RO}_2 + \text{RO}_2$ reactions, (iii) NO in the atmosphere lead to $\text{RO}_2 + \text{NO}$ reactions, formation of highly oxidized HOM NO_3 -monomers and suppression of HOM dimer formation, and (iv) NO_3 radical oxidation of monoterpenes during nighttime leads to more highly oxidized dimers containing nitrate groups.

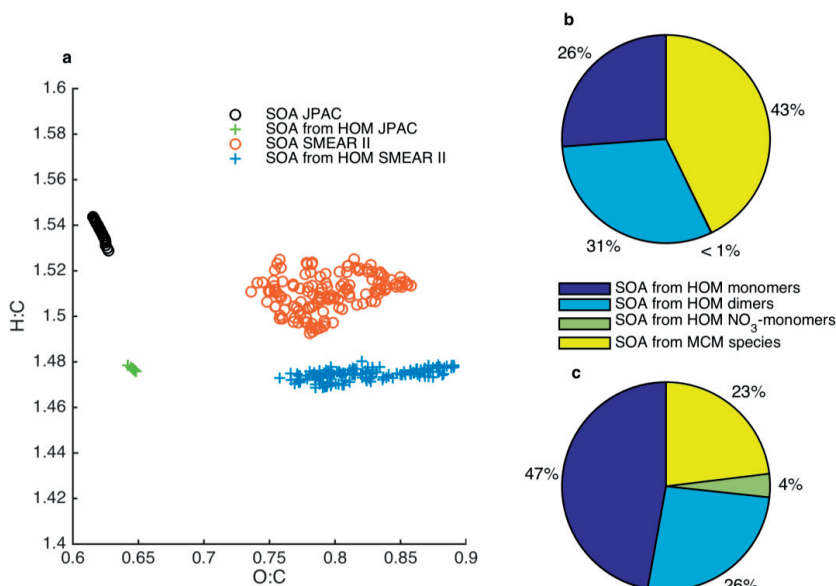


Figure 4. Modelled (a) SOA elemental compositions in JPAC and at SMEAR II during the PEGASOS campaign, (b) modelled SOA composition in JPAC and (c) modelled average SOA composition at SMEAR II during the PEGASOS campaign.

Figure 5 shows the modelled (Fig 5a) and observed (Fig 5b) particle number size distributions at SMEAR II during spring 2014 (15th of April to 6th of May). When we compare the modelled and measured particle number size distributions it is clear that ADCHEM for most days correctly captures if there was or was not a clear new particle formation event day at SMEAR II; the exceptions are April the 25th, 26th and 30th and May the 1st and 4th when ADCHEM predicts that new particle formation events occur at SMEAR II, but the measurements do not. One reason for this could be if ADCHEM underestimates the condensation sink during the non-event days, but when comparing the H_2SO_4 condensation sink (CS) derived from the modelled and measured particle number size distributions, it is clear that ADCHEM generally captures the absolute values and the temporal variability of the CS at SMEAR II (Fig. S6). Other possible reasons why ADCHEM overestimates the number of NPF events may be overestimated NH_3 and H_2SO_4 concentrations, which then lead to too strong new particle formation in ACDC. ADCHEM also has a tendency to overestimate the number of formed new particles during the new particle formation event days, but underestimates the particle growth. ADCHEM cannot either predict the new particle formation events where the apparent particle growth can be followed over several days at SMEAR II. Uncertainties in the air mass origin more than 24 hours upwind of the station, is one possible source to this model deficiency. The clearest NPF event both in the model and observations occurs on the 23rd of April. If we zoom in on the particle number size distribution evolution of particles between 1 and 50 nm in diameter on this specific day (Fig. S7) it is clear that the modelled apparent particle growth at SMEAR II gradually is increasing from about 1 nm h^{-1} for particles smaller than 3 nm in diameter to over 2 nm h^{-1} for particles larger than 15 nm. In the observations the apparent growth at SMEAR II is almost constant and higher ($\sim 3.5 \text{ nm h}^{-1}$). Also if we instead follow one single air mass over time, the modelled “true growth rate” of the newly formed particles is also increasing with the size of the particles (Fig S8), which is an indication that the modelled initial growth is limited by the relatively low concentrations of extremely low-volatility organic compounds (e.g. HOM dimers).

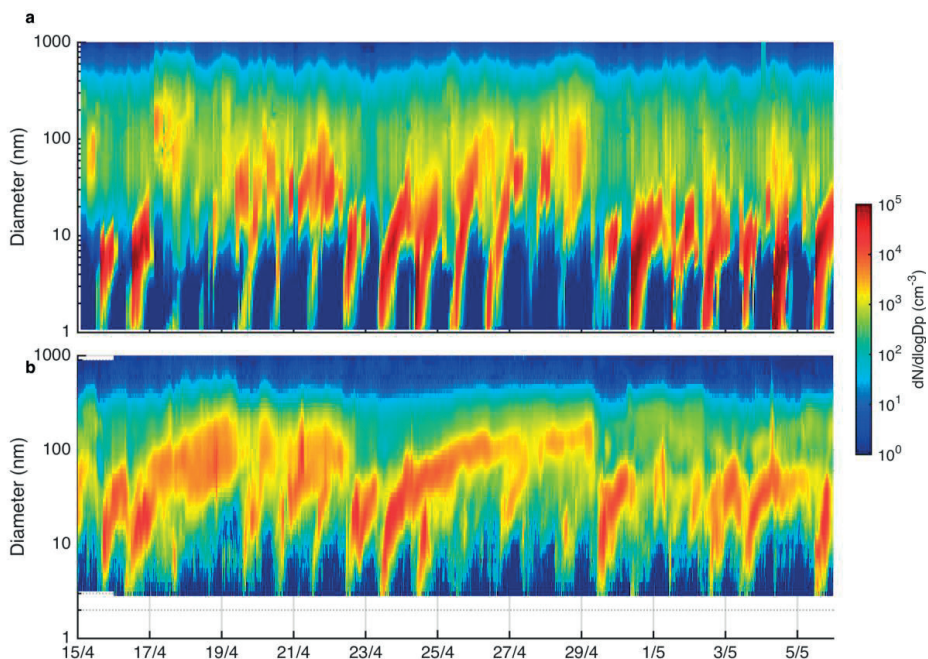


Figure 5. Modelled (a) and measured (b) particle number size distributions at SMEAR II during spring 2014. The HOM p_0 was estimated with the SIMPOL functional group contribution method.

In this work we have developed and constrained a novel gas-phase chemistry mechanism for the formation of highly oxidized molecules (HOM) from autoxidation of monoterpenes. Both our simulations of smog chamber SOA formation experiments and atmospheric simulations of HOM(g) concentrations at the SMEAR II station indicate that not all HOM formed from monoterpenes are extremely-low volatility organic compounds. The best agreement between the observations in the smog chamber is achieved if the HOM pure liquid saturation vapour pressures are equal or slightly larger than the values predicted by the functional group contribution method SIMPOL. Despite that we for the first time implement a new novel HOM mechanism for simulations of the new particle formation and growth at the SMEAR II station, the model underestimates the particle growth rates, but overestimate the new particle formation rates. This, indicates that although HOM most likely are very important for the initial growth of new particles in the atmosphere, other unaccounted compounds or processes (e.g. heterogeneous reactions) are also needed in order to capture the growth of the new particles into the CCN size range.

Method

We have further developed the peroxy radical autoxidation mechanism (PRAM) for ozonolysis of monoterpenes based on the work by Ehn *et al.* (1) and coupled it to the Master Chemical Mechanism version 3.3.1 (MCMv3.3.1) (30-35). PRAM comprises 718 reactions and 74 species (*SI Appendix*).

The complete gas-phase chemistry mechanism (MCMv3.3.1 + PRAM) (3560 species and 10645 reactions) was implemented into the Aerosol Dynamics, gas- and particle-phase chemistry kinetic multilayer model for laboratory CHAMber studies (ADCHAM) (37) and the process-based chemistry transport model ADCHEM (38-39). The ADCHAM model was used to constrain the volatility of the formed HOM species, their contribution to the observed SOA formation and the elemental composition of the SOA during an α -pinene ozonolysis Ammonium Sulfate (AS) seed particle experiments in the Jülich Plant Atmosphere Chamber (JPAC) (1). ADCHAM and ADCHEM considered condensation of all HOM species and other organic molecules from MCMv3.3.1 with pure liquid saturation vapour pressures (p_0) $< 10^{-2}$ Pa. The HOM p_0 were either estimated with the functional group contribution method SIMPOL (21) or based on detailed quantum-chemistry continuum solvent model COSMO-RS (COnductor-like Screening MOdel for Real Solvents) calculations (8). p_0 estimated with COSMO-RS are generally substantially higher than what is predicted by SIMPOL. Because the pure liquid saturation vapour pressures from COSMO-RS has not been calculated for all HOM species considered by the HOM mechanism we derived correction factors based on the difference between the SIMPOL and COSMO-RS

p_0 . For the HOM monomers the correction factor is $10^{2.8 \times \text{O:C} - 0.1}$, where O:C is the oxygen-to-carbon ratio. For the HOM dimers we estimated a fixed correction factor of 10^4 (39).

ADCHEM was implemented for simulations of aerosol particle and trace gas concentrations during two measurement campaigns at the SMEAR II field station in Finland (61.85° N, 24.28° E). During the first campaign, the 2013 PEGASOS spring campaign, ADCHEM was operated as a stationary column model at SMEAR II, with the purpose to evaluate the PRAM mechanism. ADCHEM was continuously reading in the observed concentrations of NO₂, O₃, CO and total monoterpene at eight different altitudes between 4.2 to 125 m above ground level (a.g.l.), SO₂ at 16.8 m and particle number size distributions for particles between 2.8 and 1000 nm in diameter. The particle number size distribution was assumed to be constant in the whole model domain (0 - 2500 m a.g.l.). The emissions of α -pinene, carene, β -pinene and limonene were modelled with a 1D version of the MEGAN 2.1 (Model of Emissions of Gases and Aerosols from Nature) (41,42), where the individual monoterpene emissions, were based on the measured average emissions from 40 Scots pine trees around SMEAR II (43). The modelled total monoterpene concentrations within the lowermost 125 m, was then scaled for each model time step in order to match the observed total monoterpene concentrations at SMEAR II. All other trace gas concentrations as well as the particle chemical composition and hygroscopic growth were calculated in order to provide the most realistic condensation losses of HOM and other condensable compounds.

During PEGASOS HOM(g) was measured at ~2 m altitude using a nitrate-ion-based chemical ionization atmospheric pressure-interface time-of-flight mass spectrometer (CI-API-TOF). Unfortunately, only very few new particle formation (NPF) events could be observed at SMEAR II during the 2013 PEGASOS campaign. Thus, in order to be able to evaluate the HOM contribution to the growth of new ~1 nm in diameter particles into the CCN size range we also setup ADCHEM for a second campaign from spring 2014. During this campaign, NPF events with consecutive growth could be observed at more than 50 % of the days (Fig 5b). Unfortunately, the CI-API-TOF measurements at SMEAR II were not functioning during spring 2014.

For the spring 2014 campaign ADCHEM was operated as a Lagrangian vertical column model following in total 168 individual air mass trajectories starting 4 days backward in time before they reached SMEAR II, with 3 hour in-between the arrival of each trajectory, covering in total 21 consecutive days. Anthropogenic emissions of NO_x, SO₂, CO, NH₃, VOC with a resolution of 0.1°x0.1° were retrieved from EMEP (European Monitoring and Evaluation Programme) database (EMEP/CEIP 2014, present state of emissions as used in EMEP models (44) and the monoterpene and isoprene emissions were modelled with MEGAN. Size resolved anthropogenic primary particle emissions were derived from new a global 0.5°x0.5° emission inventory (45). The new particle formation was modelled using the Atmospheric Cluster Dynamics Code (ACDC) (40), which explicitly simulates the growth, evaporation and coagulation losses of ammonia-sulphuric acid clusters up to a size of 1.07 nm in diameter. After this the consecutive growth is modelled with the condensation model in ADCHEM. Because of the Lagrangian approach, ADCHEM was run without any input constraints from observations at the SMEAR II station. In *SI Appendix* we provide more detailed descriptions of the ADCHEM and ADCHEM model setup.

References

1. Ehn, M., Thornton, J. A., Kleist, E., Sipilä, M., Junninen, H., Pullinen, I., Springer, M., Rubach, F., Tillmann, R., Lee, B., Lopez-Hilfiker, F., Andres, S., Acir, I.-H., Rissanen, M., Jokinen, T., Schobesberger, S., Kangasluoma, J., Kontkanen, J., Nieminen, T., Kurtén, T., Nielsen, L. B., Jørgensen, S., Kjaergaard, H. G., Canagaratna, M., Dal Maso, M., Berndt, T., Petäjä, T., Wahner, A., Kerminen, V.-M., Kulmala, M., Worsnop, D. R., Wildt, J., and Mentel, T. F.: A large source of low-volatility secondary organic aerosol, *Nature*, 506, 476–479, <https://doi.org/10.1038/nature13032>, 2014.
2. Jimenez, J. L., Canagaratna, M. R., Donahue, N. M., Prevot, A. S. H., Zhang, Q., Kroll, J. H., DeCarlo, P. F., Allan, J. D., Coe, H., Ng, N. L., Aiken, A. C., Docherty, K. S., Ulbrich, I. M., Grieshop, A. P., Robinson, A. L., Duplissy, J., Smith, J. D., Wilson, K. R., Lanz, V. A., Hueglin, C., Sun, Y. L., Tian, J., Laaksonen, A., Raatikainen, T., Rautiainen, J., Vaattovaara, P., Ehn, M., Kulmala, M., Tomlinson, J. M., Collins, D. R., Cubison, M. J., Dunlea, E. J., Huffman, J. A., Onasch, T. B., Alfarra, M. R., Williams, P. I., Bower, K., Kondo, Y., Schneider, J., Drewnick, F., Borrmann, S., Weimer, S., Demerjian, K., Salcedo, D., Cottrell, L., Griffin, R., Takami, A., Miyoshi, T., Hatakeyama, S., Shimono, A., Sun, J. Y., Zhang, Y. M., Dzepina, K., Kimmel, J. R., Sueper, D., Jayne, J. T., Herndon, S. C., Trimborn, A. M., Williams, L. R., Wood, E. C., Middlebrook, A. M., Kolb, C. E., Baltensperger, U., and Worsnop, D. R.: Evolution of Organic Aerosols in the Atmosphere, *Science*, 326, 1525–1529, 2009.
3. Shrivastava, M., Cappa, C. D., Fan, J., Goldstein, A. H., Guenther, A. B., Jimenez, J. L., Kuang, C., Laskin, A., Martin, S. T., Ng, N. L., Petaja, T., Pierce, J. R., Rasch, P. J., Roldin, P., Seinfeld, J. H., Shilling, J., Smith, J. N., Thornton, J. A., Volkamer, R., Wang, J., Worsnop, D. R., Zaveri, R. A., Zelenyuk, A., Zhang Q: Recent advances in understanding secondary organic aerosol: Implications for global climate forcing, *Rev. Geophys.*, 55, 509–559, [doi:10.1002/2016RG000540](https://doi.org/10.1002/2016RG000540), 2017.

4. Makkonen, R., Asmi, A., Kerminen, V.-M., Boy, M., Arneth, A., Hari, P., and Kulmala, M.: Air pollution control and decreasing new particle formation lead to strong climate warming, *Atmos. Chem. Phys.*, 12, 1515–1524, <https://doi.org/10.5194/acp-12-1515-2012>, 2012.
5. Carslaw, K. S., Lee, L. A., Reddington, C. L., Pringle, K. J., Rap, A., Forster, P. M., Mann, G. W., Spracklen, D. V., Woodhouse, M. T., Regayre, L. A. and Pierce, J. R.: Large contribution of natural aerosols to uncertainty in indirect forcing, *Nature* 503(7474)67–71, 2013.
6. Boucher O, et al. Clouds and aerosols. *Climate Change 2013 The Physical Science Basis. Contribution of Working Group I to the Fifth Assessment Report of the Intergovernmental Panel on Climate Change*, eds Stocker TF, et al. (Cambridge Univ Press, Cambridge, UK), 2013.
7. Riipinen, I., Yli-Juuti, T., Pierce, J. R., Petäjä, T., Worsnop, D. R., Kulmala, M., and Donahue, N. M.: The contribution of organics to atmospheric nanoparticle growth, *Nat. Geosci.*, 5, 453–458, 2012.
8. Kurtén, T., Tiisanen, K., Roldin, P., Rissanen, M., Luy, J.-N., Boy, M., Ehn, M., and Donahue, N.: α -Pinene Autoxidation Products May Not Have Extremely Low Saturation Vapor Pressures Despite High O:C Ratios, *J. Phys. Chem. A*, 120, 2569–2582, <https://doi.org/10.1021/acs.jpca.6b02196>, 2016.
9. Jokinen, T., Berndt, T., Makkonen, R., Kerminen, V.-M., Junninen, H., Paasonen, P., Stratmann, F., Herrmann, H., Guenther, A. B., Worsnop, D. R., Kulmala, M., Ehn, M., and Sipilä, M.: Production of extremely low volatile organic compounds from biogenic emissions: Measured yields and atmospheric implications, *P. Natl. Acad. Sci. USA*, 112, 7123–7128, <https://doi.org/10.1073/pnas.1423977112>, 2015.
10. Crounse, J. D., Nielsen, L. B., Jørgensen, S., Kjaergaard, H. G., Wennberg, P. O. Autooxidation of Organic Compounds in the Atmosphere. *J. Phys. Chem. Lett.*, 4, 3513–3520, 2013.
11. Rissanen, M. P., Kurtén, T., Sipilä, M., Thornton, J. A., Kangasluoma, J., Sarnela, N., Junninen, H., Jørgensen, S., Schallhart, S., Kajos, M. K. et al. The Formation of Highly Oxidized Multifunctional Products in the Ozonolysis of Cyclohexene. *J. Am. Chem. Soc.*, 136, 15596–15606, 2014.
12. Mentel, T. F., Springer, M., Ehn, M., Kleist, E., Pullinen, I., Kurtén, T., Rissanen, M., Wahner, A., Wildt, J. Formation of Highly Oxidized Multifunctional Compounds Autoxidation of Peroxy Radicals Formed in the Ozonolysis of Alkenes – Deduced from Structure–Product Relationships. *Atmos. Chem. Phys.*, 15, 6745–6765, 2015.
13. Jokinen, T., Sipilä, M., Richters, S., Kerminen, V.-M., Paasonen, P., Stratmann, F., Worsnop, D., Kulmala, M., Ehn, M., Herrmann, H. et al. Rapid Autoxidation Forms Highly Oxidized RO₂ Radicals in the Atmosphere. *Angew. Chem., Int. Ed.*, 53, 14596–14600, 2014.
14. Rissanen, M., Kurtén, T., Sipilä, M., Thornton, J. A., Kausiala, O., Garmash, O., Kjaergaard, H. G., Petäjä, T., Worsnop, D. R., Ehn, M. et al. Effects of Chemical Complexity on the Autoxidation Mechanisms of Endocyclic Alkene Ozonolysis Products From Methylcyclohexenes toward Understanding α -Pinene. *J. Phys. Chem. A*, 119, 4633–4650, 2015.
15. Berndt, T., Richters, S., Kaethner, R., Voigtländer, J., Stratmann, F., Sipilä, M., Kulmala, M., Herrmann, H. Gas-Phase Ozonolysis Cycloalkenes Formation of Highly Oxidized RO₂ Radicals and Their Reactions with NO, NO₂, SO₂, and Other RO₂ Radicals. *J. Phys. Chem. A* 2015, 119, 10336–10348.
16. Mutzel, A., Poulain, L., Berndt, T., Iinuma, Y., Rodigast, M., Böge, O., Richters, S., Spindler, G., Sipilä, M., Jokinen, T. et al. Highly Oxidized Multifunctional Organic Compounds Observed in Tropospheric Particles A Field and Laboratory Study. *Environ. Sci. Technol.*, 49, 7754–7761, 2015.
17. Peeters, J., Müller, J.-F. HO_x Radical Regeneration in Isoprene Oxidation via Peroxy Radical Isomerisations. II Experimental Evidence and Global Impact. *Phys. Chem. Chem. Phys.*, 12, 14227–14235, 2010.
18. Vereecken, L., Müller, J.-F., Peeters, J. Low-Volatility Poly-Oxygenates in the OH-Initiated Atmospheric Oxidation of α -pinene Impact of Non-Traditional Peroxyl Radical Chemistry. *Phys. Chem. Chem. Phys.*, 9, 5241–5248, 2007.
19. Donahue, N. M., Ortega, I. K., Chuang, W., Riipinen, I., Riccobono, F., Schobesberger, S., Dommen, J., Baltensperger, U., Kulmala, M., Worsnop, D. R., and Vehkamäki, H.: How do organic vapors contribute to new-particle formation? *Faraday Discuss.*, 165, 91–104, 2013.
20. Elm, J.; Myllys, N.; Hyttinen, N.; Kurtén, T. Computational Study of the Clustering of a Cyclohexene Autoxidation Product C₆H₈O₇ with Itself and Sulfuric Acid. *J. Phys. Chem. A*, 119, 8414–8421, 2015.
21. Pankow, J. F. and Asher, W. E.: SIMPOL.1: a simple group contribution method for predicting vapor pressures and enthalpies of vaporization of multifunctional organic compounds, *Atmos. Chem. Phys.*, 8, 2773–2796, <https://doi.org/10.5194/acp-8-2773-2008>, 2008.
22. Compornolle, S.; Ceulemans, K.; Müller, J.-F. EVAPORATION: a new vapour pressure estimation method for organic molecules including non-additivity and intramolecular interactions. *Atmos. Chem. Phys.* 2011, 11, 9431–9450.
23. Eckert, F. and Klamt, A.: Fast Solvent Screening via Quantum Chemistry: COSMO-RS Approach, *AIChE J.*, 48, 369–385, 2002.
24. Eckert, F. and Klamt, A.: COSMOTerm, Version C3.0, Release 15.01; COSMologic GmbH & Co. KG,

- Leverkusen, Germany, 2014.
25. Yan, C., Nie, W., Äijälä, M., Rissanen, M. P., Canagaratna, M. R., Massoli, P., Junninen, H., Jokinen, T., Sarnela, N., Häme, S. A. K., Schobesberger, S., Canonaco, F., Yao, L., Prévôt, A. S. H., Petäjä, T., Kulmala, M., Sipilä, M., Worsnop, D. R., and Ehn, M.: Source characterization of highly oxidized multifunctional compounds in a boreal forest environment using positive matrix factorization, *Atmos. Chem. Phys.*, 16, 12715–12731, <https://doi.org/10.5194/acp-16-12715-2016>, 2016.
 26. Shiraiwa, M., Yee, L. D., Schilling, K. A., Loza, C. L., Craven, J. S., Zuend, A., Ziemann, P. J., and Seinfeld, J. H.: Size distribution dynamics reveal particle-phase chemistry in organic aerosol formation, *P. Natl. Acad. Sci.*, 110, 11746–11750, 2013.
 27. Roldin, P., Liao, L., Mogensen, D., Dal Maso, M., Rusanen, A., Kerminen, V.-M., Mentel, T. F., Wildt, J., Kleist, E., Kiendler-Scharr, A., Tillmann, R., Ehn, M., Kulmala, M., and Boy, M.: Modelling the contribution of biogenic volatile organic compounds to new particle formation in the Jülich plant atmosphere chamber, *Atmos. Chem. Phys.*, 15, 10777–10798, <https://doi.org/10.5194/acp-15-10777-2015>, 2015.
 28. Virtanen, A., Joutsensaari, J., Koop, T., Yli-Pirilä, P., Leskinen, J., Mäkelä, J. M., Holopainen, J. K., Pöschl, U., Kulmala, M., Worsnop, D. R. and Laaksonen, A.: An amorphous solid state of biogenic secondary organic aerosol particles, *Nature*, 467, 824–827, 2010.
 29. Vaden, T. D., Imreb, D., Beránka, J., Shrivastava, M., and Zelenyuka, A.: Evaporation kinetics and phase of laboratory and ambient secondary organic aerosol, *P. Natl. Acad. Sci.*, 108, 2190–2195, 2011.
 30. Jenkin, M. E., Saunders, S. M., and Pilling, M. J.: The tropospheric degradation of volatile organic compounds: a protocol for mechanism development, *Atmos. Environ.*, 31, 81–104, [https://doi.org/10.1016/S1352-2310\(96\)00105-7](https://doi.org/10.1016/S1352-2310(96)00105-7), 1997.
 31. Saunders, S. M., Jenkin, M. E., Derwent, R. G., and Pilling, M. J.: Protocol for the development of the Master Chemical Mechanism, MCM v3 (Part A): tropospheric degradation of non-aromatic volatile organic compounds, *Atmos. Chem. Phys.*, 3, 161–180, <https://doi.org/10.5194/acp-3-161-2003>, 2003.
 32. Jenkin, M. E., Saunders, S. M., Wagner, V., and Pilling, M. J.: Protocol for the development of the Master Chemical Mechanism, MCM v3 (Part B): tropospheric degradation of aromatic volatile organic compounds, *Atmos. Chem. Phys.*, 3, 181–193, [doi:10.5194/acp-3-181-2003](https://doi.org/10.5194/acp-3-181-2003), 2003.
 33. Bloss, C., Wagner, V., Jenkin, M. E., Volkamer, R., Bloss, W. J., Lee, J. D., Heard, D. E., Wirtz, K., Martin-Reviejo, M., Rea, G., Wenger, J. C., and Pilling, M. J.: Development of a detailed chemical mechanism (MCMv3.1) for the atmospheric oxidation of aromatic hydrocarbons, *Atmos. Chem. Phys.*, 5, 641–664, [doi:10.5194/acp-5-641-2005](https://doi.org/10.5194/acp-5-641-2005), 2005.
 34. Jenkin, M. E., Wyche, K. P., Evans, C. J., Carr, T., Monks, P. S., Alfara, M. R., Barley, M. H., McFiggans, G. B., Young, J. C., and Rickard, A. R.: Development and chamber evaluation of the MCM v3.2 degradation scheme for β -caryophyllene, *Atmos. Chem. Phys.*, 12, 5275–5308, <https://doi.org/10.5194/acp-12-5275-2012>, 2012.
 35. Jenkin, M. E., Young, J. C., and Rickard, A. R.: The MCM v3.3.1 degradation scheme for isoprene, *Atmos. Chem. Phys.*, 15, 11433–11459, <https://doi.org/10.5194/acp-15-11433-2015>, 2015.
 36. Damian, V., Sandu, A., Damian, M., Potra, F., and Carmichael, G. R.: The kinetic preprocessor KPP-a software environment for solving chemical kinetics, *Comput. Chem. Eng.*, 26, 1567–1579, [https://doi.org/10.1016/S0098-1354\(02\)00128-X](https://doi.org/10.1016/S0098-1354(02)00128-X), 2002.
 37. Roldin, P., Eriksson, A. C., Nordin, E. Z., Hermansson, E., Mogensen, D., Rusanen, A., Boy, M., Swietlicki, E., Svenningsson, B., Zelenyuk, A. and Pagels, J.: Modelling non-equilibrium secondary organic aerosol formation and evaporation with the aerosol dynamics, gas- and particle-phase chemistry kinetic multilayer model ADCHAM, *Atmos. Chem. Phys.*, 14, 7953–7993, <https://doi.org/10.5194/acp-14-7953-2014>, 2014.
 38. Roldin, P., Swietlicki, E., Schurgers, G., Arneth, A., Lehtinen, K. E. J., Boy, M., and Kulmala, M.: Development and evaluation of the aerosol dynamics and gas phase chemistry model ADCHEM, *Atmos. Chem. Phys.*, 11, 5867–5896, <https://doi.org/10.5194/acp-11-5867-2011>, 2011.
 39. Öström, E., Roldin, P., Schurgers, G., Mishurov, M., Putian, Z., Kivekäs, N., Lihavainen, H., Ehn, M., Rissanen, M. P., Kurtén, T., Boy, M., and Swietlicki, E.: Model data for simulation of secondary organic aerosol formation over the boreal forest, link to NetCDF files in zip archive, PANGAEA, <https://doi.org/10.1594/PANGAEA.877695>, 2017.
 40. Olenius, T., Kupiainen-Määttä, O., Ortega, I. K., Kurtén, T. and Vehkamäki, H.: Free energy barrier in the growth of sulfuric acid–ammonia and sulfuric acid–dimethylamine clusters, *J. Chem. Phys.*, 139(8), 84312, [doi:10.1063/1.4819024](https://doi.org/10.1063/1.4819024), 2013.
 41. Guenther, A. B., Jiang, X., Heald, C. L., Sakulyanontvittaya, T., Duhl, T., Emmons, L. K., and Wang, X.: The Model of Emissions of Gases and Aerosols from Nature version 2.1 (MEGAN2.1): an extended and updated framework for modeling biogenic emissions, *Geosci. Model Dev.*, 5, 1471–1492, [doi:10.5194/gmd-5-1471-2012](https://doi.org/10.5194/gmd-5-1471-2012), 2012.

42. Smolander, S., He, Q., Mogensen, D., Zhou, L., Bäck, J., Ruuskanen, T., Noe, S., Guenther, A., Aaltonen, H., Kulmala, M. and Boy, M.: Comparing three vegetation monoterpene emission models to measured gas concentrations with a model of meteorology, air chemistry and chemical transport, *Biogeosciences*, 11(19), 5425–5443, doi:10.5194/bg-11-5425-2014, 2014.
43. Bäck, J., Aalto, J., Henriksson, M., Hakola, H., He, Q., and Boy, M.: Chemodiversity of a Scots pine stand and implications for terpene air concentrations, *Biogeosciences*, 9, 689–702, doi:10.5194/bg-9-689-2012, 2012.
44. http://www.ceip.at/webdab_emepdatabase/emissions_emepmodels/
45. Paasonen, P., Kupiainen, K., Klimont, Z., Visschedijk, A., Denier van der Gon, H. A. C. and Amann, M.: Continental anthropogenic primary particle number emissions, *Atmos. Chem. Phys.*, 16(11), 6823–6840, doi:10.5194/acp-16-6823-2016, 2016.

Acknowledgement

This work was supported by the Cryosphere-atmosphere interactions in a changing Arctic climate – CRAICC, the Swedish Research Council Formas, Project Nr. 2014-1445, the EU FP7 projects ACTRIS (Aerosols, Clouds, and Trace gases Research Infra Structure Network), the European Research Council (Grant 638703-COALA), eSTICC, the Swedish Strategic Research Program MERGE, Modeling the Regional and Global Earth System. The authors would like to thank Fredrik Söderberg at the Centre for Environmental and Climate Research at Lund University for providing help to set up the model at the high performance-computing cluster Aurora, provided by the Swedish National Infrastructure for Computing (SNIC) centre LUNARC.

SI Appendix

Additional results

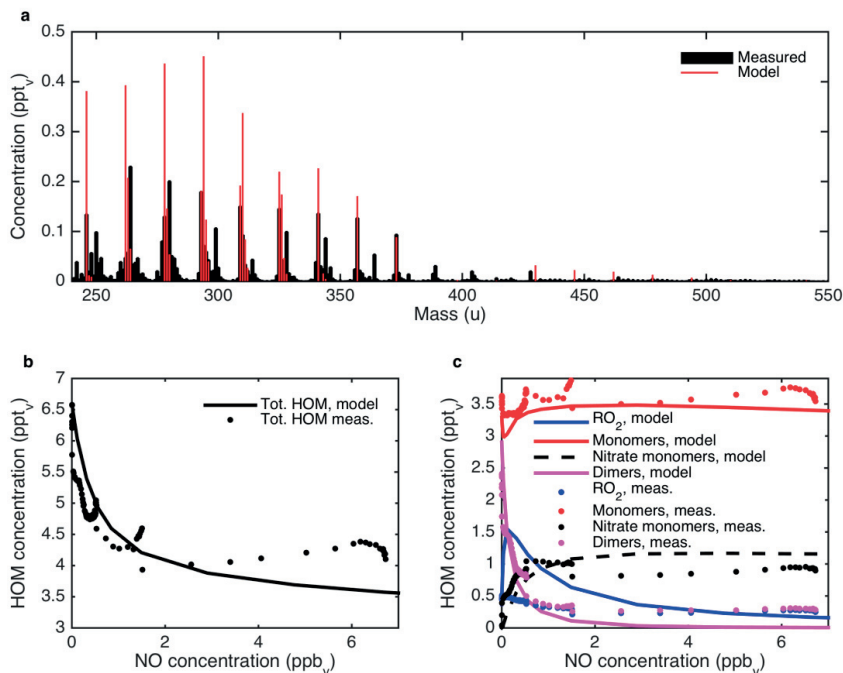


Figure S1. Modelled and measured HOM concentrations during an α -pinene ozonolysis experiment in the Jülich Plant Atmosphere Chamber where the NO concentration was gradually increased while the α -pinene and O₃ were kept approximately constant at around 6.5 ppb_v and 85 ppb_v, respectively (1). Figure **a** compares the modelled and measured HOM(g) mass spectrum at an NO concentration of 1.5 ppb_v, figure **b** shows how the modelled and measured total HOM(g) concentration changes when the NO concentration increases and figure **c** shows how the modelled and measured HOM peroxy radicals (RO₂), HOM non-radical monomers and dimers changes with increasing NO concentration in the chamber. Figure **c** also shows the concentration of the modelled and measured monomers containing nitrate functional groups.

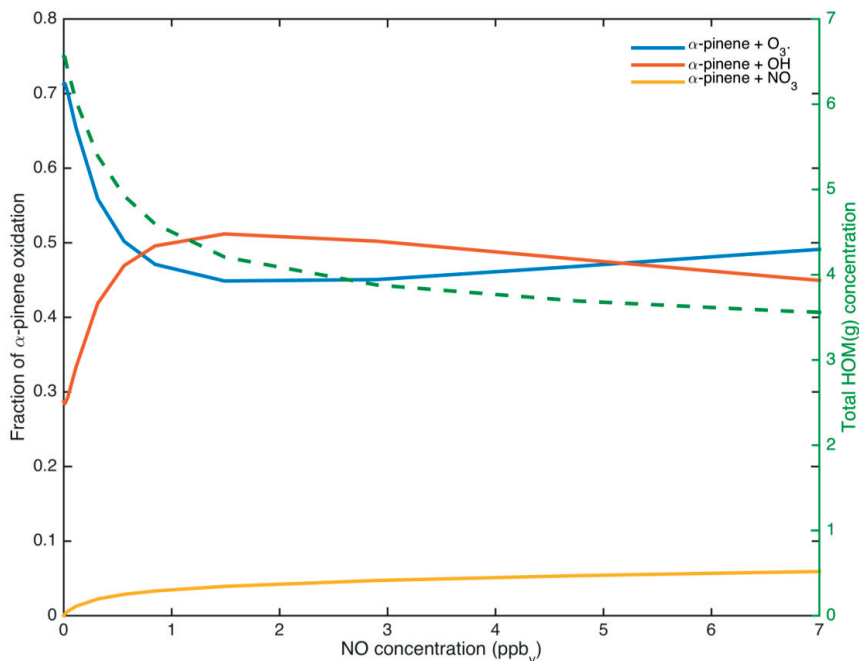


Figure S2. Modelled fraction of α -pinene that are oxidized by O_3 , OH and NO_3 at variable NO concentrations in JPAC. Shown are also the modelled total HOM(g) concentration (dashed green line).

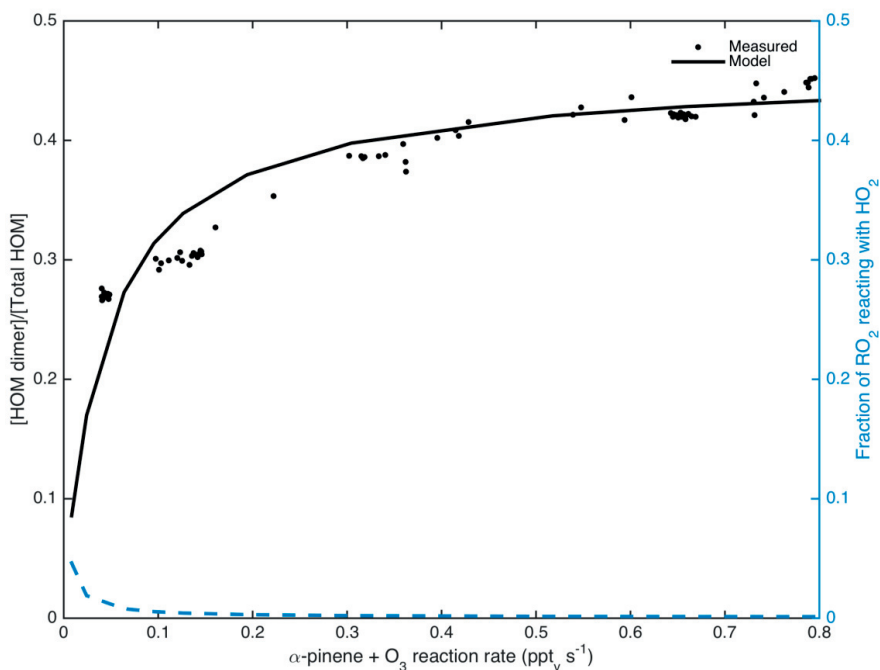


Figure S3. Measured and modelled relative fraction of HOM species that are dimers at variable α -pinene + O_3 reaction rates and the fraction of the autooxidation RO₂ that are consumed by RO₂ + HO₂ reactions (dashed blue line).

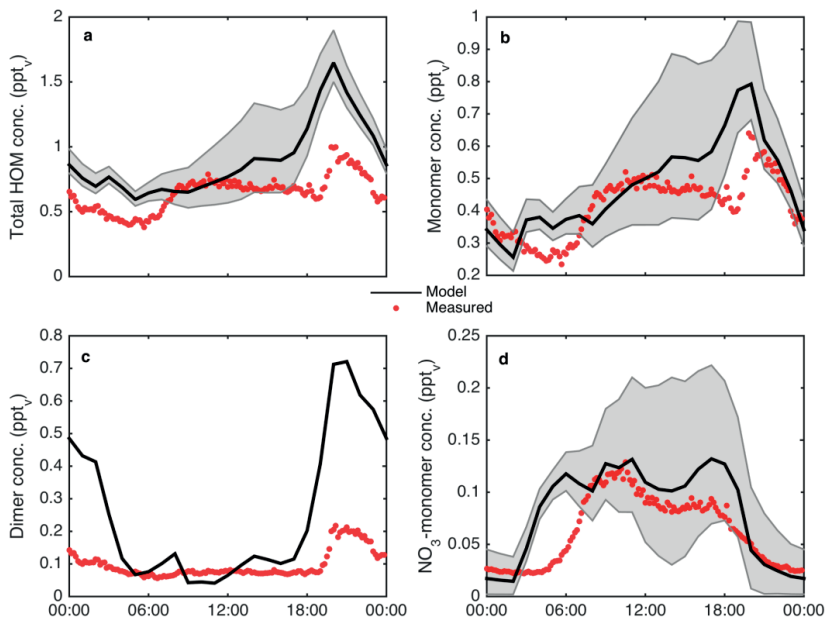


Figure S4. Modelled and measured average diurnal concentration trends 15th to 25th of May, 2013 of different HOM(g) species classes at around 2 m above ground. The grey areas represent the difference in the concentrations caused by the choice of HOM p_0 , where the SIMPOL $p_0 \times 3$ gives the upper limits and $p_0 = 0$ the lower limits. The results from simulations using the p_0 from SIMPOL are given by the solid black lines.

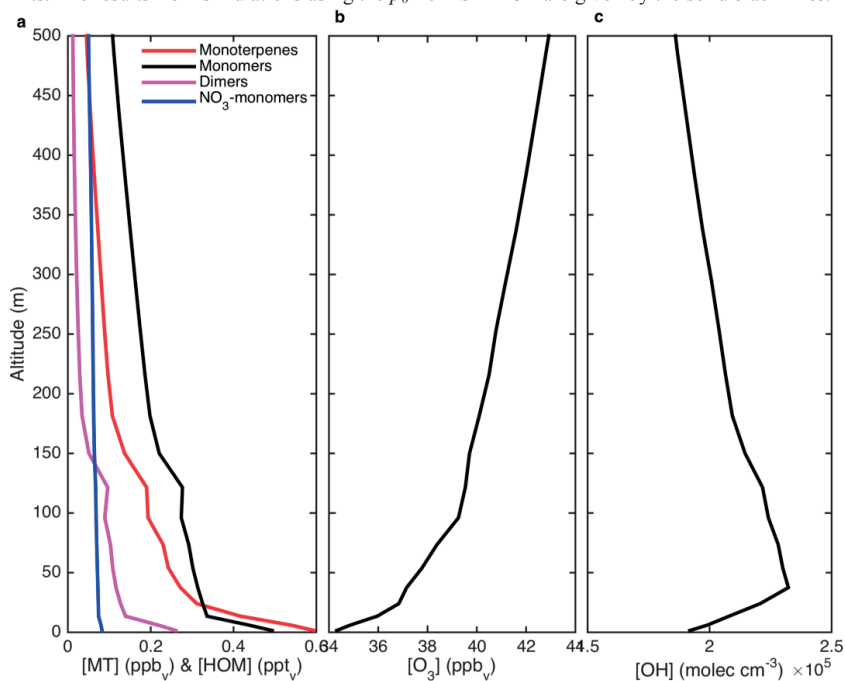


Figure S5. Modelled average vertical concentration profiles 15th to 25th of May, 2013 of **a** monoterpenes, HOM monomers without NO₃ groups, HOM dimers and HOM monomers with NO₃ groups, **b** O₃ and **c** OH. The results are from the simulation where the p_0 were estimated using SIMPOL.

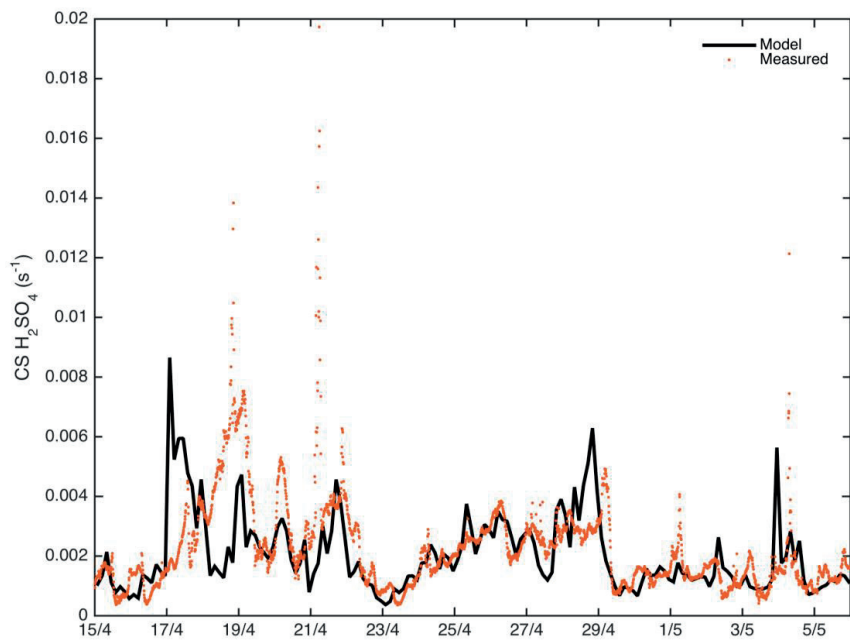


Figure S6. Modelled and measured sulphuric acid condensation sink during the SMEAR II 2014 spring campaign. The condensation sinks were calculated based on the modelled and measured dry particle number size distributions.

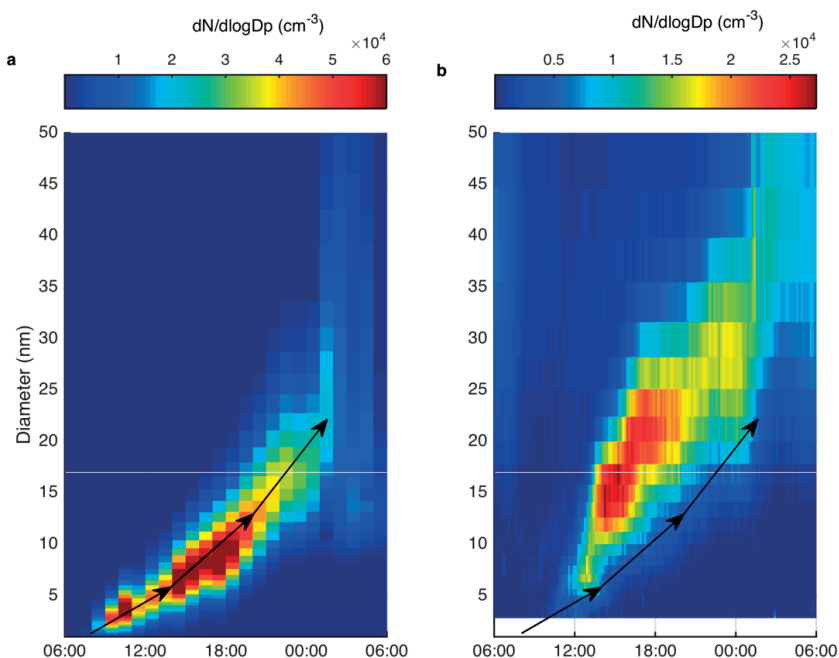


Figure S7. Modelled (a) and measured (b) particle number size distribution evolution at SMEAR II during the NPF event on the 23rd of April 2014. The modelled growth rate is visualized with black arrows, both in figure a and b.

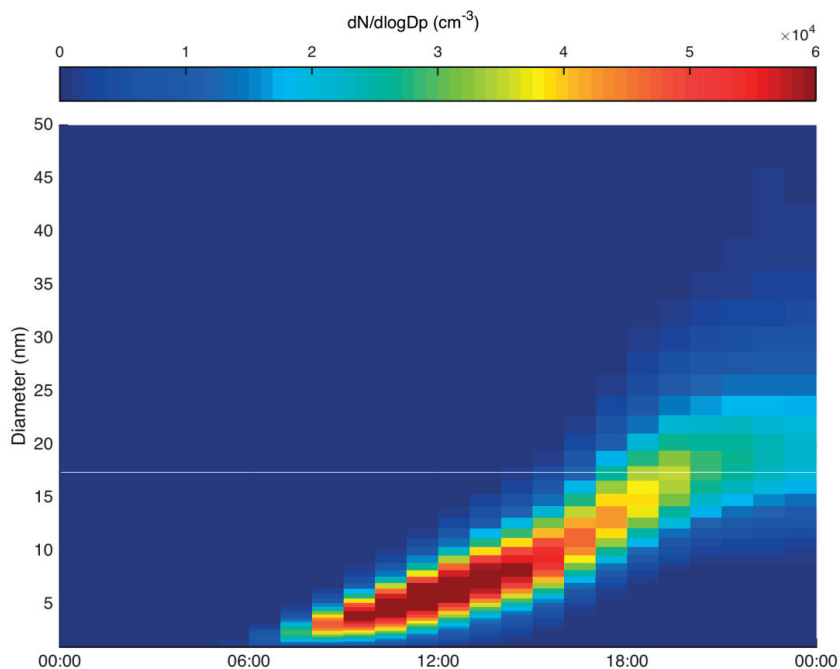


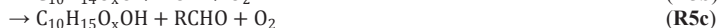
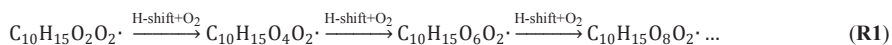
Figure S8. Modelled particle number size distribution evolution during a NPF event on the 23rd of April 2014. The particle number size distributions are from one ADCHEM model simulation that follows one air mass over time. At around 20:00 the air mass arrives at the SMEAR II station.

Extended Method

The peroxy radical autoxidation mechanism (PRAM)

Below we first give a general description of the theory behind PRAM followed by tables listing all PRAM species (Table S1), the MCMv3.3.1 species that are influencing/influenced by the chemical reactions in PRAM (Table S2) and the full PRAM mechanism with all 718 reactions (Table S3).

PRAM explicitly simulates how the autoxidation proceed via a chain of sequential intra-molecular peroxy radical hydrogen shifts (H-shifts) and O₂ additions (**R1**). The autoxidation can be terminated by reactions with NO, HO₂, other peroxy radicals (RO₂) (1) or unimolecular reactions (2) (**R2-R6**). When two peroxy radicals react with each other, the product(s) will either be monomers (**R5a, b, c**) or a dimer (**R5d**).



PRAM uses the same reaction rate coefficients for all RO₂ + NO and RO₂ + HO₂ reactions and the reaction rates are identical to the KRO2NO and KRO2HO2 reaction rates used in MCMv3.3.1. For the RO₂ + HO₂ reactions the formed product is always a non-radical species with a hydroperoxide functional group (-OOH) replacing the peroxy radical group (-OO•) (**R4**, R79 – R88 in Table S3). For the RO₂ + NO reactions the branching ratio between the channel forming organonitrate HOM (**R2a**) and the channel forming an alkoxy radical (RO) and NO₂ (**R2b**) varies depend on the RO₂ species. The RO formed from **R2b** is either assumed to rapidly react with O₂ and form new RO₂ species (**R3a**) (R39 – R48 in Table S3), decompose and form more volatile species (**R3b**) (R49 – R58 in Table S3), or react with O₂ and form a HOM monomer with an additional carbonyl group (**R3c**) (R59 – R68 in Table S3). In the mechanism the fragmentation products from **R3b** are represented by the MCM species C717O2 (an RO₂) and CH₃COCH₃ (acetone).

PRAM assumes that all RO₂ + RO₂ reactions (**R5**) exclusively occurs between RO₂ formed from the PRAM autoxidation mechanism (**R1**, R11 – R18 in Table S3) and in total 19 other selected RO₂ species formed in the MCMv3.3.1 chemical mechanism. The 19 RO₂ from MCMv3.3.1, which is listed in Table S2, all contain 10 carbon atoms (C10) and three to five oxygen atoms. All these C10 RO₂ are either formed from oxidation of α -pinene or limonene in MCMv3.3.1. PRAM use a fixed reaction rate equal to $1.1 \times 10^{-11} \text{ cm}^3 \text{ molec}^{-1} \text{ s}^{-1}$ for the RO₂ + RO₂ reaction channel leading to dimers (ROOR) (**R5d**) (R89 – R278 in Table S3). The total reaction rate for the channels leading to non-radical monomers and RO (**R5a, b, c**) is always $6 \times 10^{-11} \text{ cm}^3 \text{ molec}^{-1} \text{ s}^{-1}$, but the branching ratios between **R5a**, **R5b** and **R5c** varies depending on which MCM C10 RO₂ that are involved in the reactions (R279 – R718 in Table S3), following the procedure in MCMv3.3.1.

PRAM also includes the possibility to implement unimolecular reactions of RO₂ leading to non-radical monomers (**R6**). However, in the present work these reactions were set to zero because the agreement between the model results and the observations are not substantially improving when we include these reactions.

Model setup and description

In this work we use the Aerosol Dynamics gas- and particle phase chemistry model for laboratory CHAMber studies (ADCHAM, 3,4) and the trajectory model for Aerosol Dynamics, gas and particle phase CHEMistry and radiative transfer (ADCHEM 5,6). ADCHAM and ADCHEM use identical aerosol dynamics and gas-phase chemistry codes. They take into account the condensation, dissolution and evaporation of H_2SO_4 , NH_3 , HNO_3 and all organic oxidation products from Master Chemical Mechanism version 3.3.1 (MCM v.3.3.1) and from the PRAM mechanism (Table S1 and S2) with pure liquid saturation vapour pressures (p_0) less than 10^{-2} Pa. p_0 for compounds from MCM v3.3.1 were estimated with the functional group contribution method from Nannoolal et al. (7). p_0 for the PRAM products were estimated either with the functional group contribution method SIMPOL (8) or based on the detailed quantum-chemistry continuum solvent model, COSMO-RS (9), which gives substantially higher p_0 than SIMPOL. In practice the p_0 which was estimated based on COSMO-RS was derived by first calculating the HOM p_0 with SIMPOL and then multiplying these values with a correction factor of $10^{(2.8 \times \text{O/C} - 0.1)}$ for all monomers and 10^4 for dimers (6). These factors are based on calculated p_0 for 16 potential α -pinene autoxidation products (9).

The first order wall losses of HOM and other organic vapours ($k_{\text{wall},i}$) for the JPAC smog chamber simulations were estimated based the experimentally derived HOM wall losses (1) of HOM monomers with molecular formula $\text{C}_{10}\text{H}_{16}\text{O}_8$ of $1/75 \text{ s}^{-1}$ and scaling the individual HOM wall losses based on their molecular diffusion coefficients (D_i) (Eq. 1). D_i were calculated based on the Fuller's method (10). For a dimer with molecular formula $\text{C}_{20}\text{H}_{30}\text{O}_{11}$ the estimated first order wall loss rate become $1/100 \text{ s}^{-1}$, which is slightly lower than the experimentally derived values for HOM dimers with the same molecular formula of $1/90 \text{ s}^{-1}$ (1)

$$k_{\text{wall},i} = k_{\text{wall},\text{C}_{10}\text{H}_{16}\text{O}_8} \frac{D_i}{D_{\text{C}_{10}\text{H}_{16}\text{O}_8}} \quad (1)$$

All HOM species were assumed to deposit irreversible on the JPAC chamber walls, motivated by their generally low volatility and expectedly high reactivity (9). However, for the other condensable organic compounds from MCMv3.3.1 we expect that the VOC wall partitioning are more of a reversible nature. For smog chambers with Teflon walls, theories have been developed which takes into account the reversible partitioning of VOC assuming that the Teflon wall itself behaves like an large effective organic mass (C_{wall}) where VOC can be absorbed (11, 3). For JPAC where the walls are made out of glass, the release of semi-volatile non-reactive VOC back to the gas-phase from the walls ($k_{\text{wall,back},i}$), most likely are larger than for smog chamber made out of Teflon. In this work we still use the theory developed for Teflon walls (Eq. 2) but assume that the C_{wall} is smaller than what generally is used for Teflon smog chamber walls. With a C_{wall} of $5 \mu\text{mol m}^{-3}$ ADCHAM are able to reproduce the observed SOA mass formation in JPAC (Fig 2). This value can be compared with literature values of 9, 20, 50 and $120 \mu\text{mol m}^{-3}$ for alkanes, alkenes, alcohols and ketones absorbing on Teflon walls (11).

$$k_{\text{wall,back},i} = k_{\text{wall},i} \frac{p_{0,i}}{RT C_{\text{wall}}} \quad (2)$$

$p_{0,i}$ in Eq. 2 is the pure liquid saturation vapour pressure of compound i , R is the universal gas constant $8.3145 \text{ J mol}^{-1} \text{ K}^{-1}$ and T is the temperature in K.

For the ADCHEM model run the condensable vapours are formed from the MCMv3.3.1 precursors listed in Table S4. In the present study we use ADCHEM as a one-dimensional column model consisting of 40 vertical layers, logarithmically spaced, with intervals increasing from 3 m to 100 m with altitude. The model domain extends up to 2500 m a. g. l. The atmospheric diffusion equation is solved in the vertical direction using a diffusion coefficient based on a slightly modify Grisogono scheme (12). The aerosol dynamics include new particle formation, Brownian coagulation, dry and wet deposition and condensation/evaporation. The particle number size distributions are represented with 100 fixed size bins between 1.07 nm and $2.5 \mu\text{m}$ in dry diameter. The formation of the smallest particles with a diameter of 1.07 nm was modelled using the Atmospheric Cluster Dynamics Code (ACDC) (13), which explicitly simulates the growth, evaporation and coagulation losses of ammonia-sulphuric acid clusters up to a cluster size of 5 ammonia and 5 sulphuric acid molecules. Once the clusters have reached the uppermost size in ACDC they are assumed to behave like aerosol particles and are introduced into ADCHEM, which simulates the consecutive condensation growth, evaporation and losses by coagulation and deposition.

The emissions of α -pinene, carene, β -pinene and limonene were modelled with a 1D version of MEGAN 2.1 (Model of Emissions of Gases and Aerosols from Nature) (14, 15). The individual monoterpene emissions were estimated based on the measurements from 40 Scots pine trees around SMEAR II, which on average emit 43.7 % α -pinene, 39.6 % carene, 9 % β -pinene and 2.3 % limonene (16). In ADCHEM the three lowermost model layers at 0-3 m, 3-9 m, and 9-18 m are within the forest canopy at SMEAR II, and MEGAN simulates the BVOC emissions in each of these model layers.

Of all monoterpenes MCMv3.3.1 only includes chemical mechanisms for α -pinene, β -pinene, and limonene. However, since almost 40 % of the monoterpenes emitted at SMEAR II is carene we include the initial oxidation reactions between carene and OH, O₃ or NO₃ in the gas-phase chemistry mechanism, and assume that the formed oxidation products are identical to the products formed from the α -pinene oxidation in MCMv3.3.1. This also means that we assume that carene form HOM with the same yield and composition as α -pinene. Like α -pinene, carene has one endocyclic double bond and is therefore expected to produce HOM in similar extent as α -pinene. However, this assumption is still one of the largest sources of uncertainties in the modelled HOM concentration in the atmosphere. Gas-phase emission of dimethyl sulphide (DMS) in the marine boundary layer was estimated based on monthly mean seawater concentrations (17) and a sea-to-air transfer velocity parameterization (18). Anthropogenic emissions of NO_x, SO₂, CO, NH₃, VOC with a resolution of 0.1°x0.1° were retrieved from EMEP (European Monitoring and Evaluation Programme) database (EMEP/CEIP 2014, present state of emissions as used in EMEP models (19)).

Size resolved anthropogenic continental primary particle emissions were derived from a global 0.5°x0.5° emission inventory (20). Primary particle emission from ship traffic was parameterized based on the gas-phase emission of SO₂ by using a conversion factor of 8.33×10^{14} particles (g SO₂)⁻¹ (21). The size distribution of the primary particles from ships was estimated based on a study by Jonsson et al. (22). Primary particle emissions of wind-generated marine aerosols were also included (23).

The model was initialized with an aerosol particle number concentration of 100 cm⁻³ in each vertical layer, with a unimodal lognormal particle number size distribution having a geometric mean diameter of 120 nm and a geometric standard deviation of 2.90 %, respectively 10 %, of the dry particle volume in each size bin was assumed to be composed of non-volatile organic material and ammonium sulphate.

ADCHEM was implemented for simulations of aerosol particle and trace gas concentrations during two measurement campaigns at the SMEAR II field station in Finland (61.85° N, 24.28° E). During the first campaign, the 2013 PEGASOS spring campaign, ADCHEM was operated as a stationary column model at SMEAR II, with the purpose to evaluate the PRAM mechanism. ADCHEM was continuously reading in the observed concentrations of NO₂, O₃, CO and total monoterpene at eight different altitudes between 4.2 to 125 m above ground level (a.g.l.), SO₂ at 16.8 m and particle number size distributions for particles between 2.8 and 1000 nm in diameter. The particle number size distribution was assumed to be constant in the whole model domain (0 - 2500 m a.g.l.). The modelled total monoterpene concentrations within the lowermost 125 m was scaled for each model time step in order to match the observed total monoterpene concentrations at SMEAR II. All other trace gas concentrations as well as the particle chemical composition and hygroscopic growth were calculated in order to provide the most realistic condensation losses of HOM and other condensable compounds.

During PEGASOS HOM(g) was measured at ~2 m altitude using a nitrate-ion-based chemical ionization atmospheric pressure-interface time-of-flight mass spectrometer (CI-API-TOF). Unfortunately, only one a few new particle formation (NPF) events could be observed at SMEAR II during the 2013 PEGASOS campaign. Thus, in order to be able to evaluate the HOM contribution to the growth of new ~1 nm in diameter particles into the CCN size range we also setup ADCHEM for a second campaign from spring 2014. During this campaign, NPF events with consecutive growth could be observed at more than 50 % of the days (Fig 4b). Unfortunately, the CI-API-TOF measurements at SMEAR II were not functioning during spring 2014.

For the spring 2014 campaign ADCHEM was operated as a Lagrangian vertical column model following in total 168 individual air mass trajectories starting 4 days backward in time before they reached SMEAR II, with 3 hour in-between the arrival of each trajectory, covering in total 21 consecutive days. The trajectories were calculated with the Hybrid Single Particle Lagrangian Integrated Trajectory Model (HYSPLIT) (24) with meteorological data from the Global Data Assimilation System (GDAS), downloaded from NOAA Air Resource Laboratory Real-time Environmental Application and Display sYstem (READY) (25).

Table S1. List of PRAM species names, molecular formula, compound type, and functional groups used when estimating their vapour pressure using SIMPOL. The peroxy and alkoxy radical functional groups are not listed.

PRAM name	Molecular formula	Type	Alcohol	Aldehyde	Ketone	Carboxylic acid	Nitrate	Peroxide	Hydrogen peroxide	Carbonyl peroxy acid
C10H15O2O2	C ₁₀ H ₁₅ O ₄	RO ₂		1	1					
C10H15O3O2	C ₁₀ H ₁₅ O ₅	RO ₂		1	2					
C10H15O4O2	C ₁₀ H ₁₅ O ₆	RO ₂	1	1	2					
C10H15O5O2	C ₁₀ H ₁₅ O ₇	RO ₂		1	2				1	
C10H15O6O2	C ₁₀ H ₁₅ O ₈	RO ₂			2	1			1	
C10H15O7O2	C ₁₀ H ₁₅ O ₉	RO ₂		1	2				2	
C10H15O8O2	C ₁₀ H ₁₅ O ₁₀	RO ₂		1	1			1	2	
C10H15O9O2	C ₁₀ H ₁₅ O ₁₁	RO ₂	1	1	1			1	2	
C10H15O10O2	C ₁₀ H ₁₅ O ₁₂	RO ₂		1	1			1	3	
C10H15O11O2	C ₁₀ H ₁₅ O ₁₃	RO ₂	1	1	1			1	3	
C10H15O12O2	C ₁₀ H ₁₅ O ₁₄	RO ₂	1		1			1	2	1
C10H15O2O	C ₁₀ H ₁₅ O ₃	RO		1	1					
C10H15O3O	C ₁₀ H ₁₅ O ₄	RO		1	2					
C10H15O4O	C ₁₀ H ₁₅ O ₅	RO	1	1	2					
C10H15O5O	C ₁₀ H ₁₅ O ₆	RO		1	2				1	
C10H15O6O	C ₁₀ H ₁₅ O ₇	RO			2	1			1	
C10H15O7O	C ₁₀ H ₁₅ O ₈	RO		1	2				2	
C10H15O8O	C ₁₀ H ₁₅ O ₉	RO		1	1			1	2	
C10H15O9O	C ₁₀ H ₁₅ O ₁₀	RO	1	1	1			1	2	
C10H15O10O	C ₁₀ H ₁₅ O ₁₁	RO		1	1			1	3	
C10H15O11O	C ₁₀ H ₁₅ O ₁₂	RO	1	1	1			1	3	
C10H14O3	C ₁₀ H ₁₄ O ₃	RC=O		1	2					
C10H14O4	C ₁₀ H ₁₄ O ₄	RC=O		2	2					
C10H14O5	C ₁₀ H ₁₄ O ₅	RC=O		1	2	1				
C10H14O6	C ₁₀ H ₁₄ O ₆	RC=O	1	1	2	1				
C10H14O7	C ₁₀ H ₁₄ O ₇	RC=O			2	1				1
C10H14O8	C ₁₀ H ₁₄ O ₈	RC=O			2	2			1	
C10H14O9	C ₁₀ H ₁₄ O ₉	RC=O			2	1			1	1
C10H14O10	C ₁₀ H ₁₄ O ₁₀	RC=O			1	1		1	1	1
C10H14O11	C ₁₀ H ₁₄ O ₁₁	RC=O			2			1	2	1
C10H14O12	C ₁₀ H ₁₄ O ₁₂	RC=O			1	1		1	2	1
C10H14O13	C ₁₀ H ₁₄ O ₁₃	RC=O	1		1	1		1	2	1
C10H14O14	C ₁₀ H ₁₄ O ₁₄	RC=O	2		1	1		1	2	1
C10H16O4	C ₁₀ H ₁₆ O ₄	ROOH or ROH		1	1				1	
C10H16O5	C ₁₀ H ₁₆ O ₅	ROOH or ROH		1	2				1	
C10H16O6	C ₁₀ H ₁₆ O ₆	ROOH or ROH	1		2					1
C10H16O7	C ₁₀ H ₁₆ O ₇	ROOH or ROH			2				1	1
C10H16O8	C ₁₀ H ₁₆ O ₈	ROOH or ROH			2	1			2	
C10H16O9	C ₁₀ H ₁₆ O ₉	ROOH or ROH			2				2	1
C10H16O10	C ₁₀ H ₁₆ O ₁₀	ROOH or ROH			1			1	2	1
C10H16O11	C ₁₀ H ₁₆ O ₁₁	ROOH or ROH	1		1			1	2	1
C10H16O12	C ₁₀ H ₁₆ O ₁₂	ROOH or ROH			1			1	3	1
C10H16O13	C ₁₀ H ₁₆ O ₁₃	ROOH or ROH	1		1			1	3	1

C10H15O2NO3	C ₁₀ H ₁₅ NO ₅	R-O-NO ₂	1	1	1				
C10H15O3NO3	C ₁₀ H ₁₅ NO ₆	R-O-NO ₂	1	2	1				
C10H15O4NO3	C ₁₀ H ₁₅ NO ₇	R-O-NO ₂		1	1				1
C10H15O5NO3	C ₁₀ H ₁₅ NO ₈	R-O-NO ₂		2	1				1
C10H15O6NO3	C ₁₀ H ₁₅ NO ₉	R-O-NO ₂		2	1	1		1	
C10H15O7NO3	C ₁₀ H ₁₅ NO ₁₀	R-O-NO ₂		2	1			1	1
C10H15O8NO3	C ₁₀ H ₁₅ NO ₁₁	R-O-NO ₂		1	1	1		1	1
C10H15O9NO3	C ₁₀ H ₁₅ NO ₁₂	R-O-NO ₂	1	1	1	1		1	1
C10H15O10NO3	C ₁₀ H ₁₅ NO ₁₃	R-O-NO ₂		1	1	1		2	1
C10H15O11NO3	C ₁₀ H ₁₅ NO ₁₄	R-O-NO ₂	1	1	1	1		2	1
C20H30O6	C ₂₀ H ₃₀ O ₆	ROOR		4		1			
C20H30O7	C ₂₀ H ₃₀ O ₇	ROOR		5		1			
C20H30O8	C ₂₀ H ₃₀ O ₈	ROOR		6		1			
C20H30O9	C ₂₀ H ₃₀ O ₉	ROOR	1	6		1			
C20H30O10	C ₂₀ H ₃₀ O ₁₀	ROOR	2	6		1			
C20H30O11	C ₂₀ H ₃₀ O ₁₁	ROOR	3	6		1			
C20H30O12	C ₂₀ H ₃₀ O ₁₂	ROOR	2	4		1		2	
C20H30O13	C ₂₀ H ₃₀ O ₁₃	ROOR	3	4		1		2	
C20H30O14	C ₂₀ H ₃₀ O ₁₄	ROOR	2	4		1		3	
C20H30O15	C ₂₀ H ₃₀ O ₁₅	ROOR	2	4		1		2	1
C20H31O4NO3	C ₂₀ H ₃₁ NO ₇	ROOR-O-NO ₂		2	1	1			
C20H31O5NO3	C ₂₀ H ₃₁ NO ₈	ROOR-O-NO ₂		3	1	1			
C20H31O6NO3	C ₂₀ H ₃₁ NO ₉	ROOR-O-NO ₂		4	1	1			
C20H31O7NO3	C ₂₀ H ₃₁ NO ₁₀	ROOR-O-NO ₂	1	5	1	1			
C20H31O8NO3	C ₂₀ H ₃₁ NO ₁₁	ROOR-O-NO ₂	2	5	1	1			
C20H31O9NO3	C ₂₀ H ₃₁ NO ₁₂	ROOR-O-NO ₂	3	5	1	1			
C20H31O10NO3	C ₂₀ H ₃₁ NO ₁₃	ROOR-O-NO ₂	2	3	1	1		2	
C20H31O11NO3	C ₂₀ H ₃₁ NO ₁₄	ROOR-O-NO ₂	3	3	1	1		2	
C20H31O12NO3	C ₂₀ H ₃₁ NO ₁₅	ROOR-O-NO ₂	2	3	1	1		3	
C20H31O13NO3	C ₂₀ H ₃₁ NO ₁₆	ROOR-O-NO ₂	2	3	1	1		2	1

Tabel S2. List of species from MCMv3.3.1 that are involved in the PRAM mechanism and the PRAM reactions (listed in Table S3) that they are involved in.

Name	Role in PRAM
NO	React with the autooxidation RO ₂ species and form RO, R-O-NO ₂ , RC=O species or fragmentation of the C10 RO ₂ species (R39 – R78)
O ₃	React with monoterpenes containing endocyclic double bonds and form the CI APINOOA and LIMOOA which decomposes and form the RO ₂ (C10H15O2O2) that initializes the autooxidation mechanism.
HO ₂	React with the autooxidation RO ₂ species and form ROOH (R69 - R78).
OH	React with the monoterpenes and form RO ₂ species that can undergo autooxidation (R7 - R9) and is also formed when the CI from the ozonolysis of monoterpenes is decomposing and form the RO ₂ species that initialize the autooxidation chain (R1-R6), and upon unimolecular termination of the RO ₂ autooxidation (R19 - R28).
α -pinene	Small branching ratio of the RO ₂ formed during the OH oxidation of α -pinene are assumed to undergo autooxidation (R7).
β -pinene	Small branching ratio of the RO ₂ formed during the OH oxidation of β -pinene are assumed to undergo autooxidation (R8).
Limonene	Small branching ratio of the RO ₂ formed during the OH oxidation of limonene are assumed to undergo autooxidation (R9).
Carene	After the initial oxidation with O ₃ carene is assumed to for the same CI as α -pinene and thus form HOM with identical yields and composition as α -pinene.
APINOOA	CI formed from the α -pinene + O ₃ reaction and assumed to be formed from the carene + O ₃ reaction. This CI is assumed to decompose and form the initial RO ₂ initiating the autooxidation mechanism (R5).
LIMOOA	CI formed from the limonene + O ₃ reaction. This CI is assumed to decompose and form the initial RO ₂ initiating the autooxidation mechanism (R6).
APINAO ₂	RO ₂ species with 10 carbon and 3 oxygen atoms from α -pinene reacting with OH. React with RO ₂ from the autooxidation mechanism.
APINBO ₂	RO ₂ species with 10 carbon and 3 oxygen atoms from α -pinene reacting with OH. React with RO ₂ from the autooxidation mechanism.
APINCO ₂	RO ₂ species with 10 carbon and 3 oxygen atoms from α -pinene reacting with OH. React with RO ₂ from the autooxidation mechanism.
C107O ₂	RO ₂ species with 10 carbon and 4 oxygen atoms from α -pinene reacting with O ₃ . React with RO ₂ from the autooxidation mechanism.
C109O ₂	RO ₂ species with 10 carbon and 4 oxygen atoms from α -pinene reacting with O ₃ . React with RO ₂ from the autooxidation mechanism.
C106O ₂	RO ₂ species with 10 carbon and 5 oxygen atoms formed as a second-generation product from α -pinene oxidation. React with RO ₂ from the autooxidation mechanism.
C920CO ₃	RO ₂ species with 10 carbon and 5 oxygen atoms formed as a second-generation product from α -pinene oxidation. React with RO ₂ from the autooxidation mechanism.
C108O ₂	RO ₂ species with 10 carbon and 5 oxygen atoms formed as a second-generation product from α -pinene oxidation. React with RO ₂ from the autooxidation mechanism.
PINALO ₂	RO ₂ species with 10 carbon and 4 oxygen atoms formed as a second-generation product from α -pinene oxidation. React with RO ₂ from the autooxidation mechanism.
C96CO ₃	RO ₂ species with 10 carbon and 4 oxygen atoms formed as a second-generation product from α -pinene oxidation. React with RO ₂ from the autooxidation mechanism.
C923CO ₃	RO ₂ species with 10 carbon and 4 oxygen atoms formed as a second-generation product from limonene oxidation. React with RO ₂ from the autooxidation mechanism.
LIMAO ₂	RO ₂ species with 10 carbon and 3 oxygen atoms formed from limonene reacting with OH React with RO ₂ from the autooxidation mechanism.
LIMALBO ₂	RO ₂ species with 10 carbon and 4 oxygen atoms formed from limonene reacting with O ₃ React with RO ₂ from the autooxidation mechanism.
LIMCO ₂	RO ₂ species with 10 carbon and 3 oxygen atoms formed from limonene reacting with OH React with RO ₂ from the autooxidation mechanism.
LIMALO ₂	RO ₂ species with 10 carbon and 5 oxygen atoms formed as a second-generation product from limonene oxidation. React with RO ₂ from the autooxidation mechanism.
LIMBO ₂	RO ₂ species with 10 carbon and 3 oxygen atoms formed from limonene reacting with OH React with RO ₂ from the autooxidation mechanism.
LIMALAO ₂	RO ₂ species with 10 carbon and 4 oxygen atoms formed from limonene reacting with O ₃ React with RO ₂ from the autooxidation mechanism.
NAPINAO ₂	RO ₂ species with 10 carbon, 5 oxygen and one nitrogen atom from α -pinene reacting with NO ₃ . React with RO ₂ from the autooxidation mechanism.
NAPINBO ₂	RO ₂ species with 10 carbon, 5 oxygen one nitrogen atom from α -pinene reacting with NO ₃ . React with RO ₂ from the autooxidation mechanism.
APINBOH	ROH, formed from RO ₂ + RO ₂ reactions (R279, 323, 367, 411, 455, 499, 543, 587 631 & 675).
APINAO	RO, formed from RO ₂ + RO ₂ reactions (R280, 324, 368, 412, 456, 500, 544, 588, 632 & 676).
APINBOH	ROH, formed from RO ₂ + RO ₂ reactions (R281, 325, 369, 413, 457, 501, 545, 589, 623 & 677).
APINBO	RO, formed from RO ₂ + RO ₂ reactions (R282, 326, 370, 414, 458, 502, 546, 590, 634 & 678).
APINBCO	R=O, formed from RO ₂ + RO ₂ reactions (R283, 327, 371, 415, 459, 503, 547, 591, 635 & 679).
APINCO	RO, formed from RO ₂ + RO ₂ reactions (R284, 328, 372, 416, 460, 504, 548, 592, 636 & 680).
APINCOH	ROH, formed from RO ₂ + RO ₂ reactions (R285, 329, 373, 417, 461, 505, 549, 593, 637 & 681).
C107O	RO, formed from RO ₂ + RO ₂ reactions (R286, 330, 374, 418, 462, 506, 550, 594, 638 & 682).
C107OH	ROH, formed from RO ₂ + RO ₂ reactions (R287, 331, 375, 419, 463, 507, 551, 595, 639 & 683).
C109O	RO, formed from RO ₂ + RO ₂ reactions (R288, 332, 376, 420, 464, 508, 552, 596, 640 & 684).
C109OH	ROH, formed from RO ₂ + RO ₂ reactions (R289, 333, 377, 421, 465, 509, 553, 597, 641 & 685).
C109CO	R=O, formed from RO ₂ + RO ₂ reactions (R290, 334, 378, 422, 466, 510, 554, 598, 642 & 686).
C106O	RO, formed from RO ₂ + RO ₂ reactions (R291, 335, 379, 423, 467, 511, 555, 599, 643 & 687).
C106OH	ROH, formed from RO ₂ + RO ₂ reactions (R292, 336, 380, 424, 468, 512, 556, 600, 644 & 688).

C92O2	RO, formed from RO ₂ + RO ₂ reactions (R293, 337, 381, 425, 469, 513, 557, 601, 645 & 689).
HOPINONIC	ROH, formed from RO ₂ + RO ₂ reactions (R294, 338, 382, 426, 470, 514, 558, 602, 646 & 690).
C108O	RO, formed from RO ₂ + RO ₂ reactions (R295, 339, 383, 427, 471, 515, 559, 603, 647 & 691).
C108OH	ROH, formed from RO ₂ + RO ₂ reactions (R296, 340, 384, 428, 472, 516, 560, 604, 648 & 692).
PINALO	RO, formed from RO ₂ + RO ₂ reactions (R297, 341, 385, 429, 473, 517, 561, 605, 649 & 693).
PINALOH	ROH, formed from RO ₂ + RO ₂ reactions (R298, 342, 386, 430, 474, 518, 562, 606, 650 & 694).
C96O2	RO, formed from RO ₂ + RO ₂ reactions (R299, 343, 387, 431, 475, 519, 563, 607, 651 & 695).
PINONIC	ROH, formed from RO ₂ + RO ₂ reactions (R300, 344, 388, 432, 476, 520, 564, 608, 652 & 696).
C923O2	RO, formed from RO ₂ + RO ₂ reactions (R301, 345, 389, 433, 477, 521, 565, 609, 653 & 697).
LIMONONIC	ROH, formed from RO ₂ + RO ₂ reactions (R302, 346, 390, 434, 478, 522, 566, 610, 654 & 698).
LIMAO	RO, formed from RO ₂ + RO ₂ reactions (R303, 347, 391, 435, 479, 523, 567, 611, 655 & 699).
LIMAOH	ROH, formed from RO ₂ + RO ₂ reactions (R304, 312, 348, 356, 392, 400, 436, 444, 480, 488, 524, 532, 568, 576, 612, 620, 656, 664, 700, 708).
LIMALBCO	R=O, formed from RO ₂ + RO ₂ reactions (R305, 349, 393, 437, 481, 525, 569, 613, 657 & 701).
LIMALBO	RO, formed from RO ₂ + RO ₂ reactions (R306, 350, 394, 438, 482, 526, 570, 614, 658 & 702).
LIMALBOH	ROH, formed from RO ₂ + RO ₂ reactions (R307, 351, 395, 439, 483, 527, 571, 615, 659 & 703).
LIMCO	RO, formed from RO ₂ + RO ₂ reactions (R308, 352, 396, 440, 484, 528, 572, 616, 660 & 704).
LIMCOH	ROH, formed from RO ₂ + RO ₂ reactions (R309, 353, 397, 441, 485, 529, 573, 617, 661 & 705).
LIMALO	RO, formed from RO ₂ + RO ₂ reactions (R310, 354, 398, 442, 486, 530, 574, 618, 662 & 706).
LIMALOH	ROH, formed from RO ₂ + RO ₂ reactions (R311, 355, 399, 443, 487, 531, 575, 619, 663 & 707).
LIMBCO	R=O, formed from RO ₂ + RO ₂ reactions (R313, 357, 401, 445, 489, 533, 577, 621, 665 & 709).
LIMBO	RO, formed from RO ₂ + RO ₂ reactions (R314, 358, 402, 446, 490, 534, 578, 622, 666 & 710).
LIMALACO	R=O, formed from RO ₂ + RO ₂ reactions (R315, 359, 403, 447, 491, 535, 579, 623, 667 & 711).
LIMALAO	RO, formed from RO ₂ + RO ₂ reactions (R316, 360, 404, 448, 492, 536, 580, 624, 668 & 712).
LIMALAOH	ROH, formed from RO ₂ + RO ₂ reactions (R317, 361, 405, 449, 493, 537, 581, 625, 669 & 713).
APINBNO3	ROH – NO ₃ , formed from RO ₂ + RO ₂ reactions (R318, 362, 406, 450, 494, 538, 582, 626, 670 & 714).
NAPINAO	RO – NO ₃ , formed from RO ₂ + RO ₂ reactions (R319, 363, 407, 451, 495, 539, 583, 627, 671 & 715).
APINANO3	ROH – NO ₃ , formed from RO ₂ + RO ₂ reactions (R320, 364, 408, 452, 496, 540, 584, 628, 672 & 716).
NAPINBO	RO – NO ₃ , formed from RO ₂ + RO ₂ reactions (R321, 365, 409, 453, 497, 541, 585, 629, 673 & 717).
NC101CO	R=O – NO ₃ , formed from RO ₂ + RO ₂ reactions (R322, 366, 410, 454, 498, 542, 586, 630, 674 & 718).
C717O2	Assumed fragmentation product from the RO ₂ + NO reactions (R49 - R58).
CH3COCH3	Assumed fragmentation product from the RO ₂ + NO reactions (R49 - R58).

Table S3. List of all reactions and their reaction rates in PRAM

If not others specified the unit of the reaction rates are $\text{cm}^3 \text{molecules}^{-1} \text{s}^{-1}$

PRAM apply the simple rate coefficients KDEC, KRO2NO and KRO2HO2 from MCMv3.3.1:

$$\text{KDEC} = 1\text{E}6 \text{ s}^{-1}$$

$$\text{KRO2NO} = 2.7\text{E}-12 * \text{EXP}(360/\text{T}) \text{ cm}^3 \text{ molec}^{-1} \text{ s}^{-1}$$

$$\text{KRO2HO2} = 2.91\text{E}-13 * \text{EXP}(1300/\text{T}) \text{ cm}^3 \text{ molec}^{-1} \text{ s}^{-1}$$

(Used for unimolecular decomposition of alkoxy radicals to peroxy radicals)

(Used for the reactions between peroxy radicals and NO)

(Used for the reactions between peroxy radicals and HO₂)

Reaction	Reaction rate	Comment / ref.
APINENE + O ₃ → APINOOA	$8.05\text{E}-16 * \text{EXP}(-640/\text{T}) * 0.6$	MCMv3.3.1
APINENE + O ₃ → APINOOB	$8.05\text{E}-16 * \text{EXP}(-640/\text{T}) * 0.4$	MCMv3.3.1
LIMONENE + O ₃ → LIMOOA	$2.80\text{E}-15 * \text{EXP}(-770/\text{T}) * 0.730$	MCMv3.3.1
LIMONENE + O ₃ → LIMOOB	$2.80\text{E}-15 * \text{EXP}(-770/\text{T}) * 0.27$	MCMv3.3.1
APINENE + OH → Products	$1.2\text{E}-11 * \text{EXP}(440/\text{T})$	MCMv3.3.1
BPINENE + OH → Products	$2.38\text{E}-11 * \text{EXP}(357/\text{T})$	MCMv3.3.1
LIMONENE + OH → Products	$4.28\text{E}-11 * \text{EXP}(401/\text{T})$	MCMv3.3.1
CARENE + O ₃ → APINOOA	$3.70\text{D}-17 * 0.6$	See motiv. above
CARENE + O ₃ → APINOOB	$3.70\text{D}-17 * 0.4$	See motiv. above

Initial Criegee intermediate unimolecular decomposition to peroxy radicals undergoing autoxidation

1. APINOOA → C107O2 + OH	KDEC*0.55*0.85	
2. APINOOA → C109O2 + OH	KDEC*0.45*0.85	
3. LIMOOA → LIMALAO2 + OH	KDEC*0.5*0.7	
4. LIMOOA → LIMALBO2 + OH	KDEC*0.5*0.7	
5. APINOOA → C10H15O2O2 + OH	KDEC*0.15	Max yield = 9.0%
6. LIMOOA → C10H15O2O2 + OH	KDEC*0.30	Max yield = 21.9%

Initial reactions leading to HOM formation OH oxidation

7. APINENE + OH → C10H15O2O2	$0.01 * 1.2\text{E}-11 * \text{EXP}(440/\text{T})$	Max yield = 1.0%
8. BPINENE + OH → C10H15O2O2	$0.014 * 2.38\text{E}-11 * \text{EXP}(357/\text{T})$	Max yield = 1.4%
9. LIMONENE + OH → C10H15O2O2	$0.025 * 4.28\text{E}-11 * \text{EXP}(401/\text{T})$	Max yield = 2.5%

Autoxidation reaction rates (H-shifts + O₂)

11. C10H15O2O2 → C10H15O4O2	1000.0	Unit s ⁻¹
12. C10H15O3O2 → C10H15O5O2	1000.0	Unit s ⁻¹
13. C10H15O4O2 → C10H15O6O2	5.0	Unit s ⁻¹
14. C10H15O5O2 → C10H15O7O2	0.1	Unit s ⁻¹
15. C10H15O6O2 → C10H15O8O2	0.06	Unit s ⁻¹
16. C10H15O7O2 → C10H15O9O2	0.04	Unit s ⁻¹
17. C10H15O8O2 → C10H15O10O2	0.02	Unit s ⁻¹
18. C10H15O9O2 → C10H15O11O2	0.01	Unit s ⁻¹

Unimolecular self-termination of peroxy radicals to non-radical compounds (RO₂ → RC=O + OH)

In the present version PRAM does not include any unimolecular self termination reactions of the peroxy radicals undergoing autoxidation but the mechanism include the flexibility to add these equations if needed.

19. C10H15O2O2 → C10H14O3 + OH	0.0	Unit s ⁻¹
20. C10H15O3O2 → C10H14O4 + OH	0.0	Unit s ⁻¹
21. C10H15O4O2 → C10H14O5 + OH	0.0	Unit s ⁻¹
22. C10H15O5O2 → C10H14O6 + OH	0.0	Unit s ⁻¹
23. C10H15O6O2 → C10H14O7 + OH	0.0	Unit s ⁻¹
24. C10H15O7O2 → C10H14O8 + OH	0.0	Unit s ⁻¹
25. C10H15O8O2 → C10H14O9 + OH	0.0	Unit s ⁻¹
26. C10H15O9O2 → C10H14O10 + OH	0.0	Unit s ⁻¹
27. C10H15O10O2 → C10H14O11 + OH	0.0	Unit s ⁻¹
28. C10H15O11O2 → C10H14O12 + OH	0.0	Unit s ⁻¹

Conversion of alkoxy radicals to peroxy radicals (RO + O₂ → RO₂)

29. C10H15O2O → C10H15O3O2	KDEC	Unit s ⁻¹
30. C10H15O3O → C10H15O4O2	KDEC	Unit s ⁻¹
31. C10H15O4O → C10H15O5O2	KDEC	Unit s ⁻¹
32. C10H15O5O → C10H15O6O2	KDEC	Unit s ⁻¹
33. C10H15O6O → C10H15O7O2	KDEC	Unit s ⁻¹
34. C10H15O7O → C10H15O8O2	KDEC	Unit s ⁻¹
35. C10H15O8O → C10H15O9O2	KDEC	Unit s ⁻¹
36. C10H15O9O → C10H15O10O2	KDEC	Unit s ⁻¹
37. C10H15O10O → C10H15O11O2	KDEC	Unit s ⁻¹
38. C10H15O11O → C10H15O12O2	KDEC	Unit s ⁻¹

Peroxy radicals reacting with NO and forming an alkoxy radical and NO₂ (RO₂ + NO → RO + NO₂)

39. C10H15O2O2 + NO → C10H15O2O + NO ₂	KRO2NO*0.9
40. C10H15O3O2 + NO → C10H15O3O + NO ₂	KRO2NO*0.9
41. C10H15O4O2 + NO → C10H15O4O + NO ₂	KRO2NO*0.9
42. C10H15O5O2 + NO → C10H15O5O + NO ₂	KRO2NO*0.9
43. C10H15O6O2 + NO → C10H15O6O + NO ₂	KRO2NO*0.8
44. C10H15O7O2 + NO → C10H15O7O + NO ₂	KRO2NO*0.7
45. C10H15O8O2 + NO → C10H15O8O + NO ₂	KRO2NO*0.6

46. C10H15O9O2 + NO → C10H15O9O + NO2	KRO2NO*0.5
47. C10H15O10O2 + NO → C10H15O10O + NO2	KRO2NO*0.3
48. C10H15O11O2 + NO → C10H15O11O + NO2	KRO2NO*0.0

Lumped reactions describing the fragmentation of autoxidation products when they react with NO ($\text{RO}_2 + \text{NO} \rightarrow \text{RO} + \text{NO}_2$ followed by fast fragmentation of the formed alkoxy radicals).

The fragmentation products are assumed to be the MCM compounds C717O2 (a peroxy radical) and CH3COCH3 (acetone) irrespectively of which autoxidation peroxy radical that react with NO. This is a simplification that violates the mass balance for O atoms but not for the N and C atoms.

49. C10H15O2O2 + NO → C717O2 + CH3COCH3 + NO2	KRO2NO*0.1
50. C10H15O3O2 + NO → C717O2 + CH3COCH3 + NO2	KRO2NO*0.1
51. C10H15O4O2 + NO → C717O2 + CH3COCH3 + NO2	KRO2NO*0.1
52. C10H15O5O2 + NO → C717O2 + CH3COCH3 + NO2	KRO2NO*0.1
53. C10H15O6O2 + NO → C717O2 + CH3COCH3 + NO2	KRO2NO*0.1
54. C10H15O7O2 + NO → C717O2 + CH3COCH3 + NO2	KRO2NO*0.15
55. C10H15O8O2 + NO → C717O2 + CH3COCH3 + NO2	KRO2NO*0.2
56. C10H15O9O2 + NO → C717O2 + CH3COCH3 + NO2	KRO2NO*0.2
57. C10H15O10O2 + NO → C717O2 + CH3COCH3 + NO2	KRO2NO*0.3
58. C10H15O11O2 + NO → C717O2 + CH3COCH3 + NO2	KRO2NO*0.4

Peroxy radicals reacting with NO forming monomers with an additional carbonyl group:

$\text{RO}_2 + \text{NO} \rightarrow \text{RO} + \text{NO}_2$

$\text{RO} + \text{O}_2 \rightarrow \text{RC=O} + \text{HO}_2$ (Fast)

Net: $\text{RO}_2 + \text{NO} + \text{O}_2 \rightarrow \text{RC=O} + \text{NO}_2 + \text{HO}_2$

59. C10H15O2O2 + NO → C10H14O3 + NO2 + HO2	KRO2NO*0.0
60. C10H15O3O2 + NO → C10H14O4 + NO2 + HO2	KRO2NO*0.0
61. C10H15O4O2 + NO → C10H14O5 + NO2 + HO2	KRO2NO*0.0
62. C10H15O5O2 + NO → C10H14O6 + NO2 + HO2	KRO2NO*0.0
63. C10H15O6O2 + NO → C10H14O7 + NO2 + HO2	KRO2NO*0.1*2/3
64. C10H15O7O2 + NO → C10H14O8 + NO2 + HO2	KRO2NO*0.15*2/3
65. C10H15O8O2 + NO → C10H14O9 + NO2 + HO2	KRO2NO*0.2*2/3
66. C10H15O9O2 + NO → C10H14O10 + NO2 + HO2	KRO2NO*0.3*2/3
67. C10H15O10O2 + NO → C10H14O11 + NO2 + HO2	KRO2NO*0.4*2/3
68. C10H15O11O2 + NO → C10H14O12 + NO2 + HO2	KRO2NO*0.6*2/3

Peroxy radicals reacting with NO forming compounds with a nitrate functional group ($\text{RO}_2 + \text{NO} \rightarrow \text{RNO}_3$)

69. C10H15O2O2 + NO → C10H15O2NO3	KRO2NO*0.0
70. C10H15O3O2 + NO → C10H15O3NO3	KRO2NO*0.0
71. C10H15O4O2 + NO → C10H15O4NO3	KRO2NO*0.0
72. C10H15O5O2 + NO → C10H15O5NO3	KRO2NO*0.0
73. C10H15O6O2 + NO → C10H15O6NO3	KRO2NO*0.1*1/3
74. C10H15O7O2 + NO → C10H15O7NO3	KRO2NO*0.15*1/3
75. C10H15O8O2 + NO → C10H15O8NO3	KRO2NO*0.2*1/3
76. C10H15O9O2 + NO → C10H15O9NO3	KRO2NO*0.3*1/3
77. C10H15O10O2 + NO → C10H15O10NO3	KRO2NO*0.4*1/3
78. C10H15O11O2 + NO → C10H15O11NO3	KRO2NO*0.6*1/3

Peroxy radicals reacting with HO2 forming compounds with an hydrogen peroxide functional group ($\text{RO}_2 + \text{HO}_2 \rightarrow \text{ROOH} + \text{O}_2$)

79. C10H15O2O2 + HO2 → C10H16O4	KRO2HO2
80. C10H15O3O2 + HO2 → C10H16O5	KRO2HO2
81. C10H15O4O2 + HO2 → C10H16O6	KRO2HO2
82. C10H15O5O2 + HO2 → C10H16O7	KRO2HO2
83. C10H15O6O2 + HO2 → C10H16O8	KRO2HO2
84. C10H15O7O2 + HO2 → C10H16O9	KRO2HO2
85. C10H15O8O2 + HO2 → C10H16O10	KRO2HO2
86. C10H15O9O2 + HO2 → C10H16O11	KRO2HO2
87. C10H15O10O2 + HO2 → C10H16O12	KRO2HO2
88. C10H15O11O2 + HO2 → C10H16O13	KRO2HO2

Peroxy radicals reacting with other peroxy radicals forming dimers ($\text{RO}_2 + \text{RO}_2 \rightarrow \text{ROOR} + \text{O}_2$)

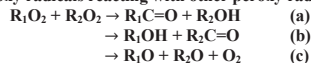
89. APINA02 + C10H15O2O2 → C20H30O6	1.1E-11
90. APINBO2 + C10H15O2O2 → C20H30O6	1.1E-11
91. APINCO2 + C10H15O2O2 → C20H30O6	1.1E-11
92. C107O2 + C10H15O2O2 → C20H30O6	1.1E-11
93. C109O2 + C10H15O2O2 → C20H30O6	1.1E-11
94. C106O2 + C10H15O2O2 → C20H30O6	1.1E-11
95. C920CO3 + C10H15O2O2 → C20H30O6	1.1E-11
96. C108O2 + C10H15O2O2 → C20H30O6	1.1E-11
97. PINALO2 + C10H15O2O2 → C20H30O6	1.1E-11
98. C96CO3 + C10H15O2O2 → C20H30O6	1.1E-11
99. C923CO3 + C10H15O2O2 → C20H30O6	1.1E-11
100. LIMA02 + C10H15O2O2 → C20H30O6	1.1E-11
101. LIMALBO2 + C10H15O2O2 → C20H30O6	1.1E-11

102. LIMCO ₂ + C ₁₀ H ₁₅ O ₂ O ₂ → C ₂₀ H ₃₀ O ₆	1.1E-11	
103. LIMALO ₂ + C ₁₀ H ₁₅ O ₂ O ₂ → C ₂₀ H ₃₀ O ₆	1.1E-11	
104. LIMBO ₂ + C ₁₀ H ₁₅ O ₂ O ₂ → C ₂₀ H ₃₀ O ₆	1.1E-11	
105. LIMALAO ₂ + C ₁₀ H ₁₅ O ₂ O ₂ → C ₂₀ H ₃₀ O ₆	1.1E-11	
106. NAPINA ₂ + C ₁₀ H ₁₅ O ₂ O ₂ → C ₂₀ H ₃₁ O ₄ NO ₃	1.1E-11	HOM dimers containing NO ₃
107. NAPINBO ₂ + C ₁₀ H ₁₅ O ₂ O ₂ → C ₂₀ H ₃₁ O ₄ NO ₃	1.1E-11	HOM dimers containing NO ₃
108. APINA ₂ + C ₁₀ H ₁₅ O ₃ O ₂ → C ₂₀ H ₃₀ O ₇	1.1E-11	
109. APINBO ₂ + C ₁₀ H ₁₅ O ₃ O ₂ → C ₂₀ H ₃₀ O ₇	1.1E-11	
110. APINCO ₂ + C ₁₀ H ₁₅ O ₃ O ₂ → C ₂₀ H ₃₀ O ₇	1.1E-11	
111. C ₁₀ H ₇ O ₂ + C ₁₀ H ₁₅ O ₃ O ₂ → C ₂₀ H ₃₀ O ₇	1.1E-11	
112. C ₁₀ H ₉ O ₂ + C ₁₀ H ₁₅ O ₃ O ₂ → C ₂₀ H ₃₀ O ₇	1.1E-11	
113. C ₁₀ H ₆ O ₂ + C ₁₀ H ₁₅ O ₃ O ₂ → C ₂₀ H ₃₀ O ₇	1.1E-11	
114. C ₉ H ₂₀ CO ₃ + C ₁₀ H ₁₅ O ₃ O ₂ → C ₂₀ H ₃₀ O ₇	1.1E-11	
115. C ₁₀ H ₈ O ₂ + C ₁₀ H ₁₅ O ₃ O ₂ → C ₂₀ H ₃₀ O ₇	1.1E-11	
116. PINALO ₂ + C ₁₀ H ₁₅ O ₃ O ₂ → C ₂₀ H ₃₀ O ₇	1.1E-11	
117. C ₉ H ₆ CO ₃ + C ₁₀ H ₁₅ O ₃ O ₂ → C ₂₀ H ₃₀ O ₇	1.1E-11	
118. C ₉ H ₂₃ CO ₃ + C ₁₀ H ₁₅ O ₃ O ₂ → C ₂₀ H ₃₀ O ₇	1.1E-11	
119. LIMAO ₂ + C ₁₀ H ₁₅ O ₃ O ₂ → C ₂₀ H ₃₀ O ₇	1.1E-11	
120. LIMALBO ₂ + C ₁₀ H ₁₅ O ₃ O ₂ → C ₂₀ H ₃₀ O ₇	1.1E-11	
121. LIMCO ₂ + C ₁₀ H ₁₅ O ₃ O ₂ → C ₂₀ H ₃₀ O ₇	1.1E-11	
122. LIMALO ₂ + C ₁₀ H ₁₅ O ₃ O ₂ → C ₂₀ H ₃₀ O ₇	1.1E-11	
123. LIMBO ₂ + C ₁₀ H ₁₅ O ₃ O ₂ → C ₂₀ H ₃₀ O ₇	1.1E-11	
124. LIMALAO ₂ + C ₁₀ H ₁₅ O ₃ O ₂ → C ₂₀ H ₃₀ O ₇	1.1E-11	
125. NAPINA ₂ + C ₁₀ H ₁₅ O ₃ O ₂ → C ₂₀ H ₃₁ O ₅ NO ₃	1.1E-11	HOM dimers containing NO ₃
126. NAPINBO ₂ + C ₁₀ H ₁₅ O ₃ O ₂ → C ₂₀ H ₃₁ O ₅ NO ₃	1.1E-11	HOM dimers containing NO ₃
127. APINA ₂ + C ₁₀ H ₁₅ O ₄ O ₂ → C ₂₀ H ₃₀ O ₈	1.1E-11	
128. APINBO ₂ + C ₁₀ H ₁₅ O ₄ O ₂ → C ₂₀ H ₃₀ O ₈	1.1E-11	
129. APINCO ₂ + C ₁₀ H ₁₅ O ₄ O ₂ → C ₂₀ H ₃₀ O ₈	1.1E-11	
130. C ₁₀ H ₇ O ₂ + C ₁₀ H ₁₅ O ₄ O ₂ → C ₂₀ H ₃₀ O ₈	1.1E-11	
131. C ₁₀ H ₉ O ₂ + C ₁₀ H ₁₅ O ₄ O ₂ → C ₂₀ H ₃₀ O ₈	1.1E-11	
132. C ₁₀ H ₆ O ₂ + C ₁₀ H ₁₅ O ₄ O ₂ → C ₂₀ H ₃₀ O ₈	1.1E-11	
133. C ₉ H ₂₀ CO ₃ + C ₁₀ H ₁₅ O ₄ O ₂ → C ₂₀ H ₃₀ O ₈	1.1E-11	
134. C ₁₀ H ₈ O ₂ + C ₁₀ H ₁₅ O ₄ O ₂ → C ₂₀ H ₃₀ O ₈	1.1E-11	
135. PINALO ₂ + C ₁₀ H ₁₅ O ₄ O ₂ → C ₂₀ H ₃₀ O ₈	1.1E-11	
136. C ₉ H ₆ CO ₃ + C ₁₀ H ₁₅ O ₄ O ₂ → C ₂₀ H ₃₀ O ₈	1.1E-11	
137. C ₉ H ₂₃ CO ₃ + C ₁₀ H ₁₅ O ₄ O ₂ → C ₂₀ H ₃₀ O ₈	1.1E-11	
138. LIMAO ₂ + C ₁₀ H ₁₅ O ₄ O ₂ → C ₂₀ H ₃₀ O ₈	1.1E-11	
139. LIMALBO ₂ + C ₁₀ H ₁₅ O ₄ O ₂ → C ₂₀ H ₃₀ O ₈	1.1E-11	
140. LIMCO ₂ + C ₁₀ H ₁₅ O ₄ O ₂ → C ₂₀ H ₃₀ O ₈	1.1E-11	
141. LIMALO ₂ + C ₁₀ H ₁₅ O ₄ O ₂ → C ₂₀ H ₃₀ O ₈	1.1E-11	
142. LIMBO ₂ + C ₁₀ H ₁₅ O ₄ O ₂ → C ₂₀ H ₃₀ O ₈	1.1E-11	
143. LIMALAO ₂ + C ₁₀ H ₁₅ O ₄ O ₂ → C ₂₀ H ₃₀ O ₈	1.1E-11	
144. NAPINA ₂ + C ₁₀ H ₁₅ O ₄ O ₂ → C ₂₀ H ₃₁ O ₆ NO ₃	1.1E-11	HOM dimers containing NO ₃
145. NAPINBO ₂ + C ₁₀ H ₁₅ O ₄ O ₂ → C ₂₀ H ₃₁ O ₆ NO ₃	1.1E-11	HOM dimers containing NO ₃
146. APINA ₂ + C ₁₀ H ₁₅ O ₅ O ₂ → C ₂₀ H ₃₀ O ₉	1.1E-11	
147. APINBO ₂ + C ₁₀ H ₁₅ O ₅ O ₂ → C ₂₀ H ₃₀ O ₉	1.1E-11	
148. APINCO ₂ + C ₁₀ H ₁₅ O ₅ O ₂ → C ₂₀ H ₃₀ O ₉	1.1E-11	
149. C ₁₀ H ₇ O ₂ + C ₁₀ H ₁₅ O ₅ O ₂ → C ₂₀ H ₃₀ O ₉	1.1E-11	
150. C ₁₀ H ₉ O ₂ + C ₁₀ H ₁₅ O ₅ O ₂ → C ₂₀ H ₃₀ O ₉	1.1E-11	
151. C ₁₀ H ₆ O ₂ + C ₁₀ H ₁₅ O ₅ O ₂ → C ₂₀ H ₃₀ O ₉	1.1E-11	
152. C ₉ H ₂₀ CO ₃ + C ₁₀ H ₁₅ O ₅ O ₂ → C ₂₀ H ₃₀ O ₉	1.1E-11	
153. C ₁₀ H ₈ O ₂ + C ₁₀ H ₁₅ O ₅ O ₂ → C ₂₀ H ₃₀ O ₉	1.1E-11	
154. PINALO ₂ + C ₁₀ H ₁₅ O ₅ O ₂ → C ₂₀ H ₃₀ O ₉	1.1E-11	
155. C ₉ H ₆ CO ₃ + C ₁₀ H ₁₅ O ₅ O ₂ → C ₂₀ H ₃₀ O ₉	1.1E-11	
156. C ₉ H ₂₃ CO ₃ + C ₁₀ H ₁₅ O ₅ O ₂ → C ₂₀ H ₃₀ O ₉	1.1E-11	
157. LIMAO ₂ + C ₁₀ H ₁₅ O ₅ O ₂ → C ₂₀ H ₃₀ O ₉	1.1E-11	
158. LIMALBO ₂ + C ₁₀ H ₁₅ O ₅ O ₂ → C ₂₀ H ₃₀ O ₉	1.1E-11	
159. LIMCO ₂ + C ₁₀ H ₁₅ O ₅ O ₂ → C ₂₀ H ₃₀ O ₉	1.1E-11	
160. LIMALO ₂ + C ₁₀ H ₁₅ O ₅ O ₂ → C ₂₀ H ₃₀ O ₉	1.1E-11	
161. LIMBO ₂ + C ₁₀ H ₁₅ O ₅ O ₂ → C ₂₀ H ₃₀ O ₉	1.1E-11	
162. LIMALAO ₂ + C ₁₀ H ₁₅ O ₅ O ₂ → C ₂₀ H ₃₀ O ₉	1.1E-11	
163. NAPINA ₂ + C ₁₀ H ₁₅ O ₅ O ₂ → C ₂₀ H ₃₁ O ₇ NO ₃	1.1E-11	HOM dimers containing NO ₃
164. NAPINBO ₂ + C ₁₀ H ₁₅ O ₅ O ₂ → C ₂₀ H ₃₁ O ₇ NO ₃	1.1E-11	HOM dimers containing NO ₃
165. APINA ₂ + C ₁₀ H ₁₅ O ₆ O ₂ → C ₂₀ H ₃₀ O ₁₀	1.1E-11	
166. APINBO ₂ + C ₁₀ H ₁₅ O ₆ O ₂ → C ₂₀ H ₃₀ O ₁₀	1.1E-11	
167. APINCO ₂ + C ₁₀ H ₁₅ O ₆ O ₂ → C ₂₀ H ₃₀ O ₁₀	1.1E-11	
168. C ₁₀ H ₇ O ₂ + C ₁₀ H ₁₅ O ₆ O ₂ → C ₂₀ H ₃₀ O ₁₀	1.1E-11	
169. C ₁₀ H ₉ O ₂ + C ₁₀ H ₁₅ O ₆ O ₂ → C ₂₀ H ₃₀ O ₁₀	1.1E-11	
170. C ₁₀ H ₆ O ₂ + C ₁₀ H ₁₅ O ₆ O ₂ → C ₂₀ H ₃₀ O ₁₀	1.1E-11	

171. C920CO3 + C10H15O6O2 → C20H30O10	1.1E-11	
172. C108O2 + C10H15O6O2 → C20H30O10	1.1E-11	
173. PINALO2 + C10H15O6O2 → C20H30O10	1.1E-11	
174. C96CO3 + C10H15O6O2 → C20H30O10	1.1E-11	
175. C923CO3 + C10H15O6O2 → C20H30O10	1.1E-11	
176. LIMAO2 + C10H15O6O2 → C20H30O10	1.1E-11	
177. LIMALBO2 + C10H15O6O2 → C20H30O10	1.1E-11	
178. LIMCO2 + C10H15O6O2 → C20H30O10	1.1E-11	
179. LIMALO2 + C10H15O6O2 → C20H30O10	1.1E-11	
180. LIMBO2 + C10H15O6O2 → C20H30O10	1.1E-11	
181. LIMALAO2 + C10H15O6O2 → C20H30O10	1.1E-11	
182. NAPINAO2 + C10H15O6O2 → C20H31O8NO3	1.1E-11	HOM dimers containing NO ₃
183. NAPINBO2 + C10H15O6O2 → C20H31O8NO3	1.1E-11	HOM dimers containing NO ₃
184. APINAO2 + C10H15O7O2 → C20H30O11	1.1E-11	
185. APINBO2 + C10H15O7O2 → C20H30O11	1.1E-11	
186. APINCO2 + C10H15O7O2 → C20H30O11	1.1E-11	
187. C107O2 + C10H15O7O2 → C20H30O11	1.1E-11	
188. C109O2 + C10H15O7O2 → C20H30O11	1.1E-11	
189. C106O2 + C10H15O7O2 → C20H30O11	1.1E-11	
190. C920CO3 + C10H15O7O2 → C20H30O11	1.1E-11	
191. C108O2 + C10H15O7O2 → C20H30O11	1.1E-11	
192. PINALO2 + C10H15O7O2 → C20H30O11	1.1E-11	
193. C96CO3 + C10H15O7O2 → C20H30O11	1.1E-11	
194. C923CO3 + C10H15O7O2 → C20H30O11	1.1E-11	
195. LIMAO2 + C10H15O7O2 → C20H30O11	1.1E-11	
196. LIMALBO2 + C10H15O7O2 → C20H30O11	1.1E-11	
197. LIMCO2 + C10H15O7O2 → C20H30O11	1.1E-11	
198. LIMALO2 + C10H15O7O2 → C20H30O11	1.1E-11	
199. LIMBO2 + C10H15O7O2 → C20H30O11	1.1E-11	
200. LIMALAO2 + C10H15O7O2 → C20H30O11	1.1E-11	
201. NAPINAO2 + C10H15O7O2 → C20H31O9NO3	1.1E-11	HOM dimers containing NO ₃
202. NAPINBO2 + C10H15O7O2 → C20H31O9NO3	1.1E-11	HOM dimers containing NO ₃
203. APINAO2 + C10H15O8O2 → C20H30O12	1.1E-11	
204. APINBO2 + C10H15O8O2 → C20H30O12	1.1E-11	
205. APINCO2 + C10H15O8O2 → C20H30O12	1.1E-11	
206. C107O2 + C10H15O8O2 → C20H30O12	1.1E-11	
207. C109O2 + C10H15O8O2 → C20H30O12	1.1E-11	
208. C106O2 + C10H15O8O2 → C20H30O12	1.1E-11	
209. C920CO3 + C10H15O8O2 → C20H30O12	1.1E-11	
210. C108O2 + C10H15O8O2 → C20H30O12	1.1E-11	
211. PINALO2 + C10H15O8O2 → C20H30O12	1.1E-11	
212. C96CO3 + C10H15O8O2 → C20H30O12	1.1E-11	
213. C923CO3 + C10H15O8O2 → C20H30O12	1.1E-11	
214. LIMAO2 + C10H15O8O2 → C20H30O12	1.1E-11	
215. LIMALBO2 + C10H15O8O2 → C20H30O12	1.1E-11	
216. LIMCO2 + C10H15O8O2 → C20H30O12	1.1E-11	
217. LIMALO2 + C10H15O8O2 → C20H30O12	1.1E-11	
218. LIMBO2 + C10H15O8O2 → C20H30O12	1.1E-11	
219. LIMALAO2 + C10H15O8O2 → C20H30O12	1.1E-11	
220. NAPINAO2 + C10H15O8O2 → C20H31O10NO3	1.1E-11	HOM dimers containing NO ₃
221. NAPINBO2 + C10H15O8O2 → C20H31O10NO3	1.1E-11	HOM dimers containing NO ₃
222. APINAO2 + C10H15O9O2 → C20H30O13	1.1E-11	
223. APINBO2 + C10H15O9O2 → C20H30O13	1.1E-11	
224. APINCO2 + C10H15O9O2 → C20H30O13	1.1E-11	
225. C107O2 + C10H15O9O2 → C20H30O13	1.1E-11	
226. C109O2 + C10H15O9O2 → C20H30O13	1.1E-11	
227. C106O2 + C10H15O9O2 → C20H30O13	1.1E-11	
228. C920CO3 + C10H15O9O2 → C20H30O13	1.1E-11	
229. C108O2 + C10H15O9O2 → C20H30O13	1.1E-11	
230. PINALO2 + C10H15O9O2 → C20H30O13	1.1E-11	
231. C96CO3 + C10H15O9O2 → C20H30O13	1.1E-11	
232. C923CO3 + C10H15O9O2 → C20H30O13	1.1E-11	
233. LIMAO2 + C10H15O9O2 → C20H30O13	1.1E-11	
234. LIMALBO2 + C10H15O9O2 → C20H30O13	1.1E-11	
235. LIMCO2 + C10H15O9O2 → C20H30O13	1.1E-11	
236. LIMALO2 + C10H15O9O2 → C20H30O13	1.1E-11	
237. LIMBO2 + C10H15O9O2 → C20H30O13	1.1E-11	
238. LIMALAO2 + C10H15O9O2 → C20H30O13	1.1E-11	
239. NAPINAO2 + C10H15O9O2 → C20H31O11NO3	1.1E-11	HOM dimers containing NO ₃
240. NAPINBO2 + C10H15O9O2 → C20H31O11NO3	1.1E-11	HOM dimers containing NO ₃

241. APINAO2 + C10H15O10O2 → C20H30O14	1.1E-11	
242. APINBO2 + C10H15O10O2 → C20H30O14	1.1E-11	
243. APINCO2 + C10H15O10O2 → C20H30O14	1.1E-11	
244. C107O2 + C10H15O10O2 → C20H30O14	1.1E-11	
245. C109O2 + C10H15O10O2 → C20H30O14	1.1E-11	
246. C106O2 + C10H15O10O2 → C20H30O14	1.1E-11	
247. C920CO3 + C10H15O10O2 → C20H30O14	1.1E-11	
248. C108O2 + C10H15O10O2 → C20H30O14	1.1E-11	
249. PINALO2 + C10H15O10O2 → C20H30O14	1.1E-11	
250. C96CO3 + C10H15O10O2 → C20H30O14	1.1E-11	
251. C923CO3 + C10H15O10O2 → C20H30O14	1.1E-11	
252. LIMA02 + C10H15O10O2 → C20H30O14	1.1E-11	
253. LIMALBO2 + C10H15O10O2 → C20H30O14	1.1E-11	
254. LIMCO2 + C10H15O10O2 → C20H30O14	1.1E-11	
255. LIMALO2 + C10H15O10O2 → C20H30O14	1.1E-11	
256. LIMBO2 + C10H15O10O2 → C20H30O14	1.1E-11	
257. LIMALAO2 + C10H15O10O2 → C20H30O14	1.1E-11	
258. NAPINAO2 + C10H15O10O2 → C20H31O12NO3	1.1E-11	HOM dimers containing NO ₃
259. NAPINBO2 + C10H15O10O2 → C20H31O12NO3	1.1E-11	HOM dimers containing NO ₃
260. APINAO2 + C10H15O11O2 → C20H30O15	1.1E-11	
261. APINBO2 + C10H15O11O2 → C20H30O15	1.1E-11	
262. APINCO2 + C10H15O11O2 → C20H30O15	1.1E-11	
263. C107O2 + C10H15O11O2 → C20H30O15	1.1E-11	
264. C109O2 + C10H15O11O2 → C20H30O15	1.1E-11	
265. C106O2 + C10H15O11O2 → C20H30O15	1.1E-11	
266. C920CO3 + C10H15O11O2 → C20H30O15	1.1E-11	
267. C108O2 + C10H15O11O2 → C20H30O15	1.1E-11	
268. PINALO2 + C10H15O11O2 → C20H30O15	1.1E-11	
269. C96CO3 + C10H15O11O2 → C20H30O15	1.1E-11	
270. C923CO3 + C10H15O11O2 → C20H30O15	1.1E-11	
271. LIMA02 + C10H15O11O2 → C20H30O15	1.1E-11	
272. LIMALBO2 + C10H15O11O2 → C20H30O15	1.1E-11	
273. LIMCO2 + C10H15O11O2 → C20H30O15	1.1E-11	
274. LIMALO2 + C10H15O11O2 → C20H30O15	1.1E-11	
275. LIMBO2 + C10H15O11O2 → C20H30O15	1.1E-11	
276. LIMALAO2 + C10H15O11O2 → C20H30O15	1.1E-11	
277. NAPINAO2 + C10H15O11O2 → C20H31O13NO3	1.1E-11	HOM dimers containing NO ₃
278. NAPINBO2 + C10H15O11O2 → C20H31O13NO3	1.1E-11	HOM dimers containing NO ₃

Autoxidation peroxy radicals reacting with other peroxy radicals with different branching ratios for a, b and c:



The branching ratios a, b and c are identical with the ratios used in MCMv3.3.1 when the respective MCM RO₂ species (listed in Table S2) react with other RO₂ in MCMv3.3.1.

279. APINAO2 + C10H15O2O2 → C10H14O3 + APINBOH	6E-11*0.3
280. APINAO2 + C10H15O2O2 → C10H15O2O + APINAO	6E-11*0.7
281. APINBO2 + C10H15O2O2 → C10H14O3 + APINBOH	6E-11*0.2
282. APINBO2 + C10H15O2O2 → C10H15O2O + APINBO	6E-11*0.6
283. APINBO2 + C10H15O2O2 → C10H16O3 + APINBCO	6E-11*0.2
284. APINCO2 + C10H15O2O2 → C10H15O2O + APINCO	6E-11*0.7
285. APINCO2 + C10H15O2O2 → C10H14O3 + APINCOH	6E-11*0.3
286. C107O2 + C10H15O2O2 → C10H15O2O + C107O	6E-11*0.7
287. C107O2 + C10H15O2O2 → C10H14O3 + C107OH	6E-11*0.3
288. C109O2 + C10H15O2O2 → C10H15O2O + C109O	6E-11*0.9
289. C109O2 + C10H15O2O2 → C10H14O3 + C109OH	6E-11*0.05
290. C109O2 + C10H15O2O2 → C10H16O3 + C109CO	6E-11*0.05
291. C106O2 + C10H15O2O2 → C10H15O2O + C106O	6E-11*0.7
292. C106O2 + C10H15O2O2 → C10H14O3 + C106OH	6E-11*0.3
293. C920CO3 + C10H15O2O2 → C10H15O2O + C920O2	6E-11*0.7
294. C920CO3 + C10H15O2O2 → C10H14O3 + HOPINONIC	6E-11*0.3
295. C108O2 + C10H15O2O2 → C10H15O2O + C108O	6E-11*0.7
296. C108O2 + C10H15O2O2 → C10H14O3 + C108OH	6E-11*0.3
297. PINALO2 + C10H15O2O2 → C10H15O2O + PINALO	6E-11*0.7
298. PINALO2 + C10H15O2O2 → C10H14O3 + PINALOH	6E-11*0.3
299. C96CO3 + C10H15O2O2 → C10H15O2O + C96O2	6E-11*0.7
300. C96CO3 + C10H15O2O2 → C10H14O3 + PINONIC	6E-11*0.3
301. C923CO3 + C10H15O2O2 → C10H15O2O + C923O2	6E-11*0.7
302. C923CO3 + C10H15O2O2 → C10H14O3 + LIMONONIC	6E-11*0.3
303. LIMA02 + C10H15O2O2 → C10H15O2O + LIMA0	6E-11*0.7
304. LIMA02 + C10H15O2O2 → C10H14O3 + LIMA0H	6E-11*0.3

305. LIMALBO2 + C10H15O2O2 → C10H16O3 + LIMALBCO	6E-11*0.05
306. LIMALBO2 + C10H15O2O2 → C10H15O2O + LIMALBO	6E-11*0.9
307. LIMALBO2 + C10H15O2O2 → C10H14O3 + LIMALBOH	6E-11*0.05
308. LIMCO2 + C10H15O2O2 → C10H15O2O + LIMCO	6E-11*0.7
309. LIMCO2 + C10H15O2O2 → C10H14O3 + LIMCOH	6E-11*0.3
310. LIMALO2 + C10H15O2O2 → C10H15O2O + LIMALO	6E-11*0.7
311. LIMALO2 + C10H15O2O2 → C10H14O3 + LIMALOH	6E-11*0.3
312. LIMBO2 + C10H15O2O2 → C10H14O3 + LIMAOH	6E-11*0.2
313. LIMBO2 + C10H15O2O2 → C10H16O3 + LIMBCO	6E-11*0.2
314. LIMBO2 + C10H15O2O2 → C10H15O2O + LIMBO	6E-11*0.6
315. LIMALAO2 + C10H15O2O2 → C10H16O3 + LIMALACO	6E-11*0.2
316. LIMALAO2 + C10H15O2O2 → C10H15O2O + LIMALAO	6E-11*0.6
317. LIMALAO2 + C10H15O2O2 → C10H14O3 + LIMALAOH	6E-11*0.2
318. NAPINAO2 + C10H15O2O2 → C10H14O3 + APINBNO3	6E-11*0.1
319. NAPINAO2 + C10H15O2O2 → C10H15O2O + NAPINAO	6E-11*0.9
320. NAPINBO2 + C10H15O2O2 → C10H14O3 + APINANO3	6E-11*0.1
321. NAPINBO2 + C10H15O2O2 → C10H15O2O + NAPINBO	6E-11*0.8
322. NAPINBO2 + C10H15O2O2 → C10H16O3 + NC101CO	6E-11*0.1
323. APINAO2 + C10H15O3O2 → C10H14O4 + APINBOH	6E-11*0.3
324. APINAO2 + C10H15O3O2 → C10H15O3O + APINAO	6E-11*0.7
325. APINBO2 + C10H15O3O2 → C10H14O4 + APINBOH	6E-11*0.2
326. APINBO2 + C10H15O3O2 → C10H15O3O + APINBO	6E-11*0.6
327. APINBO2 + C10H15O3O2 → C10H16O4 + APINBCO	6E-11*0.2
328. APINCO2 + C10H15O3O2 → C10H15O3O + APINCO	6E-11*0.7
329. APINCO2 + C10H15O3O2 → C10H14O4 + APINCOH	6E-11*0.3
330. C107O2 + C10H15O3O2 → C10H15O3O + C107O	6E-11*0.7
331. C107O2 + C10H15O3O2 → C10H14O4 + C107OH	6E-11*0.3
332. C109O2 + C10H15O3O2 → C10H15O3O + C109O	6E-11*0.9
333. C109O2 + C10H15O3O2 → C10H14O4 + C109OH	6E-11*0.05
334. C109O2 + C10H15O3O2 → C10H16O4 + C109CO	6E-11*0.05
335. C106O2 + C10H15O3O2 → C10H15O3O + C106O	6E-11*0.7
336. C106O2 + C10H15O3O2 → C10H14O4 + C106OH	6E-11*0.3
337. C920CO3 + C10H15O3O2 → C10H15O3O + C920O2	6E-11*0.7
338. C920CO3 + C10H15O3O2 → C10H14O4 + HOPINONIC	6E-11*0.3
339. C108O2 + C10H15O3O2 → C10H15O3O + C108O	6E-11*0.7
340. C108O2 + C10H15O3O2 → C10H14O4 + C108OH	6E-11*0.3
341. PINALO2 + C10H15O3O2 → C10H15O3O + PINALO	6E-11*0.7
342. PINALO2 + C10H15O3O2 → C10H14O4 + PINALOH	6E-11*0.3
343. C96CO2 + C10H15O3O2 → C10H15O3O + C96O2	6E-11*0.7
344. C96CO2 + C10H15O3O2 → C10H14O4 + PINONIC	6E-11*0.3
345. C923CO3 + C10H15O3O2 → C10H15O3O + C923O2	6E-11*0.7
346. C923CO3 + C10H15O3O2 → C10H14O4 + LIMONONIC	6E-11*0.3
347. LIMA02 + C10H15O3O2 → C10H15O3O + LIMA0	6E-11*0.7
348. LIMA02 + C10H15O3O2 → C10H14O4 + LIMAOH	6E-11*0.3
349. LIMALBO2 + C10H15O3O2 → C10H16O4 + LIMALBCO	6E-11*0.05
350. LIMALBO2 + C10H15O3O2 → C10H15O3O + LIMALBO	6E-11*0.9
351. LIMALBO2 + C10H15O3O2 → C10H14O4 + LIMALBOH	6E-11*0.05
352. LIMCO2 + C10H15O3O2 → C10H15O3O + LIMCO	6E-11*0.7
353. LIMCO2 + C10H15O3O2 → C10H14O4 + LIMCOH	6E-11*0.3
354. LIMALO2 + C10H15O3O2 → C10H15O3O + LIMALO	6E-11*0.7
355. LIMALO2 + C10H15O3O2 → C10H14O4 + LIMALOH	6E-11*0.3
356. LIMBO2 + C10H15O3O2 → C10H14O4 + LIMAOH	6E-11*0.2
357. LIMBO2 + C10H15O3O2 → C10H16O4 + LIMBCO	6E-11*0.2
358. LIMBO2 + C10H15O3O2 → C10H15O3O + LIMBO	6E-11*0.6
359. LIMALAO2 + C10H15O3O2 → C10H16O4 + LIMALACO	6E-11*0.2
360. LIMALAO2 + C10H15O3O2 → C10H15O3O + LIMALAO	6E-11*0.6
361. LIMALAO2 + C10H15O3O2 → C10H14O4 + LIMALAOH	6E-11*0.2
362. NAPINAO2 + C10H15O3O2 → C10H14O4 + APINBNO3	6E-11*0.1
363. NAPINAO2 + C10H15O3O2 → C10H15O5O + NAPINAO	6E-11*0.9
364. NAPINBO2 + C10H15O3O2 → C10H14O4 + APINANO3	6E-11*0.1
365. NAPINBO2 + C10H15O3O2 → C10H15O4O + NAPINBO	6E-11*0.8
366. NAPINBO2 + C10H15O3O2 → C10H16O4 + NC101CO	6E-11*0.1
367. APINAO2 + C10H15O4O2 → C10H14O5 + APINBOH	6E-11*0.3
368. APINAO2 + C10H15O4O2 → C10H15O4O + APINAO	6E-11*0.7
369. APINBO2 + C10H15O4O2 → C10H14O5 + APINBOH	6E-11*0.2
370. APINBO2 + C10H15O4O2 → C10H15O4O + APINBO	6E-11*0.6
371. APINBO2 + C10H15O4O2 → C10H16O5 + APINBCO	6E-11*0.2
372. APINCO2 + C10H15O4O2 → C10H15O4O + APINCO	6E-11*0.7
373. APINCO2 + C10H15O4O2 → C10H14O5 + APINCOH	6E-11*0.3
374. C107O2 + C10H15O4O2 → C10H15O4O + C107O	6E-11*0.7
375. C107O2 + C10H15O4O2 → C10H14O5 + C107OH	6E-11*0.3

376. C109O2 + C10H15O4O2 → C10H15O4O + C109O	6E-11*0.9
377. C109O2 + C10H15O4O2 → C10H14O5 + C109OH	6E-11*0.05
378. C109O2 + C10H15O4O2 → C10H16O5 + C109CO	6E-11*0.05
379. C106O2 + C10H15O4O2 → C10H15O4O + C106O	6E-11*0.7
380. C106O2 + C10H15O4O2 → C10H14O5 + C106OH	6E-11*0.3
381. C920CO3 + C10H15O4O2 → C10H15O4O + C920O2	6E-11*0.7
382. C920CO3 + C10H15O4O2 → C10H14O5 + HOPINONIC	6E-11*0.3
383. C108O2 + C10H15O4O2 → C10H15O4O + C108O	6E-11*0.7
384. C108O2 + C10H15O4O2 → C10H14O5 + C108OH	6E-11*0.3
385. PINALO2 + C10H15O4O2 → C10H15O4O + PINALO	6E-11*0.7
386. PINALO2 + C10H15O4O2 → C10H14O5 + PINALOH	6E-11*0.3
387. C96CO3 + C10H15O4O2 → C10H15O4O + C96O2	6E-11*0.7
388. C96CO3 + C10H15O4O2 → C10H14O5 + PINONIC	6E-11*0.3
389. C923CO3 + C10H15O4O2 → C10H15O4O + C923O2	6E-11*0.7
390. C923CO3 + C10H15O4O2 → C10H14O5 + LIMONONIC	6E-11*0.3
391. LIMA02 + C10H15O4O2 → C10H15O4O + LIMA0	6E-11*0.7
392. LIMA02 + C10H15O4O2 → C10H14O5 + LIMA0H	6E-11*0.3
393. LIMALBO2 + C10H15O4O2 → C10H16O5 + LIMALBCO	6E-11*0.05
394. LIMALBO2 + C10H15O4O2 → C10H15O4O + LIMALBO	6E-11*0.9
395. LIMALBO2 + C10H15O4O2 → C10H14O5 + LIMALBOH	6E-11*0.05
396. LIMCO2 + C10H15O4O2 → C10H15O4O + LIMCO	6E-11*0.7
397. LIMCO2 + C10H15O4O2 → C10H14O5 + LIMCOH	6E-11*0.3
398. LIMALO2 + C10H15O4O2 → C10H15O4O + LIMALO	6E-11*0.7
399. LIMALO2 + C10H15O4O2 → C10H14O5 + LIMALOH	6E-11*0.3
400. LIMBO2 + C10H15O4O2 → C10H14O5 + LIMA0H	6E-11*0.2
401. LIMBO2 + C10H15O4O2 → C10H16O5 + LIMBCO	6E-11*0.2
402. LIMBO2 + C10H15O4O2 → C10H15O4O + LIMBO	6E-11*0.6
403. LIMALAO2 + C10H15O4O2 → C10H16O5 + LIMALACO	6E-11*0.2
404. LIMALAO2 + C10H15O4O2 → C10H15O4O + LIMALAO	6E-11*0.6
405. LIMALAO2 + C10H15O4O2 → C10H14O5 + LIMALAOH	6E-11*0.2
406. NAPINA02 + C10H15O4O2 → C10H14O5 + APINBNO3	6E-11*0.1
407. NAPINA02 + C10H15O4O2 → C10H15O4O + NAPINA0	6E-11*0.9
408. NAPINBO2 + C10H15O4O2 → C10H14O5 + APINANO3	6E-11*0.1
409. NAPINBO2 + C10H15O4O2 → C10H15O4O + NAPINBO	6E-11*0.8
410. NAPINBO2 + C10H15O4O2 → C10H16O5 + NC101CO	6E-11*0.1
411. APINA02 + C10H15O5O2 → C10H14O6 + APINBOH	6E-11*0.3
412. APINA02 + C10H15O5O2 → C10H15O5O + APINA0	6E-11*0.7
413. APINBO2 + C10H15O5O2 → C10H14O6 + APINBOH	6E-11*0.2
414. APINBO2 + C10H15O5O2 → C10H15O5O + APINBO	6E-11*0.6
415. APINBO2 + C10H15O5O2 → C10H16O6 + APINBCO	6E-11*0.2
416. APINCO2 + C10H15O5O2 → C10H15O5O + APINCO	6E-11*0.7
417. APINCO2 + C10H15O5O2 → C10H14O6 + APINCOH	6E-11*0.3
418. C107O2 + C10H15O5O2 → C10H15O5O + C107O	6E-11*0.7
419. C107O2 + C10H15O5O2 → C10H14O6 + C107OH	6E-11*0.3
420. C109O2 + C10H15O5O2 → C10H15O5O + C109O	6E-11*0.9
421. C109O2 + C10H15O5O2 → C10H14O6 + C109OH	6E-11*0.05
422. C109O2 + C10H15O5O2 → C10H16O6 + C109CO	6E-11*0.05
423. C106O2 + C10H15O5O2 → C10H15O5O + C106O	6E-11*0.7
424. C106O2 + C10H15O5O2 → C10H14O6 + C106OH	6E-11*0.3
425. C920CO3 + C10H15O5O2 → C10H15O5O + C920O2	6E-11*0.7
426. C920CO3 + C10H15O5O2 → C10H14O6 + HOPINONIC	6E-11*0.3
427. C108O2 + C10H15O5O2 → C10H15O5O + C108O	6E-11*0.7
428. C108O2 + C10H15O5O2 → C10H14O6 + C108OH	6E-11*0.3
429. PINALO2 + C10H15O5O2 → C10H15O5O + PINALO	6E-11*0.7
430. PINALO2 + C10H15O5O2 → C10H14O6 + PINALOH	6E-11*0.3
431. C96CO3 + C10H15O5O2 → C10H15O5O + C96O2	6E-11*0.7
432. C96CO3 + C10H15O5O2 → C10H14O6 + PINONIC	6E-11*0.3
433. C923CO3 + C10H15O5O2 → C10H15O5O + C923O2	6E-11*0.7
434. C923CO3 + C10H15O5O2 → C10H14O6 + LIMONONIC	6E-11*0.3
435. LIMA02 + C10H15O5O2 → C10H15O5O + LIMA0	6E-11*0.7
436. LIMA02 + C10H15O5O2 → C10H14O6 + LIMA0H	6E-11*0.3
437. LIMALBO2 + C10H15O5O2 → C10H16O6 + LIMALBCO	6E-11*0.05
438. LIMALBO2 + C10H15O5O2 → C10H15O5O + LIMALBO	6E-11*0.9
439. LIMALBO2 + C10H15O5O2 → C10H14O6 + LIMALBOH	6E-11*0.05
440. LIMCO2 + C10H15O5O2 → C10H15O5O + LIMCO	6E-11*0.7
441. LIMCO2 + C10H15O5O2 → C10H14O6 + LIMCOH	6E-11*0.3
442. LIMALO2 + C10H15O5O2 → C10H15O5O + LIMALO	6E-11*0.7
443. LIMALO2 + C10H15O5O2 → C10H14O6 + LIMALOH	6E-11*0.3
444. LIMBO2 + C10H15O5O2 → C10H14O6 + LIMA0H	6E-11*0.2
445. LIMBO2 + C10H15O5O2 → C10H16O6 + LIMBCO	6E-11*0.2
446. LIMBO2 + C10H15O5O2 → C10H15O5O + LIMBO	6E-11*0.6
447. LIMALAO2 + C10H15O5O2 → C10H16O6 + LIMALACO	6E-11*0.2
448. LIMALAO2 + C10H15O5O2 → C10H15O5O + LIMALAO	6E-11*0.6

449. LIMALAO2 + C10H15O5O2 → C10H14O6 + LIMALAOH	6E-11*0.2
450. NAPINAO2 + C10H15O5O2 → C10H14O6 + APINBNO3	6E-11*0.1
451. NAPINAO2 + C10H15O5O2 → C10H15O5O + NAPINAO	6E-11*0.9
452. NAPINBO2 + C10H15O5O2 → C10H14O6 + APINANO3	6E-11*0.1
453. NAPINBO2 + C10H15O5O2 → C10H15O5O + NAPINBO	6E-11*0.8
454. NAPINBO2 + C10H15O5O2 → C10H16O6 + NC101CO	6E-11*0.1
455. APINAO2 + C10H15O6O2 → C10H14O7 + APINBOH	6E-11*0.3
456. APINAO2 + C10H15O6O2 → C10H15O6O + APINAO	6E-11*0.7
457. APINBO2 + C10H15O6O2 → C10H14O7 + APINBOH	6E-11*0.2
458. APINBO2 + C10H15O6O2 → C10H15O6O + APINBO	6E-11*0.6
459. APINBO2 + C10H15O6O2 → C10H16O7 + APINBCO	6E-11*0.2
460. APINCO2 + C10H15O6O2 → C10H15O6O + APINCO	6E-11*0.7
461. APINCO2 + C10H15O6O2 → C10H14O7 + APINCOH	6E-11*0.3
462. C107O2 + C10H15O6O2 → C10H15O6O + C107O	6E-11*0.7
463. C107O2 + C10H15O6O2 → C10H14O7 + C107OH	6E-11*0.3
464. C109O2 + C10H15O6O2 → C10H15O6O + C109O	6E-11*0.9
465. C109O2 + C10H15O6O2 → C10H14O7 + C109OH	6E-11*0.05
466. C109O2 + C10H15O6O2 → C10H16O7 + C109CO	6E-11*0.05
467. C106O2 + C10H15O6O2 → C10H15O6O + C106O	6E-11*0.7
468. C106O2 + C10H15O6O2 → C10H14O7 + C106OH	6E-11*0.3
469. C920CO3 + C10H15O6O2 → C10H15O6O + C920O2	6E-11*0.7
470. C920CO3 + C10H15O6O2 → C10H14O7 + HOPINONIC	6E-11*0.3
471. C108O2 + C10H15O6O2 → C10H15O6O + C108O	6E-11*0.7
472. C108O2 + C10H15O6O2 → C10H14O7 + C108OH	6E-11*0.3
473. PINALO2 + C10H15O6O2 → C10H15O6O + PINALO	6E-11*0.7
474. PINALO2 + C10H15O6O2 → C10H14O7 + PINALOH	6E-11*0.3
475. C96CO3 + C10H15O6O2 → C10H15O6O + C96O2	6E-11*0.7
476. C96CO3 + C10H15O6O2 → C10H14O7 + PINONIC	6E-11*0.3
477. C923CO3 + C10H15O6O2 → C10H15O6O + C923O2	6E-11*0.7
478. C923CO3 + C10H15O6O2 → C10H14O7 + LIMONONIC	6E-11*0.3
479. LIMAO2 + C10H15O6O2 → C10H15O6O + LIMAO	6E-11*0.7
480. LIMAO2 + C10H15O6O2 → C10H14O7 + LIMAOH	6E-11*0.3
481. LIMALBO2 + C10H15O6O2 → C10H16O7 + LIMALBCO	6E-11*0.05
482. LIMALBO2 + C10H15O6O2 → C10H15O6O + LIMALBO	6E-11*0.9
483. LIMALBO2 + C10H15O6O2 → C10H14O7 + LIMALBOH	6E-11*0.05
484. LIMCO2 + C10H15O6O2 → C10H15O6O + LIMCO	6E-11*0.7
485. LIMCO2 + C10H15O6O2 → C10H14O7 + LIMCOH	6E-11*0.3
486. LIMALO2 + C10H15O6O2 → C10H15O6O + LIMALO	6E-11*0.7
487. LIMALO2 + C10H15O6O2 → C10H14O7 + LIMALOH	6E-11*0.3
488. LIMBO2 + C10H15O6O2 → C10H14O7 + LIMAOH	6E-11*0.2
489. LIMBO2 + C10H15O6O2 → C10H16O7 + LIMBCO	6E-11*0.2
490. LIMBO2 + C10H15O6O2 → C10H15O6O + LIMBO	6E-11*0.6
491. LIMALAO2 + C10H15O6O2 → C10H16O7 + LIMALACO	6E-11*0.2
492. LIMALAO2 + C10H15O6O2 → C10H15O6O + LIMALAO	6E-11*0.6
493. LIMALAO2 + C10H15O6O2 → C10H14O7 + LIMALAOH	6E-11*0.2
494. NAPINAO2 + C10H15O6O2 → C10H14O7 + APINBNO3	6E-11*0.1
495. NAPINAO2 + C10H15O6O2 → C10H15O6O + NAPINAO	6E-11*0.9
496. NAPINBO2 + C10H15O6O2 → C10H14O7 + APINANO3	6E-11*0.1
497. NAPINBO2 + C10H15O6O2 → C10H15O6O + NAPINBO	6E-11*0.8
498. NAPINBO2 + C10H15O6O2 → C10H16O7 + NC101CO	6E-11*0.1
499. APINAO2 + C10H15O7O2 → C10H14O8 + APINBOH	6E-11*0.3
500. APINAO2 + C10H15O7O2 → C10H15O7O + APINAO	6E-11*0.7
501. APINBO2 + C10H15O7O2 → C10H14O8 + APINBOH	6E-11*0.2
502. APINBO2 + C10H15O7O2 → C10H15O7O + APINBO	6E-11*0.6
503. APINBO2 + C10H15O7O2 → C10H16O8 + APINBCO	6E-11*0.2
504. APINCO2 + C10H15O7O2 → C10H15O7O + APINCO	6E-11*0.7
505. APINCO2 + C10H15O7O2 → C10H14O8 + APINCOH	6E-11*0.3
506. C107O2 + C10H15O7O2 → C10H15O7O + C107O	6E-11*0.7
507. C107O2 + C10H15O7O2 → C10H14O8 + C107OH	6E-11*0.3
508. C109O2 + C10H15O7O2 → C10H15O7O + C109O	6E-11*0.9
509. C109O2 + C10H15O7O2 → C10H14O8 + C109OH	6E-11*0.05
510. C109O2 + C10H15O7O2 → C10H16O8 + C109CO	6E-11*0.05
511. C106O2 + C10H15O7O2 → C10H15O7O + C106O	6E-11*0.7
512. C106O2 + C10H15O7O2 → C10H14O8 + C106OH	6E-11*0.3
513. C920CO3 + C10H15O7O2 → C10H15O7O + C920O2	6E-11*0.7
514. C920CO3 + C10H15O7O2 → C10H14O8 + HOPINONIC	6E-11*0.3
515. C108O2 + C10H15O7O2 → C10H15O7O + C108O	6E-11*0.7
516. C108O2 + C10H15O7O2 → C10H14O8 + C108OH	6E-11*0.3
517. PINALO2 + C10H15O7O2 → C10H15O7O + PINALO	6E-11*0.7
518. PINALO2 + C10H15O7O2 → C10H14O8 + PINALOH	6E-11*0.3
519. C96CO3 + C10H15O7O2 → C10H15O7O + C96O2	6E-11*0.7
520. C96CO3 + C10H15O7O2 → C10H14O8 + PINONIC	6E-11*0.3
521. C923CO3 + C10H15O7O2 → C10H15O7O + C923O2	6E-11*0.7

522. C923CO3 + C10H15O7O2 → C10H14O8 + LIMONONIC	6E-11*0.3
523. LIMA02 + C10H15O7O2 → C10H15O7O + LIMA0	6E-11*0.7
524. LIMA02 + C10H15O7O2 → C10H14O8 + LIMA0H	6E-11*0.3
525. LIMALBO2 + C10H15O7O2 → C10H16O8 + LIMALBCO	6E-11*0.05
526. LIMALBO2 + C10H15O7O2 → C10H15O7O + LIMALBO	6E-11*0.9
527. LIMALBO2 + C10H15O7O2 → C10H14O8 + LIMALBOH	6E-11*0.05
528. LIMCO2 + C10H15O7O2 → C10H15O7O + LIMCO	6E-11*0.7
529. LIMCO2 + C10H15O7O2 → C10H14O8 + LIMCOH	6E-11*0.3
530. LIMALO2 + C10H15O7O2 → C10H15O7O + LIMALO	6E-11*0.7
531. LIMALO2 + C10H15O7O2 → C10H14O8 + LIMALOH	6E-11*0.3
532. LIMBO2 + C10H15O7O2 → C10H14O8 + LIMA0H	6E-11*0.2
533. LIMBO2 + C10H15O7O2 → C10H16O8 + LIMBCO	6E-11*0.2
534. LIMBO2 + C10H15O7O2 → C10H15O7O + LIMBO	6E-11*0.6
535. LIMALA02 + C10H15O7O2 → C10H16O8 + LIMALACO	6E-11*0.2
536. LIMALA02 + C10H15O7O2 → C10H15O7O + LIMALA0	6E-11*0.6
537. LIMALA02 + C10H15O7O2 → C10H14O8 + LIMALA0H	6E-11*0.2
538. NAPINA02 + C10H15O7O2 → C10H14O8 + APINBNO3	6E-11*0.1
539. NAPINA02 + C10H15O7O2 → C10H15O7O + NAPINA0	6E-11*0.9
540. NAPINBO2 + C10H15O7O2 → C10H14O8 + APINANO3	6E-11*0.1
541. NAPINBO2 + C10H15O7O2 → C10H15O7O + NAPINBO	6E-11*0.8
542. NAPINBO2 + C10H15O7O2 → C10H16O8 + NC101CO	6E-11*0.1
543. APINA02 + C10H15O8O2 → C10H16O9 + APINBCO	6E-11*0.3
544. APINA02 + C10H15O8O2 → C10H15O8O + APINA0	6E-11*0.7
545. APINBO2 + C10H15O8O2 → C10H14O9 + APINBOH	6E-11*0.2
546. APINBO2 + C10H15O8O2 → C10H15O8O + APINBO	6E-11*0.6
547. APINBO2 + C10H15O8O2 → C10H16O9 + APINBCO	6E-11*0.2
548. APINCO2 + C10H15O8O2 → C10H15O8O + APINCO	6E-11*0.3
549. APINCO2 + C10H15O8O2 → C10H14O9 + APINCOH	6E-11*0.7
550. C107O2 + C10H15O8O2 → C10H15O8O + C107O	6E-11*0.3
551. C107O2 + C10H15O8O2 → C10H14O9 + C107OH	6E-11*0.7
552. C109O2 + C10H15O8O2 → C10H15O8O + C109O	6E-11*0.9
553. C109O2 + C10H15O8O2 → C10H14O9 + C109OH	6E-11*0.05
554. C109O2 + C10H15O8O2 → C10H16O9 + C109CO	6E-11*0.05
555. C106O2 + C10H15O8O2 → C10H15O8O + C106O	6E-11*0.7
556. C106O2 + C10H15O8O2 → C10H14O9 + C106OH	6E-11*0.3
557. C920CO3 + C10H15O8O2 → C10H15O8O + C920O2	6E-11*0.3
558. C920CO3 + C10H15O8O2 → C10H14O9 + HOPINONIC	6E-11*0.7
559. C108O2 + C10H15O8O2 → C10H15O8O + C108O	6E-11*0.3
560. C108O2 + C10H15O8O2 → C10H14O9 + C108OH	6E-11*0.7
561. PINALO2 + C10H15O8O2 → C10H15O8O + PINALO	6E-11*0.3
562. PINALO2 + C10H15O8O2 → C10H14O9 + PINALOH	6E-11*0.7
563. C96CO3 + C10H15O8O2 → C10H15O8O + C96O2	6E-11*0.3
564. C96CO3 + C10H15O8O2 → C10H14O9 + PINONIC	6E-11*0.7
565. C923CO3 + C10H15O8O2 → C10H15O8O + C923O2	6E-11*0.7
566. C923CO3 + C10H15O8O2 → C10H14O9 + LIMONONIC	6E-11*0.3
567. LIMA02 + C10H15O8O2 → C10H15O8O + LIMA0	6E-11*0.7
568. LIMA02 + C10H15O8O2 → C10H14O9 + LIMA0H	6E-11*0.3
569. LIMALBO2 + C10H15O8O2 → C10H16O9 + LIMALBCO	6E-11*0.05
570. LIMALBO2 + C10H15O8O2 → C10H15O8O + LIMALBO	6E-11*0.9
571. LIMALBO2 + C10H15O8O2 → C10H14O9 + LIMALBOH	6E-11*0.05
572. LIMCO2 + C10H15O8O2 → C10H15O8O + LIMCO	6E-11*0.7
573. LIMCO2 + C10H15O8O2 → C10H14O9 + LIMCOH	6E-11*0.3
574. LIMALO2 + C10H15O8O2 → C10H15O8O + LIMALO	6E-11*0.7
575. LIMALO2 + C10H15O8O2 → C10H14O9 + LIMALOH	6E-11*0.3
576. LIMBO2 + C10H15O8O2 → C10H14O9 + LIMA0H	6E-11*0.2
577. LIMBO2 + C10H15O8O2 → C10H16O9 + LIMBCO	6E-11*0.2
578. LIMBO2 + C10H15O8O2 → C10H15O8O + LIMBO	6E-11*0.6
579. LIMALA02 + C10H15O8O2 → C10H16O9 + LIMALACO	6E-11*0.2
580. LIMALA02 + C10H15O8O2 → C10H15O8O + LIMALA0	6E-11*0.6
581. LIMALA02 + C10H15O8O2 → C10H14O9 + LIMALA0H	6E-11*0.2
582. NAPINA02 + C10H15O8O2 → C10H14O9 + APINBNO3	6E-11*0.1
583. NAPINA02 + C10H15O8O2 → C10H15O8O + NAPINA0	6E-11*0.9
584. NAPINBO2 + C10H15O8O2 → C10H14O9 + APINANO3	6E-11*0.1
585. NAPINBO2 + C10H15O8O2 → C10H15O8O + NAPINBO	6E-11*0.8
586. NAPINBO2 + C10H15O8O2 → C10H16O9 + NC101CO	6E-11*0.1
587. APINA02 + C10H15O9O2 → C10H14O10 + APINBOH	6E-11*0.3
588. APINA02 + C10H15O9O2 → C10H15O9O + APINA0	6E-11*0.7
589. APINBO2 + C10H15O9O2 → C10H14O10 + APINBOH	6E-11*0.2
590. APINBO2 + C10H15O9O2 → C10H15O9O + APINBO	6E-11*0.6
591. APINBO2 + C10H15O9O2 → C10H16O10 + APINBCO	6E-11*0.2
592. APINCO2 + C10H15O9O2 → C10H15O9O + APINCO	6E-11*0.7
593. APINCO2 + C10H15O9O2 → C10H14O10 + APINCOH	6E-11*0.3

594. C107O2 + C10H15O9O2 → C10H15O9O + C107O	6E-11*0.7
595. C107O2 + C10H15O9O2 → C10H14O10 + C107OH	6E-11*0.3
596. C109O2 + C10H15O9O2 → C10H15O9O + C109O	6E-11*0.9
597. C109O2 + C10H15O9O2 → C10H14O10 + C109OH	6E-11*0.05
598. C109O2 + C10H15O9O2 → C10H16O10 + C109CO	6E-11*0.05
599. C106O2 + C10H15O9O2 → C10H15O9O + C106O	6E-11*0.7
600. C106O2 + C10H15O9O2 → C10H14O10 + C106OH	6E-11*0.3
601. C920CO3 + C10H15O9O2 → C10H15O9O + C920O2	6E-11*0.7
602. C920CO3 + C10H15O9O2 → C10H14O10 + HOPINONIC	6E-11*0.3
603. C108O2 + C10H15O9O2 → C10H15O9O + C108O	6E-11*0.7
604. C108O2 + C10H15O9O2 → C10H14O10 + C108OH	6E-11*0.3
605. PINALO2 + C10H15O9O2 → C10H15O9O + PINALO	6E-11*0.7
606. PINALO2 + C10H15O9O2 → C10H14O10 + PINALOH	6E-11*0.3
607. C96CO3 + C10H15O9O2 → C10H15O9O + C96O2	6E-11*0.7
608. C96CO3 + C10H15O9O2 → C10H14O10 + PINONIC	6E-11*0.3
609. C923CO3 + C10H15O9O2 → C10H15O9O + C923O2	6E-11*0.7
610. C923CO3 + C10H15O9O2 → C10H14O10 + LIMONONIC	6E-11*0.3
611. LIMAO2 + C10H15O9O2 → C10H15O9O + LIMAO	6E-11*0.7
612. LIMAO2 + C10H15O9O2 → C10H14O10 + LIMAOH	6E-11*0.3
613. LIMALBO2 + C10H15O9O2 → C10H16O10 + LIMALBCO	6E-11*0.05
614. LIMALBO2 + C10H15O9O2 → C10H15O9O + LIMALBO	6E-11*0.9
615. LIMALBO2 + C10H15O9O2 → C10H14O10 + LIMALBOH	6E-11*0.05
616. LIMCO2 + C10H15O9O2 → C10H15O9O + LIMCO	6E-11*0.7
617. LIMCO2 + C10H15O9O2 → C10H14O10 + LIMCOH	6E-11*0.3
618. LIMALO2 + C10H15O9O2 → C10H15O9O + LIMALO	6E-11*0.7
619. LIMALO2 + C10H15O9O2 → C10H14O10 + LIMALOH	6E-11*0.3
620. LIMBO2 + C10H15O9O2 → C10H14O10 + LIMAOH	6E-11*0.2
621. LIMBO2 + C10H15O9O2 → C10H16O10 + LIMBCO	6E-11*0.2
622. LIMBO2 + C10H15O9O2 → C10H15O9O + LIMBO	6E-11*0.6
623. LIMALAO2 + C10H15O9O2 → C10H16O10 + LIMALACO	6E-11*0.2
624. LIMALAO2 + C10H15O9O2 → C10H15O9O + LIMALAO	6E-11*0.6
625. LIMALAO2 + C10H15O9O2 → C10H14O10 + LIMALAOH	6E-11*0.2
626. NAPINAO2 + C10H15O9O2 → C10H14O10 + APINBNO3	6E-11*0.1
627. NAPINAO2 + C10H15O9O2 → C10H15O9O + NAPINAO	6E-11*0.9
628. NAPINBO2 + C10H15O9O2 → C10H14O10 + APINANO3	6E-11*0.1
629. NAPINBO2 + C10H15O9O2 → C10H15O9O + NAPINBO	6E-11*0.8
630. NAPINBO2 + C10H15O9O2 → C10H16O10 + NC101CO	6E-11*0.1
631. APINAO2 + C10H15O10O2 → C10H14O11 + APINBOH	6E-11*0.3
632. APINAO2 + C10H15O10O2 → C10H15O10O + APINAO	6E-11*0.7
633. APINBO2 + C10H15O10O2 → C10H14O11 + APINBOH	6E-11*0.2
634. APINBO2 + C10H15O10O2 → C10H15O10O + APINBO	6E-11*0.6
635. APINBO2 + C10H15O10O2 → C10H16O11 + APINBCO	6E-11*0.2
636. APINCO2 + C10H15O10O2 → C10H15O10O + APINCO	6E-11*0.7
637. APINCO2 + C10H15O10O2 → C10H14O11 + APINCOH	6E-11*0.3
638. C107O2 + C10H15O10O2 → C10H15O10O + C107O	6E-11*0.7
639. C107O2 + C10H15O10O2 → C10H14O11 + C107OH	6E-11*0.3
640. C109O2 + C10H15O10O2 → C10H15O10O + C109O	6E-11*0.9
641. C109O2 + C10H15O10O2 → C10H14O11 + C109OH	6E-11*0.05
642. C109O2 + C10H15O10O2 → C10H16O11 + C109CO	6E-11*0.05
643. C106O2 + C10H15O10O2 → C10H15O10O + C106O	6E-11*0.7
644. C106O2 + C10H15O10O2 → C10H14O11 + C106OH	6E-11*0.3
645. C920CO3 + C10H15O10O2 → C10H15O10O + C920O2	6E-11*0.7
646. C920CO3 + C10H15O10O2 → C10H14O11 + HOPINONIC	6E-11*0.3
647. C108O2 + C10H15O10O2 → C10H15O10O + C108O	6E-11*0.7
648. C108O2 + C10H15O10O2 → C10H14O11 + C108OH	6E-11*0.3
649. PINALO2 + C10H15O10O2 → C10H15O10O + PINALO	6E-11*0.7
650. PINALO2 + C10H15O10O2 → C10H14O11 + PINALOH	6E-11*0.3
651. C96CO3 + C10H15O10O2 → C10H15O10O + C96O2	6E-11*0.7
652. C96CO3 + C10H15O10O2 → C10H14O11 + PINONIC	6E-11*0.3
653. C923CO3 + C10H15O10O2 → C10H15O10O + C923O2	6E-11*0.7
654. C923CO3 + C10H15O10O2 → C10H14O11 + LIMONONIC	6E-11*0.3
655. LIMAO2 + C10H15O10O2 → C10H15O10O + LIMAO	6E-11*0.7
656. LIMAO2 + C10H15O10O2 → C10H14O11 + LIMAOH	6E-11*0.3
657. LIMALBO2 + C10H15O10O2 → C10H16O11 + LIMALBCO	6E-11*0.05
658. LIMALBO2 + C10H15O10O2 → C10H15O10O + LIMALBO	6E-11*0.9
659. LIMALBO2 + C10H15O10O2 → C10H14O11 + LIMALBOH	6E-11*0.05
660. LIMCO2 + C10H15O10O2 → C10H15O10O + LIMCO	6E-11*0.7
661. LIMCO2 + C10H15O10O2 → C10H14O11 + LIMCOH	6E-11*0.3
662. LIMALO2 + C10H15O10O2 → C10H15O10O + LIMALO	6E-11*0.7
663. LIMALO2 + C10H15O10O2 → C10H14O11 + LIMALOH	6E-11*0.3
664. LIMBO2 + C10H15O10O2 → C10H14O11 + LIMAOH	6E-11*0.2
665. LIMBO2 + C10H15O10O2 → C10H16O11 + LIMBCO	6E-11*0.2
666. LIMBO2 + C10H15O10O2 → C10H15O10O + LIMBO	6E-11*0.6

667. LIMALAO2 + C10H15O10O2 → C10H16O11 + LIMALACO	6E-11*0.2
668. LIMALAO2 + C10H15O10O2 → C10H15O10O + LIMALAO	6E-11*0.6
669. LIMALAO2 + C10H15O10O2 → C10H14O11 + LIMALAOH	6E-11*0.2
670. NAPINA02 + C10H15O10O2 → C10H14O11 + APINBNO3	6E-11*0.1
671. NAPINA02 + C10H15O10O2 → C10H15O10O + NAPINA0	6E-11*0.9
672. NAPINB02 + C10H15O10O2 → C10H14O11 + APINANO3	6E-11*0.1
673. NAPINB02 + C10H15O10O2 → C10H15O10O + NAPINBO	6E-11*0.8
674. NAPINB02 + C10H15O10O2 → C10H16O11 + NC101CO	6E-11*0.1
675. APINA02 + C10H15O11O2 → C10H14O12 + APINBOH	6E-11*0.3
676. APINA02 + C10H15O11O2 → C10H15O11O + APINA0	6E-11*0.7
677. APINB02 + C10H15O11O2 → C10H14O12 + APINBOH	6E-11*0.2
678. APINB02 + C10H15O11O2 → C10H15O11O + APINBO	6E-11*0.6
679. APINB02 + C10H15O11O2 → C10H16O12 + APINBCO	6E-11*0.2
680. APINCO2 + C10H15O11O2 → C10H15O11O + APINCO	6E-11*0.7
681. APINCO2 + C10H15O11O2 → C10H14O12 + APINCOH	6E-11*0.3
682. C107O2 + C10H15O11O2 → C10H15O11O + C107O	6E-11*0.7
683. C107O2 + C10H15O11O2 → C10H14O12 + C107OH	6E-11*0.3
684. C109O2 + C10H15O11O2 → C10H15O11O + C109O	6E-11*0.9
685. C109O2 + C10H15O11O2 → C10H14O12 + C109OH	6E-11*0.05
686. C109O2 + C10H15O11O2 → C10H16O12 + C109CO	6E-11*0.05
687. C106O2 + C10H15O11O2 → C10H15O11O + C106O	6E-11*0.7
688. C106O2 + C10H15O11O2 → C10H14O12 + C106OH	6E-11*0.3
689. C920CO3 + C10H15O11O2 → C10H15O11O + C920O2	6E-11*0.7
690. C920CO3 + C10H15O11O2 → C10H14O12 + HOPINONIC	6E-11*0.3
691. C108O2 + C10H15O11O2 → C10H15O11O + C108O	6E-11*0.7
692. C108O2 + C10H15O11O2 → C10H14O12 + C108OH	6E-11*0.3
693. PINALO2 + C10H15O11O2 → C10H15O11O + PINALO	6E-11*0.7
694. PINALO2 + C10H15O11O2 → C10H14O12 + PINALOH	6E-11*0.3
695. C96CO3 + C10H15O11O2 → C10H15O11O + C96O2	6E-11*0.7
696. C96CO3 + C10H15O11O2 → C10H14O12 + PINONIC	6E-11*0.3
697. C923CO3 + C10H15O11O2 → C10H15O11O + C923O2	6E-11*0.7
698. C923CO3 + C10H15O11O2 → C10H14O12 + LIMONONIC	6E-11*0.3
699. LIMAO2 + C10H15O11O2 → C10H15O11O + LIMAO	6E-11*0.7
700. LIMAO2 + C10H15O11O2 → C10H14O12 + LIMAOH	6E-11*0.3
701. LIMALBO2 + C10H15O11O2 → C10H16O12 + LIMALBCO	6E-11*0.05
702. LIMALBO2 + C10H15O11O2 → C10H15O11O + LIMALBO	6E-11*0.9
703. LIMALBO2 + C10H15O11O2 → C10H14O12 + LIMALBOH	6E-11*0.05
704. LIMCO2 + C10H15O11O2 → C10H15O11O + LIMCO	6E-11*0.7
705. LIMCO2 + C10H15O11O2 → C10H14O12 + LIMCOH	6E-11*0.3
706. LIMALO2 + C10H15O11O2 → C10H15O11O + LIMALO	6E-11*0.7
707. LIMALO2 + C10H15O11O2 → C10H14O12 + LIMALOH	6E-11*0.3
708. LIMBO2 + C10H15O11O2 → C10H14O12 + LIMAOH	6E-11*0.2
709. LIMBO2 + C10H15O11O2 → C10H16O12 + LIMBCO	6E-11*0.2
710. LIMBO2 + C10H15O11O2 → C10H15O11O + LIMBO	6E-11*0.6
711. LIMALAO2 + C10H15O11O2 → C10H16O12 + LIMALACO	6E-11*0.2
712. LIMALAO2 + C10H15O11O2 → C10H15O11O + LIMALAO	6E-11*0.6
713. LIMALAO2 + C10H15O11O2 → C10H14O12 + LIMALAOH	6E-11*0.2
714. NAPINA02 + C10H15O11O2 → C10H14O12 + APINBNO3	6E-11*0.1
715. NAPINA02 + C10H15O11O2 → C10H15O11O + NAPINA0	6E-11*0.9
716. NAPINB02 + C10H15O11O2 → C10H14O12 + APINANO3	6E-11*0.1
717. NAPINB02 + C10H15O11O2 → C10H15O11O + NAPINBO	6E-11*0.8
718. NAPINB02 + C10H15O11O2 → C10H16O12 + NC101CO	6E-11*0.1

Table S4. Gas-phase precursors used for the ADCHEM model simulations

Gas-phase precursor
α -pinene
β -pinene
Limonene
Carene
Isoprene
Ethane
Butane
Etene
Propene
<i>o</i> -xylene
Formaldehyde
Acetaldehyde
Methyl Ethyl Ketone
Glyoxal
Methylglyoxal
1-petene
2-methylpropene
Dodecane
Benzene
Decane
Ethylbenzene
Nonane
<i>p</i> -xylene
Toluene
Undecane
<i>m</i> -xylene
1-butene
1,2,4-trimethylbenzene
1,3,5-trimethylbenzene
1,2,3-trimethylbenzene

References SI

1. Ehn, M., Thornton, J. A., Kleist, E., Sipilä, M., Junninen, H., Pullinen, I., Springer, M., Rubach, F., Tillmann, R., Lee, B., Lopez-Hilfiker, F., Andres, S., Acir, I.-H., Rissanen, M., Jokinen, T., Schobesberger, S., Kangasluoma, J., Kontkanen, J., Nieminen, T., Kurtén, T., Nielsen, L. B., Jørgensen, S., Kjaergaard, H. G., Canagaratna, M., Dal Maso, M., Berndt, T., Petäjä, T., Wahner, A., Kerminen, V.-M., Kulmala, M., Worsnop, D. R., Wildt, J., and Mentel, T. F.: A large source of low-volatility secondary organic aerosol, *Nature*, 506, 476–479, <https://doi.org/10.1038/nature13032>, 2014.
2. Rissanen, M. P.; Kurtén, T.; Sipilä, M.; Thornton, J. A.; Kangasluoma, J.; Sarnela, N.; Junninen, H.; Jørgensen, S.; Schallhart, S.; Kajos, M. K.; et al. The Formation of Highly Oxidized Multifunctional Products in the Ozonolysis of Cyclohexene. *J. Am. Chem. Soc.* 2014, 136, 15596–15606.
3. Roldin, P., Eriksson, A. C., Nordin, E. Z., Hermansson, E., Mogensen, D., Rusanen, A., Boy, M., Swietlicki, E., Svenningsson, B., Zelenyuk, A. and Pagels, J.: Modelling non-equilibrium secondary organic aerosol formation and evaporation with the aerosol dynamics, gas- and particle-phase chemistry kinetic multilayer model ADCHAM, *Atmos. Chem. Phys.*, 14, 7953–7993, <https://doi.org/10.5194/acp-14-7953-2014>, 2014.
4. Roldin, P., Liao, L., Mogensen, D., Dal Maso, M., Rusanen, A., Kerminen, V.-M., Mentel, T. F., Wildt, J., Kleist, E., Kiendler-Scharr, A., Tillmann, R., Ehn, M., Kulmala, M., and Boy, M.: Modelling the contribution of biogenic volatile organic compounds to new particle formation in the Jülich plant atmosphere chamber, *Atmos. Chem. Phys.*, 15, 10777–10798, <https://doi.org/10.5194/acp-15-10777-2015>, 2015.
5. Roldin, P., Swietlicki, E., Schurgers, G., Arneth, A., Lehtinen, K. E. J., Boy, M., and Kulmala, M.: Development and evaluation of the aerosol dynamics and gas phase chemistry model ADCHEM, *Atmos. Chem. Phys.*, 11, 5867–5896, <https://doi.org/10.5194/acp-11-5867-2011>, 2011.
6. Öström, E., Roldin, P., Schurgers, G., Mishurov, M., Putian, Z., Kivekäs, N., Lihavainen, H., Ehn, M., Rissanen, M. P., Kurtén, T., Boy, M., and Swietlicki, E.: Model data for simulation of secondary organic aerosol formation over the boreal forest, link to NetCDF files in zip archive, PANGAEA, <https://doi.org/10.1594/PANGAEA.877695>, 2017.
7. Nannoolal, Y., Rarey, J., and Ramjugernath, D.: Estimation of pure component properties, *Fluid Phase Equilib.*, 269, 117–133, <https://doi.org/10.1016/j.fluid.2008.04.020>, 2008.
8. Pankow, J. F. and Asher, W. E.: SIMPOL.1: a simple group contribution method for predicting vapor pressures and enthalpies of vaporization of multifunctional organic compounds, *Atmos. Chem. Phys.*, 8, 2773–2796, <https://doi.org/10.5194/acp-8-2773-2008>, 2008.
9. Kurtén, T., Tiusanen, K., Roldin, P., Rissanen, M., Luy, J.-N., Boy, M., Ehn, M., and Donahue, N.: α -Pinene Autoxidation Products May Not Have Extremely Low Saturation Vapor Pressures Despite High O:C Ratios, *J. Phys. Chem. A*, 120, 2569–2582, <https://doi.org/10.1021/acs.jpca.6b02196>, 2016.
10. Tang, M. J., Shiraiwa, M., Pöschl, U., Cox, R. A., and Kalberer, M.: Compilation and evaluation of gas phase diffusion coefficients of reactive trace gases in the atmosphere: Volume 2. Diffusivities of organic compounds, pressure-normalised mean free paths, and average Knudsen numbers for gas uptake calculations, *Atmos. Chem. Phys.*, 15, 5585–5598, doi:10.5194/acp-15-5585-2015, 2015
11. Matsunaga, A. and Ziemann, P. J.: Gas-Wall Partitioning of Organic Compounds in a Teflon Film Chamber and Potential Effects on Reaction Product and Aerosol Yield Measurements, *Aerosol Sci. Technol.*, 44, 881–892, 2010.
12. Jericevic, A., Kraljevic, L., Grisogono, B., Fagerli, H., and Vecenaj, Ž.: Parameterization of vertical diffusion and the atmospheric boundary layer height determination in the EMEP model, *Atmos. Chem. Phys.*, 10, 341–364, <https://doi.org/10.5194/acp-10-341-2010>, 2010.
13. Olenius, T., Kupiainen-Määttä, O., Ortega, I. K., Kurtén, T. and Vehkamäki, H.: Free energy barrier in the growth of sulfuric acid–ammonia and sulfuric acid–dimethylamine clusters, *J. Chem. Phys.*, 139(8), 84312, doi:10.1063/1.4819024, 2013.
14. Guenther, A. B., Jiang, X., Heald, C. L., Sakulyanontvittaya, T., Duhl, T., Emmons, L. K., and Wang, X.: The Model of Emissions of Gases and Aerosols from Nature version 2.1 (MEGAN2.1): an extended and updated framework for modeling biogenic emissions, *Geosci. Model Dev.*, 5, 1471–1492, doi:10.5194/gmd-5-1471-2012, 2012.
15. Smolander, S., He, Q., Mogensen, D., Zhou, L., Bäck, J., Ruuskanen, T., Noe, S., Guenther, A., Aaltonen, H., Kulmala, M. and Boy, M.: Comparing three vegetation monoterpene emission models to measured gas concentrations with a model of meteorology, air chemistry and chemical transport, *Biogeosciences*, 11(19), 5425–5443, doi:10.5194/bg-11-5425-2014, 2014.
16. Bäck, J., Aalto, J., Henriksson, M., Hakola, H., He, Q., and Boy, M.: Chemodiversity of a Scots pine stand and implications for terpene air concentrations, *Biogeosciences*, 9, 689–702, doi:10.5194/bg-9-689-2012, 2012.
17. Lana, A., Bell, T. G., Simó, R., Vallina, S. M., Ballabrera-Poy, J., Kettle, A. J., Dachs, J., Bopp, L., Saltzman, E. S., Stefels, J., Johnson, J. E. and Liss, P. S.: An updated climatology of surface dimethylsulfide concentrations and emission fluxes in the global ocean, *Global Biogeochem. Cycles*, 25(1), GB1004,

- doi:10.1029/2010GB003850, 2011.
18. Nightingale, P. D., Malin, G., Law, C. S., Watson, A. , Liss, P. S., Liddicoat, M. I., Boutin, J. and Upstill-Goddard, R. C.: In situ evaluation of air-sea gas exchange parameterizations using novel conservative and volatile tracers, *Global Biogeochem. Cycles*, 14(1), 373–387, doi:10.1029/1999GB900091, 2000.
 19. http://www.ceip.at/webdab_emepdatabase/emissions_emepmodels/
 20. Paasonen, P., Kupiainen, K., Klimont, Z., Visschedijk, A., Denier van der Gon, H. A. C. and Amann, M.: Continental anthropogenic primary particle number emissions, *Atmos. Chem. Phys.*, 16(11), 6823–6840, doi:10.5194/acp-16-6823-2016, 2016.
 21. Beecken, J., Mellqvist, J., Salo, K., Ekholm, J., Jalkanen, J.-P., Johansson, L., Litvinenko, V., Volodin, K., and Frank-Kamenetsky, D. A.: Emission factors of SO₂, NO_x and particles from ships in Neva Bay from ground-based and helicopter-borne measurements and AIS-based modeling, *Atmos. Chem. Phys.*, 15, 5229–5241, <https://doi.org/10.5194/acp-15-5229-2015>, 2015
 22. Jonsson, Å. M., Westerlund, J., and Hallquist, M.: Size-resolved particle emission factors for individual ships, *Geophys. Res. Lett.*, 38, L12809, <https://doi.org/10.1029/2011GL047672>, 2011.
 23. Mårtensson, E. M., Nilsson, E. D., de Leeuw, G., Cohen, L. H., and Hansson, H.-C.: Laboratory simulations and parameterization of the primary marine aerosol production, *J. Geophys. Res.*, 108, 4297, <https://doi.org/10.1029/2002JD002263>, 2003.
 24. Draxler, R. and Rolph, G. D.: HYSPLIT (HYbrid Single-Particle Lagrangian Integrated Trajectory) Model, NOAA Air Resources Laboratory's (ARL), Silver Spring, MD, available at: <http://ready.arl.noaa.gov/HYSPLIT.php> (last access: 18 September 2017), 2013.
 25. Rolph, G. D.: Real-time Environmental Applications and Display sYstem (READY), NOAA Air Resources Laboratory's (ARL), Silver Spring, MD, available at: <http://ready.arl.noaa.gov>, last access: 18 September 2017.

Paper IV



Potential influence on CCN from new particle formation and emissions in the polluted marine boundary layer.

Emilie Öström^{1,2}, Jan Julin³, Pontus Roldin¹, Andreas Massling⁴, Robert Lange⁴, Marianne Glasius⁵, Ville Berg-Malmberg⁶, Hanna Manninen⁷, Nikos Kalivitis⁸, Tinja Olenius³, Ilona Riipinen³ and Adam Kristensson¹

¹Division of Nuclear Physics, Department of Physics, Lund University, P. O. Box 118, SE-221 00, Lund, Sweden

²Centre for Environmental and Climate Research, Lund University, Lund, P.O. Box 118, 221 00, Sweden

³Department of Environmental Science and Analytical Chemistry (ACES), Stockholm University, SE-106 91, Stockholm, Sweden

⁴Department of Environmental Science, Aarhus University, P. O. Box 358, DK-4000 Roskilde, Denmark

⁵Department of Chemistry, Aarhus University, Langelandsgade 140, DK-8000 Aarhus C, Denmark

⁶Division of Ergonomics and Aerosol Technology, Department of Design Sciences, Lund University, P. O. Box 118, SE-221 00, Lund, Sweden

⁷Department of Physics, University of Helsinki, P. O. Box 64, FI-00014, Helsinki, Finland, 8ECPL, Department of Chemistry, University of Crete, Voutes, GR-71003 Heraklion, Greece.

Abstract

Atmospheric new particle formation of particles between 1 and 2 nm diameter has a profound influence on the global climate. Due to the growth by condensing vapours, these particles can reach sizes, where they act as cloud condensation nuclei (CCN) seed particles. These can form clouds, which effectively cool our climate due to shortwave solar light scattering. However, the climate effects of new particle formation over the polluted sea areas surrounding our continents are not properly investigated. There are also several poorly investigated sea related sources of gaseous precursor emissions leading to new particle formation or the growth of existing particles to CCN sizes over the sea and further inland. These sources include e.g., biogenic and anthropogenic vapour emissions over the continents, which are advected over the marine boundary layer, ship emissions of SO₂ and VOCs, emissions of dimethyl sulphide (DMS) and other VOCs from the sea surface layer and NH₃ emissions from sea birds. We used field data from coastal areas in Europe and complemented with modelling to address the questions whether new particle formation and natural and anthropogenic emissions over these sea areas have a regional effect on the population of CCN. We conclude that natural and anthropogenic emissions over sea might have a significant impact on CCN over the seas and continents, whereas NPF over sea areas likely do not have an important effect. The modelling over sea areas also shows that there is a need to continue working for improved model agreement with observations in coastal

areas. For example, SO₂ concentrations need to be re-examined, since these have a large influence on the particle population.

Introduction

Previous modelling attempts (Pirjola et al., 2000) and sporadic observations (Covert et al., 1992, 1996; Heintzenberg et al., 2004; Hoppel et al., 1994; Weber et al., 1998) suggest that the new particle formation (NPF) over the remote oceans is a scarce source of cloud condensation nuclei (CCN) in a global sense. However, over the waters surrounding our continents, there is a possibility that NPF constitutes a significant source of CCN. Namely, NPF in these areas might also be driven by SO₂, NH₃ and organic vapours emissions from ship emissions, land advection, and NH₃ emissions from sea birds (Croft et al., 2016). This might enhance particle formation and growth rates during NPF over polluted sea areas as compared to open oceans, where DMS is often the dominating source of sulphate and major VOC and NH₃ sources are lacking. The gaseous emissions might also spark or suppress new particle formation once the air is advecting over land and increase or decrease CCN through this process. Finally, the sea emissions might also favour condensational particle growth both over land and sea, thus creating a favourable mix of pollutants for enhanced production of CCN.

We used particle number size distribution data from the North Sea coastal station Høvsøre and the Mediterranean station Finokalia. We examined where, over the marine boundary layer, particles were formed during NPF at 1.5 nm diameter with the NanoMap method (Kristensson et al., 2014). We complimented this with Lagrangian aerosol dynamics 1D-column modelling with ADCHEM and European scale modelling with PMCAMx-UF to quantify the impact that NPF and emissions in the polluted marine boundary layer have on the concentration of particles larger than 40 and 80 nm in diameter respectively (N40 and N80). The 40 nm diameter limit is approximately the lowest limit, where aerosol particles can act as CCN if they are very hygroscopic (e.g. Furutani et al. (2008)). The 80 nm diameter limit is a more approximate common lower limit of CCN activation in a typical boundary layer environment with mixed influence of marine and continental air (e.g. Burkart et al. (2011)).

To model the influence of NPF and the precursor gases, different model case runs were attempted and compared to each other with the ADCHEM and PMCAMx-UF models:

- I. Base-case run, with all emissions and processes included.
- II. NPF removed from the sea areas surrounding Europe (to test whether the NPF over the sea areas have effect on the regional N40 and N80 concentrations).

- III. Emissions from the sea and gases emitted from ship traffic that produce NPF are removed (to test whether gaseous emissions from the sea areas have an effect on NPF and N40 and N80) (only with PMCAMx-UF).
- IV. Anthropogenic emitted vapours and particles over sea are removed (to test the role of anthropogenic emissions on NPF) (only with ADCHEM).

Methods summary

Particle number size distribution measurements data were taken from the coastal stations Høvsøre facing the eastern part of the North Sea (56.447 N, 8.152E, Kivekäs et al., 2014), and the Finokalia station on the Mediterranean island Crete (35°24' N 25°60' E, Pikridas et al., 2012). Analysis was performed on the number size distribution and NPF events at these coastal stations during spring 2012 and 2008 and 2009 respectively. By using meteorological back trajectories and the NanoMap method on these size distributions (Kristensson et al., 2014), it is possible to infer the location of formation of 1.5 nm diameter particles during NPF events in the North Sea and Mediterranean marine boundary layer and the free troposphere over the sea.

The aerosol dynamics one-dimensional column model ADCHEM with a radiative transfer model and gas- and particle phase chemistry scheme (Öström et al., 2017) was used to model the evolution of the particle number size distribution and gas and particle phase chemistry. The model was run from four days upwind of the coastal stations in the marine boundary layer until three days downwind of the stations along meteorological air mass trajectories during suitable cases with clear NPF and some days in between without NPF. Emission of anthropogenic (ECLIPSE v5a; Stohl et al. (2015)) and biogenic gases (MEGAN; Guenther et al. (2012)) were considered together with primary particle emission of wind generated marine aerosols (Mårtensson et al., 2003) as well as size resolved primary particle number emissions from ships, offshore flaring and continental anthropogenic emissions (Paasonen et al., 2016). The modelling results from ADCHEM were compared with the regional European chemical transport model PMCAMx-UF (Baranizadeh et al., 2016) model results for May 2008, especially in terms of the number concentration of particles above 40 and 80 nm in diameter (N40 and N80 respectively), to quantify the effect on the CCN population.

ADCHEM uses the Atmospheric Cluster Dynamics Code (ACDC; Olenius et al., 2013) using quantum chemical input data to simulate the binary nucleation of NH₃ and H₂SO₄ forming molecule clusters containing up to five NH₃ and five H₂SO₄ molecules. When the clusters reach this size they have an estimated diameter of 1.07 nm and are assumed to be large enough to continue to grow by condensation of H₂SO₄ and low volatile organic. PMCAMx-UF also employs results from

ACDC when calculating the formation of new particles in the atmosphere. However, due to computational restrictions ACDC cannot be run directly in PMCAMx-UF. Instead PMCAMx-UF uses a lookup table for the particle formation rates calculated based on ternary NH_3 - H_2SO_4 - H_2O nucleation theory (Baranizadeh et al., 2016).

See the extended methods section for more information about the measurements, NanoMap method and the ADCHEM model.

Results and discussion

New particle formation at Høvsøre and Finokalia

The measurements at Høvsøre during spring 2012 point to a frequency of NPF event days of 44 %. This is lower than for the spring period at the nearby semi-continental site Lille Valby in Denmark and the continental site Vavihill in Sweden, where the event frequency is between 50 and 65 % depending on the year (Kristensson et al., 2008; Wang et al., 2013). The formation and condensational growth rates of particles at Høvsøre is low compared to these sites. However, the growth rates of the newly formed particles will often increase as a consequence of increased amounts of condensable vapours over the continental boundary layer downwind of Høvsøre. Hence, the NPF over ocean may still be significant for CCN, which has been tested in this study. The NPF over the North Sea are normally observed during north-westerly winds, which is true also for the nearby semi-continental and continental sites Lille Valby and Vavihill in Denmark and Sweden, respectively (Kristensson et al., 2008; Wang et al., 2013).

The frequency of NPF event days in Finokalia is 23 % for the period investigated (June 2008 until June 2009), but with much higher formation and growth rate of particles than at Høvsøre. The air masses reaching Finokalia during NPF event days come from different wind directions, but mainly from north or south, and never from east.

NanoMap shows that the initial formation of 1.5 nm diameter particles during NPF event days observed at Høvsøre normally takes place up to two days upwind of Høvsøre in the marine boundary layer in the northern part of the North Sea, or along the Norwegian coast line (Figure 1a). The formation of particles most often takes place south or north of Finokalia, and sometimes also to the west (Figure 1b).

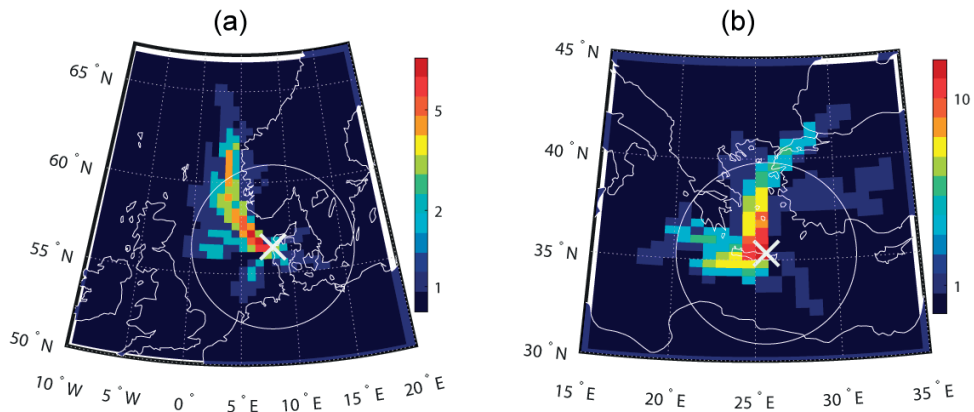


Figure 1. Position of measurement stations and NPF. (a) The position of the Høvsøre measurement station denoted with a white cross and the location of the NPF of 1.5 nm diameter particles around Høvsøre according to NanoMap. (b) The position of the Finokalia measurement station denoted with a cross and the location of NPF around Finokalia. The colour bar denotes the number of unique days of formation in each grid cell, and the white circle denotes a 500 km radius distance from each station.

Modelled and observed particle number size distributions

Four consecutive days of modelled particle number size distributions using ADCHEM were analysed and compared to observed particle number size distributions at Høvsøre and Finokalia respectively. The modelled data at the stations have a time resolution of 3 hours since the model is run along air-mass trajectories passing the stations every third hour. Each model-data point at each station is only affected by the air mass that follows one single air mass trajectory; in reality, stations are always affected by many air masses of different origin at the same time (see e.g. Fleming et al. (2012)). Thus, although the model simulates realistic conditions for single air masses, we should not expect that the results from single model simulations agree perfectly with the observations at one single point in space and time. However, by comparing the mean or median results from many model simulations with the observations at a station, the agreement between the two should improve. We have therefore chosen to primarily present the median results to smear out the effect that single air masses can have on the results. At Høvsøre, the modelled air-mass trajectories originate over the northern Atlantic Ocean and are less affected by anthropogenic emissions than the modelled air-mass trajectories passing Finokalia, which originates from Eastern Europe.

Figure 2a shows the modelled and measured median particle number size distribution at Høvsøre. Compared to the observations, the model predicts too many particles above 40 nm in diameter, whereas it underestimates the number of particles smaller than that. The particles formed upwind Høvsøre grow too fast in the model, causing the dominant mode in the particle number size distribution to be around 50 nm in diameter (i.e. many particles in the model are already

approaching CCN-sizes at Høvsøre). The particles in this 50 nm mode mainly consist of sulphate (Fig. S1), which has condensed onto the particles. Despite reducing the emission of SO₂ from ship traffic by a factor of 10 (“Extended methods” section) the model still overestimates the SO₂ concentration by about a factor of 3 to almost 10 (Fig. S2a). SO₂ reacts with OH in the atmosphere to form sulphate. The high concentration of modelled SO₂ therefore causes rapid growth by condensation of sulphate.

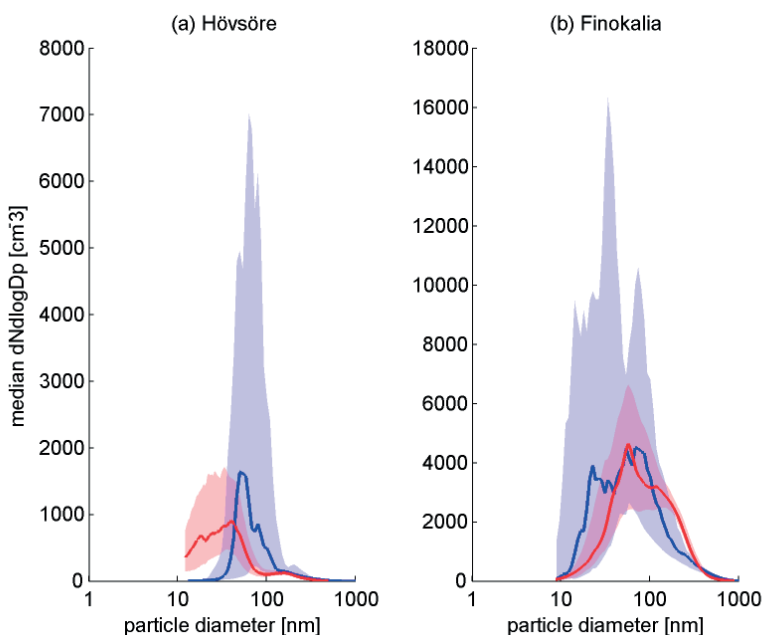


Figure 2. Median particle number size distributions during 4 days at (a) Høvsøre and (b) Finokalia. The red lines are the observed size distributions, the blue line the modelled (with the base-case set up using ADCHEM). The shaded areas are the values that fall between the 25th and 75th percentiles.

New particle formation events upwind Høvsøre are limited by the concentration of NH₃, due to the low NH₃ emissions over sea compared to over continents (Fig. 3). The air-mass trajectories that pass Høvsøre day 1 and 4 have a stronger contribution of land-based emissions, such as NH₃, than the other days, resulting in higher number concentration of particles these days (Fig S3) due to stronger NPF upwind Høvsøre

The modelled number size distribution at Finokalia agrees better with the observed distribution than the model does at Høvsøre (Figure 2b). The modelled concentration of SO₂ is in agreement with observed concentrations at Cyprus in

October 2009 (Fig. S4a), implying that the model does not significantly overestimate the SO₂ concentration at Finokalia. The modelled median size distribution at Finokalia is bimodal where both modes are a result of NPF upwind the station. The mode just above 10 nm in diameter is mostly a result of NPF over the sea (closer to the station), whereas the mode around 100 nm is a result of NPF over land (further away from the station). The particles in the 100 nm mode are more heavily aged and consist of a higher fraction of nitrate (Fig. S5).

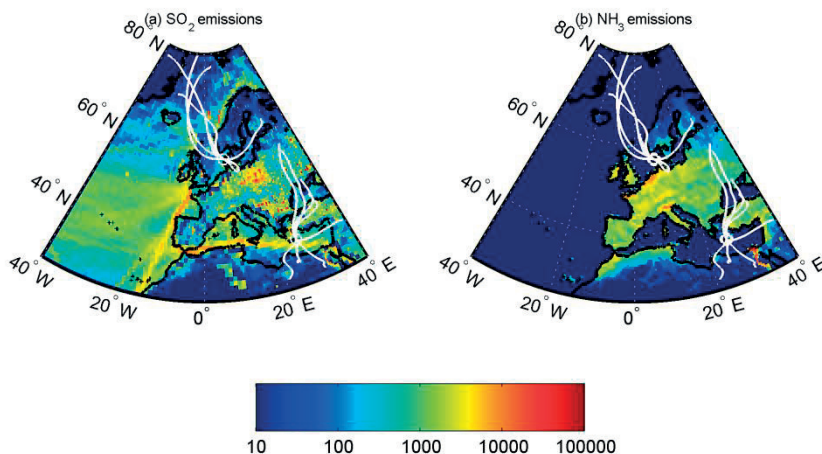


Figure 3. Modelled emissions of SO₂ (a) and NH₃ (b) from ECLIPSE v.5a. The white lines are the modelled median air-mass trajectories for each day. The air arriving in Høvsøre originates in Northern Atlantic and the air arriving at Finokalia originates in Eastern Europe.

PMCAMx-UF was run during the period May 1-29, 2008. During 8 days in May 2008 with winds from the northern part of the North Sea, the median modelled SO₂ concentration by PMCAMx-UF at Høvsøre is overestimated by about a factor 3 compared to a nearby measurement site Ulborg (Table S1). In general, SO₂ concentrations modelled with PMCAMx-UF during the period May 1-29, 2008 are overestimated by about a factor 4 at Høvsøre compared to Ulborg (Table S1). This is a contributing factor to the overestimation also in the number of NPF event days and new particle formation rates during May 2008 at Høvsøre. Modelled NPF at 1.5 nm in diameter starts almost every day upwind of Høvsøre. This gives an overestimation of Aitken mode particles (40 – 100 nm in diameter) by about a factor 2 at Høvsøre (Figure 4a, Table S2). The nucleation mode (10-40 nm in diameter) overestimation is even more pronounced (Figure 4a, Table S2). Note that the period of SMPS measurements is not the same as the model runs.

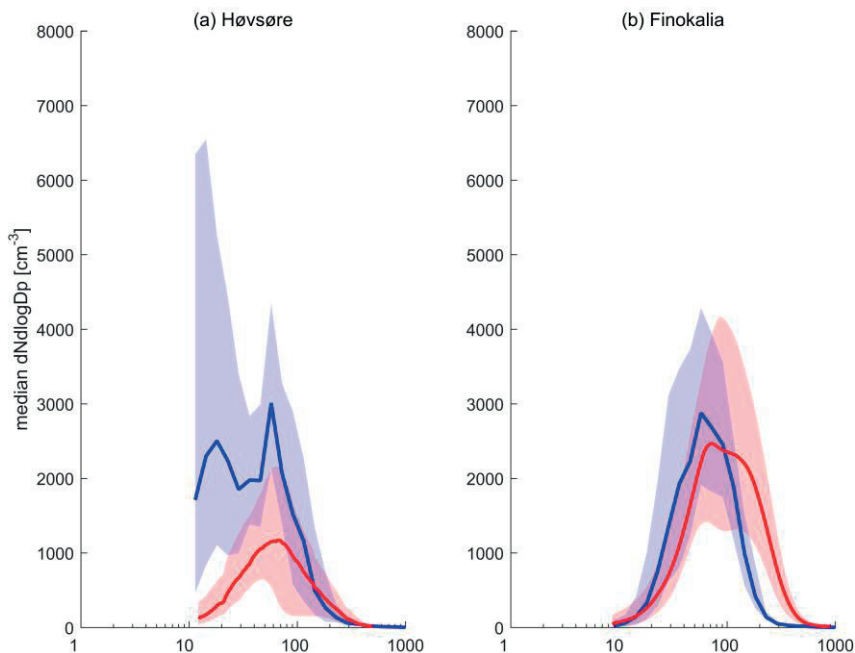


Figure 4. Median particle number size distributions at (a) Høvsøre and (b) Finokalia. The red lines are the observed size distributions, the blue line modelled with PMCAMx-UF (with the base-case set up). The shaded areas are the values that fall between the 25th and 75th percentiles. Høvsøre observation data are from May 2012. Finokalia observation data are from between June 2008 and June 2009, from the same period as the NanoMap results in Figure 1b. Modelled data for both stations are from the 29 days simulation period in May 2008.

Modelled SO_2 concentrations at Cyprus (Ayia Marina) during May 2008 are overestimated by a factor 3 compared to observations during May 2009 (or the entire year 2009) (Table S1). The dates of the observations at Ayia Marina and model runs in PMCAMx-UF do not overlap in time, but this still gives an indication that the overestimation in SO_2 is also taking place in the Mediterranean. In general, PMCAMx-UF overestimates concentrations over all investigated European sites (Table S1). The overestimation is sometimes much higher than a factor 4 at sites, where the emission database points to very high emission in the current gridcell, which might not be as high in reality (see for example Starina and O. Savinao in Table S1).

Despite the overestimation of SO_2 , modelled particle number size distributions with PMCAMx-UF at Finokalia agree well with the measured particle number size distribution in terms of the total number concentration (Figure 4b, Table S2). Note that the period of SMPS measurements is not the same as the model runs. One contributing factor for the agreement is that the condensation sink of pre-existing

particles is relatively high, giving low new particle formation rates, and a relatively low population of newly formed particles. Hence, the model is less sensitive to NPF. The low 75th percentile value of the modelled particle number concentration between 8 and 40 nm diameter is indicative of the relatively small influence from NPF (Figure 4b).

However, the count median diameter of both the Aitken and accumulation modes modelled by PMCAMx-UF are about 40 nm lower than the observed at Finokalia. This effect is generally apparent for entire Europe (Table S2) and is indicative of high formation rates, frequent NPF and slow condensational growth in the model to larger sizes, which shifts the entire size distribution towards lower sizes.

Modelled CCN concentrations downwind the stations using ADCHEM

In order to test the influence NPF and anthropogenic emissions over sea have on the CCN concentration over land, model case run II and IV were compared to the base case (run I).

The particle concentration at Høvsøre decreased by on average 71 % when NPF over sea was switched off (model run II). Switching of the anthropogenic emission over sea caused an average decrease of 53 % (model run IV). The decrease in the particle number concentration in model run II is most prominent for particles around 50 nm in diameter; the number concentration of the largest particles actually increases by a small fraction since a larger fraction of the vapours condense on the existing particles when there are no newly formed particles. In model run IV the number of particles decreases for all sizes larger than about 20 nm in diameter (Fig. S6 and Fig. S7). The decrease in number particle concentration at Høvsøre will affect the amount of CCN downwind the station; Table 1 presents the median change in CCN (with two different lower diameter limit for CCN) if NPF over sea or anthropogenic emissions over sea are turned off.

Table 1. Median change in modelled number of particles larger than 40 and 80 nm when NPF and anthropogenic emissions are switched off compared with the base-case simulation. All model simulations performed with ADCHEM.

	Model case run II	Model case run II	Model case run IV	Model case run IV
	Median change in PN40 if no NPF over sea (%)	Median change in PN80 if no NPF over sea (%)	Median change in PN40 if no anthropogenic emissions over sea (%)	Median change in PN80 if no anthropogenic emissions over sea (%)
1 day downwind Høvsøre (all traj)	3.8	1.5	55	55
2 days downwind Finokalia	-1.1	-0.82	-4.9	-7.1

The background concentration of particles around 100 nm at Høvsøre is in run II and IV mostly a result of aged particles from NPF over land and for run II also primary particles from ship traffic (Fig. S8a and Fig. S8b). In run IV, this mode is less aged than in run II due to a lack of condensing vapours over sea. In both simulation cases the background particle concentration at Høvsøre are lower than in the base case, leading to a lower condensation sink which allows strong NPF and rapid growth just downwind Høvsøre. One day downwind the station, there is a median increase in the number of particles larger than 40 nm and 80 nm of 3.8, respectively 1.5% if NPF over sea has been switched off in the model. When we turned off anthropogenic emissions over sea these numbers were 55 and 55 % one day downwind the station, due to an even less-polluted background aerosol. Due to the high concentration of SO₂ at Høvsøre, the growth seems to be dominated by land-based emission of SO₂, and is not noticeably affected when anthropogenic emissions over sea are turned off. A more realistic concentration of SO₂ may result in a weaker NPF and slower growth downwind the station. 58 % (56 %) of the aerosol particles in the Aitken mode (10-100 nm) one day downwind Høvsøre, in run II (run IV), are however composed of ammonium and nitrate, and the modelled concentration of ammonia and NO₂ agrees better with the observations (Fig. S2c and Fig. S2b).

Switching off NPF over sea almost only affects the concentration of the smallest particles in Finokalia, whereas the concentration for particles larger than 40 nm (80 nm) only decreases by on average 0.6 % (0.05 %) compared to the base case (Fig. S9 and S10). NPF and especially the growth of these newly formed particles along the air-mass trajectories, which have all started over the European continent, are inhibited over the Mediterranean Sea due to the high background particle concentration. The modelled CCN population two days downwind Finokalia is in most cases insensitive to NPF over sea (Table 1). Switching of anthropogenic emissions over sea did however lead to a slight decrease in the amount of particles larger than 40 and 80 nm (-4.9 and -7.1 % respectively) downwind Finokalia. Both upwind and downwind Finokalia the air-mass trajectories spend some time over the Mediterranean Sea (Fig. 3). Switching off emissions over sea, reduces the amount of primary particles and also vapours that may condense on existing particles; causing fewer particles to reach CCN sizes.

Table 2. Median change in modelled number of particles larger than 40 and 80 nm for the 29 day simulation period May 1-29 2008 over entire Europe when NPF and gaseous emissions are switched off compared with the base-case simulation. All model simulations performed with PMCAMx-UF.

	Model case run II	Model case run II	Model case run III	Model case run III
	Median change in PN40 if no NPF over sea (%)	Median change in PN80 if no NPF over sea (%)	Median change in PN40 if no gaseous emissions over sea (%)	Median change in PN80 if no gaseous emissions over sea (%)
30 day simulation period	-3.6	-0.4	-7.7	-23

Modelled CCN concentrations downwind the stations using PMCAMx-UF

Alike ADCHEM, PMCAMx-UF shows that turning off NPF over the sea areas (model case run II) is not affecting the CCN population in a major way (Table 2). However, turning off gaseous emissions (model case run III) leads to a decrease of about 20 % of the amount of CCN over 80 nm in diameter (Table 2). For the PMCAMx-UF results, it has to be remembered that this is a median effect in CCN concentration for the entire Europe. In other words, the sea and continental locations close to the coast experience a larger effect on the CCN population (Fig. 5).

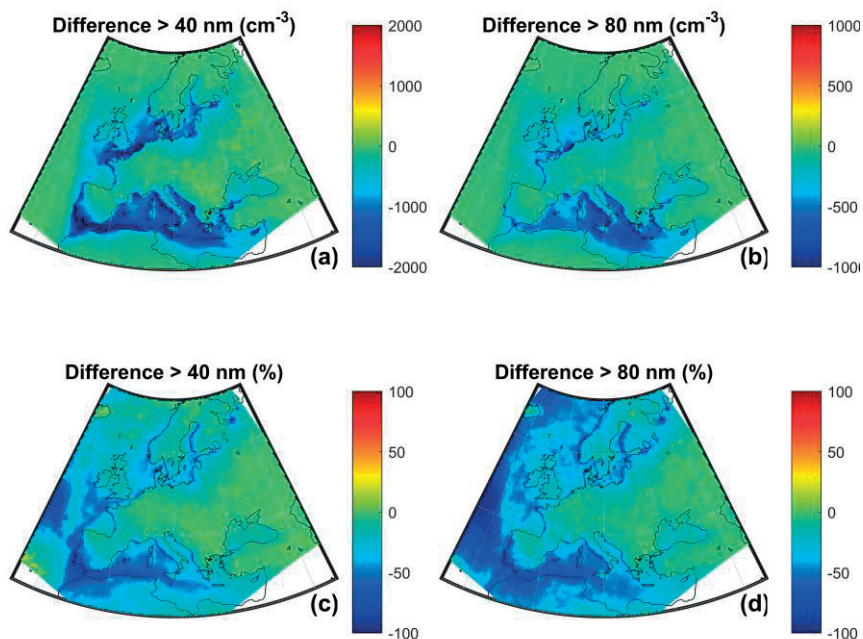


Figure 5. Median particle number concentration difference between PMCAMx-UF model run without natural and anthropogenic emissions of gaseous compounds over sea areas compared to base case run. The difference is calculated for the concentration above 40 nm (a) and 80 nm (b) diameter respectively. The relative difference given in % is shown in (c) and (d).

The strongest effect of reduced gaseous emissions in PMCAMx-UF model case run III on the CCN population is apparent over the sea, and not over land. This is likely an effect of the decreased condensational growth rate of pre-existing particles over the sea, which makes them unable to reach CCN sizes (either 40 or 80 nm diameter, Figure 5). Over land, the overestimated continental SO_2 concentrations have a larger effect on the condensation growth of sulphuric acid on pre-existing particles than the sea emissions, which is why the effect in CCN concentration due to sea emissions is reduced. Please also note that model case runs II in ADCHEM and III cannot be directly compared to each other, hence, should have different implications for the results.

In this study we have, besides using the regional chemical transport model PMCAMx-UF, used the advanced process-based model ADCHEM to simulate the chemistry and aerosol dynamics together with a state-of-the-art code to model new particle formation. The model results from ADCHEM show that the effect new particle formation and anthropogenic emissions over sea have on the amount of

particles in the CCN size range is not strait forward, e.g. turning off anthropogenic emissions over sea might, depending on various conditions, either increase or decrease the number of CCN over land. To capture this, a process-based aerosol dynamics model might be needed.

We further show that concentration of SO₂ is important for the formation and growth of particles over the marine boundary layer, which in turn might affect the climate through CCN formation over the continents and coastal areas. The modelled concentration of SO₂ is however an uncertain parameter as it depends on the emission of SO₂ and DMS as well as the loss mechanisms (Table 3). Future studies should look closer into finding closure between observed and modelled SO₂ concentrations.

Table 3. SO₂ prduction and loss mechanism used in this study.

SO ₂ production and loss mechanism	
Emission of SO ₂	ECLIPSE v.5a
Emission of DMS	Concentration from Lana et al. (2011) and sea-to-air transfer from Nightingale et al. (2000)
Dry deposition	Resistance approach, surface resistance over continent (Wesely, 1989) and over sea (Zhang et al., 2003).
Below-cloud scavenging	EMEP model (Simpson et al., 2012)
In-cloud scavenging	EMEP model (Simpson et al., 2012)
Cloud chemistry	If RH≥98, oxidation of dissolved SO ₂ and H ₂ O ₂ , and formation of sulphate aerosol mass for each activated particle size (Roldin et al., 2011)
Gas-phase chemistry	MCM v3.3

Extended methods

Measurements

The Høvsøre campaign took place between March 9 and May 31, 2012. The site was positioned in north-western Denmark peninsula, Jutland, 1.8 km inlands from the North Sea coastline (56.447 N, 8.152E) at the Test Station for Large Wind turbines, Høvsøre headed by DTU Wind Energy. The site is at a rural area surrounded by agricultural lands to the east and the coastline to the west. The site is flat, without elevation, and open to the winds blowing from the North Sea. The nearest relatively large towns are Aalborg, Aarhus, and Esbjerg located about 150 km to the northwest, east and south of the station with a population of 113 000, 269 000, and 113 000 respectively. Measurements of aerosol size distributions were performed with a TSI ® SMPS 3080 (Scanning mobility particle sizer, 12-

500 nm diameter, behind a diffusion drier, RH < 40 %) system and with an Airel® Air Ion Spectrometer (AIS, 0.8–40 nm diameter).

The Finokalia measurements were conducted between June 2008 and June 2009. Finokalia belongs to the European ACTRIS network, and the station is a remote coastal site in the south eastern Mediterranean Sea on the island of Crete (35°24' N 25°60' E), Greece at a top of a hill in the steep slope of a mountain reaching all the way to the sea. The nearest large urban centre is Heraklion with 150,000 inhabitants, located 50 km west of Finokalia and no notable human activity is present at a range of approximately 15 km from the site (Pikridas et al., 2012). There are very few trees and vegetation in the surrounding area. Aerosol particles have their sources mostly from the surrounding regions (Greece, Turkey, northern Africa, eastern and central Europe) (Pikridas et al., 2012). Particle number size distributions were monitored using a custom-made DMPS (Differential Mobility Particle Sizer, 9–900 nm diameter, behind a diffusion drier with RH < 40 %, Birmili et al., 1999) and an Airel® AIS (Air Ion Spectrometer, 0.8–40 nm in diameter) (Pikridas et al., 2012).

NanoMap

NanoMap can be applied to those NPF events that show a regional extent at a single-point field site. If the growth by condensation of the recently nucleated particles can be followed from the lowest nanometer range where they were formed and for several hours to sizes of several tens of nanometers, it means that the grown particles were formed several hours ago upwind from the field site. The place of the formation can be estimated using meteorological back-trajectories. By collecting this data for many NPF events, a map can be plotted showing the spatial distribution of regional NPF events, i.e. the number of NPF events as a function of geographical area.

To be able to use NanoMap, the following analysis steps need to be performed (Kristensson et al., 2014):

1. Traditional classification of days into regional NPF events, non-regional events, undefined events, or non-events to be able to select the days with regional events that show a clear condensational growth of the nucleated particles.
2. Produce air mass back trajectories for the site in question to be able to follow the air parcel upwind of the site.
3. Select the time period when the formation of 1.5 nm diameter starts at the site (start-time) by observing the particle number size distribution.
4. Select the time point when it is no longer possible to observe the growth of the nucleated mode (end-of-growth, EOG time). The EOG time subtracted by the period of the start-time gives the maximum number of

hours that we can follow an air mass back trajectory back to the place of formation of 1.5 nm diameter particles upwind of the site.

5. By using the data from points 1-4, it is possible to create the map of where the 1.5 nm diameter particle formation took place upwind of the current site alike the map in Figure 1.

ADCHEM model set-up and description

In this study the Aerosol Dynamics, gas and particle phase CHEMistry and radiative transfer model (ADCHEM) (Roldin et al., 2011) is used to simulate the aerosol particle and trace gas evolution along selected air-mass trajectories. The one-dimensional column version of ADCHEM (Öström et al., 2017) has been updated for this study. This section gives a brief description of ADCHEM and how it was setup for the present study.

Four consecutive days, with and without NPF, at the coastal stations Høvsøre and Finokalia respectively were selected for detailed analysis. The modelled periods were chosen based on the criteria that it should contain days with and without clear NPF and growth events and, for the Høvsøre-trajectories; all air masses should originate from the sea prior to the arrival at the measurement station. ADCHEM was run along air-mass trajectories that started 4 days upwind the stations, passing the stations at 00:00, 03:00, 06:00, 09:00, 12:00, 15:00, 18:00 and 21:00 UTC each day (except the last day at Finokalia where 18:00 and 21:00 were excluded due to lack of SMPS data), and ending 3 days downwind the stations. In total, for each model scenario, the model was run along 62 trajectories. The trajectories were calculated with the Hybrid Single Particle Lagrangian Integrated Trajectory Model (HYSPPLIT) (Draxler and Rolph, 2013) with meteorological data from the Global Data Assimilation System (GDAS), downloaded from NOAA Air Resource Laboratory Real-time Environmental Application and Display sYstem (READY) (Rolph, 2016). The meteorological data resolution was linearly interpolated from 3 h to 30 seconds (the main model time step used in the simulations). Land-use category along the trajectories was retrieved from the Global Land Cover Map for the Year 2000, GLC2000 database, European Commission Joint Research Centre (<http://forobs.jrc.ec.europa.eu/products/glc2000/products.php>).

Emission of gases and particles were added to the model layer closest to the surface each model time step. Anthropogenic gas-phase emissions included were: CO, NH₃, Non-methane volatile compounds (NMVOCs), NO_x and SO₂. These gases were retrieved from ECLIPSE V5 global emission fields (<http://www.iiasa.ac.at/web/home/research/researchPrograms/air/ECLIPSEv5.html>) created with the GAINS model (Amann et al., 2011). The resolution of the longitude-latitude emission grid was 0.5x0.5 °, except for emission from shipping

that had a resolution of $1 \times 1^\circ$. Ammonia was also assumed to be emitted from sea-bird colonies (Riddick et al., 2012a, 2012b).

SO₂ emissions from ship traffic were reduced an order of magnitude to get a better agreement between modelled and observed SO₂ concentrations. Without this reduction in SO₂ emissions the model overestimates the SO₂ concentration at Høvsøre by about a factor of 10 to 20 (Fig. S9). This overestimation is however not seen for other trace gases and not for SO₂ at Finokalia (Fig. S4a), leading us to lower only the emission of SO₂ from ship emissions. The modelled SO₂ concentrations are uncertain due to uncertainties in emission of SO₂ and DMS, but also uncertainties in deposition mechanisms of SO₂ as well as the chemical loss of SO₂ (in the gas- and aqueous phases). Chemistry transport models use various ways to model the SO₂ chemistry and deposition processes, which result in different modelled concentrations of SO₂ (Bessagnet et al., 2016; Vivanco et al., 2017). In the EURODELTA III intercomparison project, the performance of six chemical transport models were investigated and large bias of SO₂ concentrations were found in some models where the modelled values were up to a factor of 2.3-2.6 higher than the observed mean concentrations (Bessagnet et al., 2016).

Biogenic gas-phase emissions of α -pinene, β -pinene, limonene, carene and isoprene were estimated with the vegetation emission model MEGAN, by implementing the one dimensional in-canopy version of MEGAN (Smolander et al., 2014) in ADCHEM. The oceanic DMS emissions were estimated based on monthly mean seawater concentrations from Lana et al. (2011) and the sea-to-air transfer velocity parameterization from Nightingale et al. (2000). Particle-phase emissions included wind-generated marine aerosols, anthropogenic ship- and land-based emissions. The emission and size distribution of marine aerosols were estimated for every model time step when the air mass was over the sea with a parameterization from Mårtensson et al. (2003), using wind-speed data from GDAS. Emission of primary particles from ship traffic was parameterized based on the gas-phase emission of SO₂ by using a conversion factor of 8.3×10^{14} particles g_{SO₂}⁻¹ (Beecken et al., 2015). The particle number size distribution of these particles which is dominated by a mode at 39 nm in diameter was estimated based on a study by Jonsson et al. (2011). Anthropogenic land-based emissions from agriculture, waste treatment, traffic, power plants, industry, flaring and wood burning were calculated with the GAINS model.

We always initialized the model with an aerosol particle number concentration of 100 cm⁻³ in each vertical layer and with unimodal lognormal particle number size distribution with a geometric mean diameter of 120 nm and geometric standard deviation of 2. In each size bin, 90 % of the dry particle volume was assumed to be composed of non-volatile organic compounds and the remaining 10 % of ammonium sulphate. During the course of the simulation, the influence of the

initial particle number size distribution gradually decreased. At the measurement stations, the initial conditions have only a marginal impact on the simulated particle number size distributions and particle composition. The smallest primary particles added to the model (diameter less than or equal to 60 nm) were assumed to be composed of equal volume fractions sulphate and non-volatile organic material. The larger particles were assumed to have a core of soot coated with a 5 nm thick layer of sulphate and organic material (of equal volume fraction).

The one-dimensional version of ADCHEM used in this study consists of 40 vertical grid cells with logarithmic spacing, with intervals increasing from 3 m to 100 m with altitude. The model domain extends up to 2500 m a s l.

In-cloud sulphate aerosol formation and scavenging of SO_2 , H_2O_2 , NH_3 , HNO_3 and HCHO were considered in grid cells where the RH was larger or equal to 98 %, similar to Roldin et al. (2011). The clouds were assumed to resemble typical marine stratocumulus clouds with a fixed supersaturation (S) of 0.1 % and liquid water content (LWC) of 0.5 g m^{-3} . The critical supersaturation (Sc) required to activate particles in each size bin was calculated using the analytic formula for the critical supersaturations derived by Kokkola et al. (2008). This formula, which is based on Köhler theory, takes into account the impact of insoluble inclusions in the CCN. In this work, the soot particle content was the only material that was assumed to be present as an insoluble spherical inclusion in the droplets, the organic mass fraction was assumed to be fully water soluble at the critical supersaturation and inorganic salts fully dissociated. The corresponding single droplet mass for each activated aerosol particle ($Sc < S$) was calculated by dividing the LWC with the total number of activated particles, assuming that all cloud droplets had the same size. The dissolution of SO_2 and H_2O_2 and formation of sulphate aerosol mass for each activated particle size were considered as described in Roldin et al. (2011). The temperature dependent reaction rate between the dissolved SO_2 in the form of HSO_3^- and $\text{H}_2\text{O}_2(\text{aq})$ forming $\text{H}_2\text{SO}_4(\text{aq})$ was taken from table B.8 in Jacobson (2005). Below cloud scavenging of SO_2 , H_2O_2 , NH_3 , HNO_3 and HCHO were considered using the parameterization from the EMEP MSC-W chemical transport model (Simpson et al., 2012). For the wet scavenging of particles, we use the semi-empirical parameterization derived by Laakso et al. (2003).

ADCHEM solves the atmospheric diffusion equation in the vertical direction with a diffusion coefficient based on a slightly modify Grisogono scheme (Jericevic et al., 2010), depended on the height above ground, the friction velocity and the height of the atmospheric boundary layer.

The gas-phase chemistry, including selected organic and inorganic reactions from Master Chemical Mechanism (MCM) version 3.3 (Jenkin et al., 1997; Saunders et al., 2003) and a developed mechanism for highly oxidized multifunctional organic

molecules (HOMs) (Roldin et al., 2017), was solved using the Kinetic Pre-Processor (KPP) (Damian et al., 2002). For more information on the gas-phase mechanism the reader is referred to Öström et al. (2017).

The aerosol dynamics considered in this study included new particle formation, Brownian coagulation, dry and wet deposition and condensation/evaporation, modelled on a full-stationary size grid (Jacobson, 2005) consisting of 100 size bins between 1.07 nm and 2.5 μm in dry diameter. The new particle formation was modelled using the Atmospheric Cluster Dynamics Code (ACDC) (Olenius et al., 2013), which was implemented into ADCHEM. For each model time step (30 seconds) ACDC reads in the present time step temperature, concentration of NH_3 and H_2SO_4 and condensation sink of H_2SO_4 and calculates the formation, growth and evaporation of NH_3 - H_2SO_4 clusters up to a maximum size of 5 NH_3 and 5 H_2SO_4 molecules. The H_2SO_4 condensation sink is used when estimating the coagulation losses of NH_3 - H_2SO_4 clusters onto the pre-existing particle population. The largest clusters in ACDC with an estimated initial diameter of 1.07 nm serve as input values to ADCHEM where they can continue to grow by condensation of low volatile vapours (H_2SO_4 and organics). ADCHEM considers the condensation, dissolution and evaporation of H_2SO_4 , NH_3 , HNO_3 and organic compounds with a pure liquid saturation vapour pressure (p_0) less than 0.01 Pa. p_0 of the organic compounds from MCM were estimated with the group contribution method by Nannoolal et al. (2008). The estimated p_0 for the HOMs (highly oxidized multifunctional organic molecules), calculated using the group contribution method SIMPOL (Pankow and Asher, 2008), were modified with data from the detailed quantum-chemistry-based continuum solvent model COSMO-RS (Conductor-like Screening Model for Real Solvents) (Eckert and Klamt, 2002); for more information see Öström et al. (2017). In total the model considered 692 organic condensable vapours formed from the precursors listed in Table S3, included in MCM.

References

- Amann, M., Bertok, I., Borken-Kleefeld, J., Cofala, J., Heyes, C., Höglund-Isaksson, L., Klimont, Z., Nguyen, B., Posch, M., Rafaj, P., Sandler, R., Schöpp, W., Wagner, F. and Winiwarter, W.: Cost-effective control of air quality and greenhouse gases in Europe: Modeling and policy applications, *Environ. Model. Softw.*, 26(12), 1489–1501, doi:10.1016/j.envsoft.2011.07.012, 2011.
- Baranizadeh, E., Murphy, B. N., Julin, J., Falahat, S., Reddington, C. L., Arola, A., Ahlm, L., Mikkonen, S., Fountoukis, C., Patoulias, D., Minikin, A., Hamburger, T., Laaksonen, A., Pandis, S. N., Vehkamäki, H., Lehtinen, K. E. J. and Riipinen, I.: Implementation of state-of-the-art ternary new-particle formation scheme to the regional chemical transport model PMCAMx-UF in Europe, *Geosci. Model Dev.*, 9, 2741–2754, doi:10.5194/gmd-9-2741-2016, 2016.

- Beecken, J., Mellqvist, J., Salo, K., Ekholm, J., Jalkanen, J. P., Johansson, L., Litvinenko, V., Volodin, K. and Frank-Kamenetsky, D. A.: Emission factors of SO₂, NO_x and particles from ships in Neva Bay from ground-based and helicopter-borne measurements and AIS-based modeling, *Atmos. Chem. Phys.*, 15, 5229–5241, doi:10.5194/acp-15-5229-2015, 2015.
- Bessagnet, B., Pirovano, G., Mircea, M., Cuvelier, C., Aulinger, A., Calori, G., Ciarelli, G., Manders, A., Stern, R., Tsyro, S., García Vivanco, M., Thunis, P., Pay, M.-T., Colette, A., Couvidat, F., Meleux, F., Rouïl, L., Ung, A., Aksoyoglu, S., Baldasano, J. M., Bieser, J., Briganti, G., Cappelletti, A., D’Isidoro, M., Finardi, S., Kranenburg, R., Silibello, C., Carnevale, C., Aas, W., Dupont, J. C., Fagerli, H., Gonzalez, L., Menut, L., Prévôt, A. S. H., Roberts, P. and White, L.: Presentation of the EURODELTA III intercomparison exercise – evaluation of the chemistry transport models’ performance on criteria pollutants and joint analysis with meteorology, *Atmos. Chem. Phys.*, 16(19), 12667–12701, doi:10.5194/acp-16-12667-2016, 2016.
- Burkart, J., Steiner, G., Reischl, G. and Hitzenberger, R.: Long-term study of cloud condensation nuclei (CCN) activation of the atmospheric aerosol in Vienna, *Atmos. Environ.*, 45(32), 5751–5759, doi:10.1016/j.atmosenv.2011.07.022, 2011.
- Covert, D. S., Kapustin, V. N., Quinn, P. K. and Bates, T. S.: New particle formation in the marine boundary layer, *J. Geophys. Res.*, 97(D18), 20581, doi:10.1029/92JD02074, 1992.
- Covert, D. S., Wiedensohler, A., Aalto, P., Heintzenberg, J., McMurry, P. H. and Leck, C.: Aerosol number size distribution from 3 to 500 nm diameter in the Arctic marine boundary layer during summer and autumn, *Tellus B*, 48(2), 197–212, doi:10.1034/j.1600-0889.1996.t01-1-00005.x, 1996.
- Croft, B., Wentworth, G. R., Martin, R. V., Leaitch, W. R., Murphy, J. G., Murphy, B. N., Kodros, J. K., Abbatt, J. P. D. and Pierce, J. R.: Contribution of Arctic seabird-colony ammonia to atmospheric particles and cloud-albedo radiative effect, *Nat. Commun.*, 7, 13444, doi:10.1038/ncomms13444, 2016.
- Damian, V., Sandu, A., Damian, M., Potra, F. and Carmichael, G. R.: The kinetic preprocessor KPP-a software environment for solving chemical kinetics, *Comput. Chem. Eng.*, 26, 1567–1579, doi:10.1016/S0098-1354(02)00128-X, 2002.
- Eckert, F. and Klamt, A.: Fast Solvent Screening via Quantum Chemistry : COSMO-RS Approach, *AI. Chem. J.*, 48, 369–385, 2002.
- Fleming, Z. L., Monks, P. S. and Manning, A. J.: Review: Untangling the influence of air-mass history in interpreting observed atmospheric composition, *Atmos. Res.*, 104–105, 1–39, doi:10.1016/j.atmosres.2011.09.009, 2012.
- Furutani, H., Dallosto, M., Roberts, G. and Prather, K.: Assessment of the relative importance of atmospheric aging on CCN activity derived from field observations, *Atmos. Environ.*, 42(13), 3130–3142, doi:10.1016/j.atmosenv.2007.09.024, 2008.
- Guenther, A. B., Jiang, X., Heald, C. L., Sakulyanontvittaya, T., Duhl, T., Emmons, L. K. and Wang, X.: Model Development The Model of Emissions of Gases and Aerosols from Nature version 2 . 1 (MEGAN2 . 1) : an extended and updated framework for modeling biogenic emissions, *Geosci. Model Dev.*, 5, 1471–1492, doi:10.5194/gmd-5-1471-2012, 2012.
- Heintzenberg, J., Birmili, W., Wiedensohler, A., Nowak, A. and Tuch, T.: Structure,

variability and persistence of the submicrometre marine aerosol, *Tellus B*, 56(4), 357–367, doi:10.1111/j.1600-0889.2004.00115.x, 2004.

Hoppel, W. A., Frick, G. M., Fitzgerald, J. W. and Larson, R. E.: Marine boundary layer measurements of new particle formation and the effects nonprecipitating clouds have on aerosol size distribution, *J. Geophys. Res.*, 99(D7), 14443, doi:10.1029/94JD00797, 1994.

Jacobson, M. Z.: *Fundamentals of atmospheric modeling*, Second edi., Cambridge University Press, New York., 2005.

Jenkin, M. E., Saunders, S. M. and Pilling, M. J.: The tropospheric degradation of volatile organic compounds: a protocol for mechanism development, *Atmos. Environ.*, 31, 81–104, doi:10.1016/S1352-2310(96)00105-7, 1997.

Jericevic, A., Kraljevic, L., Grisogono, B., Fagerli, H. and Vecenaj, Z.: Parameterization of vertical diffusion and the atmospheric boundary layer height determination in the EMEP model, *Atmos. Chem. Phys.*, 10, 341–364, doi:10.5194/acp-10-341-2010, 2010.

Jonsson, Å. M., Westerlund, J. and Hallquist, M.: Size-resolved particle emission factors for individual ships, *Geophys. Res. Lett.*, 38, L12809, doi:10.1029/2011GL047672, 2011.

Kivekäs, N., Massling, A., Grythe, H., Lange, R., Rusnak, V., Carreno, S., Skov, H., Swietlicki, E., Nguyen, Q. T., Glasius, M. and Kristensson, A.: Contribution of ship traffic to aerosol particle concentrations downwind of a major shipping lane, *Atmos. Chem. Phys.*, 14(16), 8255–8267, doi:10.5194/acp-14-8255-2014, 2014.

Kokkola, H., Vesterinen, M., Anttila, T., Laaksonen, A. and Lehtinen, K. E. J.: Technical note: Analytical formulae for the critical supersaturations and droplet diameters of CCN containing insoluble material, *Atmos. Chem. Phys.*, 8(7), 1985–1988, doi:10.5194/acp-8-1985-2008, 2008.

Kristensson, A., Dal Maso, M., Swietlicki, E., Hussein, T., Zhou, J., Kerminen, V.-M. and Kulmala, M.: Characterization of new particle formation events at a background site in Southern Sweden: relation to air mass history, *Tellus B Chem. Phys. Meteorol.*, 60(3), 330–344, doi:10.1111/j.1600-0889.2008.00345.x, 2008.

Kristensson, A., Johansson, M., Swietlicki, E., Kivekäs, N., Hussein, T., Nieminen, T., Kulmala, M. and Dal Maso, M.: NanoMap: Geographical mapping of atmospheric new-particle formation through analysis of particle number size distribution and trajectory data, *Boreal Environ. Res.*, 19, 329–342, 2014.

Laakso, L., Grönholm, T., Rannik, Ü., Kosmale, M., Fiedler, V., Vehkamäki, H. and Kulmala, M.: Ultrafine particle scavenging coefficients calculated from 6 years field measurements, *Atmos. Environ.*, 37, 3605–3613, doi:10.1016/S1352-2310(03)00326-1, 2003.

Lana, A., Bell, T. G., Simó, R., Vallina, S. M., Ballabrera-Poy, J., Kettle, A. J., Dachs, J., Bopp, L., Saltzman, E. S., Stefels, J., Johnson, J. E. and Liss, P. S.: An updated climatology of surface dimethylsulfide concentrations and emission fluxes in the global ocean, *Global Biogeochem. Cycles*, 25(1), GB1004, doi:10.1029/2010GB003850, 2011.

Mårtensson, E. M., Nilsson, E. D., de Leeuw, G., Cohen, L. H. and Hansson, H.-C.: Laboratory simulations and parameterization of the primary marine aerosol production, *J. Geophys. Res. Atmos.*, 108(D9), 4297, doi:10.1029/2002JD002263, 2003.

Nannoolal, Y., Rarey, J. and Ramjugernath, D.: Estimation of pure component properties, *Fluid Phase Equilib.*, 269(1–2), 117–133, doi:10.1016/j.fluid.2008.04.020, 2008.

Nightingale, P. D., Malin, G., Law, C. S., Watson, A. ., Liss, P. S., Liddicoat, M. I., Boutin, J. and Upstill-Goddard, R. C.: In situ evaluation of air-sea gas exchange parameterizations using novel conservative and volatile tracers, *Global Biogeochem. Cycles*, 14(1), 373–387, doi:10.1029/1999GB900091, 2000.

Olenius, T., Kupiainen-Määttä, O., Ortega, I. K., Kurtén, T. and Vehkamäki, H.: Free energy barrier in the growth of sulfuric acid–ammonia and sulfuric acid–dimethylamine clusters, *J. Chem. Phys.*, 139(8), 84312, doi:10.1063/1.4819024, 2013.

Öström, E., Putian, Z., Schurgers, G., Mishurov, M., Kivekäs, N., Lihavainen, H., Ehn, M., Rissanen, M. P., Kurtén, T., Boy, M., Swietlicki, E. and Roldin, P.: Modeling the role of highly oxidized multifunctional organic molecules for the growth of new particles over the boreal forest region, *Atmos. Chem. Phys.*, 17(14), 8887–8901, doi:10.5194/acp-17-8887-2017, 2017.

Paasonen, P., Kupiainen, K., Klimont, Z., Visschedijk, A., Denier van der Gon, H. A. C. and Amann, M.: Continental anthropogenic primary particle number emissions, *Atmos. Chem. Phys.*, 16(11), 6823–6840, doi:10.5194/acp-16-6823-2016, 2016.

Pankow, J. F. and Asher, W. E.: SIMPOL.1: a simple group contribution method for predicting vapor pressures and enthalpies of vaporization of multifunctional organic compounds, *Atmos. Chem. Phys.*, 8(10), 2773–2796, doi:10.5194/acp-8-2773-2008, 2008.

Pikridas, M., Riipinen, I., Hildebrandt, L., Kostenidou, E., Manninen, H., Mihalopoulos, N., Kalivitis, N., Burkhardt, J. F., Stohl, A., Kulmala, M. and Pandis, S. N.: New particle formation at a remote site in the eastern Mediterranean, *J. Geophys. Res. Atmos.*, 117(D12), D12205, doi:10.1029/2012JD017570, 2012.

Pirjola, L., O'Dowd, C. D., Brooks, I. M. and Kulmala, M.: Can new particle formation occur in the clean marine boundary layer?, *J. Geophys. Res. Atmos.*, 105(D21), 26531–26546, doi:10.1029/2000JD900310, 2000.

Riddick, S. N., Dragosits, U., Blackall, T. D., Daunt, F., Wanless, S. and Sutton, M. A.: Global ammonia emissions from seabirds, *NERC Environ. Inf. Data Cent.*, doi:10.5285/C9E802B3-43C8-4B36-A3A3-8861D9DA8EA9, 2012a.

Riddick, S. N., Dragosits, U., Blackall, T. D., Daunt, F., Wanless, S. and Sutton, M. A.: The global distribution of ammonia emissions from seabird colonies, *Atmos. Environ.*, 55, 319–327, doi:10.1016/j.atmosenv.2012.02.052, 2012b.

Roldin, P., Öström, E., Taipale, D., Kurtén, T., Rissanen, M., Kulmala, M., Olenius, T., Riipinen, I., Virtanen, A., Ehn, M. and Boy, M.: Manuscript in preparation: Constraining the role of highly oxidized organic molecules for the growth of new particles over the boreal forest., 2017.

Roldin, P., Swietlicki, E., Schurgers, G., Arneth, A., Lehtinen, K. E. J., Boy, M. and Kulmala, M.: Development and evaluation of the aerosol dynamics and gas phase chemistry model ADCHEM, *Atmos. Chem. Phys.*, 11, 5867–5896, doi:10.5194/acp-11-5867-2011, 2011.

Rolph, G. D.: Real-time Environmental Applications and Display sYstem (READY) Website (<http://ready.arl.noaa.gov>), Sliver Spring, MD., 2016.

Saunders, S. M., Jenkin, M. E., Derwent, R. G. and Pilling, M. J.: Protocol for the development of the Master Chemical Mechanism, MCM v3 (Part A): tropospheric degradation of non-aromatic volatile organic compounds, *Atmos. Chem. Phys.*, 3, 161–

180, doi:10.5194/acp-3-161-2003, 2003.

Simpson, D., Benedictow, A., Berge, H., Bergström, R., Emberson, L. D., Fagerli, H., Flechard, C. R., Hayman, G. D., Gauss, M., Jonson, J. E., Jenkin, M. E., Nyíri, A., Richter, C., Semeena, V. S., Tsyro, S., Tuovinen, J.-P., Valdebenito, Á. and Wind, P.: The EMEP MSC-W chemical transport model – technical description, *Atmos. Chem. Phys.*, 12(16), 7825–7865, doi:10.5194/acp-12-7825-2012, 2012.

Smolander, S., He, Q., Mogensen, D., Zhou, L., Bäck, J., Ruuskanen, T., Noe, S., Guenther, A., Aaltonen, H., Kulmala, M. and Boy, M.: Comparing three vegetation monoterpene emission models to measured gas concentrations with a model of meteorology, air chemistry and chemical transport, *Biogeosciences*, 11(19), 5425–5443, doi:10.5194/bg-11-5425-2014, 2014.

Stohl, A., Aamaas, B., Amann, M., Baker, L. H., Bellouin, N., Berntsen, T. K., Boucher, O., Cherian, R., Collins, W., Daskalakis, N., Dusinska, M., Eckhardt, S., Fuglestedt, J. S., Harju, M., Heyes, C., Hodnebrog, Ø., Hao, J., Im, U., Kanakidou, M., Klimont, Z., Kupiainen, K., Law, K. S., Lund, M. T., Maas, R., MacIntosh, C. R., Myhre, G., Myriokefalitakis, S., Olivie, D., Quaas, J., Quennehen, B., Raut, J.-C., Rumbold, S. T., Samset, B. H., Schulz, M., Seland, Ø., Shine, K. P., Skeie, R. B., Wang, S., Yttri, K. E. and Zhu, T.: Evaluating the climate and air quality impacts of short-lived pollutants, *Atmos. Chem. Phys.*, 15(18), 10529–10566, doi:10.5194/acp-15-10529-2015, 2015.

Vivanco, M. G., Bessagnet, B., Cuvelier, C., Theobald, M. R., Tsyro, S., Pirovano, G., Aulinger, A., Bieser, J., Calori, G., Ciarelli, G., Manders, A., Mircea, M., Aksoyoglu, S., Briganti, G., Cappelletti, A., Colette, A., Couvidat, F., D’Isidoro, M., Kranenburg, R., Meleux, F., Menut, L., Pay, M. T., Rouil, L., Silibello, C., Thunis, P. and Ung, A.: Joint analysis of deposition fluxes and atmospheric concentrations of inorganic nitrogen and sulphur compounds predicted by six chemistry transport models in the frame of the EURODELTAIII project, *Atmos. Environ.*, 151, 152–175, doi:10.1016/j.atmosenv.2016.11.042, 2017.

Wang, F., Zhang, Z., Massling, A., Ketzel, M. and Kristensson, A.: Particle formation events measured at a semirural background site in Denmark, *Environ. Sci. Pollut. Res. Int.*, 20(5), 3050–3059, 2013.

Weber, R. J., McMurtry, P. H., Mauldin, L., Tanner, D. J., Eisele, F. L., Brechtel, F. J., Kreidenweis, S. M., Kok, G. L., Schillawski, R. D. and Baumgardner, D.: A study of new particle formation and growth involving biogenic and trace gas species measured during ACE 1, *J. Geophys. Res. Atmos.*, 103(D13), 16385–16396, doi:10.1029/97JD02465, 1998.

Wesely, M. L.: Parameterization of surface resistances to gaseous dry deposition in regional-scale numerical models, *Atmos. Environ.*, 23(6), 1293–1304, doi:10.1016/0004-6981(89)90153-4, 1989.

Zhang, L., Brook, J. R. and Vet, R.: A revised parameterization for gaseous dry deposition in air-quality models, *Atmos. Chem. Phys.*, 3(6), 2067–2082, doi:10.5194/acp-3-2067-2003, 2003.

SI Appendix

SI Tables

Table S1. Median SO₂ concentrations measured at different sites and modelled by PMCAMx-UF during May 1-29, 2008. The median concentration during entire 2008 is compared at selected stations, except at Ayia Marina, where all measurements are from 2009.

Station	PMCAMx-UF SO ₂ (ppb) May 1-29, 2008	Measured SO ₂ (ppb) May 1-29, 2008	Observed SO ₂ (ppb) 2008
Ulborg ¹	0.70	0.16	0.077
Ulborg (North Sea) ²	0.24	0.087	
Westerland ³	0.72	0.25	0.25
Birkenes ⁴	0.47	0.12	0.03
Starina ⁵	0.98	0.093	0.25
La Tardiere ⁶	0.24	0.13	0.11
O Savinao ⁷	3.5	0.099	0.099
Ayia Marina ⁸	2.2	0.65 (May 2009)	0.66 (2009)

¹56° 17' N 8° 25' E (Denmark, close to Høvsøre).

²During 8 days with winds from northern North Sea in the period May 8 – May 22, 2008.

³54° 55' N 8° 18' E (North Sea coastal station, north-eastern Germany).

⁴58° 23' N, 8° 15' E (southern Norway, close to North Sea coast line).

⁵49° 03' N 22° 16' E (eastern Slovakia, typical eastern European site).

⁶46° 39' N 0° 45' W (western France, typical western European site).

⁷43° 14' N 7° 41' W (north-western Spain).

⁸35° 02' N 33° 03' E (Cyprus, relatively close to Finokalia station in the Mediterranean).

Table S2. Median Particle number concentrations (cm⁻³) in different particle diameter intervals for several European sites during May 1-29, 2008 as modelled by PMCAMx-UF as well as observed concentrations.

Station	PMCAMx-UF 10-40 nm	PMCAMx-UF 40-100 nm	PMCAMx-UF > 100 nm	Data 10-40 nm	Data 40-100 nm	Data >100 nm
Hovsore ¹	3950	2332	553	647	1081	576
Finokalia ²	1501	2813	873	657	2194	2166
Vavihill ³	4784	2143	488	688	1123	833
Cabauw ⁴	5538	3991	1255	1623	3561	1990
Mace Head ⁵	4387	2219	382	754	975	796
Puy de Dome ⁶	2291	1590	463	688	985	959
K-Puszt ⁷	9025	3537	488	1919	1588	1464

¹ 56° 17' N 8° 9' E (Denmark, North Sea coast line, observation data May 2012).

² 35° 19' N 25° 40' E (Crete, eastern Mediterranean, observation data June 2008 – June 2009).

³ 56° 1' N, 13° 9' E (southwestern Sweden).

⁴ 51° 58' N 4° 56' E (northern Netherlands).

⁵ 53° 20' N 9° 54' W (western Ireland).

⁶ 45° 46' N 2° 57' E (southern France).

⁷ 46° 58' N 19° 35' E (Hungary).

Table S3. Gas-phase precursors

Gas-phase precursor	Emission database/Emission model
α -pinene	MEGAN
β -pinene	MEGAN
Limonene	MEGAN
Other monoterpenes (treated as carene)	MEGAN
Isoprene	MEGAN
Ethane	ECLIPSE
Butane	ECLIPSE
Etene	ECLIPSE
Propene	ECLIPSE
Oxylene	ECLIPSE
Formaldehyde	ECLIPSE
Acetaldehyde	ECLIPSE
Methyl Ethyl Ketone	ECLIPSE
Glyoxal	ECLIPSE
Methylglyoxal	ECLIPSE
1-petene	ECLIPSE
2-methylpropene	ECLIPSE
Dodecane	ECLIPSE
Benzene	ECLIPSE
Decane	ECLIPSE
Ethylbenzene	ECLIPSE
Nonane	ECLIPSE
p-xylene	ECLIPSE
Toluene	ECLIPSE
Undecane	ECLIPSE
m-xylene	ECLIPSE
1-butene	ECLIPSE
1,2,4-trimethylbenzene	ECLIPSE
1,3,5-trimethylbenzene	ECLIPSE
1,2,3-trimethylbenzene	ECLIPSE

SI Figures

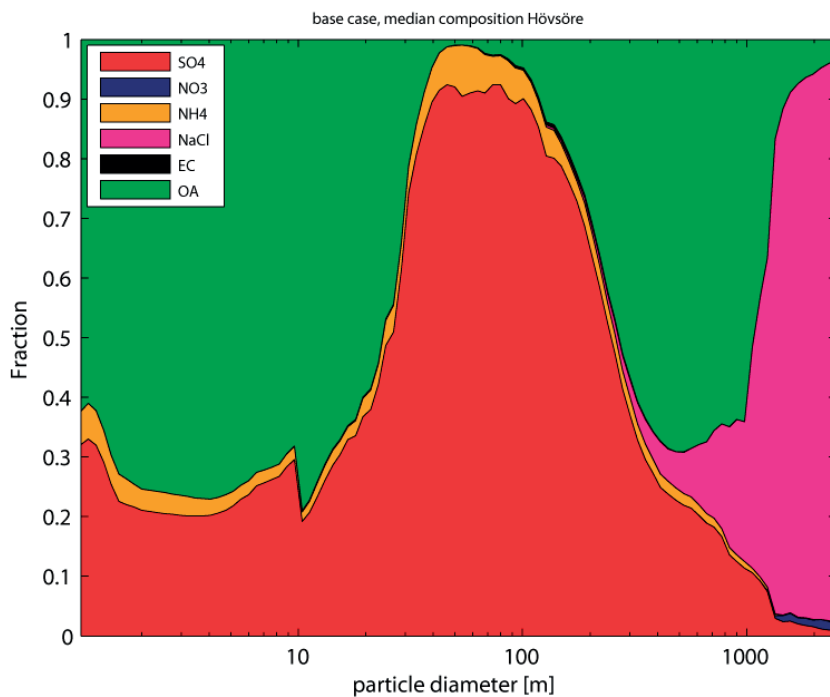


Figure S1. Modelled median chemical composition at Høvsøre using ADCHEM. Aitken mode particles are dominated by sulphate.

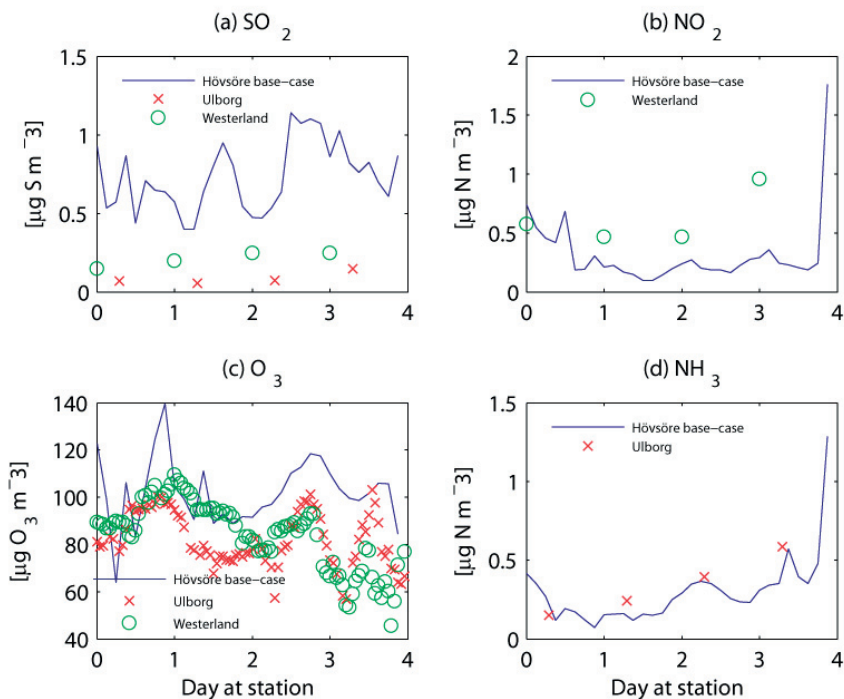


Figure S2. Modelled (with ADCHEM) gas-phase concentration of (a) SO_2 , (b) NO_2 , (c) O_3 and (d) NH_3 , compared with observed concentration at stations relatively close to Høvsøre: Ulborg (56.28 N, 8.43 E) about 30 km southeast of Høvsøre and Westerland (54.93N, 8.31 E) about 200 km south of Høvsøre, located on an island outside the German/Danish coastline.

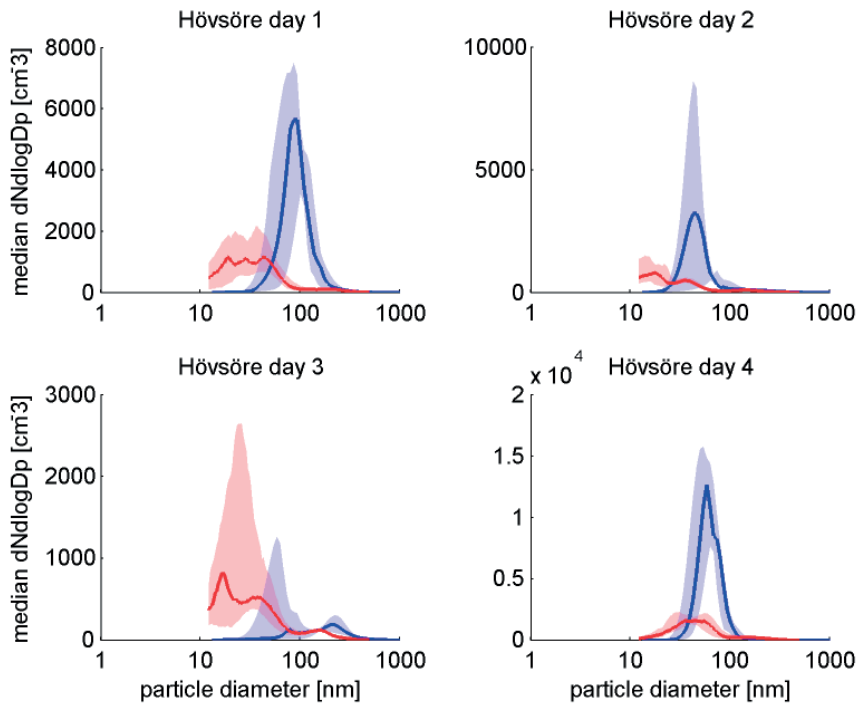


Figure S3. The median particle number size distribution each day at Høvsøre modelled with the base-case scenario (ADCHEM, reduced SO₂ emissions). The modelled air masses arriving at Høvsøre especially day 1 and 4 have contributions from land-based emissions. Note the different scales.

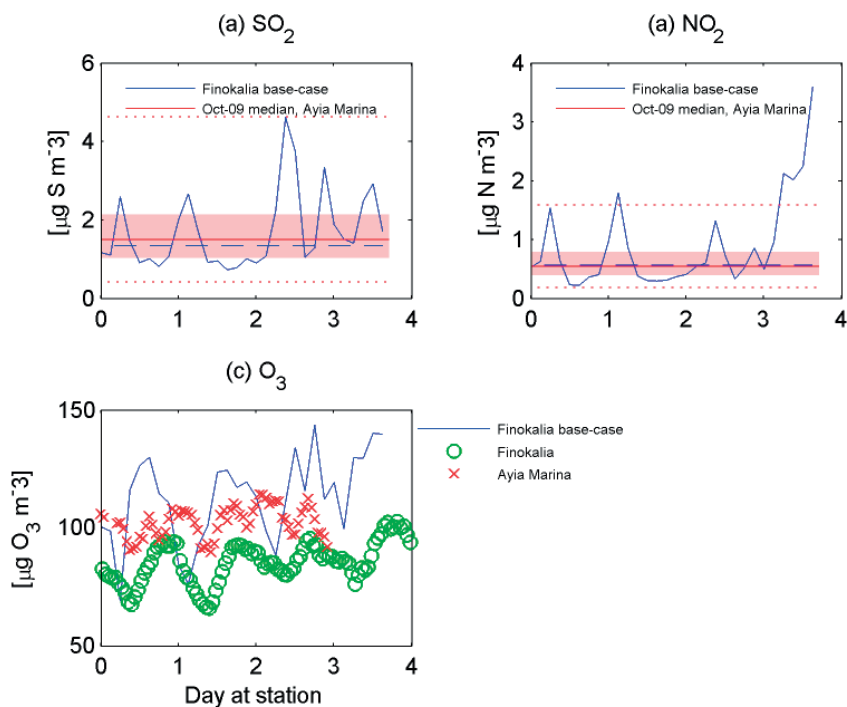


Figure S4. Modelled (with ADCHEM) gas-phase concentration of (a) SO₂, (b) NO₂ and (c) O₃, compared with observed median concentration at: Ayia Marina (35.04 N, 33.06 E) at Cyprus October 2009, a year later than the modelled concentration at Finokalia. Also shown are the median modelled gas-phase concentrations (dashed, blue line) and the 5th and 95th percentiles of the observed concentrations (red dashed lines) and the 25th and 75 percentiles of the observed concentrations (shaded areas). The ozone measurements were conducted 11th to 14th October 2008, and also at Finokalia, which enabled a direct comparison to the modelled ozone concentrations.

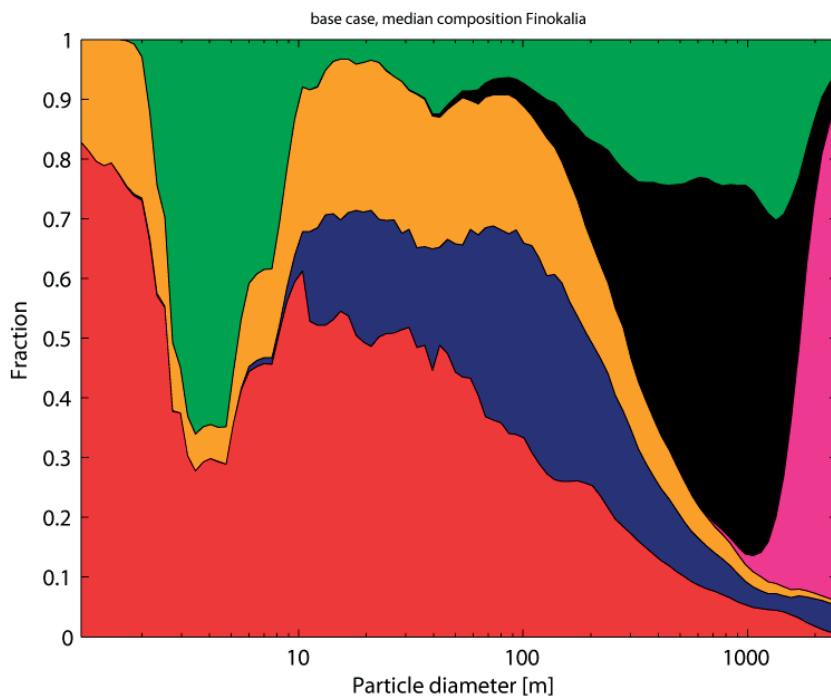


Figure S5. Modelled median chemical composition at Finokalia using ADCHEM. Aitken mode particles are dominated by ammonium sulphate and ammonium nitrate.

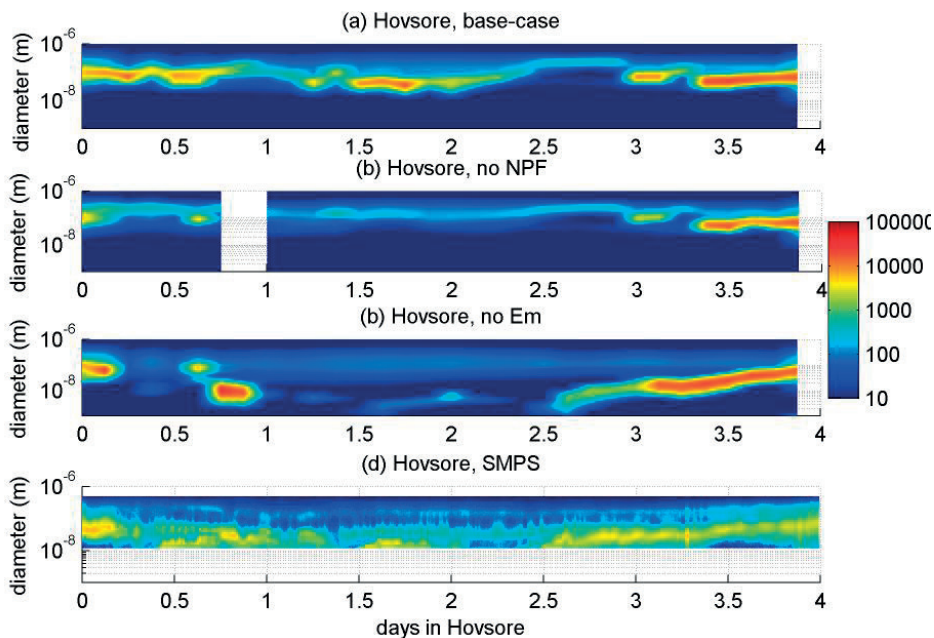


Figure S6. Particle number size distribution at Høvsøre during four days in May 2012 (4-7th May), modelled with (a) base-case scenario, (b) no-NPF over sea scenario and (c) no anthropogenic emissions over sea scenario compared with (d) observed size distribution. All model results are from ADCHEM, with reduced SO₂ emissions.

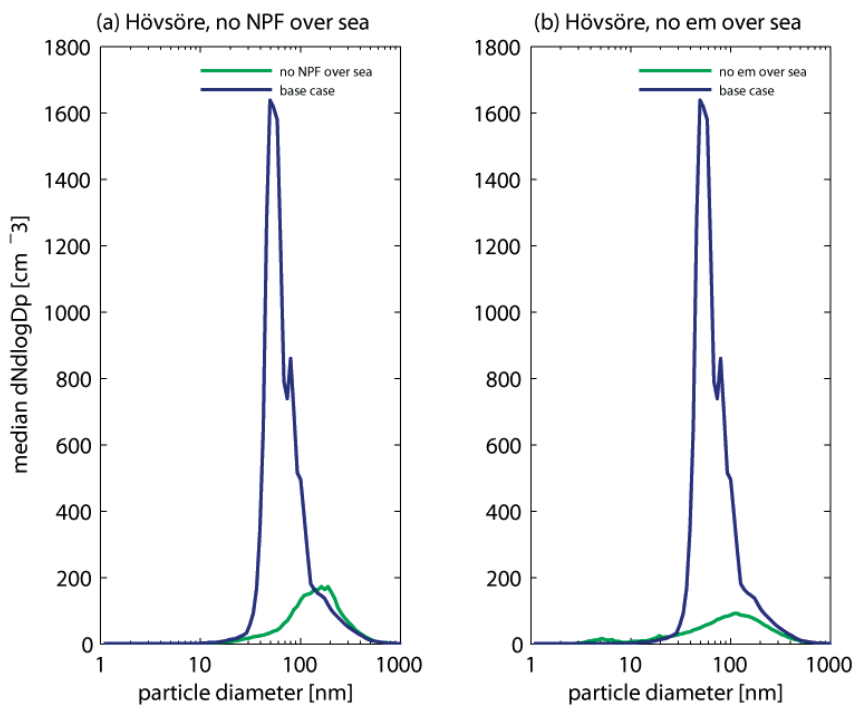


Figure S7. The modelled (using ADCHEM with reduced SO₂ emissions) median particle number size distribution at Høvsøre modelled with (a) the no-NPF over sea scenario and (b) the no anthropogenic emission over sea scenario, compared to the modelled base-case scenario (blue lines).

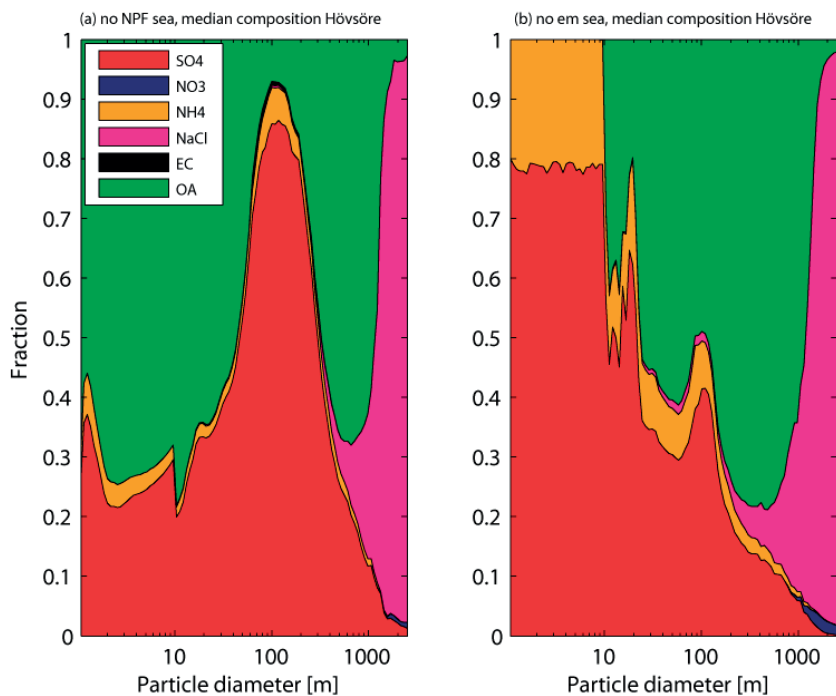


Figure S8. Chemical composition at Høvsøre modelled using ADCHEM, with (a) the no NPF over sea scenario and (b) the no antropogenic emission over sea scenario.

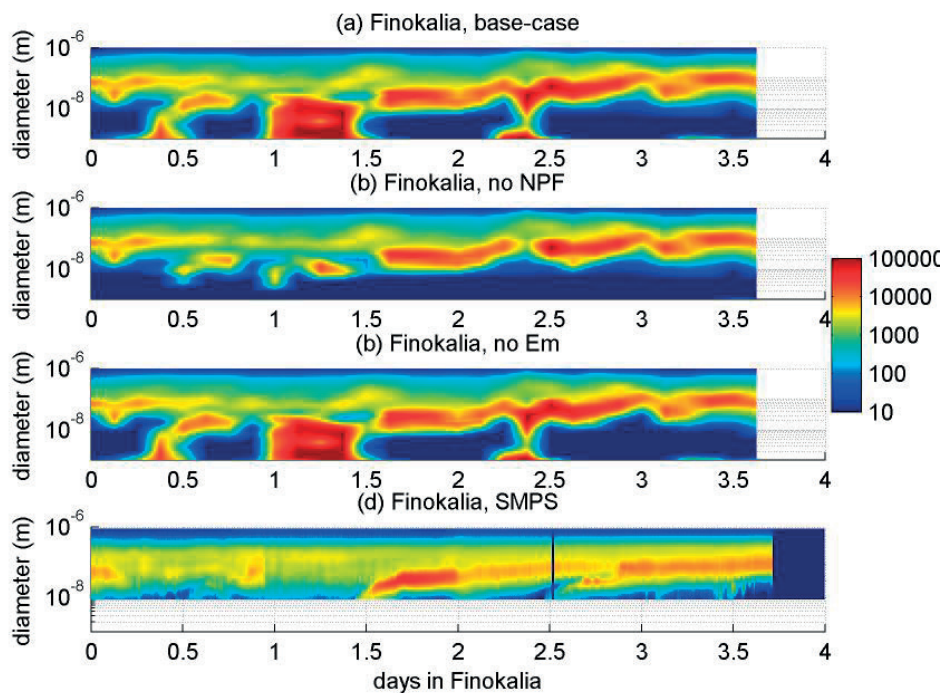


Figure S9. Particle number size distribution at Finokalia during four days in October 2008 (11–14th October), modelled using ADCHEM, with (a) base-case scenario, (b) no-NPF over sea scenario and (c) no anthropogenic emissions over sea scenario compared with (d) observed size distribution.

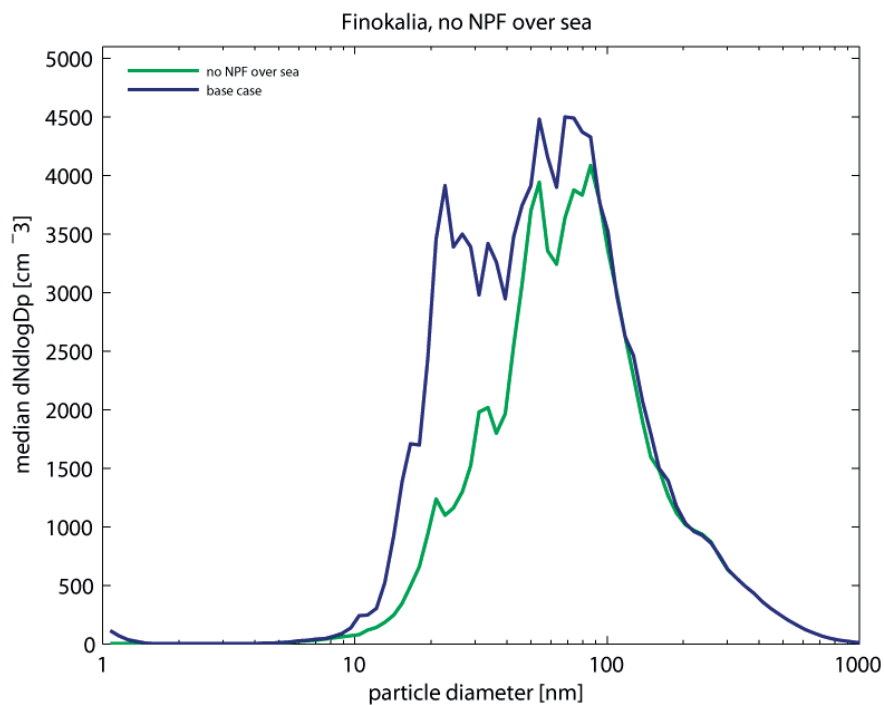


Figure S10. The median particle number size distribution at Finokalia modelled using ADCHEM, with the no-NPF over sea scenario (green line), compared to the modelled base-case scenario (blue line).

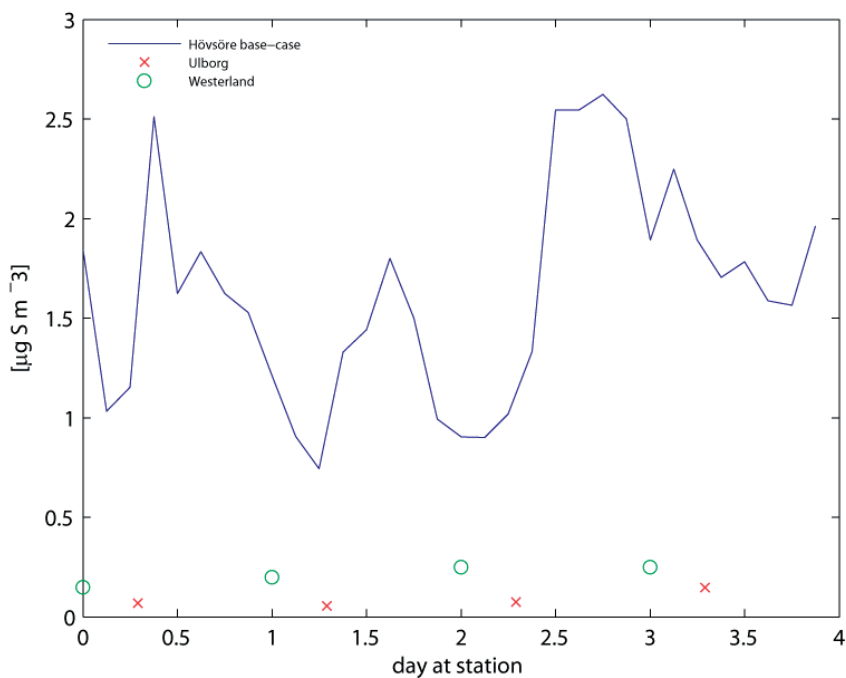


Figure S10. Modelled (with ADCHEM) gas-phase concentration of SO₂ without lowering the emission of SO₂ from ship traffic, compared with observed concentration at stations relatively close to Høvsøre: Ulborg (56.28 N, 8.43 E) about 30 km southeast of Høvsøre and Westerland (54.93N, 8.31 E) about 200 km south of Høvsøre, located on an island outside the German/Danish coastline.

DOCTORAL THESES PUBLISHED IN ENVIRONMENTAL SCIENCE, LUND UNIVERSITY

1. Georg K.S. Andersson (2012) Effects of farming practice on pollination across space and time. Department of Biology/Centre for Environmental and Climate Research
2. Anja M. Ödman (2012) Disturbance regimes in dry sandy grasslands – past, present and future. Department of Biology/ Centre for Environmental and Climate Research
3. Johan Genberg (2013) Source apportionment of carbonaceous aerosol. Department of Physics/Centre for Environmental and Climate Research
4. Petra Bragée (2013) A palaeolimnological study of the anthropogenic impact on dissolved organic carbon in South Swedish lakes. Department of Geology/ Centre for Environmental and Climate Research
5. Estelle Larsson (2013) Sorption and transformation of anti-inflammatory drugs during wastewater treatment. Department of Chemistry/ Centre for Environmental and Climate Research
6. Magnus Ellström (2014) Effects of nitrogen deposition on the growth, metabolism and activity of ectomycorrhizal fungi. Department of Biology/ Centre for Environmental and Climate Research
7. Therese Irminger Street (2015) Small biotopes in agricultural landscapes: importance for vascular plants and effects on management. Department of physical geography and ecosystem science/ Department of Biology/ Centre for Environmental and Climate Research
8. Helena I. Hanson (2015) Natural enemies: Functional aspects of local management in agricultural landscapes. Department of Biology/ Centre for Environmental and Climate Research
9. Lina Nikoleris (2016) The estrogen receptor in fish and effects of estrogenic substances in the environment: ecological and evolutionary perspectives and societal awareness Department of Biology/ Centre for Environmental and Climate Research

10. Cecilia Hultin (2016) Estrogen receptor and multixenobiotic resistance genes in freshwater fish and snails: identification and expression analysis after pharmaceutical exposure. Centre for Environmental and Climate Research
11. Annika M. E. Söderman (2016) Small biotopes: Landscape and management effects on pollinators. Department of Biology/ Centre for Environmental and Climate Research
12. Wenxin Ning (2016) Tracking environmental changes of the Baltic Sea coastal zone since the mid-Holocene. Department of Geology/Centre for Environmental and Climate Research
13. Karin Mattsson (2016) Nanoparticles in the aquatic environment, Particle characterization and effects on organisms. Department of Chemistry/Center for Environmental and Climate Research
14. Ola Svahn (2016) Tillämpad miljöanalytisk kemi för monitorering och åtgärder av antibiotika- och läkemedelsrester I Vattenriket. School of Education and Environment, Kristianstad university
15. Pablo Urrutia Cordero (2016) Putting food web theory into action: Local adaptation of freshwaters to global environmental change. Department of Biology/Centre for Environmental and Climate Research
16. Lin Yu (2016) Dynamic modelling of the forest ecosystem: Incorporation of the phosphorous cycle. Centre for environmental and Climate Research
17. Behnaz Pirzamanbein (2016) Recontruction of past European land cover based on fossil pollen data: Gaussian Markov random field models for compositional data. Centre for mathematical sciences/Centre for environmental and climate research
18. Arvid Bolin (2017) Ecological interactions in human modified landscapes – Landscape dependent remedies for the maintenance of biodiversity and ecosystem services. Department of Biology/Centre for Environmental and Climate Research
19. Johan Martinsson (2017) Development and Evaluation of Methods in Source Apportionment of the Carbonaceous Aerosol. Department of Physics/Centre for Environmental an Climate Research
20. Emilie Öström (2017) Modeling of new particle formation and growth in the atmospheric boundary layer. Department of Physics/Centre for Environmental an Climate Research

- I. Hermansson, E., Roldin, P., Rusanen, A., Mogensen, D., Kivekäs, N., Väänänen, R., Boy, M., and Swietlicki, E. (2014). Biogenic SOA formation through gas-phase oxidation and gas-to-particle partitioning – a comparison between process models of varying complexity. *Atmospheric Chemistry and Physics*, 14, 11853-11869, doi:10.5194/acp-14-11853-2014
- II. Öström, E., Putian, Z., Schurgers, G., Mishurov, M., Kivekäs, N., Lihavainen, H., Ehn, M., Rissanen, M.P., Kurtén, T., Boy, M., Swietlicki, E. and Roldin, P. (2016). Modeling the role of highly oxidized multifunctional organic molecules for the growth of new particles over the boreal forest region. *Atmospheric Chemistry and Physics*, 17, 8887-8901, doi: 10.5194/acp-17-8887-2017
- III. Roldin, P., Öström, E., Kurtén, T., Olenius, T., Rissanen, M., Rantala, P., Hao, L., Kulmala, M., Virtanen, A., Riipinen, I., Ehn, M. and Boy, M. Constraining the concentrations and contribution of highly oxidized organic molecules to the growth of new particles over the Boreal forest. Manuscript in preparation.
- IV. Öström, E., Roldin, P., Julin, J., Massling, A., Lange, R., Glasius, M., Berg-Malmberg, V., Manninen, H., Kalivitis N., Olenius, T., Riipinen, I. and Kristensson, A. Potential influence on CCN from new particle formation and emissions in the polluted marine boundary layer. Manuscript in preparation.

